Dioxygen Activation by Thiolate Ligated Complexes with Tunable π-acceptor N-heterocyclic Ligands

Chaau Yan Poon

A dissertation

submitted in partial fulfillment of the

requirements for the degree of

Doctor of Philosophy

University of Washington

2021

Reading Committee:

Julie A. Kovacs, Chair

Brandi M. Cossairt

Daniel R. Gamelin

Program Authorized to Offer Degree:

Chemistry

University of Washington

Abstract

Dioxygen Activation by Thiolate Ligated Complexes
with Tunable π-acceptor N-heterocyclic Ligands

Chaau Yan Poon

Chair of the Supervisory Committee:
Professor Julia A. Kovacs
Department of Chemistry

Dioxygen reduction and water oxidation are critical processes for aerobic life. Developing a better understanding of O-O bond activation and formation mechanisms mediated by metalloenzymes involving first-row transition metals such as Fe and Mn, would provide valuable insights for catalyst and drug development. While synthetic iron and copper oxo species generated from O_2 have been extensively studied, the process of manganese dioxygen activation and its intermediates is comparatively unexplored. This dissertation focuses on the synthesis, characterization, and dioxygen reactivity of structurally analogous Mn- and Fe-thiolate complexes with tunable N-heterocyclic amine ligands. Chapter one provides an introduction to oxygen-evolving and oxygen-dependent metalloenzymes containing Mn and Fe metallocofactors. Chapter two highlights how metal ion Lewis acidity and steric properties influence the kinetics and thermodynamics of O_2 activation by a series of structurally analogous Mn-thiolate complexes. A total of four high-valent Mn-oxo intermediates were observed along the O_2 activation pathway, including $Mn^{III}Mn^{IV}$(μ-oxo)(μ-OH) intermediates. Chapter three

covers the hydrogen atom transfer activity by the $Mn^{III}Mn^{IV}$(μ-oxo)(μ-OH) intermediate characterized in chapter two. Chapter four focuses on the synthesis, characterization, and preliminary O_2 reactivity of Fe-thiolate complexes that possess a tunable N-heterocyclic amine, wherein a less Lewis acidic Fe^{II} species within the structurally analogous series led to the observation of a new O_2 activation intermediate. Chapter five discusses the comparison between the structures and reactivities of alkoxide- and thiolate-ligated Mn alkylperoxo species with otherwise identical ligand frameworks, which demonstrates key insight into how the primary coordination sphere of active sites could alter their reactivity.

TABLE OF CONTENTS

List of Figures

List of Tables

List of Schemes

Glossary

Common Abbreviations:

τ	5-coordinate geometry index
δ	Isomer shift
$\sigma_{\theta(oct)}^2$	6-coordinate geometry index
μ_{eff}	Effective magnetic moment
$\perp$-mode	perpendicular-mode
Å	Angström
BDE	Bond dissociation energy
CDO	Cysteine Dioxygenase
CHD	1,4-cyclohexadiene
Cys	Cysteine
CT	Charge transfer
CV	Cyclic voltammetry
DCM	Dichloromethane
deg	Degrees
DFT	Density functional theory
e^-	Electron
E_a	Activation energy
EAS	Electronic absorption spectrum
EPR	Electron paramagnetic resonance
ESI-MS	Electrospray-ionization mass spectroscopy

ET	Electron transfer
Et	Ethyl
Et_2O	Diethyl ether
EtCN	Propionitrile
Fc	Ferrocene
Fc^+	Ferrocenium
Fe	Iron
g	Gauss
GC-MS	Gas chromatography-mass spectrometry
$H^\bullet$	Hydrogen atom
H^+	Proton
HAT	Hydrogen atom transfer
HOMO	Highest occupied molecular orbital
Hz	Hertz
KIE	Kinetic isotope effect
LMCT	Ligand-to-metal charge transfer
MeCN	Acetonitrile
MeOH	Methanol
MLCT	Metal-to-ligand charge transfer
Mn	Manganese
N_3^-	Azide anion
NMR	Nuclear magnetic resonance
O_2	Dioxygen

O_2^-	Superoxide
OEC	Oxygen-evolving complex
PCET	Proton-coupled electron transfer
ppm	Parts per million
Pr	Propyl
PSII	Photosystem II
PT	Proton transfer
RDS	Rate determining step
RNR	Ribonucleotide reductase
ROS	Reactive oxygen species
RS^-	Thiolate
SCE	Saturated calomel electrode
SOD	Superoxide dismutase
SOR	Superoxide reductase
^{t}BuOOH	*tert*-butyl hydroperoxide
TD-DFT	Time dependent density functional theory
TEA	Triethylamine
TEMPO$^\bullet$	2,2,6,6-tetramethylpiperidinyloxy
TEMPOH	1-hydroxy-2,2,6,6-tetramethyl-piperidine
THF	Tetrahydrofuran
V	Volt
Y$^\bullet$	Tyrosyl radical

List of Numbered Compounds (by chapter)

Chapter 2 and 3

L^{Mepy} (6-Me-DPEN)$N_4{}^{Me2}S^-$

L^{Py} (6-H-DPEN)$N_4{}^{Me2}S^-$

L^{Quino} (QuinoEN)$N_4{}^{Me2}S^-$

L^{MeOpy} (6-MeO-DPEN)$N_4{}^{Me2}S^-$

1^{Mepy} $[Mn^{II}(L^{Mepy})]^+$

1^{Py} $[Mn^{II}(L^{Py})]^+$

1^{Quino} $[Mn^{II}(L^{Quino})]^+$

1^{MeOpy} $[Mn^{II}(L^{MeOpy})]_2{}^{2+}$

2^{Mepy} $[Mn(L^{Mepy})(O_2)]^+$

2^{Quino} $[Mn(L^{Quino})(O_2)]^+$

2^{MeOpy} $[Mn(L^{MeOpy})(O_2)]^+$

3^{Mepy} $\{[Mn^{III}(L^{Mepy})]_2(\mu\text{-}O_2)\}^{2+}$

3^{Quino} $\{[Mn^{III}(L^{Quino})]_2(\mu\text{–}O_2)\}^{2+}$

3^{MeOpy} $\{[Mn^{III}(L^{MeOpy})]_2(\mu\text{–}O_2)\}^{2+}$

4^{MeOpy} $\{[Mn^{IV}(L^{MeOpy})]_2(\mu\text{–}O_2)\}^{2+}$

5^{MeOpy} $[(Mn^{IV}(L^{MeOpy}))(\mu^2\text{-}O)(\mu^2\text{-}OH)(Mn^{III}(L^{MeOpy}))]^{2+}$

6^{Mepy} $\{[Mn^{III}(L^{Mepy})]_2(\mu\text{-}O)\}^{2+}$

6^{Py} $\{[Mn^{III}(L^{Py})]_2(\mu\text{-}O)\}^{2+}$

6^{Quino} $\{[Mn^{III}(L^{Quino})]_2(\mu\text{–}O)\}^{2+}$

6^{MeOpy} $\{[Mn^{III}(L^{MeOpy})]_2(\mu\text{–}O)\}^{2+}$

Chapter 4

1^{Tren}	$[Fe^{II}(S^{Me2}N_4(tren))]^+$
1^{Py}	$[Fe^{II}(S^{Me2}N_4(6\text{-H-DPEN}))]^+$
1^{Py}-OMe	$[Fe^{II}(S^{Me2}N_4(6\text{-H-DPEN}))(OMe)]^+$
1$^{Py}_2$-MeCN	$[Fe^{II}(S^{Me2}N_4(6\text{-H-DPEN}))(\mu\text{-}S^{Me2}N_4(6\text{-H-DPEN})Fe^{II})(MeCN)](PF_6)_2$
1^{Mepy}	$[Fe^{II}(S^{Me2}N_4(6\text{-Me-DPEN}))]^+$
1^{Quino}	$[Fe^{II}(S^{Me2}N_4(QuinoEN))]^+$
2^{Tren}	$[Fe^{III}(S^{Me2}N_4(tren))(OOH)]^+$
3^{Py}	$[Fe^{II}(S^{Me2}N_4(6\text{-H-DPEN}))(N_3)]^+$
3^{Mepy}	$[Fe^{II}(S^{Me2}N_4(6\text{-Me-DPEN}))(N_3)]^+$
3^{Quino}	$[Fe^{II}(S^{Me2}N_4(QuinoEN))(N_3)]^+$
4^{Tren}	$[Fe^{III}(S^{Me2}N_4(tren))(MeCN)]^{2+}$
4^{Py}	$[Fe^{III}(S^{Me2}N_4(6\text{-H-DPEN}))]^{2+}$
4^{Mepy}	$[Fe^{III}(S^{Me2}N_4(6\text{-Me-DPEN}))]^{2+}$
4^{Quino}	$[Fe^{III}(S^{Me2}N_4(QuinoEN))]^{2+}$
5^{Tren}	$[Fe^{III}(S^{Me2}N_4(tren))(N_3)]^+$
5^{Py}	$[Fe^{III}(S^{Me2}N_4(6\text{-H-DPEN}))(N_3)]^+$
5^{Mepy}	$[Fe^{III}(S^{Me2}N_4(6\text{-Me-DPEN}))(N_3)]^+$
5^{Quino}	$[Fe^{III}(S^{Me2}N_4(QuinoEN))(N_3)]^+$
6^{Py}	$[Fe^{III}(S^{Me2}N_4(6\text{-H-DPEN}))]_2(\mu\text{-O})(PF_6)_2$
6^{Mepy}	$[Fe^{III}(S^{Me2}N_4(6\text{-Me-DPEN}))]_2(\mu\text{-O})(PF_6)_2$
6^{Quino}	$[Fe^{III}(S^{Me2}N_4(QuinoEN))]_2(\mu\text{-O})(PF_6)_2$

Chapter 5

1	$[Mn^{III}(S^{Me2}N_4(6\text{-Me-DPEN})(OO^tBu))^+$
2	$[Mn^{II}(S^{Me2}N_4(6\text{-Me-DPEN}))]^+$
3	$[Mn^{II}(S^{Me2}N_4(6\text{-MeDPPN}))]^+$
4	$[Mn^{III}(S^{Me2}N_4(6\text{-Me-DPPN})(OO^tBu))^+$
5	$[Mn^{II}(O^{Me2}N_4(6\text{-Me-DPPN}))]^+$
6	$[Mn^{II}(HO^{Me2}N_4(6\text{-Me-DPEN})(MeCN))]^+$
7	$[Mn^{II}(HO^{Me2}N_4(6\text{-Me-DPEN}))(CHO_2)]^+$
7-PF_6	$[Mn^{II}(HO^{Me2}N_4(6\text{-Me-DPEN}))(CHO_2)](BPh_4)\bullet MeCN$
7-BPh_4	$[Mn^{II}(HO^{Me2}N_4(6\text{-Me-DPEN}))(CHO_2)](BPh_4)\bullet MeCN\bullet Et_2O$
8	$[Mn^{III}(O^{Me2}N_4(6\text{-Me-DPEN}))(OO^tBu)]^+$
9	$[Mn^{III}(dpaq^{2Me})(OO^tBu)]^+$
10	$[Mn^{III}(S^{Me2}N_4(quinoEN))(OO^tBu)]^+$
11	$[Mn^{III}(S^{Me2N}{}_4(quinoPN))(OO^tBu)]^+$

Chapter Contributions

Much of the work included in the following chapters would not have been possible without the valuable efforts of a number of collaborators. Their individual contributions are gratefully acknowledged below.

Chapter 2: Audra Johansen for establishing ligand and metal complex synthesis and preliminary investigation into O_2 reactivity with Mn^{II} $\mathbf{1}^{\mathbf{MeOpy}}$. Ellen Hayes in the group of Prof. Stefan Stoll for collecting and processing EPR data. Xianru Sun, Guang Yang, and Marc Piquette in the group of Prof. Elena Rybak-Akimova for performing stopped-flow kinetic experiments. Maksym Dedushko and Julian Rees for performing DFT calculations. Michael Coggins, Audra Johansen, Werner Kaminsky for the crystallographic characterization of $\mathbf{3}^{\mathbf{Quino}}$, $\mathbf{1}^{\mathbf{MeOpy}}$, and $\mathbf{6}^{\mathbf{MeOpy}}$.

Chapter 4: Santiago Toledo, Morgan Gleaves, Dylan Rogers, Werner Kaminsky for the crystallographic characterization of Fe^{II}-$\mathbf{1}^{\mathbf{Mepy}}$, $\mathbf{1}^{\mathbf{Quino}}$, and $\mathbf{1}^{\mathbf{PyPN}}$ and Fe^{III}_2-μ-oxo $\mathbf{6}^{\mathbf{Mepy}}$, $\mathbf{6}^{\mathbf{Quino}}$, and $\mathbf{6}^{\mathbf{Py}}$.

Chapter 5: Alexandra Downing for performing DFT and TD-DFT calculations. Michael Coggins for establishing metal complex synthesis and investigation and characterization into ^{t}BuOOH reactivity with alkoxide-ligated Mn^{II}-**7**. Michael Coggins and Werner Kaminsky for the crystallographic characterization of **5**, **6**, **7**-$\mathbf{BPh_4}$, **8**.

Acknowledgements

First and foremost, I would like to express my gratitude to Professor Julie Kovacs, my graduate advisor, for her boundless support (both scientific and emotional) and mentorship throughout my time in the Kovacs group. I had the pleasure of working with Julie as an undergraduate student during my senior year and her unmatched passion for science had truly inspired me. Throughout my graduate school journey, I have very much enjoyed our enthusiastic science discussion in Julie's office, and (unfortunately) through Zoom. These electrifying conversations have not only supported me to understand my science better, but also carried me through graduate school.

I would like to thank former Kovacs group members, Dr. Ben Leipzig, Audra Johansen, Dr. Julian Rees, and Dr. Maike Blakely for their support. A special shout out to the amazing fantasy football master, Ben, who took on the role as my mentor during my post-bac year and continued to inspire and support me throughout grad school. I will miss our sports (and science) conversation in the office. The group's future is very exciting with the current members Dr. Maksym Dedushko, Alexandra Downing, Dylan Rogers, Maria Greiner, Julian Smith-Jones, Paige Gannon, Bennet Karel, Chris Lowe, Douglas Baumgardner, Antonio Vazquez, and Christopher Woodburn. I would like to thank all of them for their support, especially Alex, who has been an amazing friend and the very much needed calming influence throughout my time here at UW. I will miss the refreshing food adventures (Korean BBQ, pork belly, Musashi…) Alex, Maria, and I had together! I would like to also thank Brandon Roberts for all the miserable data processing time he has saved me with the UV-Vis Spectroscopy Data Output Transformer he developed.

I would like to acknowledge my committee members throughout this journey, Professors Brandi Cossairt, Karen Goldberg, Daniel Gamelin, Stefan Stoll, and Jerry Seidler for their advice and encouragement. My grad school adventure would not have been possible without the support from the inorganic department. I would like to thank Hannah Zeitler, Louise Guard, Jenny Stein, and Nayon Park for their friendship and support! Grad school wouldn't have been as much fun without them.

I am extremely grateful for my American families, Deborah Shaw, Keith, Rebekah, Hannah, and Lucas Allen. They have welcomed me through my years in the United States. None of these 11.5 years would have been possible without their love and support. I would love to express my gratitude to my best friends, Christy Cheung, Xing Yee Gan, and Wenbi Wu, Jennifer Jeng and Sean Lay. They have been by my side throughout this roller-coaster and believed in me even when I doubted myself, especially Xing Yee, who really has been amazingly supportive throughout the toughest time. Words cannot express how much I appreciate your friendships.

Finally, I would not be here without my wonderful parents. They have given me everything they possibly can and supported me wholeheartedly throughout this journey. Thank you.

DEDICATION

My parents.

Chapter 1. Introduction

1.1 Bioinorganic Chemistry

Proteins, made of amino acids, are critical for biological processes in living organisms. One third of crystallographically characterized proteins are shown to contain metal cofactors, most of them are first row transition metals, such as manganese, iron, cobalt, nickel, copper, and zinc.[1,2] Apart from nickel, the five earth abundant transition metals named above are essential to human health.[3] Among them, redox active manganese, iron, cobalt, and copper are involved in many catalytic processes, such as water oxidation[4,5], DNA replication and repair[6], dioxygen transport[7], and removing reactive oxygen species (ROS)[8,9]. The availability of different oxidation states of these transition metals affords various available coordination geometries and allows for changes in ligand affinities. These properties are crucial for molecule and electron transfer reactions. Further understanding of these well-tailored metalloenzymes' processes would provide insights into probing catalysts and drugs[10]. However, direct mechanism studies on these metalloenzymes have limitations due to the highly reactive nature of their intermediates. Isolation and characterization of short-lived intermediates in the enzymatic systems have proven to be difficult due to the solubility and temperature constraints of the large-size proteins, and the amino acid residues surrounding the active site of interest.

The field of bioinorganic chemistry is a combination of many disciplines, including biochemistry, inorganic chemistry, coordination chemistry, molecular and structural biology.[3] As the environments of active sites in natural metalloenzymes are well-tailored for their specific processes, it is important to understand the reasoning behind the selections of metal cofactor and substrates. Through small synthetic transition metal complexes mimicking the primary coordination sphere of the metal active sites, bioinorganic chemists are able to gain important

insights into the functions of metalloproteins, and their catalytic mechanisms. With biomimetic models, one could replace the metal centers as well as modifying the ligand scaffold for electronic and steric purposes.[11] This benefit will be illustrated throughout this dissertation, as the N-heterocyclic ligand scaffold of the study was modified with more electron donating and less sterically bulky substituents.

1.2 Oxygen Evolving Complex of Photosystem II

Using the isotopic ratio of sulfur formed, it was determined that concentration of dioxygen, key to all aerobic life, increased significantly and became a major component of the Earth's atmosphere roughly 2.45 billion years ago, also known as the "Great Oxidation Event".[12,13] Dioxygen in the atmosphere, along with four protons and four electrons, are the products of sunlight-powered water oxidation in photosynthesis. (Equation 1.1) Along with oxygen reduction, the two redox reactions are, without a doubt, the most crucial processes for all aerobic organisms.

$$2H_2O \rightarrow O_2 + 4H^+ + 4e^- \qquad (1.1)$$

Photosystem II (PSII), found in algae, plants, and cyanobacteria, is the most efficient natural system in converting solar energy into chemical energy. The catalytic core in PSII, known as oxygen evolving complex (OEC), is a $CaMn_4O_x$ cluster, which accumulates oxidizing equivalents in the water oxidation processes through a range of Mn oxidation states.[14–17] (Figure 1.1) The proposed catalytic cycle for water splitting by this heteronuclear oxo-bridged cluster is known as the Kok cycle, shown in Scheme 1.1.[18,19] Each of the S states (S_0 to S_4) represents five different manganese oxidation states of the OEC throughout the process of water oxidation and

dioxygen evolution. Specifically, the Kok cycle begins with the most reduced cluster (S_0 state, $Mn^{III}_3Mn^{IV}$), followed by stepwise oxidations to the cluster, forming the dark-stable S_1 state ($Mn^{III}_2Mn^{IV}_2$), and then the S_2 state ($Mn^{III}Mn^{IV}_3$). Umena *et al.* reported a high-resolution X-ray structure of the S_1 state with 1.9 Å resolution in 2001.[20] However, while significant progress on characterization of the cluster and mechanistic pathway has been developed for the conversion from S_0 to S_3 (Mn^{IV}_4) states through electronic absorption, X-ray, and EPR spectroscopies,[14,15,21–23] the crucial process from S_3 to S_0 involving the O-O bond formation and O_2 evolution remain elusive.[16] The O-O bond formation prior to the release of O_2 involving the transient S_4 state is believed to be the rate-determining step (RDS) of water splitting of the OEC.[15,24,25] An unobserved peroxo intermediate is proposed along S_3 to S_0, prior to the O_2 evolution.[24,26–32]

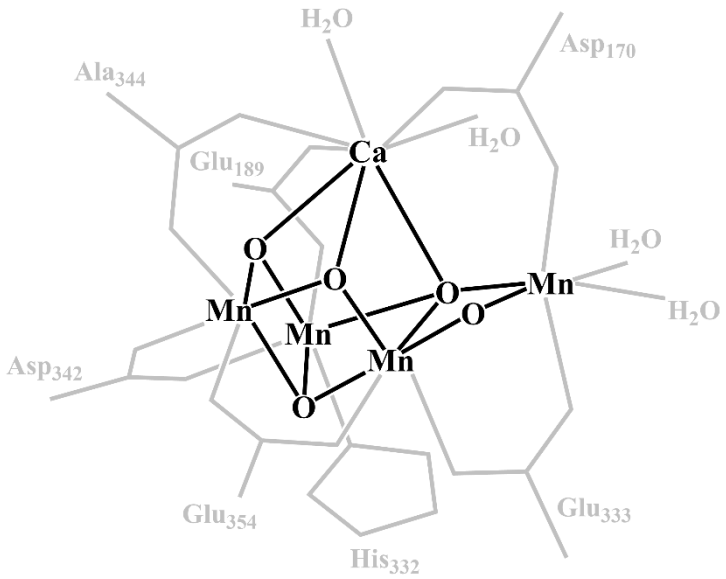

Figure 1.1. ChemDraw representation of oxygen evolving complex (OEC), a $CaMn_4O_5$ cluster, and its ligand environment.[4,20]

Scheme 1.1. Kok cycle[18] of water oxidation by oxygen evolving complex. Each S states (S_0 to S_4) represents the $CaMn_4O_x$ cluster intermediates at different Mn oxidation states, labelled in yellow boxes.[15]

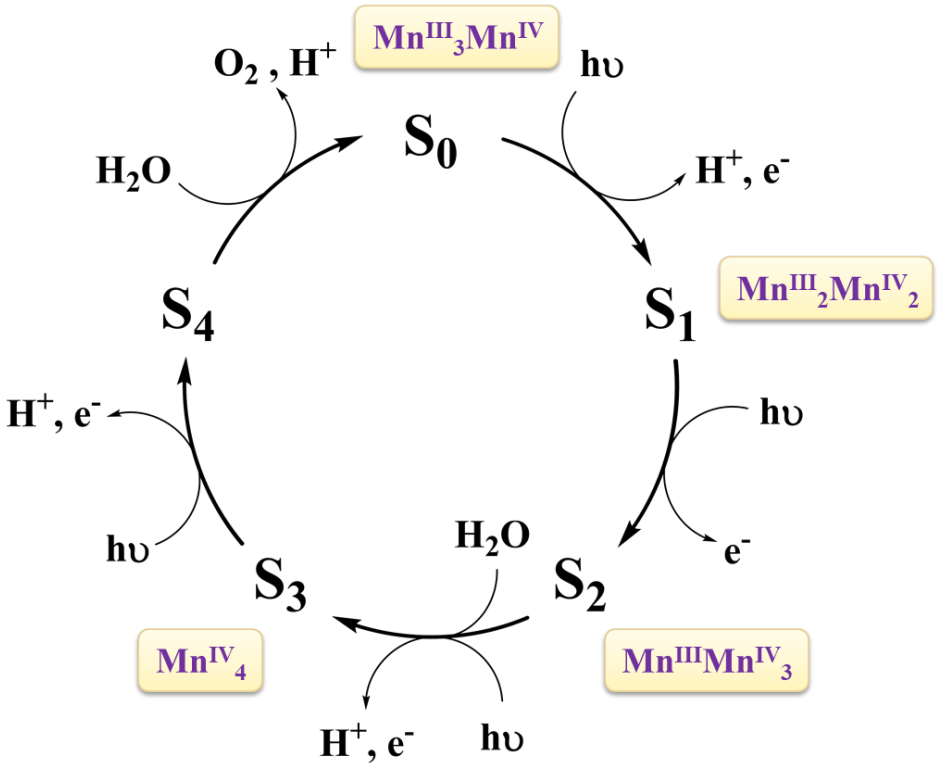

Biomimetic models have been developed in the hopes of providing more thorough structural, spectroscopic properties of the OEC, not only for a better understanding of the water splitting mechanism, but also for the development of water oxidation catalyst. Recently, the Agapie group successfully synthesized a rare tetranuclear $Mn^{IV}_4O_4$ cluster that mimics the high valent S_3 state of OEC.[33] This $S = 3$ ground state model not only matches the Mn oxidation states of the S_3 state, but also reported a spin state change mirroring the oxidation from S_2 ($S = 1/2$) to S_3 state ($S = 3$), which is its reduced form $Mn^{III}Mn^{IV}_3$.[33] In spite of the efforts contributed to harnessing the water oxidation power of OEC, the development of manganese oxo clusters mimicking the active site, even more so for synthetic models that could perform water oxidation, has been proven challenging.[34] Hence, studies on O_2 activation, the microscopic reverse of O-O

bond formation, would be beneficial for insight on the unobserved intermediates proposed for the S_3 to S_0 mechanism.

1.3 Dioxygen Chemistry with Manganese Synthetic Models

Unlike Fe and Cu[35–41], which nature often employs for enzymatic O_2 activation, manganese dioxygen chemistry with synthetic models remains relatively unexplored.[42–45] The exploration of manganese-oxo intermediates continuously provides a more complete picture for the O-O bond cleavage pathway.[42,46–50] (Scheme 1.2) Previously the Kovacs group has shown a crystallographically characterized Mn^{III}_2-μ-peroxo with O_2 activation by a Mn^{II}-thiolate complex, $[Mn^{II}(L^{Mepy})]^+$ (L^{Mepy} = (6-Me-DPEN)$N_4{}^{Me2}S^-$).[42] An unobserved Mn^{IV}=O intermediate was proposed to be following the O-O bond cleavage of the peroxo intermediate, *en route* to the thermodynamic product Mn^{III}_2-(μ-oxo).[42] (Scheme 1.2, gold highlight) A Mn^{III}-OH species can be generated through hydrolysis from Mn^{III}_2-(μ-oxo).[51] Further discussion expanding on O_2 activation with structurally analogous Mn^{II} complexes will be discussed in chapter two.

Another two pathways are demonstrated by the Borovik group[52] (Scheme 1.2, purple highlight) and Duboc group[50,53] (Scheme 1.2, grey highlight). Dioxygen reactivity with tripodal-ligated $[Mn^{II}(1^{cyp})(OAC)]^{2-}$ reported by the Borovik group results in a Mn^{III}-OH, through hydrogen atom transfer (HAT) by a proposed Mn^{IV}=O intermediate[52]. (Scheme 1.2, purple highlight) Meanwhile, a dinuclear $[Mn^{II}_2(LS)(LSH)]^+$ complex characterized by the Duboc group reacts with O_2 and forms a Mn^{IV}_2(μ-oxo)(μ-hydroperoxo) intermediate, which comproportionates with the starting Mn^{II}_2 species to form a Mn^{III}_2(μ-OH) product.[50,53] (Scheme 1.2, grey highlight)

Scheme 1.2. Generic proposed mechanisms for dioxygen activation by synthetic MnII complexes, the O_2 activation products for each system are highlighted in: Purple: O_2 reaction scheme with $[Mn^{II}(1^{cyp})(OAC)]^{2-}$ proposed by Borovik et al., yielding a Mn^{III}-OH product[52]; Gold: O2 activation with thiolate ligated $[Mn^{II}(L^{Mepy})]^{+}$ by the Kovacs group, forming Mn^{III}_2-μ-oxo, which further reacts with H_2O, forming Mn^{III}-OH.[42,51]; Grey: O-O bond cleavage by $[Mn^{II}_2(LS)(LSH)]^{+}$ reported by the Duboc ground, resulting in a Mn^{III}_2(μ-OH) species[50,53].

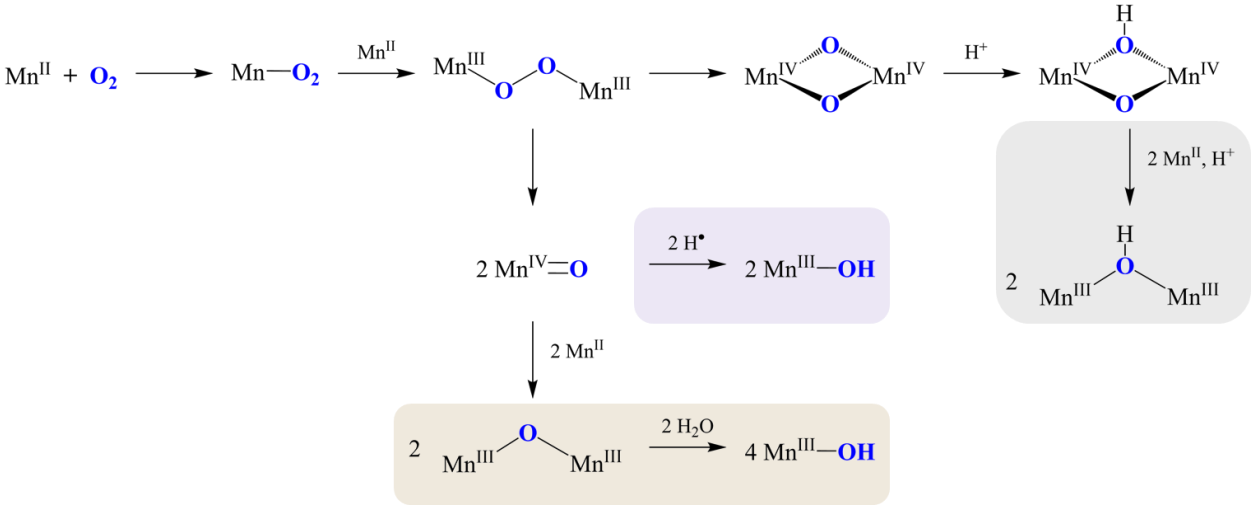

While various mechanisms of Mn^{II} O_2 activation have been proposed with synthetic models, understanding on the ability to tune the O_2 activation landscape by a systemic alteration of the ligand environment is limited.[47] Chapter two of this dissertation will unfold the investigation of how metal ion Lewis acidity and steric properties influence the kinetics and thermodynamics of O_2 activation by a series of structurally analogous Mn-thiolate complexes. With the aid of stopped-flow experiments, a total of four intermediates, including a superoxo and peroxo intermediates were observed.

1.4 Ribonucleotide Reductase

Iron and manganese, being the fourth most abundant element and third most abundant transition metal in the Earth's crust respectively, are found in about 14% of metalloenzymes.[54] Both ions with +2 oxidation state, proximal in the Irving-Williams series[55], have similar ionic radii, coordination number preferences, and ligand affinities. Mis-metalation between the two ions have been shown in enzymes,[56–58] leading to defective function of the protein. The determinants of how nature selects their transition metals, in particular between iron and manganese for reasons mentioned above, have yet to be thoroughly explored.[54,56,58–60] The bimetallic Class I of ribonucleotide reductase (RNR) might shed light onto this matter.

Ribonucleotide reductase mediates the synthesis of deoxynucleotides, which is essential for accurate DNA replication and repair in all organisms. The family of RNRs are categorized into three classes (Class I to III) depending on their oxygen dependence (aerobic versus anaerobic), quaternary structure of the enzyme, as well as the type of metal and cofactor.[6,61,62] Class I RNRs are consist of two homodimeric subunits, $\alpha 2$ and $\beta 2$. Catalytic ribonucleotide reduction occurs at $\alpha 2$ while tyrosyl radical ($Y^{\bullet}$) is generated in subunit $\beta 2$.[6,61,62] The tyrosyl radical is then transferred via proton-coupled electron transfer (PCET) to oxidize a cysteine thiyl radical responsible for reducing nucleotides are the surface of the protein.[6,63] While the metal cofactors in the radical generating active sites of aerobic Class I RNR $\beta 2$ subunit share common environment, two histidine residues and four carboxylate ligands, the family of proteins are divided into five subclasses (Class 1a to 1e), based on the radical species and/or binuclear metallocofactors (Fe/Fe, Mn/Fe, or Mn/Mn) that participate place in the generation of tyrosyl radical ($Y^{\bullet}$).[6,61,62]

The metallocofactors in the radical generating Class Ia and Ib RNR, are $Fe^{III}Fe^{III}$ and $Mn^{III}Mn^{III}$, respectively. While both classes are oxygen dependent, Class Ia enzymes can be found in all eukaryotes, apart from unicellular E*uglena gracilis*, and Class Ib, on the other hand, are found in eubacteria.[61,62] While the inactive diiron ($Fe^{II}Fe^{II}$) cofactor of Class Ia is activated by O_2 (Scheme 1.3, top), the resting dimaganese cofactor ($Mn^{II}Mn^{II}$, Figure 1.2) in Class Ib is unreactive towards O_2 and is oxidized by superoxide ($O_2^{\bullet-}$).[64,65] A flavoprotein activator (NrdI) is essential to reduce O_2 to superoxide prior to the oxidation of $Mn^{II}Mn^{II}$ to $Mn^{III}Mn^{III}$, required for the radical generation.[64,65] (Scheme 1.3, bottom) Grāve et al. has shown with *Bacillus anthracis* class Ib RNR, that the enzyme naturally chooses manganese over iron.[59] It was suggested that the residue near the metal binding site plays a significant role in metal selectivity between the two metals.[59] Other than active site environment, the reduction potential difference between the weakly binding Fe and Mn is among the key aspects considered for nature's discrimination between the two metals, despite defying the Irving-William series.[66]

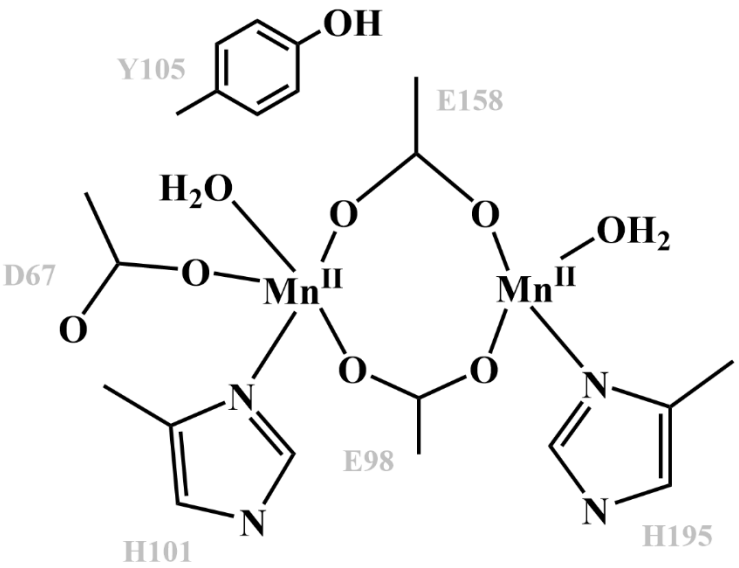

Figure 1.2. ChemDraw representation of dimanganese active site of Class Ib ribonucleotide reductase from *Escherichia coli* and its ligand environment.[67]

Scheme 1.3. Metallocofactor activation and radical generation pathways in Class Ia (top) and Class Ib (bottom) RNRs.[64]

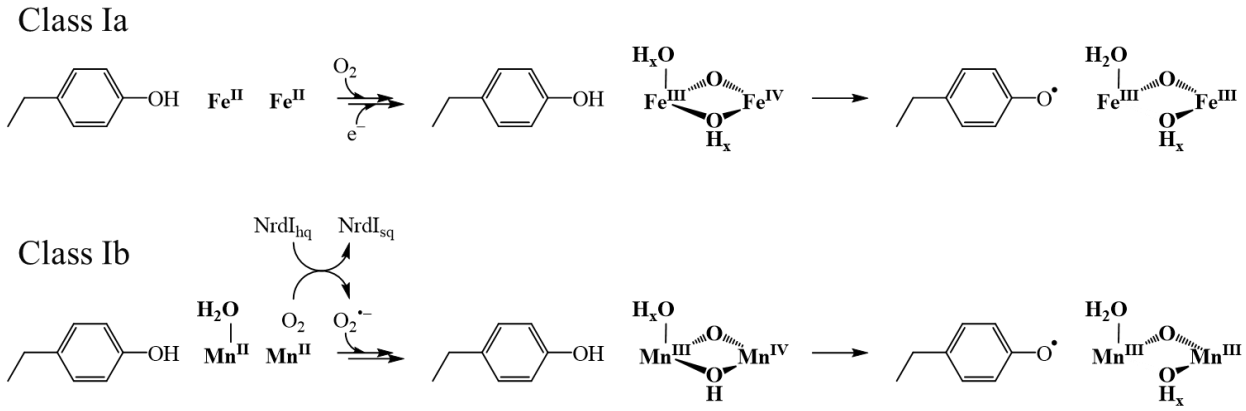

As the mechanisms of tyrosyl oxidation for Class Ia and Ib are explored (Scheme 1.3), further knowledge on the properties of their intermediates could provide insights to the discernment between iron and manganese in these systems. In both radical activation pathways, the $Fe^{III}Fe^{III}$ and $Mn^{III}Mn^{III}$ cofactors are oxidized by O_2 and $O_2^{\bullet-}$ to form an $Fe^{III}Fe^{IV}$ and $Mn^{III}Mn^{IV}$ intermediates, respectively.[6,64] The $Mn^{III}Mn^{IV}$ intermediate has been observed and characterized by stopped-flow UV-vis spectroscopy and rapid freeze quench electron paramagnetic resonance (EPR) spectroscopy.[65] The two manganese ions are proposed to bridge through an oxo and a hydroxo. (Scheme 1.3, bottom) As a means to understand this short-lived intermediate better and potentially provide explanation for nature's selection between the two transition metals, synthetic biomimetic models and their reactivities with dioxygen and other reactive oxygen species (ROS) are heavily relied upon. In chapter two and three, characterization and reactivities of a binuclear $Mn^{III}Mn^{IV}$ intermediate, generated via O_2 activation by a Mn^{II}-thiolate complex, will be discussed.

1.5 Importance of Thiolate

Amino acid residue cysteine (Cys) has been found in key metalloenzymes that promote electron transfer and bond activation.[68,69] The thiolate (RS^-) of the residue is found to be ligated to the first row transition metal cofactors, including iron[70–72] and copper[41,68], at the active sites. For example, the electron donating cysteinate in cytochrome P450 has been shown to be responsible for the enzymes' ability to activate C-H bonds of saturated hydrocarbons (100 kcal/mol).[69] Thiolates (RS^-) have been shown to form highly covalent bonds to transition metals, which helps lower the metal's reduction potential and stabilize the metal at higher oxidation states through electron transfer and bond activation processes.[73–75] Low spin states of cysteine-ligated metallocofactors are favored due to the nephelauxetic effect, i.e., the delocalization of electrons promoted by the covalent metal-thiolate bonds lowering the electron pairing energy.[76–78]

1.6 Reactive Oxygen Species and Superoxide Reductases

As mentioned previously, water oxidation and dioxygen reduction are the most crucial processes for human and other aerobic life. The four-electron oxidizing power of life-depending O_2, byproduct of the 4 protons, 4 electrons water splitting by OEC of PSII, provides the energy sustaining all living organisms through protein mediated biochemical processes.[6,8,9,79–81] However, the highly endothermic spin-forbidden conversion from the triplet ground state to singlet ground state of O_2 provides significant challenges for the thermodynamically favored O_2 activation.[9,82–85] Nature employs well-refined proteins, most of which are known to contain transition metal cofactor, to overcome the barrier to nature's four-electron storage, and

efficiently control the reduction process of O_2.[37,40,86–88] As illustrated with Class Ia ribonucleotide reductase earlier, the stable $Fe^{II}Fe^{II}$ cofactor was activated by O_2 prior to the radical generation by the oxidized $Fe^{III}Fe^{IV}$ cofactor.[6,61,62]

However, along the process of O_2 reduction to water (equation 1.2), the formation of excess reactive oxygen species (ROS), including superoxide ($O_2^{\bullet-}$), hydrogen peroxide (H_2O_2), and hydroxyl radical ($HO^{\bullet}$)[85], (Scheme 1.4) are known to cause cancer, Parkinson's and Alzheimer's diseases.[89–92] Nature employs metalloproteins, including catalase[93,94], superoxide dismutase[9,17,81,95], superoxide reductase[8,9,96,97], and peroxidase[98–100], to protect against the accumulation of harmful ROS species in living systems. Among these antioxidant enzymes, superoxide dismutase (SOD) and superoxide reductase (SOR) are nature's seasoned weapons to lower the concentration of the potent superoxide in both aerobic and anaerobic organisms since the start of the "Great Oxidation Event"[13].

$$O_2 + 4H^+ + 4e^- \rightarrow 2H_2O \qquad (1.2)$$

Scheme 1.4. Sequential four-electron, four-proton reductions of dioxygen to water.

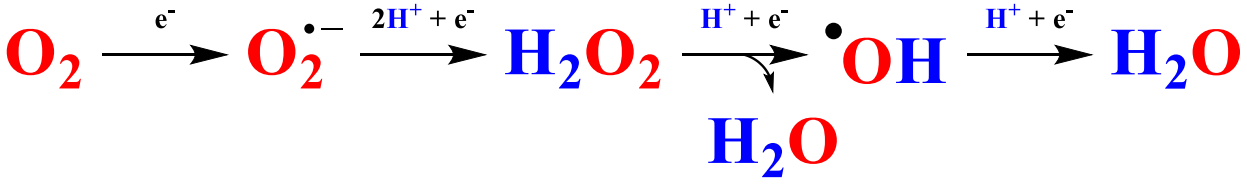

Even through both SODs and SORs are redox-active metalloenzymes detoxifying superoxide, the four SODs (FeSOD, MnSOD, NiSOD, and CuZnSOD) disproportionate $O_2^{\bullet-}$ to O_2 and H_2O_2 in aerobic organisms[9,101], while Fe-only SORs reduce $O_2^{\bullet-}$ in anaerobic organisms to hydrogen peroxide (H_2O_2)[8,102]. Each of these enzymes are found in a wide range of archaea,

bacteria, and/or eukarya, with different quaternary structures (e.g., dimer, tetramer, hexamer).[9] The active site of FeSOD contains a trigonal bipyramidal $Fe^{III/II}$ metal center, ligated by three histidine residues, a carboxylate, and a H_2O (Fe^{II}) or HO^- (Fe^{III}) molecule.[9,101] (Figure 1.3, left) In contrast, the square pyramidal Fe^{II} catalytic site of FeSOR is surrounded by four histidine moieties and a cysteinate trans to the open site.[9,102] (Figure 1.3, right) The electron rich properties of the cysteinate, and highly covalent Fe-SR bonds, have been shown to favor superoxide reduction by lowering the Fe^{II} oxidation potential.[96] Better understanding on how the surrounding environment of the metallocofactor affects the superoxide reduction pathway by FeSOR would improve biomimetic catalyst and drug design to avoid the buildup of toxic superoxide radical.

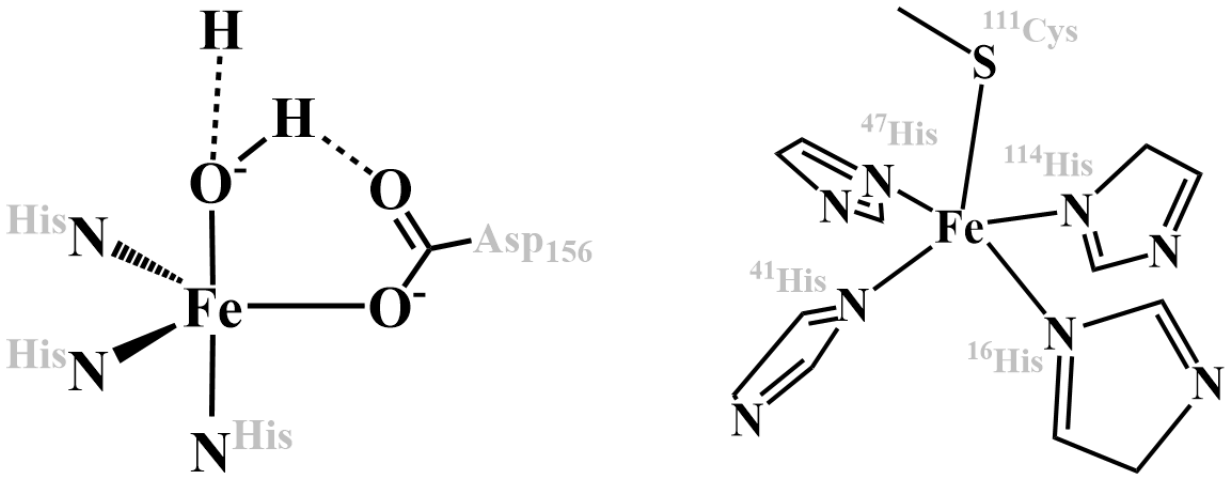

Figure 1.3. Left: ChemDraw representation of FeSOD active site and its ligand environment. Right: ChemDraw representation of FeSOR active site and its ligand environment.

Although the superoxide reduction process by SOR has been extensively investigated,[8,9,103] the first step involving the formation of Fe^{III}-OOH species remains open for debate.[102] Two potential pathways for the ferric intermediate, includes, (a) a sequential oxidative addition of $O_2^{\bullet-}$ to the Fe^{II} center, affording an unobserved Fe^{II}-$O_2^{\bullet-}$ species, which converts to

the Fe^{III}-OOH by abstracting a proton (H^+); (b) superoxide ion reacts with a proton (equation 1.3), prior to concerted addition of the resulting HO_2 to the ferrous open site. (Scheme 1.5) Computational studies by the Nivière and Klein groups suggest the binding of superoxide ion to the ferrous center, forming an Fe^{II}-$O_2^{\bullet-}$ prior to the protonation converting to Fe^{III}-OOH.[104,105] Chapter four in this thesis will discuss the synthesis and characterization of an intensely colored Fe^{II}-thiolate complex containing π-accepting N-heterocyclic ligand, allowing Fe^{II} reactivity with small molecules to be monitored with electronic absorption spectroscopy (EAS), and, specifically, the preliminary investigation into its dioxygen reactivity.

$$O_2^{\bullet-} + HA \leftrightarrow HO_2 + A^- \qquad (1.3)$$

Scheme 1.5. Proposed mechanisms (concerted versus sequential) for the formation of Fe^{III}-OOH intermediate in superoxide reduction by SOR.

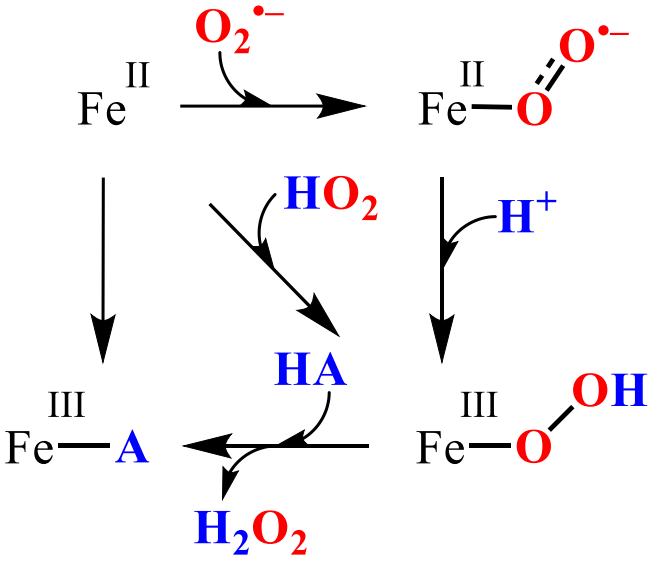

1.7 References

(1) Mounicou, S.; Szpunar, J.; Lobinski, R. Metallomics: The Concept and Methodology. *Chem. Soc. Rev.* **2009**, *38*, 1119–1138.

(2) Tainer, J. A.; Roberts, V. A.; Getzoff, E. D. Metal-Binding Sites in Proteins. *Curr. Opin. Biotechnol.* **1991**, *2*, 582–591.

(3) Sigel, H.; Sigel, A. The Bio-Relevant Metals of the Periodic Table of the Elements. *Zeitschrift fur Naturforsch. - Sect. B J. Chem. Sci.* **2019**, *74*, 461–471.

(4) Suga, M.; Akita, F.; Hirata, K.; Ueno, G.; Murakami, H.; Nakajima, Y.; Shimizu, T.; Yamashita, K.; Yamamoto, M.; Ago, H.; Shen, J. R. Native Structure of Photosystem II at 1.95A° Resolution Viewed by Femtosecond X-Ray Pulses. *Nature* **2015**, *517*, 99–103.

(5) Young, I. D.; Ibrahim, M.; Chatterjee, R.; Gul, S.; Fuller, F. D.; Koroidov, S.; Brewster, A. S.; Tran, R.; Alonso-Mori, R.; Kroll, T.; Michels-Clark, T.; Laksmono, H.; Sierra, R. G.; Stan, C. A.; Hussein, R.; Zhang, M.; Douthit, L.; Kubin, M.; De Lichtenberg, C.; Vo Pham, L.; Nilsson, H.; Cheah, M. H.; Shevela, D.; Saracini, C.; Bean, M. A.; Seuffert, I.; Sokaras, D.; Weng, T. C.; Pastor, E.; Weninger, C.; Fransson, T.; Lassalle, L.; Bräuer, P.; Aller, P.; Docker, P. T.; Andi, B.; Orville, A. M.; Glownia, J. M.; Nelson, S.; Sikorski, M.; Zhu, D.; Hunter, M. S.; Lane, T. J.; Aquila, A.; Koglin, J. E.; Robinson, J.; Liang, M.; Boutet, S.; Lyubimov, A. Y.; Uervirojnangkoorn, M.; Moriarty, N. W.; Liebschner, D.; Afonine, P. V.; Waterman, D. G.; Evans, G.; Wernet, P.; Dobbek, H.; Weis, W. I.; Brunger, A. T.; Zwart, P. H.; Adams, P. D.; Zouni, A.; Messinger, J.; Bergmann, U.; Sauter, N. K.; Kern, J.; Yachandra, V. K.; Yano, J. Structure of Photosystem II and Substrate Binding at Room Temperature. *Nature* **2016**, *540*, 453–457.

(6) Greene, B. L.; Kang, G.; Cui, C.; Bennati, M.; Nocera, D. G.; Drennan, C. L.; Stubbe, J.

Annual Review of Biochemistry Ribonucleotide Reductases: Structure, Chemistry, and Metabolism Suggest New Therapeutic Targets. *Annu. Rev. Biochem.* **2020**, *89*, 45–75.

(7) Antonini, E.; Brunori, M. *Hemoglobin and Myoglobin in Their Reactions with Ligands*; Amsterdam : North-Holland, 1971, 1971; Vol. 21.

(8) Pereira, A. S.; Tavares, P.; Folgosa, F.; Almeida, R. M.; Moura, I.; Moura, J. J. G. Superoxide Reductases. *Eur. J. Inorg. Chem.* **2007**, No. 18, 2569–2581.

(9) Sheng, Y.; Abreu, I. A.; Cabelli, D. E.; Maroney, M. J.; Miller, A. F.; Teixeira, M.; Valentine, J. S. Superoxide Dismutases and Superoxide Reductases. *Chem. Rev.* **2014**, *114*, 3854–3918.

(10) Crans, D. C.; Kostenkova, K. Open Questions on the Biological Roles of First-Row Transition Metals. *Comm. Chem.* **2020**, *3*, 1–4.

(11) Anything You Can Do…. *Nat. Rev. Chem.* **2018**, *2*, 195–196.

(12) Farquhar, J.; Bao, H.; Thiemens, M. Atmospheric Influence of Earth's Earliest Sulfur Cycle. *Science (80-.).* **2000**, *289*, 756–758.

(13) Sessions, A. L.; Doughty, D. M.; Welander, P. V; Summons, R. E.; Newman, D. K. Review The Continuing Puzzle of the Great Oxidation Event. *Curr. Biol.* **2009**, *19*, 567–574.

(14) Askerka, M.; Brudvig, G. W.; Batista, V. S. The O2-Evolving Complex of Photosystem II: Recent Insights from Quantum Mechanics/Molecular Mechanics (QM/MM), Extended X-Ray Absorption Fine Structure (EXAFS), and Femtosecond X-Ray Crystallography Data. *Acc. Chem. Res.* **2017**, *50*, 41–48.

(15) Pantazis, D. A. Missing Pieces in the Puzzle of Biological Water Oxidation. *ACS Catal.* **2018**, *8*, 9477–9507.

(16) Cox, N.; Pantazis, D. A.; Lubitz, W. Current Understanding of the Mechanism of Water Oxidation in Photosystem II and Its Relation to XFEL Data. *Annu. Rev. Biochem.* **2020**, *89*, 795–820.

(17) Schmidt, S. B.; Husted, S. The Biochemical Properties of Manganese in Plants. *Plants* **2019**, *8*, 381–395.

(18) Kok, B.; Forbush, B.; Mcgloin, M. Cooperation of Charges in Photosynthetic O2 Evolution–I. A Linear Four Step Mechanism. *Photochem. Photobiol.* **1970**, *11*, 457–475.

(19) Cox, N.; Pantazis, D. A.; Neese, F.; Lubitz, W. Biological Water Oxidation. *Acc. Chem. Res.* **2013**, *46*, 1588–1596.

(20) Umena, Y.; Kawakami, K.; Shen, J. R.; Kamiya, N. Crystal Structure of Oxygen-Evolving Photosystem II at a Resolution of 1.9Å. *Nature* **2011**, *473*, 55–60.

(21) Ibrahim, M.; Fransson, T.; Chatterjee, R.; Cheah, M. H.; Hussein, R.; Lassalle, L.; Sutherlin, K. D.; Young, I. D.; Fuller, F. D.; Gul, S.; Kim, I. S.; Simon, P. S.; de Lichtenberg, C.; Chernev, P.; Bogacz, I.; Pham, C. C.; Orville, A. M.; Saichek, N.; Northen, T.; Batyuk, A.; Carbajo, S.; Alonso-Mori, R.; Tono, K.; Owada, S.; Bhowmick, A.; Bolotovsky, R.; Mendez, D.; Moriarty, N. W.; Holton, J. M.; Dobbek, H.; Brewster, A. S.; Adams, P. D.; Sauter, N. K.; Bergmann, U.; Zouni, A.; Messinger, J.; Kern, J.; Yachandra, V. K.; Yano, J. Untangling the Sequence of Events during the S2 → S3 Transition in Photosystem II and Implications for the Water Oxidation Mechanism. *Proc. Natl. Acad. Sci. U. S. A.* **2020**, *117*, 12624–12635.

(22) Corry, T. A.; O'Malley, P. J. Molecular Identification of a High-Spin Deprotonated Intermediate during the S2to S3Transition of Nature's Water-Oxidizing Complex. *J. Am. Chem. Soc.* **2020**, *142*, 10240–10243.

(23) Marchiori, D. A.; Debus, R. J.; Britt, R. D. Pulse EPR Spectroscopic Characterization of the S3State of the Oxygen-Evolving Complex of Photosystem II Isolated from Synechocystis. *Biochemistry* **2020**, *59*, 4864–4872.

(24) Shoji, M.; Isobe, H.; Shigeta, Y.; Nakajima, T.; Yamaguchi, K. Concerted Mechanism of Water Insertion and O2 Release during the S4 to S0 Transition of the Oxygen-Evolving Complex in Photosystem II. *J. Phys. Chem. B* **2018**, *122*, 6491–6502.

(25) Vinyard, D. J.; Brudvig, G. W. Progress Toward a Molecular Mechanism of Water Oxidation in Photosystem II. *Annu. Rev. Phys. Chem.* **2017**, *68*, 101–117.

(26) Cox, N.; Retegan, M.; Neese, F.; Pantazis, D. A.; Boussac, A.; Lubitz, W. Electronic Structure of the Oxygen-Evolving Complex in Photosystem II Prior to O-O Bond Formation. *Science (80-.).* **2014**, *345*, 804–808.

(27) Brudvig, G. W. Water Oxidation Chemistry of Photosystem II. *Philos. Trans. R. Soc. B Biol. Sci.* **2008**, *363*, 1211–1219.

(28) Charles Dismukes, G.; Brimblecombe, R.; Felton, G. A. N.; Pryadun, R. S.; Sheats, J. E.; Spiccia, L.; Swiegers, G. F. Development of Bioinspired Mn4O4-Cubane Water Oxidation Catalysts: Lessons from Photosynthesis. *Acc. Chem. Res.* **2009**, *42*, 1935–1943.

(29) Shoji, M.; Isobe, H.; Yamaguchi, K. Concerted Bond Switching Mechanism Coupled with One-Electron Transfer for the Oxygen-Oxygen Bond Formation in the Oxygen-Evolving Complex of Photosystem II. *Chem. Phys. Lett.* **2018**, *714*, 219–226.

(30) Isobe, H.; Shoji, M.; Shen, J. R.; Yamaguchi, K. Chemical Equilibrium Models for the S3 State of the Oxygen-Evolving Complex of Photosystem II. *Inorg. Chem.* **2016**, *55*, 502–511.

(31) Pushkar, Y.; Davis, K. M.; Palenik, M. C. Model of the Oxygen Evolving Complex Which

Is Highly Predisposed to O-O Bond Formation. *J. Phys. Chem. Lett.* **2018**, *9*, 3525–3531.

(32) Armstrong, F. A. Why Did Nature Choose Manganese to Make Oxygen? *Philos. Trans. R. Soc. B Biol. Sci.* **2008**, *363*, 1263–1270.

(33) Lee, H. B.; Marchiori, D. A.; Chatterjee, R.; Oyala, P. H.; Yano, J.; Britt, R. D.; Agapie, T. S = 3 Ground State for a Tetranuclear MnIV4O4 Complex Mimicking the S3 State of the Oxygen-Evolving Complex. *J. Am. Chem. Soc.* **2020**, *142*, 3753–3761.

(34) Li, Y.; Yao, R.; Chen, Y.; Xu, B.; Chen, C.; Zhang, C. Mimicking the Catalytic Center for the Water-Splitting Reaction in Photosystem II. *Catalysts* **2020**, *10*, 185.

(35) Lee, J. Y.; Karlin, K. D. Elaboration of Copper-Oxygen Mediated C-H Activation Chemistry in Consideration of Future Fuel and Feedstock Generation. *Curr. Opin. Chem. Biol.* **2015**, *25*, 184–193.

(36) Lewis, E. A.; Tolman, W. B. Reactivity of Dioxygen-Copper Systems. *Chem. Rev.* **2004**, *104*, 1047–1076.

(37) Tinberg, C. E.; Lippard, S. J. Dioxygen Activation in Soluble Methane Monooxygenase. *Acc. Chem. Res.* **2011**, *44*, 280–288.

(38) Solomon, E. I.; Wong, S. D.; Liu, L. V.; Decker, A.; Chow, M. S. Peroxo and Oxo Intermediates in Mononuclear Nonheme Iron Enzymes and Related Active Sites. *Curr. Opin. Chem. Biol.* **2009**, *13*, 99–113.

(39) Green, M. T. C-H Bond Activation in Heme Proteins: The Role of Thiolate Ligation in Cytochrome P450. *Curr. Opin. Chem. Biol.* **2009**, *13*, 84–88.

(40) Costas, M.; Mehn, M. P.; Jensen, M. P.; Que, L. Dioxygen Activation at Mononuclear Nonheme Iron Active Sites: Enzymes, Models, and Intermediates. *Chem. Rev.* **2004**, *104*, 939–986.

(41) Solomon, E. I.; Heppner, D. E.; Johnston, E. M.; Ginsbach, J. W.; Cirera, J.; Qayyum, M.; Kieber-Emmons, M. T.; Kjaergaard, C. H.; Hadt, R. G.; Tian, L. Copper Active Sites in Biology. *Chem. Rev.* **2014**, *114*, 3659–3853.

(42) Coggins, M. K.; Sun, X.; Kwak, Y.; Solomon, E. I.; Rybak-Akimova, E.; Kovacs, J. A. Characterization of Metastable Intermediates Formed in the Reaction between a Mn(II) Complex and Dioxygen, Including a Crystallographic Structure of a Binuclear Mn(III)-Peroxo Species. *J. Am. Chem. Soc.* **2013**, *135*, 5631–5640.

(43) Shook, R. L.; Gunderson, W. A.; Greaves, J.; Ziller, J. W.; Hendrich, M. P.; Borovik, A. S. A Monomeric MnIII-Peroxo Complex Derived Directly from Dioxygen. *J. Am. Chem. Soc.* **2008**, *130*, 8888–8889.

(44) Rees, J. A.; Martin-Diaconescu, V.; Kovacs, J. A.; DeBeer, S. X-Ray Absorption and Emission Study of Dioxygen Activation by a Small-Molecule Manganese Complex. *Inorg. Chem.* **2015**, *54*, 6410–6422.

(45) Bossek, U.; Weyhermiiller, T.; Wieghardt, K.; Nuber, B.; Weiss, J. [L2Mn2(μ-O)2(μ-O2)](ClO4)2: The First Binuclear (g-Peroxo)Dimanganese(LV) Complex (L = 1,4,7-Trimethyl-1,4,7-TriazacycIononane). A Model for the S4 → S0 Transformation in the Oxygen-Evolving Complex in Photosynthesis. *J. Am. Chem. Soc.* **1990**, *112*, 6387–6388.

(46) Poon, P. C. Y.; Dedushko, M. A.; Sun, X.; Yang, G.; Toledo, S.; Hayes, E. C.; Johansen, A.; Piquette, M. C.; Rees, J. A.; Stoll, S.; Rybak-Akimova, E.; Kovacs, J. A. How Metal Ion Lewis Acidity and Steric Properties Influence the Barrier to Dioxygen Binding, Peroxo O-O Bond Cleavage, and Reactivity. *J. Am. Chem. Soc.* **2019**, *141*, 15046–15057.

(47) Parham, J. D.; Wijeratne, G. B.; Mayfield, J. R.; Jackson, T. A. Steric Control of Dioxygen Activation Pathways for MnII Complexes Supported by Pentadentate, Amide-

Containing Ligands. *Dalt. Trans.* **2019**, *48*, 13034–13045.

(48) Guo, M.; Lee, Y. M.; Gupta, R.; Seo, M. S.; Ohta, T.; Wang, H. H.; Liu, H. Y.; Dhuri, S. N.; Sarangi, R.; Fukuzumi, S.; Nam, W. Dioxygen Activation and O-O Bond Formation Reactions by Manganese Corroles. *J. Am. Chem. Soc.* **2017**, *139*, 15858–15867.

(49) Larson, V. A.; Battistella, B.; Ray, K.; Lehnert, N.; Nam, W. Iron and Manganese Oxo Complexes, Oxo Wall and Beyond. *Nat. Rev. Chem.* **2020**, *4*, 404–419.

(50) Brazzolotto, D.; Cantú Reinhard, F. G.; Smith-Jones, J.; Retegan, M.; Amidani, L.; Faponle, A. S.; Ray, K.; Philouze, C.; de Visser, S. P.; Gennari, M.; Duboc, C. A High-Valent Non-Heme μ-Oxo Manganese(IV) Dimer Generated from a Thiolate-Bound Manganese(II) Complex and Dioxygen. *Angew. Chemie Int. Ed.* **2017**, *56*, 8211–8215.

(51) Coggins, M. K.; Brines, L. M.; Kovacs, J. A. Synthesis and Structural Characterization of a Series of MnIIIOR Complexes, Including a Water-Soluble MnIIIOH That Promotes Aerobic Hydrogen-Atom Transfer. *Inorg. Chem.* **2013**, *52*, 12383–12393.

(52) Shirin, Z.; Young, V. G.; Borovik, A. S. Synthesis and Structure of a MnIII(OH) Complex Generated from Dioxygen. *Chem. Commun.* **1997**, *32*, 1967–1968.

(53) Gennari, M.; Duboc, C. Bio-Inspired, Multifunctional Metal-Thiolate Motif: From Electron Transfer to Sulfur Reactivity and Small-Molecule Activation. *Acc. Chem. Res.* **2020**, *53*, 2753–2761.

(54) Foster, A. W.; Osman, D.; Robinson, N. J. Metal Preferences and Metallation. *J. Biol. Chem.* **2014**, *289*, 28095–28103.

(55) Irving, B. H.; Williams, R. J. P. The Stability of Transition-Metal Complexes. *J. Chem. Soc.* **1953**, 3192–3210.

(56) Dudev, T.; Lim, C. Competition among Metal Ions for Protein Binding Sites:

Determinants of Metal Ion Selectivity in Proteins. *Chem. Rev.* **2014**, *114*, 538–556.

(57) Imlay, J. A. The Mismetallation of Enzymes during Oxidative Stress. *J. Biol. Chem.* **2014**, *289*, 28121–28128.

(58) Cotruvo, J. A.; Stubbe, J. Metallation and Mismetallation of Iron and Manganese Proteins in Vitro and in Vivo: The Class i Ribonucleotide Reductases as a Case Study. *Metallomics* **2012**, *4*, 1020–1036.

(59) Grāve, K.; Griese, J. J.; Berggren, G.; Bennett, M. D.; Högbom, M. The Bacillus Anthracis Class Ib Ribonucleotide Reductase Subunit NrdF Intrinsically Selects Manganese over Iron. *J. Biol. Inorg. Chem.* **2020**, *25*, 571–582.

(60) Emerson, J. P.; Kovaleva, E. G.; Farquhar, E. R.; Lipscomb, J. D.; Que, L.; by Martin Bollinger, E. J. Swapping Metals in Fe-and Mn-Dependent Dioxygenases: Evidence for Oxygen Activation without a Change in Metal Redox State. *PNAS* **2008**, *105*, 7347–7352.

(61) Torrents, E. Ribonucleotide Reductases: Essential Enzymes for Bacterial Life. *Front. Cell. Infect. Microbiol.* **2014**, *4*, 52.

(62) Nordlund, P.; Reichard, P. Ribonucleotide Reductases. *Annu. Rev. Biochem.* **2006**, *75*, 681–706.

(63) Migliore, A.; Polizzi, N. F.; Therien, M. J.; Beratan, D. N. Biochemistry and Theory of Proton-Coupled Electron Transfer. *Chem. Rev.* **2014**, *114*, 3381–3465.

(64) Rose, H. R.; Ghosh, M. K.; Maggiolo, A. O.; Pollock, C. J.; Blaesi, E. J.; Hajj, V.; Wei, Y.; Rajakovich, L. J.; Chang, W. C.; Han, Y.; Hajj, M.; Krebs, C.; Silakov, A.; Pandelia, M. E.; Bollinger, J. M.; Boal, A. K. Structural Basis for Superoxide Activation of Flavobacterium Johnsoniae Class i Ribonucleotide Reductase and for Radical Initiation by Its Dimanganese Cofactor. *Biochemistry* **2018**, *57*, 2679–2693.

(65) Cotruvo, J. A.; Stich, T. A.; Britt, R. D.; Stubbe, J. Mechanism of Assembly of the Dimanganese-Tyrosyl Radical Cofactor of Class Ib Ribonucleotide Reductase: Enzymatic Generation of Superoxide Is Required for Tyrosine Oxidation via a Mn(III)Mn(IV) Intermediate. *J. Am. Chem. Soc.* **2013**, *135*, 4027–4039.

(66) Valdez, C. E.; Smith, Q. A.; Nechay, M. R.; Alexandrova, A. N. Mysteries of Metals in Metalloenzymes. *Acc. Chem. Res.* **2014**, *47*, 3110–3117.

(67) Cotruvo, J. A.; Stubbe, J. Escherichia Coli Class Ib Ribonucleotide Reductase Contains a Dimanganese(III)-Tyrosyl Radical Cofactor in Vivo. *Biochemistry* **2011**, *50*, 1672–1681.

(68) Solomon, E. I.; Szilagyi, R. K.; DeBeer George, S.; Basumallick, L. Electronic Structures of Metal Sites in Proteins and Models: Contributions to Function in Blue Copper Proteins. *Chem. Rev.* **2004**, *104*, 419–458.

(69) Groves, J. T. Enzymatic C-H Bond Activation: Using Push to Get Pull. *Nat. Chem.* **2014**, *6*, 89–91.

(70) Krest, C. M.; Onderko, E. L.; Yosca, T. H.; Calixto, J. C.; Karp, R. F.; Livada, J.; Rittle, J.; Green, M. T. Reactive Intermediates in Cytochrome P450 Catalysis. *J. Biol. Chem.* **2013**, *288*, 17074–17081.

(71) Dunham, N. P.; Arnold, F. H. Nature's Machinery, Repurposed: Expanding the Repertoire of Iron-Dependent Oxygenases. *ACS Catal.* **2020**, *10*, 12239–12255.

(72) Romao, C. V.; Matias, P. M.; Sousa, C. M.; Pinho, F. G.; Pinto, A. F.; Teixeira, M.; Bandeiras, T. M. Insights into the Structures of Superoxide Reductases from the Symbionts Ignicoccus Hospitalis and Nanoarchaeum Equitans. *Biochemistry* **2018**, *57*, 5271–5281.

(73) Shoner, S. C.; Barnhart, D.; Kovacs, J. A. A Model for the Low-Spin, Non-Heme,

Thiolate-Ligated Iron Site of Nitrile Hydratase. *Inorg. Chem.* **1995**, *34*, 4517–4518.

(74) Ellison, J. J.; Nienstedt, A.; Shoner, S. C.; Barnhart, D.; Cowen, J. A.; Kovacs, J. A. Reactivity of Five-Coordinate Models for the Thiolate-Ligated Fe Site of Nitrile Hydratase. *J. Am. Chem. Soc.* **1998**, *120*, 5691–5700.

(75) Jackson, H. L.; Shoner, S. C.; Rittenberg, D.; Cowen, J. A.; Lovell, S.; Barnhart, D.; Kovacs, J. A. Probing the Influence of Local Coordination Environment on the Properties of Fe-Type Nitrile Hydratase Model Complexes. *Inorg. Chem.* **2001**, *40*, 1646–1653.

(76) Kovacs, J. A. Synthetic Analogues of Cysteinate-Ligated Non-Heme Iron and Non-Corrinoid Cobalt Enzymes. *Chem. Rev.* **2004**, *104*, 825–848.

(77) Kennepohl, P.; Neese, F.; Schweltzer, D.; Jackson, H. L.; Kovacs, J. A.; Solomon, E. I. Spectroscopy of Non-Heme Iron Thiolate Complexes: Insight into the Electronic Structure of the Low-Spin Active Site of Nitrile Hydratase. *Inorg. Chem.* **2005**, *44*, 1826–1836.

(78) Green, M. T. Role of the Axial Ligand in Determining the Spin State of Resting Cytochrome P450 [7]. *J. Am. Chem. Soc.* **1998**, *120*, 10772–10773.

(79) Blaesi, E. J.; Fox, B. G.; Brunold, T. C. Spectroscopic and Computational Investigation of Iron(III) Cysteine Dioxygenase: Implications for the Nature of the Putative Superoxo-Fe(III) Intermediate. *Biochemistry* **2014**, *53*, 5759–5770.

(80) Denisov, I. G.; Makris, T. M.; Sligar, S. G.; Schlichting, I. Structure and Chemistry of Cytochrome P450. *Chem. Rev.* **2005**, *105*, 2253–2277.

(81) Brites Campos-Shimada, L.; Hideo Gilglioni, E.; Fernandes Garcia, R.; Rizato Martins-Maciel, E.; Fernandes Garcia, angela; Luiza Ishii-Iwamoto, E.; Luzia Salgueiro-Pagadigorria, C. Superoxide Dismutase: A Review and a Modified Protocol for Activities Measurements in Rat Livers. *Arch. Physiol. Biochem.* **2020**, *126*, 292–299.

(82) Kovacs, J. A. How Iron Activates O2. *Science (80-.).* **2003**, *299*, 1024–1025.

(83) Groves, J. T. High-Valent Iron in Chemical and Biological Oxidations. *J. Inorg. Biochem.* **2006**, *100*, 434–447.

(84) Groves, J. T. The Bioinorganic Chemistry of Iron in Oxygenases and Supramolecular Assemblies. *PNAS* **2003**, *100*, 3569–3574.

(85) Huang, X.; Groves, J. T. Oxygen Activation and Radical Transformations in Heme Proteins and Metalloporphyrins. *Chem. Rev.* **2018**, *118*, 2491–2553.

(86) Machan, C. W. Advances in the Molecular Catalysis of Dioxygen Reduction. *ACS Catal.* **2020**, *10*, 2640–2655.

(87) Elwell, C. E.; Gagnon, N. L.; Neisen, B. D.; Dhar, D.; Spaeth, A. D.; Yee, G. M.; Tolman, W. B. Copper-Oxygen Complexes Revisited: Structures, Spectroscopy, and Reactivity. *Chem. Rev.* **2017**, *117*, 2059–2107.

(88) Fiedler, A. T.; Fischer, A. A. Oxygen Activation by Mononuclear Mn, Co, and Ni Centers in Biology and Synthetic Complexes. *J. Biol. Inorg. Chem.* **2017**, *22*, 407–424.

(89) Jeschke, J.; O'Hagan, H. M.; Zhang, W.; Vatapalli, R.; Calmon, M. F.; Danilova, L.; Nelkenbrecher, C.; Van Neste, L.; Bijsmans, I. T. G. W.; Van Engeland, M.; Gabrielson, E.; Schuebel, K. E.; Winterpacht, A.; Baylin, S. B.; Herman, J. G.; Ahuja, N. Frequent Inactivation of Cysteine Dioxygenase Type 1 Contributes to Survival of Breast Cancer Cells and Resistance to Anthracyclines. *Clin. Cancer Res.* **2013**, *19*, 3201–3211.

(90) Dietrich, D.; Krispin, M.; Dietrich, J.; Fassbender, A.; Lewin, J.; Harbeck, N.; Schmitt, M.; Eppenberger-Castori, S.; Vuaroqueaux, V.; Spyratos, F.; Foekens, J. A.; Lesche, R.; Martens, J. W. CDO1 Promoter Methylation Is a Biomarker for Outcome Prediction of Anthracycline Treated, Estrogen Receptor-Positive, Lymph Node-Positive Breast Cancer

Patients. *BMC Cancer* **2010**, *10*, 247–254.

(91) Thomas Heafield, M.; Fearn, S.; Steventon, G. B.; Waring, R. H.; Williams, A. C.; Sturman, S. G. Plasma Cysteine and Sulphate Levels in Patients with Motor Neurone, Parkinson's and Alzheimer's Disease. *Neurosci. Lett.* **1990**, *110*, 216–220.

(92) Meller, S.; Zipfel, L.; Gevensleben, H.; Dietrich, J.; Ellinger, J.; Majores, M.; Stein, J.; Sailer, V.; Jung, M.; Kristiansen, G.; Dietrich, D.; Orn Dietrich, J.; Org Ellinger, J. CDO1 Promoter Methylation Is Associated with Gene Silencing and Is a Prognostic Biomarker for Biochemical Recurrence-Free Survival in Prostate Cancer Patients. *Epigenetics* **2016**, *11*, 871–880.

(93) Nicholls, P. Classical Catalase: Ancient and Modern. *Arch. Biochem. Biophys.* **2012**, *525*, 95–101.

(94) Whittaker, J. W. Non-Heme Manganese Catalase-The "other" Catalase. *Arch. Biochem. Biophys.* **2012**, *525*, 111–120.

(95) Jackson, T. A.; Brunold, T. C. Combined Spectroscopic/Computational Studies on Fe-and Mn-Dependent Superoxide Dismutases: Insights into Second-Sphere Tuning of Active Site Properties. *Acc. Chem. Res.* **2004**, *37*, 461–470.

(96) Kovacs, J. A.; Brines, L. M. Understanding How the Thiolate Sulfur Contributes to the Function of the Non-Heme Iron Enzyme Superoxide Reductase. *Acc. Chem. Res.* **2007**, *40*, 501–509.

(97) Mathé, C.; Weill, C. O.; Mattioli, T. A.; Berthomieu, C.; Houée-Levin, C.; Tremey, E.; Nivière, V. Assessing the Role of the Active-Site Cysteine Ligand in the Superoxide Reductase from Desulfoarculus Baarsii. *J. Biol. Chem.* **2007**, *282*, 22207–22216.

(98) Berglund, G. I.; Carlsson, G. H.; Smith, A. T.; Szöke, H.; Henriksen, A.; Hajdu, J. The

Catalytic Pathway of Horseradish Peroxidase at High Resolution. *Nature* **2002**, *417*, 463–468.

(99) Denisov, I. G.; Makris, T. M.; Sligar, S. G. Formation and Decay of Hydroperoxo-Ferric Heme Complex in Horseradish Peroxidase Studied by Cryoradiolysis. *J. Biol. Chem.* **2002**, *277*, 42706–42710.

(100) Kurtz, D. M. Avoiding High-Valent Iron Intermediates: Superoxide Reductase and Rubrerythrin. *J. Inorg. Biochem.* **2006**, *100*, 679–693.

(101) Abreu, I. A.; Cabelli, D. E. Superoxide Dismutases-a Review of the Metal-Associated Mechanistic Variations. *Biochim. Biophys. Acta* **2010**, *1804*, 263–274.

(102) Martins, M. C.; Romão, C. V; Folgosa, F.; Borges, P. T.; Frazão, C.; Teixeira, M. How Superoxide Reductases and Flavodiiron Proteins Combat Oxidative Stress in Anaerobes. *Free Radic. Biol. Med.* **2019**, *140*, 36–60.

(103) Adams, M. W.; Jenney, F. E.; Clay, M. D.; Johnson, M. K. Superoxide Reductase: Fact or Fiction? *J. Biol. Inorg. Chem.* **2002**, *7*, 647–652.

(104) Bonnot, F.; Molle, T.; Ménage, S.; Moreau, Y.; Duval, S.; Favaudon, V.; Houée-Levin, C.; Nivière, V. Control of the Evolution of Iron Peroxide Intermediate in Superoxide Reductase from Desulfoarculus Baarsii. Involvement of Lysine 48 in Protonation. *J. Am. Chem. Soc.* **2012**, *134*, 5120–5130.

(105) Sit, P. H. L.; Migliore, A.; Ho, M. H.; Klein, M. L. Quantum Mechanical and Quantum Mechanical/Molecular Mechanical Studies of the Iron-Dioxygen Intermediates and Proton Transfer in Superoxide Reductase. *J. Chem. Theory Comput.* **2010**, *6*, 2896–2909.

Chapter 2. Metal Ion Lewis Acidity and Steric Properties Influence the Barrier to Dioxygen Binding, Peroxo O-O Bond Cleavage, and Reactivity

Components of this chapter have been republished or adapted with permission of the Journal of the American Chemical Society from How Metal Ion Lewis Acidity and Steric Properties Influence the Barrier to Dioxygen Binding, Peroxo O-O Bond Cleavage, and Reactivity, Poon, Penny Chaau Yan; Dedushko, Maksym A.; Sun, Xianru; Yang, Guang; Toledo, Santiago; Hayes, Ellen C.; Johansen, Audra; Piquette, Marc C.; Rees, Julian A.; Stoll, Stefan; Rybak-Akimova, Elena; Kovacs, Julie A. *J. Am. Chem. Soc.* **2019**. *141*, 15046-15057.; Copyright 2019 American Chemical Society.

2.1 Introduction

Fundamental scientific research is needed in order to develop methods for efficiently capturing sunlight and converting its energy into storable fuels. Nature accomplishes this via photosynthesis, which converts solar energy into energy that is stored in a chemical bond by extracting electrons from H_2O to form O_2.[1–4] The sluggish kinetics of H_2O oxidation has been a major concern for existing fuel cells.[5] Nature had a few billion years to refine its Mn-containing photosynthetic H_2O oxidation catalyst, therefore understanding the mechanism by which it facilitates this reaction, or its microscopic reverse, would be of value. However, despite its relevance to photosynthesis,[6–9] the dioxygen chemistry of Mn remains relatively unexplored,[6,10–12] relative to that of Fe and Cu.[13–19] Very little is known about the Mn-induced O-O bond

forming step,[20] because it occurs following the rate-determining step.[21–25] An unobserved peroxo intermediate is proposed to form during photosynthesis,[22–24] which then readily evolves O_2.[26]

Previously we showed that coordinatively unsaturated $[Mn^{II}(L^{Mepy})]^+$ (**1**^{Mepy}, L^{Mepy}= (6-Me-DPEN)$N_4^{Me2}S^-$) reacts with O_2 at low temperatures (-40 °C) to form dioxygen-bound $[Mn(L^{Mepy})(O_2)]^+$ (**2**^{Mepy}), *en route* to the first example of a crystallographically characterized binuclear peroxo-bridged dimer, $\{[Mn^{III}(L^{Mepy})]_2(\mu\text{-}O_2)\}^{2+}$ (**3**^{Mepy}).[6] Dioxygen binding to **1**^{Mepy} was shown to occur on the millisecond time-scale.[6] A thiolate was incorporated into our ligand scaffold in order to 1) provide a chromophore that facilitates the spectroscopic observation of metastable intermediates,[6,27–31] 2) lower the activation barrier to O_2 binding, and 3) provide stability to highly reactive M-O_2 species.[32,33] The rate at which peroxo-bridged **3**^{Mepy} forms is slow enough at -40 °C to monitor using a benchtop UV-vis spectrometer. However, with the L^{Mepy} ligand system it was not possible to determine the mechanism by which the O-O bond of peroxo-bridged **3**^{Mepy} cleaves to afford mono-oxo bridged Mn^{III}-O-Mn^{III} (**6**^{Mepy}, Scheme 2.1), because this step was shown to be rate-determining.[6]

Scheme 2.1. Low temperature reaction between **1**^{Mepy} and O_2 affords **6**^{Mepy} via observable superoxo **2**^{Mepy} and peroxo **3**^{Mepy} intermediates.

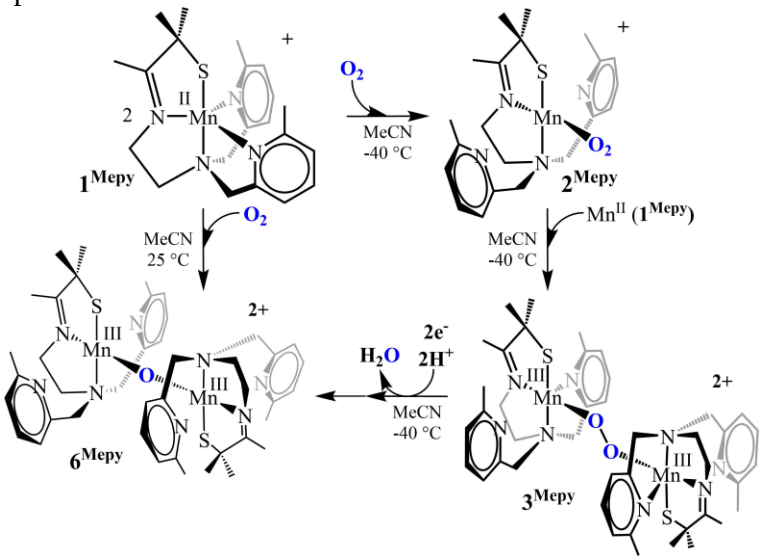

Mechanisms for O-O bond cleavage with Fe and Cu have been shown to involve either protonation of a M-OOH at the distal oxygen,[34] or the addition of a second metal ion to the distal oxygen to form a bridging peroxo. Ideally an η^2, η^2-side-on peroxo forms so as to maximize overlap with the empty σ*(O-O).[14,19] In contrast, mechanistic details regarding Mn-promoted O-O bond cleavage versus formation remain relatively unexplored.[35–41] An end-on peroxo complex is expected to be more stable than a side-on peroxo complex, perhaps explaining why we were able to crystallize $\mathbf{3^{Mepy}}$.[6] Prior to our work,[6] there were no crystallographically characterized examples of binuclear end-on or side-on Mn^{III}-peroxos, and there were only a handful of examples of monomeric η^2-side-on Mn^{III}-peroxos,[10,42–45]only one of which is derived from O_2,[10] an end-on Mn^{III}-peroxo compound, however it was not crystallographically characterized.[46]

A series of structurally analogous five-coordinate, thiolate-ligated Mn^{II} complexes (e.g., $\mathbf{1^{Mepy}}$ of Scheme 2.1) was previously reported by our group, which incorporate readily derivatized N-heterocycles amines (N^{Ar} = 6-H-pyridine ($\mathbf{1^{Py}}$), 6-Me-pyridine ($\mathbf{1^{Mepy}}$), and quinoline ($\mathbf{1^{Quino}}$)), providing us with a method for tuning their steric and electronic properties.[6,47] In order to obtain more information regarding the mechanism of the O-O bond cleaving step, we explore herein the low-temperature dioxygen chemistry of quinoline-ligated $[Mn^{II}(L^{Quino})]^+$ ($\mathbf{1^{Quino}}$),[48] in addition to that of a new Mn^{II} complex, $[Mn^{II}(L^{MeOpy})]^+$ ($\mathbf{1^{MeOpy}}$), containing a more electron donating substituent on the pyridine ring. We will show that the energetic barriers of the reaction, including O_2 binding and release, and O-O bond cleavage, can be adjusted by changing the electron donor character of the ligand.[47]

2.2 Experimental

General Methods. All manipulations were performed using Schlenk techniques or under an N_2 atmosphere in a glovebox. Reagents and solvents were purchased from commercial vendors, were of highest available purity, and were used without further purification unless otherwise noted. Methylene chloride (DCM), tetrahydrofuran (THF), diethyl ether (Et_2O), and acetonitrile (MeCN) were rigorously degassed, and purified using solvent purification columns housed in a custom stainless-steel cabinet, dispensed via a stainless steel Schlenk-line (GlassContour). Methanol (MeOH) was dried over magnesium methoxide and distilled prior to use. ^{1}H NMR spectra were recorded on a Bruker AV 300 FT NMR spectrometer at ambient temperature and were referenced to residual solvent. Chemical shifts are listed in parts per million (ppm), and coupling constants (*J*) in Hz. UV-vis spectra were recorded on a Varian Cary 50 spectrophotometer equipped with a fiber optic cable connected to an ATR "dip" probe (C-technologies). A custom-built two-neck solution sample holder equipped with a threaded glass connector was sized specifically to fit the "dip" probe. Electrospray-ionization mass spectrometry (ESI-MS) data were obtained on a Bruker Esquire Liquid Chromatograph-Ion Trap mass spectrometer. Cyclic voltammograms were recorded in MeCN with ^{n}Bu$_4$N(PF_6) supporting electrolyte (0.100 M) using a CH Instruments (CHI600E) potentiostat with a glassy carbon working electrode, an $Ag^+/AgNO_3$ reference electrode, and a platinum auxiliary electrode. EPR spectra were recorded on a Bruker E580 CW-EPR spectrometer operating at X-band frequency and equipped with an Oxford helium cryostat and dual mode cavity. EPR data were fit with EasySpin.[49] X-ray crystallography data were recorded on a Bruker APEX II single Crystal X-ray diffractometer with Mo Kα radiation. Magnetic moments (solution state) were obtained using the Evans' method as modified for super-conducting solenoids.[50,51] Organic ligands, 1-(tert-

butyloxycarbonyl)ethyldiamine (NNBoc) and 3-methyl-3-metcapto-2-butanone, Mn^{II} complex $\mathbf{1^{Quino}}$ were synthesized according to a published procedure.[48,52]

2.2.1. Synthesis of methyl 6-methyloxy-2-pyridinecarboxylate (L_1). To a stirred suspension of 6-hydroxypyridine-2-carboxylic acid (1.50 g, 10.8 mmol) and silver carbonate (4.46 g, 16.2 mmol) in 500 mL $CHCl_3$ was added iodomethane (2.75 mL, 43.2 mmol) at room temperature in the dark. The mixture was brought to reflux overnight. After cooling back to room temperature, the mixture was filtered over Celite and the filtrate concentrated to give $\mathbf{L_1}$ as a dark yellow oil. The product was purified by column chromatography (4:1 Hexanes/EtOAc) to give the final product $\mathbf{L_1}$ as a colorless solid (1.57 g 83.2%). ^{1}H NMR (300 MHz, $CDCl_3$) δ 7.70 (m, 2H), 6.94 (d, *J*= 7.3 Hz, 1H), 4.03 (s, 3H), 3.97 (s, 3H); ESI-MS m/z: 168.2 ($M+H^+$).

2.2.2. Synthesis of 6-methoxy-2-pyridinemethanol (L_2). To a stirring suspension of $LiAlH_4$ (0.808 g, 21.3 mmol) in THF (80 mL) at 0 °C was added $\mathbf{L_1}$ (1.780 g, 10.7 mmol) dropwise as a solution in THF (20 mL). The reaction mixture was warmed to room temperature and allowed to stir until the reaction is complete. The reaction mixture was then cooled to 0 °C and quenched with DI H_2O. The mixture was filtered through Celite and the filtrate was concentrated *in vacuo* to give the final product $\mathbf{L_2}$ as a colorless oil (0.953 g, 64%). ^{1}H NMR (300 MHz, $CDCl_3$) δ 7.57 (t, *J*= 7.5 Hz, 1H), 6.82 (d, *J*= 7.3 Hz, 1H), 6.65 (d, 8.2 Hz, 1H), 4.69 (d, *J*= 4.2 Hz, 2H), 3.58 (t, *J*= 4.4 Hz, 3H) ; ESI-MS m/z: 140.1 ($M+H^+$).

2.2.3. Synthesis of 2-(chloromethyl)-6-methoxypyridine hydrochloride (L_3). Thionyl chloride (4.827 g, 40.6 mmol) was added dropwise to a solution of 6- methoxy-2-pyridinemethanol (0.941 g, 6.76 mmol) in dry DCM (10 mL) at 0 °C. The reaction mixture was stirred for one hour. Volatiles were removed *in vacuo* and the resulting solid was dissolved in a minimum amount of hot ethanol and cooled to -30 °C overnight, inducing crystallization of the product $\mathbf{L_3}$

as colorless needles. ^{1}H NMR (300 MHz, $CDCl_3$) δ 7.98 (t, *J*= 7.9 Hz, 1H), 7.33 (d, *J*= 7.5 Hz, 1H), 6.95 (d, *J*= 8.4 Hz, 1H), 5.00 (s, 2H), 4.15 (s, 3H).

2.2.4. Synthesis of N-(tert-butyloxycarbonyl)-N',N'-[bis(6-methoxy-2-pyridilmethyl)ethane-1,2-diamine] (6-MeO-DPENBoc, L_4). NNBoc (0.542 g, 3.38 mmol) and $\mathbf{L_3}$ (6.67 mmol) were dissolved in 5 M NaOH (7 mL) and stirred at room temperature for 4 days in air. Water (10 mL) was added and the aqueous layer was extracted 3x with DCM (30 mL each). The organic extracts were washed twice with brine (30 mL each) and dried over sodium sulfate. Removal of solvent *in vacuo* yielded $\mathbf{L_4}$ as a dark orange oil. If shown necessary by TLC, product may be further purified by column chromatography (5% MeOH/DCM). ^{1}H NMR (300 MHz, $CDCl_3$) δ 7.48 (t, *J*= 7.6 Hz, 2H), 6.97 (d, *J*= 7.2 Hz, 2H), 6.58 (d, *J*= 8.2 Hz, 2H), 5.55 (bs, 1H), 3.92 (s, 6H), 3.72 (s, 4H), 3.23 (m, 2H), 2.70 (t, *J*= 5.8 Hz, 2H), 1.40 (s, 9H); ESI-MS m/z: 403.2 ($M+H^+$).

2.2.5. Synthesis of N,N-bis(6-methoxy-2-pyridilmethyl)ethane-1,2-diamine (6-MeO-DPEN, $\mathbf{L^5}$). Trifluoroacetic acid (4.625 g, 40.6 mmol) was added dropwise to a solution of $\mathbf{L_4}$ (1.360 g, 3.38 mmol) in DCM (15 mL) at 0 °C. The mixture was slowly warmed to room temperature while stirring and the volatiles were removed *in vacuo.* To the remaining oil, 5 M NaOH (20 mL) was added and the mixture was extracted with DCM (3 x 30 mL). The combined organic extracts were washed with brine (2 x 30 mL) and dried over sodium sulfate. Concentration of organic extracts *in vacuo* gave $\mathbf{L^5}$ as a dark orange oil. ^{1}H NMR (300 MHz, $CDCl_3$) δ 7.49 (t, *J*= 7.5 Hz, 2H), 7.04 (d, *J*= 7.2 Hz, 2H), 6.55 (d, *J*= 8.2 Hz, 2H), 3.88 (s, 6H), 3.73 (s, 4H), 2.77 (t, *J*= 5.5 Hz, 2H), 2.65 (t, *J*= 5.5 Hz, 2H), 1.41 (bs, 2H); ESI-MS m/z: 303.1 ($M+H^+$).

2.2.6. Synthesis of $[Mn^{II}(S^{Me2}N_4(6\text{-MeO-DPEN}))]_2(PF_6)_2$ $(1^{MeOpy})(PF_6)_2$. Sodium methoxide (0.079 g, 1.46 mmol), 3-mercapto-3-methyl-2-butanone (0.173 g, 1.46 mmol), 6-MeO-DPEN ($\mathbf{L^5}$, 0.441 g, 1.46 mmol), manganese sulfate monohydrate (0.247 g, 1.46 mmol), and sodium

hexafluorophosphate (0.245 g, 1.46 mmol) were each dissolved or slurred in MeOH (2 mL) under an inert atmosphere in a dry box. Each reagent was subsequently added to a Schlenk flask charged with a stir bar. After gently stirring the resulting reaction mixture at room temperature for two days. All volatiles were removed to afford a crude yellow solid. The crude product was redissolved in minimal MeCN (~5 mL) and filtered through a fine fritted filter. The resulting solution was layered with ~15 mL Et_2O and was allowed to crystallize at -30 ºC to afford the title product as a slight purple solid in 39 % yield (0.345 g, 0.574 mmol).

2.2.7. Synthesis of $[Mn^{II}(S^{Me2}N_4$(6-MeO-DPEN))$]_2(BPh_4)_2$ $(\mathbf{1}^{MeOpy})(BPh_4)_2$. Sodium methoxide (0.079 g, 1.46 mmol), 3-mercapto-3-methyl-2-butanone (0.173 g, 1.46 mmol), 6-MeO-DPEN (**L**^{5}, 0.441 g, 1.46 mmol), manganese sulfate monohydrate (0.247 g, 1.46 mmol), and sodium tetraphenylborate (0.499 g, 1.46 mmol) were each dissolved or slurred in MeOH (2 mL) under an inert atmosphere in a dry box. Each reagent was subsequently added to a Schlenk flask charged with a stir bar. After gently stirring the resulting reaction mixture at room temperature for two days. All volatiles were removed to afford a crude yellow solid. The crude product was redissolved in minimal MeCN (~5 mL) and filtered through a fine fritted filter. The resulting solution was layered with ~15mL Et_2O and was allowed to crystallize at -30 ºC to afford the title product as a slight purple solid in 39% yield (0.345 g, 0.574 mmol).

2.2.8. Synthesis of $[Mn^{III}(S^{Me2}N_4$(6-MeO-DPEN))$]_2$(μ-O) $(BPh_4)_2$ $(\mathbf{6}^{MeOpy})(BPh_4)_2$. A solution of $(\mathbf{1}^{MeOpy})(BPh_4)_2$ (0.300 g, 0.499 mmol) was prepared in MeCN (1 mL) under an inert atmosphere in a dry box. The solution was allowed to stir in air at ambient temperature for approximately five minutes during which time the colorless solution turned dark purple. The resulting solution was then carefully layered with Et_2O (9mL). The mixture was allowed to diffuse together at room temperature overnight. Recrystallization of the resulting dark purple

solid afforded the title compound in 37.6 % yield (0.124 g, 0.187 mmol). Electronic absorption spectrum: λmax (nm) (ε ($M^{-1}cm^{-1}$)) MeCN: 565 (958), DCM: 575 (1013). ESI-MS: Expected *m/z* for $[C_{42}H_{58}N_8O_5S_2Mn_2]^{2+}$ = 464.1, found *m/z* = 463.0.

2.2.9. Formation of Putative $Mn^{III}Mn^{IV}$ (5^{MeOpy}) via O_2 Addition to 1^{MeOpy} at -73 °C. A solution of $\mathbf{1}^{MeOpy}$ (3.75 x 10^{-6} mmol) was dissolved in 5 mL DCM, placed in an argon purged dip probe cell and brought to -73 °C using acetone/dry ice bath. After 10 minutes, a stream of O_2 was introduced to the solution. The formation of the metastable $Mn^{III}Mn^{IV}$ ($\mathbf{5}^{MeOpy}$) was characterized by UV-vis with λ_{max} = 505 nm.

2.2.13. Stopped Flow Kinetic Measurements. Acetonitrile (MeCN) or propionitrile (EtCN) solutions of the reagents were prepared in an MBraun glove box filled with ultra-high purity argon and placed into Hamilton gastight syringes. Time-resolved spectra (400-800 nm) were acquired at low temperatures using a Hi-Tech Scientific SF-61DX2 Multi-Mixing CryoStopped-Flow instrument (TgK Scientific Ltd.) equipped with a MCS UV/NIR light source (Spectralytics, DenMark) and a J&M TIDAS-DAQ diode array detector. The stopped-flow instrument was equipped with PEEK tubing fitted inside stainless-steel plumbing, a 1.00 cm^3 quartz mixing cell, and an anaerobic kit purged with argon. The temperature in the mixing cell was maintained to 0.1 °C and the mixing time was 2-3 ms. All flow lines of the instrument were extensively washed with degassed, anhydrous acetonitrile before charging the driving syringes with reactant solutions. The reactions were studied by rapid scanning spectrophotometry under pseudo-first-order conditions with excess O_2. Saturated solutions of O_2 were prepared by bubbling dry O_2 gas for 15 minutes into gastight syringes containing dry MeCN or EtCN; dilutions of the O_2 saturated solvent were performed anaerobically to obtain the desired [O_2]. The solubility of O_2 was taken as 8.1 mM in MeCN at 25°C.[53] All of the experiments were performed in a single-

mixing mode of the instrument, with a 1:1 (v/v) mixing ratio. A series of three or four measurements gave an acceptable standard deviation (within 10%). Data analysis was performed with Kinetic Studio (TgK Scientific Ltd.) and ReactLab Kinetics (JPlus Consulting Pty Ltd.) software programs.

2.2.14. X-ray Crystallographic Structure Determination.

A black block of peroxo-bridged **3**$^{\mathbf{Quino}}$, with dimensions 0.03 x 0.03 x 0.01 mm^3, was mounted on a glass capillary with oil. Data was collected at -173 ˚C. The crystal-to-detector distance was set to 40 mm and the exposure time was 100 seconds per degree for all sets of exposure. The scan width was 0.5˚. Data collection was 96.6% complete to 25.0˚ in ϑ. A total of 11,234 partial and complete reflections were collected covering the indices h = -16 to 16, k = -16 to 16, l = -11 to 17. 8,380 reflections were symmetry independent and the R_{int} = 0.2126 indicated that the data was very poor (0.07 average quality). Indexing and unit cell refinement indicated a triclinic P lattice with the space group P $\bar{1}$ (No.2).

A colorless prism of **1**$^{\mathbf{MeOpy}}$, measuring 0.10 x 0.04 x 0.035 mm^3 was mounted on a loop with oil. Data was collected at -173 ˚C on a Bruker APEX II single crystal X-ray diffractometer, Mo-radiation. The crystal-to-detector distance was set to 40 mm and the exposure time was 20 seconds per frame for all sets of exposure. The scan width was 0.5˚. Data collection was 100% complete to 25˚ in ϑ. A total of 67246 reflections were collected covering the indices, h = -13 to 13, k = -16 to 16, l = -18 to 18. 7942 reflections were symmetry independent and the R_{int} = 0.1095 indicated that the data was of slightly less than average quality (0.07). Indexing and unit cell refinement indicated a triclinic lattice. The space group was found to be P $\bar{1}$ (No.2). A purple rod of mono oxo-bridged **6**$^{\mathbf{MeOpy}}$, measuring 0.10 x 0.10 x 0.05 mm^3 was mounted on a loop with oil. Data was collected at -163 ˚C on a Bruker APEX II single crystal X-ray

diffractometer, Mo-radiation. The crystal-to-detector distance was set to 40 mm, and exposure time was 100 seconds per degree for all sets. The scan width was 0.5°. Data collection was 100% complete to 25° in ϑ. A total of 51131 (merged) reflections were collected covering the indices, h = -16 to 16, k = -24 to 25, l = -23 to 17. 10048 reflections were symmetry independent and the R_{int} = 0.0937 indicated that the data was of less than average quality (0.07). Indexing and unit cell refinement indicated a primitive monoclinic lattice. The space group was found to be P 2_1/c (No.14).

All X-ray data sets were integrated and scaled using hkl-SCALEPACK or SAINT, SADABS within the APEX2 software package by Bruker.[54] Solutions obtained via direct methods (SHELXS, SIR97)[55,56] produced complete heavy atom phasing models consistent with each proposed structure. Structures were completed via difference Fourier synthesis with SHELXL97,[57,58] or SHELXTL 6.10. Scattering factors were taken from Waasmair and Kirfel.[59] Hydrogen atoms were placed in geometrically idealized positions and constrained to ride on their parent atoms with C-H distances in the range 0.95-1.00 Å. Isotropic thermal parameters U_{eq} were fixed such that they were 1.2U_{eq} of their parent atom U_{eq} for C-Hs and 1.5U_{eq} for methyl groups. All non-hydrogen atoms were refined anisotropically by full-matrix least-squares.

2.2.15. Computational Details. Calculations were performed using the ORCA v. 4.0.0 quantum chemistry package developed by Neese and coworkers.[60] Initial geometry optimizations utilized B3LYP hybrid functional and 6-311G basis set for all complexes. Further geometry optimizations employed a polarized triple-zeta def2-TZVP basis set, the def2/J auxiliary basis set for Coulomb fitting, and the atom-pairwise dispersion correction of Grimme (D3BJ).[61] Tight convergence criteria were required for self-consistent field (SCF) solutions. The Grid4 (GridX4)

integration grid size, and the conductor-like polarizable continuum model (CPCM), were used for geometry optimizations.[62] Geometry optimizations and analytical frequency calculations were performed using the PBE0 functional, with the resolution of identity (RI) chain-of-spheres (RIJCOSX) approximation,[63,64] and initiated from the crystallographic coordinates when available. Analytical frequency calculations were performed on all optimized structures to determine whether the obtained stationary points corresponded to local minima.

Crystal structures of $[Mn^{II}(L^{Mepy})]^{+}$ (**1**$^{\mathbf{Mepy}}$) and $[Mn^{II}(L^{Quino})]^{+}$ (**1**$^{\mathbf{Quino}}$) were used as a starting point for geometry optimizations using a B3LYP/6-311G functional/basis set, followed by PBE0/def2-TZVP optimization. A monomeric $[Mn^{II}(L^{MeOpy})]^{+}$ (**1**$^{\mathbf{MeOpy}}$) model was constructed by replacing methyl groups of **1**$^{\mathbf{Mepy}}$ with methoxy moieties, since crystallographic coordinates were not available. Crystallographic coordinates were used as a starting point for geometry optimizations of peroxo $\{[Mn^{III}(L^{Quino})]_2(\mu\text{–}O_2)\}^{2+}$ (**3**$^{\mathbf{Quino}}$) using a B3LYP/6-311G functional/basis set. Since a structure was not available peroxo-bridged $\{[Mn^{III}(L^{MeOpy}]_2(\mu\text{–}O_2)\}^{2+}$ (**3**$^{\mathbf{MeOpy}}$), the μ-oxo bridged structure of $\{[Mn^{III}(L^{MeOpy}]_2(\mu\text{–}O)\}^{2+}$ (**6**$^{\mathbf{MeOpy}}$) was used as a starting point by replacing the bridging oxo atom with peroxo moiety, with Mn-O bond length of 1.875 Å ,and O-O bond distance of 1.450 Å.

The broken-symmetry formalism to model the coupled paramagnetic sites of peroxo-bridged **3**$^{\mathbf{Quino}}$ and **3**$^{\mathbf{MeOpy}}$. This involved SCF calculations for the high spin (HS) state of the Mn-peroxo complex, $Mn^{III}(S = 4/2, \uparrow)\text{-}O_2\text{-}Mn^{III}(S = 4/2, \uparrow)$. Next, a broken symmetry state was set up with the spin-flip chosen at one of the Mn centers (final total m_s = 0) and another SCF calculation was carried out in order to calculate energy of the "broken symmetry" (BS), $Mn^{III}(S = 4/2, \downarrow)\text{-}O_2\text{-}Mn^{III}(S = 4/2, \uparrow)$. state. Finally, the energies of both the HS and BS states were used to estimate the coupling constant, *J,* (associated with the phenomenological Hamiltonian $\hat{H}$ = –

$2J_{12}\hat{S}_1\hat{S}_2$) using the equation $J = -(E_{HS} - E_{BS})/(\langle S^2\rangle_{HS} - \langle S^2\rangle_{BS})$, which is valid over the entire coupling strength regime. Where, E_{HS} and E_{BS} are the energies of the high-spin (HS), and the broken-symmetry (BS) states, respectively, and $\langle S^2\rangle$ are the expectation values of the squared spin operator for the HS and BS states.[65] The coupling constant of $J^{calc} = 3.8$ cm^{-1} was obtained for $\mathbf{3}^{\mathbf{Quino}}$ and $J^{calc} = -0.53$ cm^{-1} for $\mathbf{3}^{\mathbf{MeOpy}}$.

Hybrid time-dependent DFT (TD-DFT) calculations employed the RIJCOSX and the Tamm-Dancoff approximations (TDA).[66,67] Excited states from TD-DFT calculations were analyzed using Natural Transition orbitals (NTOs) and by visualizing their difference densities between the ground and excited states. Canonical molecular orbital isosurfaces and natural transition orbitals in the TD-DFT calculations were visualized at an isovalue of 0.05 a_0^3 using UCSF Chimera.[68]

2.3 Results and Discussion

2.3.1 *Ligand Design Rationale*

Rationale for the ligand design of the complexes studied herein stems in part from a previous study in which a correlation between peroxo O-O bond lengths and Mn•••N^{Ar} distances (N^{Ar} = N-heterocycle) was observed with a series of alkylperoxo $^{Quino,Mepy}LMn^{III}$-OOR (R = ^{t}Bu, Cm) compounds.[69] We refer to the interaction between the Mn ion and the N^{Ar} ligand as Mn•••N^{Ar}, because, although not within bond distance, the N^{Ar} ligand was shown (by X-ray crystallography) to point directly towards the metal ion, and (by spectroscopic methods) to influence properties of the complex in a systematic way. A decrease in the mean Mn•••N^{Ar} distance (from 2.510 Å to 2.411 Å) was found to elongate the peroxo O-O bond (from 1.431 Å to

1.468 Å).[6,7] In addition, the kinetic barrier to alkylperoxo O-O bond cleavage ($\Delta H^{\ddagger}$) was shown to directly correlate with the Mn•••N^{Ar} distance was shown to depend upon the steric properties of the N^{Ar} ligand scaffold.[11,69] Inspection of space filling models shows that the substituent in the 6-position of the pyridine ring clashes with one of the gem-dimethyls adjacent to the thiolate sulfur. This prevents the pyridine nitrogen from approaching the metal to the optimum Mn^{III}-N^{Ar} bond distance, if the substituent is larger than a hydrogen. With a hydrogen in the 6-position, the Mn-N^{Ar} distance is within the normal bonding range (Table 2.1), and thus the use of a single line to represent a bond. With larger substituents, the Mn•••N^{Ar} separation is well outside the normal bonding range. For example, with a methyl group, the Mn•••N^{Ar}_{avg} separation is 0.33 Å longer than that of the less sterically encumbered 6-H derivative, $\mathbf{6^{Py}}$ (Table 2.1), resulting in a more Lewis acidic metal ion. If this is extrapolated to the corresponding peroxo compounds, the more Lewis acidic metal ion associated with bulkier substituents would facilitate π back-donation of electron density out of the peroxo antibonding π*(O-O) to the metal ion, thereby strengthening the peroxo O-O bond.[69] Conversely, the shorter Mn^{III}-N^{Ar} bond associated with 6-H-pyridine would be more electron-rich, thereby weakening the peroxo O-O bond, and facilitating its cleavage. Consistent with this, no intermediates are observed in the reaction between O_2 and $[Mn^{II}(L^{py})]^+$ ($\mathbf{1^{Py}}$),[48] even at temperatures as low as -78 °C, whereas peroxo compound $\mathbf{3^{Mepy}}$ **(**Scheme 2.2) is stable enough to crystallize.

Scheme 2.2. Low temperature reaction between **1** and O_2 affords mono oxo bridged **6** via superoxo **2** and peroxo **3** intermediates. L = pyridine, 6-Me-pyridine, 6-MeO-pyridine, and quinoline.

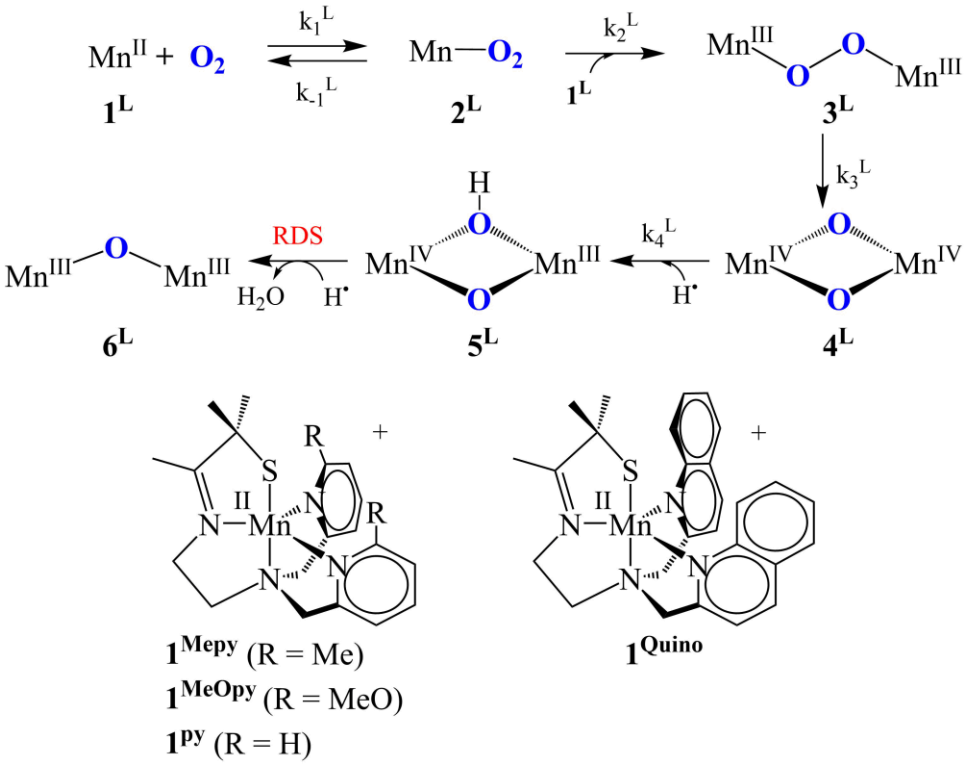

In order to obtain more information regarding the O-O bond-cleaving step, we turned to ligand systems that support a Mn•••N^{Ar} separation in the crystallographically characterized binuclear oxo-bridged, $\{[Mn^{III}(L^{NAr})]_2\text{-}(\mu\text{-}O)\}^{2+}$ (**6**), which is shorter than 6-Me-pyridine $\mathbf{6^{Mepy}}$, but longer than pyridine $\mathbf{6^{Py}}$. Distances in **6** were used as a predictive parameter since we do not have structures for all the peroxo compounds. Quinoline $\{[Mn^{III}(L^{Quino})]_2\text{-}(\mu\text{-}O)\}^{2+}$ ($\mathbf{6^{Quino}}$)[48] and 6-MeO-pyridine $\{[Mn^{III}(L^{MeOpy})]_2\text{-}(\mu\text{-}O)\}^{2+}$ ($\mathbf{6^{MeOpy}}$) both fit this criterion (Table 2.1).

Table 2.1. Mean crystallography-determined Mn•••N^{Ar} distance for bimetallic mono-oxo bridged Mn^{III} complexes, **6**.

N^{Ar}	Complex	Mn•••N^{Ar}_{avg} (Å)
6-H-pyridine	$\mathbf{6^{Py}}$	2.23(1)
6-MeO-pyridine	$\mathbf{6^{MeOpy}}$	2.413(3)
Quinoline	$\mathbf{6^{Quino}}$	2.5(1)
6-Me-pyridine	$\mathbf{6^{Mepy}}$	2.56(2)

Below, we examine the temperature-dependent kinetics of the reaction between O_2 and the Mn^{II} precursors to $\mathbf{6^{Quino}}$ and $\mathbf{6^{MeOpy}}$, $[Mn^{II}(L^{Quino})]^+$ ($\mathbf{1^{Quino}}$) and $[Mn^{II}(L^{MeOpy})]^+$ ($\mathbf{1^{MeOpy}}$), respectively. We will show that the relative stability and reactivity of metastable intermediates, and the barriers to O_2 barriers to O_2 binding or release, and peroxo O-O bond cleavage, is highly dependent on the supporting ligands. By changing the solvents and corresponding C-H bond strength, or by adding a sacrificial H-atom donor, we are able to spectroscopically observe two new intermediates, each of which is capable of abstracting H-atoms from strong X-H bonds (X = C, or O).

2.3.2 *Reactivity of 1^{Quino} with Dioxygen*

The low-temperature (-73 °C) reaction between colorless $[Mn^{II}(L^{Quino})]^+$ ($\mathbf{1^{Quino}}$)[48] and O_2 affords a metastable green intermediate, $\mathbf{3^{Quino}}$, which rapidly converts to mono oxo-bridged $\mathbf{6^{Quino}}$ (λ_{max} = 580 nm).[48] The stability of $\mathbf{3^{Quino}}$ is temperature-dependent. In MeCN (f.p. = -40 °C, C-H BDE = 93 kcal/mol), metastable species $\mathbf{3^{Quino}}$ decays in ~30 seconds at -40 °C, and is therefore best observed using a stopped-flow instrument. In DCM, (f. p. = -90 °C, C-H BDE = 98 kcal/mol), on the other hand, intermediate $\mathbf{3^{Quino}}$ is more stable at -90 °C ($t^{\mathbf{3Quino \rightarrow 6Quino}}$ = 7 minutes) making it possible to obtain a spectrum using a benchtop UV-vis spectrometer (Figure 2.1). Given the close similarity of its electronic absorption spectrum, to that of peroxo-bridged $\mathbf{3^{Mepy}}$ (λ_{max} = 640 nm),[6] it was deemed likely that $\mathbf{3^{Quino}}$ is also a peroxo-bridged dimer, $\{[Mn^{III}(L^{Quino})]_2(\mu\text{-}O_2)\}^{2+}$ ($\mathbf{3^{Quino}}$).

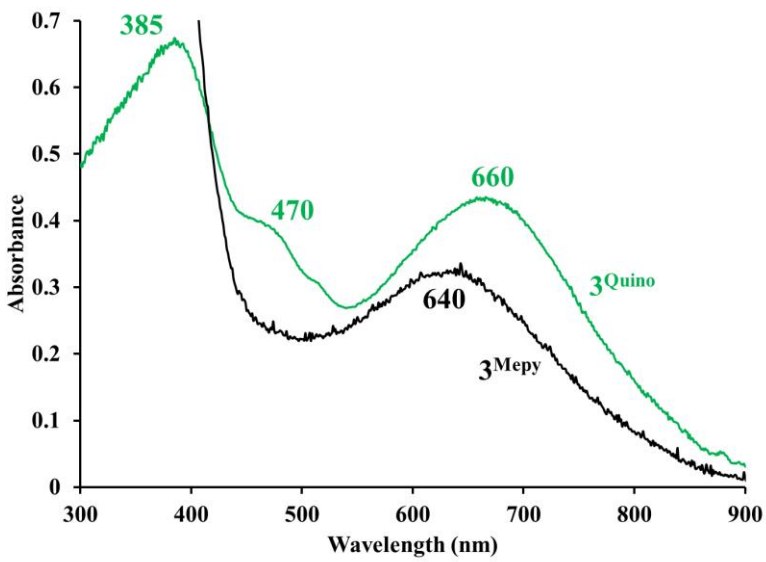

Figure 2.1. Electronic absorption spectrum of putative peroxo **3**$^{\mathbf{Quino}}$ (green) generated via the addition of O_2 to 1.0 mM **1**$^{\mathbf{Quino}}$ in DCM at -73 °C, and **3**$^{\mathbf{Mepy}}$ (black) generated via the addition of O_2 to 0.9 mM **1**$^{\mathbf{Mepy}}$ and O_2 in MeCN at -40 °C.

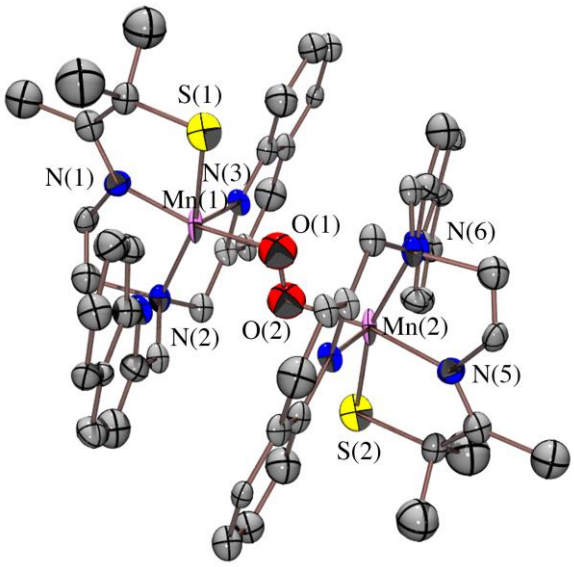

Figure 2.2. ORTEP diagram of low resolution (R^2 = 20%) X-ray structure showing connectivity of metastable **3**$^{\mathbf{Quino}}$.

This is supported by a low-resolution crystal structure (Figure 2.2), the connectivity of which indicates that there are two bridging oxygens (Table 2.2). In addition, 0.48 equivalent of H_2O_2 are released per Mn ion upon the addition of 1.34 equivalents of H_2SO_4 to **3**$^{\mathbf{Quino}}$ consistent with a peroxo-bridged dimer. Metrical parameters (Table 2.3) of the DFT optimized structure

(Figure 2.3), calculated using the spin-unrestricted B3LYP hybrid functional and the 6-311G basis set, are consistent with a *trans*-μ-1,2-peroxo-bridged Mn^{III}_2 dimer (O-O = 1.516 Å, Mn(1)-O(1) = 1.856 Å, Mn(2)-O(2) = 1.846 Å, Mn-S_{avg} = 2.35 Å, Mn(1)•••Mn(2) = 4.244 Å, Mn-O_{avg} = 101°). The time-dependent DFT (TD-DFT) calculated electronic absorption spectrum (Figure 2.3) is in good agreement with the experimental spectrum (Figure 2.1).

Table 2.2. Comparison of selected bond distances (Å) and angles (°), obtained from crystal structure of $[Mn^{III}(L^{Quino})]_2(\mu\text{-}O)(PF_6)_2\bullet(CH_2Cl_2)$ (**6**$^{\mathbf{Quino}}$), $[Mn^{III}(L^{quino})]_2(\mu\text{-}O_2)(BPh_4)_2\bullet CH_3CH_2CN$ (**3**$^{\mathbf{Quino}}$), and $[Mn^{III}(L^{Mepy})]_2(\mu\text{-}O_2)(BPh_4)_2\bullet 2CH_3CH_2CN$ (**3**$^{\mathbf{Quino}}$).[6,48]

	1$^{\mathbf{Quino}}$	**6**$^{\mathbf{Quino}}$	**3**$^{\mathbf{Quino}}$	**3**$^{\mathbf{Mepy}}$
Mn(1)-S(1)	2.3835(9)	2.292(1)	2.25(1)	2.2747(12)
Mn(1)-N(1)	2.170(2)	2.010(3)	1.88(3)	2.040(3)
Mn(1)-N(2)	2.274(2)	2.130(3)	2.17(3)	2.203(3)
Mn(1)-N(3)	2.225(3)	2.543(3)	2.38(1)	2.410(3)
Mn(1)-N(4)	2.200(3)	2.370(3)	2.48(1)	2.492(3)
Mn(1)-O(1)	N/A	1.7599(6)	1.82(5)	1.832(3)
O(1)-O(2)	N/A	N/A	1.24(6)	1.452(5)
S(1)-Mn(1)-N(1)	82.20(7)	82.60(8)	82(1)	105.61(9)
S(1)-Mn(1)-N(2)	156.10(7)	163.90(9)	163(1)	163.3(1)
S(1)-Mn(1)-N(3)	106.98(7)	101.40(8)	118.4(7)	109.0(1)
S(1)-Mn(1)-N(4)	123.09(7)	109.23(8)	103.7(5)	105.6(1)
O(1)-Mn(1)-S(1)	N/A	99.20(3)	89(1)	85.12(9)
Mn(1)-O(1)-O(2)	N/A	N/A	103(5)	97.5(6)
Mn(1)•••Mn(2)	N/A	3.512	4.09	4.113

Transition-difference density plots show that these bands correspond to charge transfer transitions, and involve a mixed peroxo/thiolate → Mn(d) transition at higher energies and a thiolate → Mn(d) transition at lower energies (Figure 2.3). The calculated exchange coupling constant, J^{calc} = 3.8 cm^{-1}, indicates that the two Mn^{III} ions are essentially uncoupled. The calculated peroxo O-O bond length of **3**$^{\mathbf{Quino}}$ is 0.06 Å longer than the crystallographically determined O-O bond of peroxo-bridged **3**$^{\mathbf{Mepy}}$ (1452(5) Å),[6] indicating that this bond should be more readily cleaved in **3**$^{\mathbf{Quino}}$.

Table 2.3. Selected DFT optimized bond lengths (Å) and angles (°) for peroxo-bridged $[Mn^{III}(L^{Quino})]_2(\mu\text{-}O_2)^{2+}$ (**3^{quino}**).

Metrical Parameters	Calculated Distance (Å) and Angles (°)
O(1)-O(2)	1.516
Mn(1)-O(1)	1.856
Mn(2)-O(2)	1.846
Mn(1)-S(1)	2.349
Mn(2)-S(2)	2.351
Mn(1)•••Mn(2)	4.244
Mn•••N(3)$_{avg}$	2.480
Mn•••N(4)$_{avg}$	2.348
Mn(1)-O(1)-O(2)	97.4
Mn2)-O(2)-O(1)	104.1
N(1)-Mn(1)-O(1)	166.4
N(5)-Mn(2)-O(2)	168.6
S(1)-Mn(1)-O(1)	85.1
S(2)-Mn(2)-O(2)	86.6

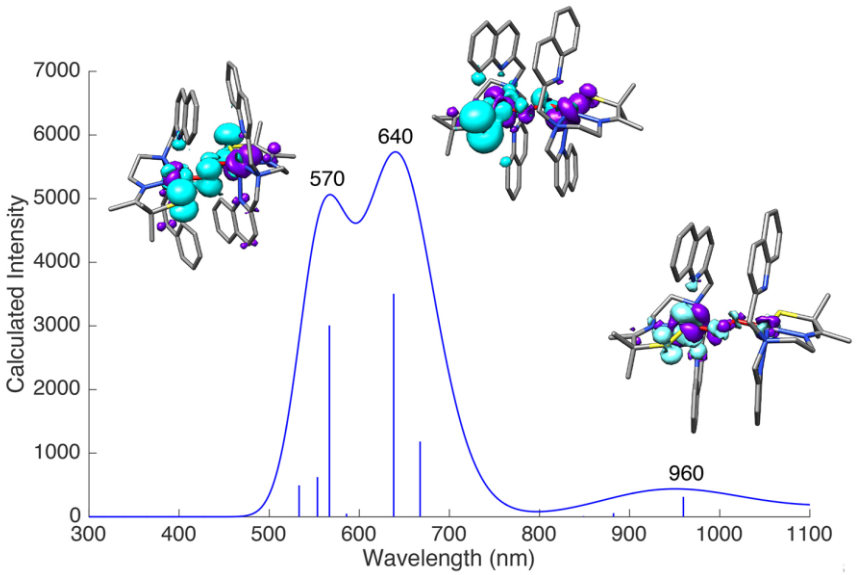

Figure 2.3. TD-DFT calculated electronic absorption spectrum of peroxo-bridged $[Mn^{III}(L^{Quino})]_2(\mu\text{-}O_2)(BPh_4)_2$ (**3^{Quino}**). Transition difference densities for the most intense transitions are shown at an isovalue of 0.003 a_0^3, with areas of decreased electron density (donors) shown in teal and increased electron density (acceptors) shown in purple.

2.3.3 *Temperature-Dependent Kinetics for the Formation of Peroxo* 3^{Quino}

Kinetics data for the formation of peroxo **3**^{Quino} and its subsequent conversion to mono-oxo bridged **6**^{Quino}, were collected at low temperatures using a stopped-flow instrument in collaboration with the Rybak-Akimova group. The build-up and decay of **3**^{Quino} was followed at 749 nm, where interference from **6**^{Quino} is minimal. As illustrated in the time-resolved electronic absorption spectra of Figure 2.4, intermediate **3**^{Quino} forms in less than 10 s at -20 °C (blue trace, λ_{max} = 652 nm) *en route* to the purple mono oxo bridged product, **6**^{Quino} (pink trace, λ_{max} = 565 nm).

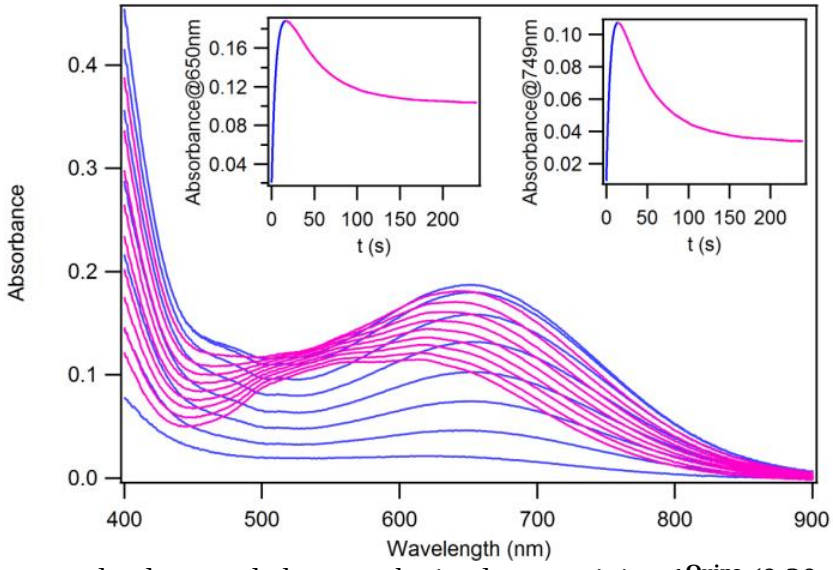

Figure 2.4. Time-resolved spectral changes obtained upon mixing **1**^{Quino} (0.30 mM) and O_2 (4.05 mM) at -20 °C in MeCN. *Insets*: kinetic traces at λ = 650 nm (left) and λ = 749 nm (right) showing formation of peroxo intermediate **3**^{Quino} (blue traces) and its subsequent conversion to **3**^{Quino} (pink traces). All concentrations are reported after mixing.

No additional intermediates, prior to **3**^{Quino}, or in between **3**^{Quino} and **6**^{Quino}, were detected with this ligand system (*vide infra*). The general kinetic scheme reflecting the two spectrophotometrically observed processes is shown in equations 2.1 and 2.2 below. Under pseudo first-order conditions, in the presence of excess O_2, kinetic traces could be fit to the bi-

exponential equation 2.3, affording the pseudo-first-order rate constants (k_{1obs}'^{Quino} and k_{3obs}^{Quino}) of equations 2.1 and 2.2, respectively.

$$2\ Mn^{II}\ (\mathbf{1^{Quino}}) + O_2 \xrightarrow[k_{1obs}\text{'}^{Quino}]{} Mn^{III}\text{-}O_2\text{-}Mn^{III}\ (\mathbf{3^{Quino}}) \qquad 2.1$$

$$Mn^{III}\text{-}O_2\text{-}Mn^{III}\ (\mathbf{3^{Quino}}) \xrightarrow[k_{3obs}^{Quino}]{2H^{\bullet}} Mn^{III}\text{-}O\text{-}Mn^{III}\ (\mathbf{6^{Quino}}) + H_2O \qquad 2.2$$

$$\text{rate} = ae^{-k_{1obs}\text{'}^{Quino}t} + be^{-k_{3obs}^{Quino}t} \qquad 2.3$$

Residuals were slightly larger for fits to a single exponential relative to fits to a bi-exponential. The observed rate constant for equation 2.1, k_{1obs}'^{Quino}, was found to increase linearly (Table 2.4) with increasing O_2 concentration (Figure 2.5), indicating that the reaction is 1st order with respect to [O_2]. The second-order rate constant (k_1'^{Quino}) was obtained from the slope of k_{1obs}'^{Quino} vs [O_2] plots (Table 2.5) at four different temperatures.

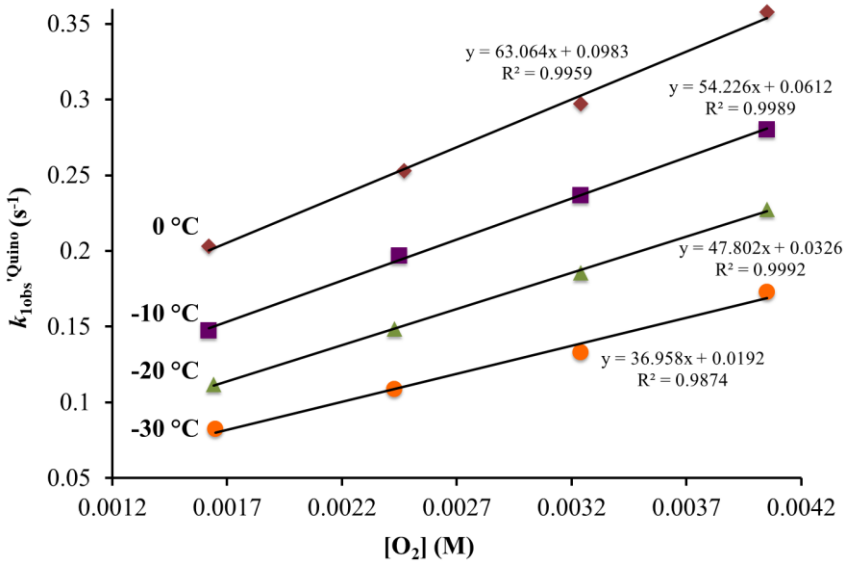

Figure 2.5. Plot of pseudo first order rate constants (k_{1obs}'^{Quino}) for the formation of peroxo **3^{Quino}** as a function of dioxygen concentration and temperature. The slope of each line provides the second-order rate constants (k_1'^{Quino}).

Table 2.4. Observed pseudo first order rate constants for peroxo $\mathbf{3^{Quino}}$ formation as a function of dioxygen concentration and temperature. [Mn^{II} ($\mathbf{1^{Quino}}$)] = 0.3 mM.

Temperature (K)	$[O_2]$ (mM)	k_{1obs}'^{Quino} (s^{-1})
233.15	1.62	0.06357
	2.43	0.08565
	3.24	0.10717
	4.05	0.13156
243.15	1.65	0.08239
	2.43	0.10872
	3.24	0.13306
	4.05	0.1729
253.15	1.64	0.11179
	2.43	0.14862
	3.24	0.18557
	4.05	0.22757
263.15	1.62	0.14739
	2.45	0.19665
	3.24	0.23654
	4.05	0.2801
273.15	1.62	0.20301
	2.45	0.25301
	3.24	0.29725
	4.05	0.35773

The non-zero, and increasing value of the y-intercept with temperature in Figure 2.5, indicates that either peroxo $\mathbf{3^{Quino}}$ formation (equation 2.1), or a step prior to peroxo formation, is reversible. The final absorbance values associated with the maximum accumulation of $\mathbf{6^{Quino}}$ were found to be independent of $[O_2]$, providing support for irreversible formation of peroxo $\mathbf{3^{Quino}}$. Together these suggest that a step prior to peroxo $\mathbf{3^{Quino}}$ formation, i.e. O_2 binding, is reversible (*vide infra*). The observed pseudo first-order rate constants, k_{3obs}^{Quino}, for equation 2.2 were found to be independent of $[O_2]$ over the temperature range examined (Figure 2.6) indicating that the rate of $\mathbf{3^{Quino}}$ to $\mathbf{6^{Quino}}$ conversion is zero-order with respect to $[O_2]$.

Table 2.5. Experimental obtained rate constants and activation parameters for the formation of peroxo-bridged **3^{Quino}** (k_1'^{Quino}), from **1^{Quino}** (0.30 mM) + O_2 (4.1 mM) in MeCN, and its conversion to mono oxo-bridged **6^{Quino}** (k_3^{Quino}).

Temperature (K)	k_1'^{Quino} (M^{-1} s^{-1})	k_3^{Quino} (M^{-1} s^{-1})
243.15	$3.7 \pm 0.3 \times 10^{1}$	$1.49 \pm 0.78 \times 10^{-2}$
253.15	$4.78 \pm 0.08 \times 10^{1}$	$2.07 \pm 0.26 \times 10^{-2}$
263.15	$5.42 \pm 0.06 \times 10^{1}$	$3.01 \pm 0.13 \times 10^{-2}$
273.15	$6.3 \pm 0.2 \times 10^{1}$	$3.33 \pm 0.11 \times 10^{-2}$
$\Delta H^{\ddagger}$ (kJ mol^{-1})	7.8(9)	13(1)
$\Delta S^{\ddagger}$ (J mol^{-1} K^{-1})	-182 (3)	-220(4)
E_a (kJ mol^{-1})	10(1)	15(1)

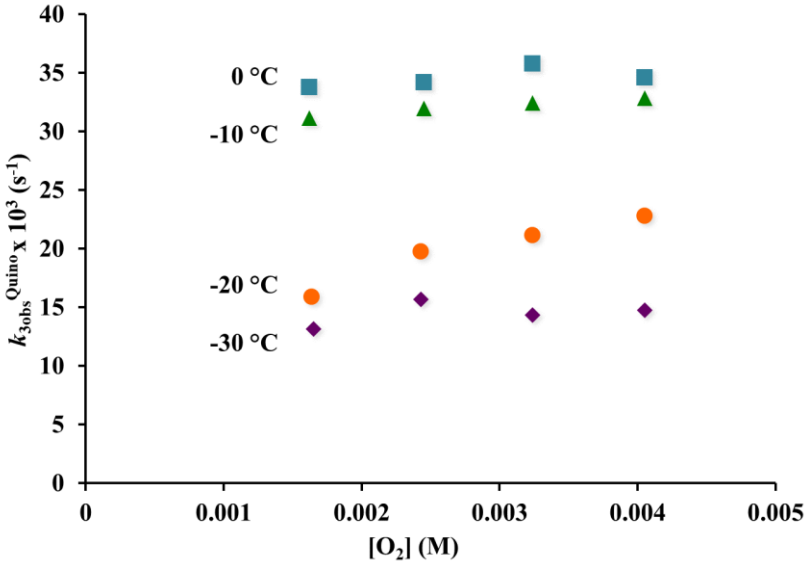

Figure 2.6. Plot of pseudo first order rate constants (k_{3obs}^{Quino}) for conversion of **3^{Quino}** to mono oxo-bridged {[Mn^{III}(L^{Quino})]$_2$(μ-O)}$^{2+}$ (**6^{Quino}**) in MeCN, as a function of [O_2] and temperature, showing that the rate of formation of **6^{Quino}** is independent of [O_2].

In the next set of stopped-flow experiments, the concentration of **1^{Quino}** was varied (0.2-0.8 mM after mixing) while maintaining a fixed excess concentration of O_2 (4.1 mM after mixing) at -10 °C), allowing us to verify the proposed mechanism, and determine the reaction order with respect to Mn^{II} (**1^{Quino}**). The observed rate constants (k_{1obs}^{Quino} and k_{3obs}^{Quino}) were obtained by fitting kinetic traces to equation 2.3. The observed pseudo-first-order rate constant for the formation of **3^{Quino}** in the presence of excess [O_2] (Figure 2.7), confirming second-order

dependence on Mn^{II} overall. This would be consistent with $\mathbf{3^{Quino}}$ being a binuclear peroxo (Figures 2.2 and 2.3). A large non-zero intercept (Figure 2.7) indicates that a process that is first order in Mn^{II} (e.g., equation 2.4) contributes to the rate-determining step. Observed rate constants, $k_{3obs}{}^{Quino}$, for the conversion of peroxo $\mathbf{3^{Quino}}$ to oxo-bridged $\mathbf{6^{Quino}}$, in the presence of excess [O_2], are independent of [$\mathbf{1^{Quino}}$] indicating that this step (equation 2.6) is zero-order with respect to Mn (Figure 2.8).

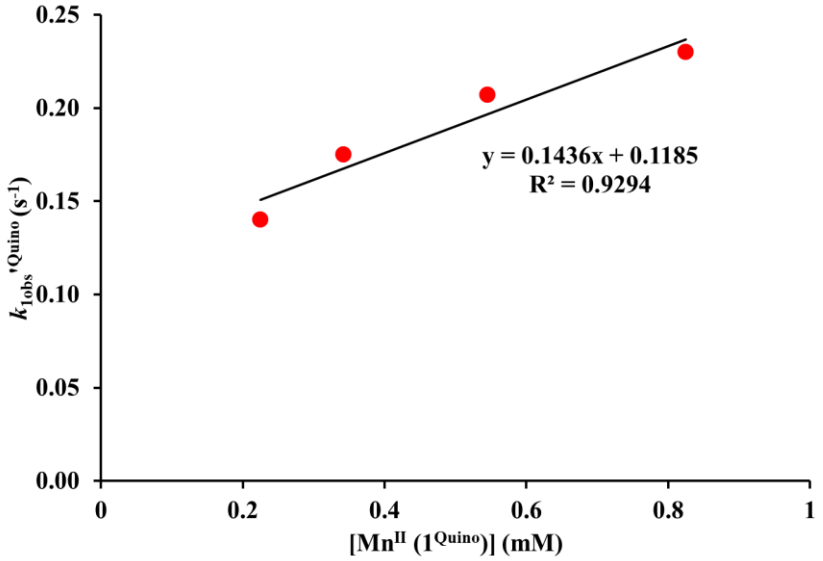

Figure 2.7. Plot of the observed rate constant ($k_{1obs}{}'^{Quino}$), for the formation of peroxo $\mathbf{3^{Quino}}$, from $\mathbf{1^{Quino}}$ + excess O_2 in MeCN, versus the concentration of $\mathbf{1^{Quino}}$ at -10 °C in MeCN. [O_2] after mixing = 4.1 mM. The dependence of $k_{1obs}{}'^{Quino}$ on [$\mathbf{1^{Quino}}$] indicates that the reaction is second order overall with respect to [Mn^{II}]. A large, non-zero intercept indicates that a process that is first order in Mn contributes to the rate-limiting step.

$$Mn^{II}\ (\mathbf{1^{Quino}}) + O_2 \xrightarrow[k_1{}^{Quino}]{} Mn^{III}\text{-}O_2\ (\mathbf{2^{Quino}}) \qquad 2.4$$

$$Mn^{III}\text{-}O_2\ (\mathbf{2^{Quino}}) + Mn^{II}\ (\mathbf{1^{Quino}}) \xrightarrow[k_2{}^{Quino}]{} Mn^{III}\text{-}O_2\text{-}Mn^{III}\ (\mathbf{3^{Quino}}) \qquad 2.5$$

$$Mn^{III}\text{-}O_2\text{-}Mn^{III}\ (\mathbf{3^{Quino}}) \xrightarrow[k_3{}^{Quino}]{2H^{\bullet}} Mn^{III}\text{-}O\text{-}Mn^{III}\ (\mathbf{6^{Quino}}) + H_2O \qquad 2.6$$

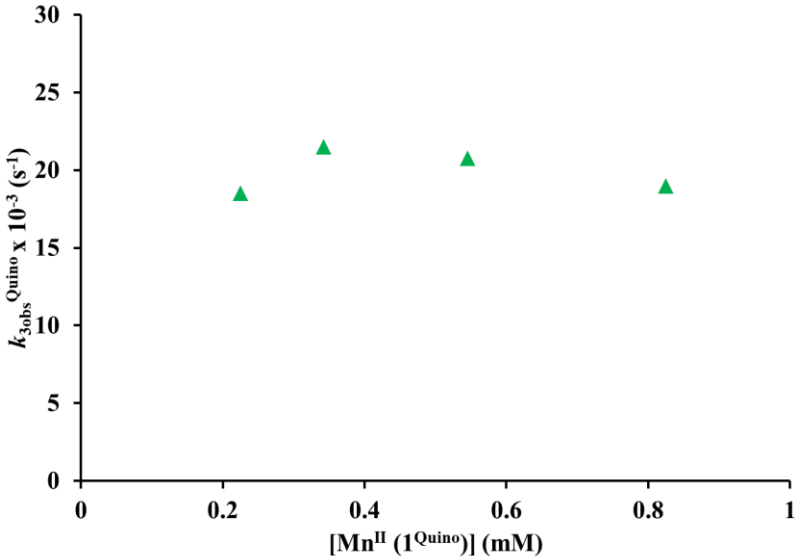

Figure 2.8. Plot of the observed rate constant (k_{3obs}^{Quino}) for the conversion of peroxo **3**^{Quino} to mono oxo-bridged **6**^{Quino} in MeCN, versus [**1**^{Quino}] at -10 °C, showing that the process is independent of **1**^{Quino}. [O_2] after mixing = 4.1 mM.

Collectively, the O_2 and Mn^{II} concentration-dependence experiments described above are consistent with the proposed stepwise mechanism, outlined in equations 2.4 through 2.6 above. This reaction sequence is analogous to that previously established for the reaction between Mn^{II} **1**^{Mepy} and O_2. Although not directly observed spectrophotometrically, superoxo $[Mn(L^{Quino})(O_2)]^+$ (**2**^{Quino}) is proposed to form as a transient intermediate (equation 2.4), prior to the formation of the observable peroxo intermediate **3**^{Quino} (equation 2.5). The analogous 6-Me-pyridine superoxo **2**^{Mepy} (Scheme 2.1) is, in contrast, directly observed by stopped-flow.[6] The rate laws for each step in the mechanism are provided in equations 2.7 through 2.9 below.

$$rate_1 = k_1^{Quino}[Mn^{II}(\mathbf{1}^{Quino})][O_2] \qquad 2.7$$

$$rate_2 = k_2^{Quino}[Mn\text{-}O_2(\mathbf{2}^{Quino})][Mn^{II}(\mathbf{1}^{Quino})] \qquad 2.8$$

$$rate_3 = k_3^{Quino}[Mn^{III}\text{-}O_2\text{-}Mn^{III}(\mathbf{3}^{Quino})] \qquad 2.9$$

The first two rate laws, equations 2.7 and 2.8, are analogous to that previously established for $[Mn^{II}(L^{Mepy})]^+$ (**1**$^{\mathbf{Mepy}}$, Scheme 2.1).[6] Information regarding the rate of peroxo O-O bond cleavage was not available for the 6-Me-pyridine system, however, as this step was too slow to be observed with stopped-flow experiments.

Table 2.6. Calculated rate constants, obtained from global fits to time-resolved spectra, and activation parameters for the formation of putative superoxo **2**$^{\mathbf{Quino}}$ ($k_{1calc}{}^{Quino}$), peroxo-bridged **3**$^{\mathbf{Quino}}$ ($k_{2calc}{}^{Quino}$), and oxo-bridged **6**$^{\mathbf{Quino}}$ ($k_{3calc}{}^{Quino}$) in the reaction between **1**$^{\mathbf{Quino}}$ and O_2 in MeCN.

Temperature (K)	$k_{1calc}{}^{Quino}$ (M^{-1} s^{-1})	$k_{2calc}{}^{Quino}$ (M^{-1} s^{-1})	$k_{3calc}{}^{Quino}$ (s^{-1})
243.15	$1.79 \pm 0.05 \times 10^{1}$	$8.80 \pm 0.05 \times 10^{3}$	$1.54 \pm 0.16 \times 10^{-2}$
253.15	$2.24 \pm 0.01 \times 10^{1}$	$1.30 \pm 0.20 \times 10^{4}$	$2.31 \pm 0.12 \times 10^{-2}$
263.15	$3.00 \pm 0.08 \times 10^{1}$	$1.59 \pm 0.06 \times 10^{4}$	$3.07 \pm 0.30 \times 10^{-2}$
273.15	$4.98 \pm 0.09 \times 10^{1}$	$2.30 \pm 0.30 \times 10^{4}$	$3.12 \pm 0.25 \times 10^{-2}$
$\Delta H^{\ddagger}$ (kJ mol^{-1})	16(3)	15(6)	16(2)
$\Delta S^{\ddagger}$ (J mol^{-1} K^{-1})	-150(12)	-106(5)	-211(6)
E_a (kJ mol^{-1})	18(3)	17(5)	18(3)

The proposed mechanism for the formation of quinoline peroxo **3**$^{\mathbf{Quino}}$ and its conversion to mono oxo-bridged **6**$^{\mathbf{Quino}}$, summarized in equations 2.4-2.6, was verified using global fits to the time-resolved spectra using ReactLab. The rate constants ($k_{1calc}{}^{Quino}$, $k_{3calc}{}^{Quino}$) obtained from these global fits (Table 2.6) show that the rate at which O_2 binds to **1**$^{\mathbf{Quino}}$ ($k_{1calc}{}^{Quino}$, Table 2.5, Scheme 2.3). In other words, the rate-determining step in peroxo **3**$^{\mathbf{Quino}}$ formation involves O_2 binding. Consistent with this, the rate at which superoxo **2**$^{\mathbf{Quino}}$ converts to peroxo **3**$^{\mathbf{Quino}}$ ($k_2{}^{Quino}$) is two orders of magnitude faster (Table 2.6) than the rate at which it forms ($k_1{}^{Quino}$), making it impossible to observe (Scheme 2.3). Calculated spectra (Figure 2.9) are in good agreement with the experimentally measured spectrum (Figure 2.1).[48]

Scheme 2.3. Dioxygen reactivity of Mn^{II} $\mathbf{1}^{Quino}$, showing rate constant labeling scheme, as well as observed versus unobserved intermediates.

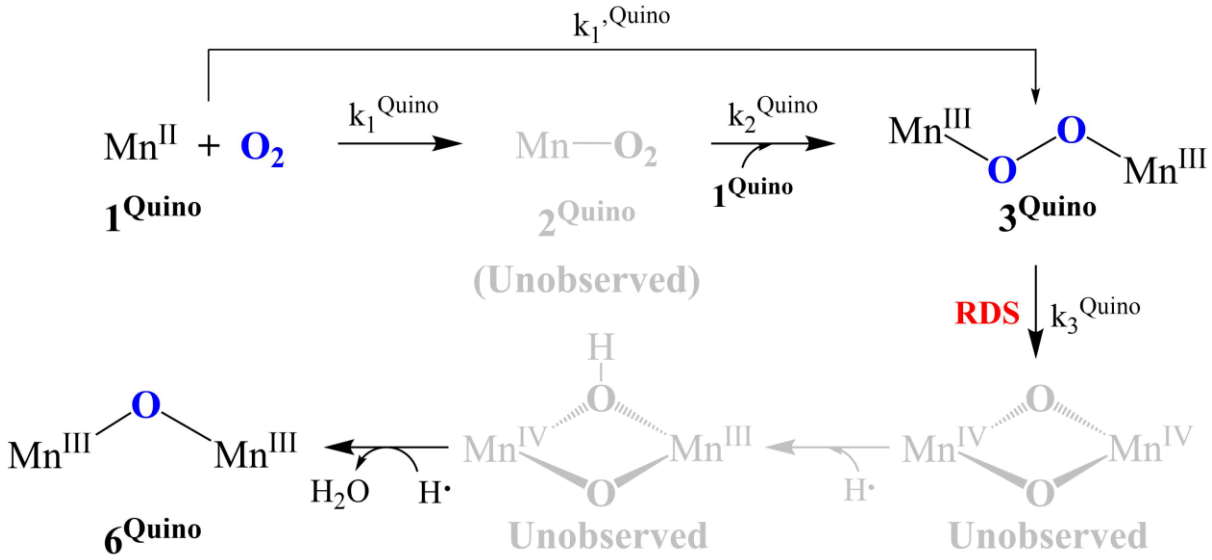

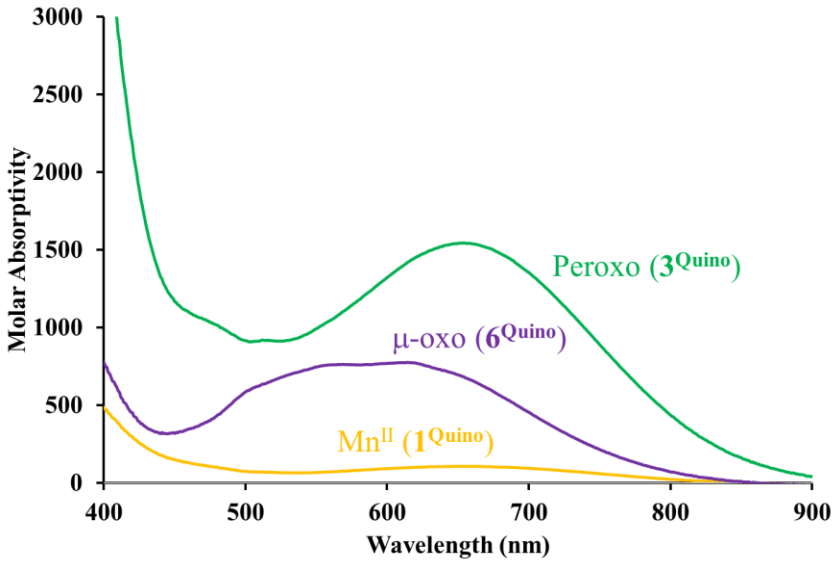

Figure 2.9. Calculated spectra obtained from global fits (ReactLab) to the time-resolved spectra in MeCN. $[Mn^{II}$ $(\mathbf{1}^{Quino})]_0$ = 0.3 mM and $[O_2]_0$ = 4.1 mM after mixing at -20 °C.

A comparison with our previously reported system,[6] shows that the rate at which O_2 binds to $\mathbf{1}^{Quino}$ (30.0(8) M^{-1} s^{-1}, Table 2.6) is two orders of magnitude slower than the rate at which O_2 binds to $\mathbf{1}^{Mepy}$ (3.8(2) x 10^3 M^{-1} s^{-1}) at 263 K. The rate at which superoxo $\mathbf{2}^{Quino}$ converts to peroxo $\mathbf{3}^{Quino}$ (1.6(6) x 10^4 M^{-1} s^{-1}, Table 2.6), on the other hand, is two orders of

magnitude faster (at 263 K) than the conversion (Scheme 2.1) of superoxo **2**$^{\mathbf{Mepy}}$ to peroxo **3**$^{\mathbf{Mepy}}$ (k_2^{Mepy} = 4.17(3) x 10^2 $M^{-1}s^{-1}$).[6] It is worth noting that the rate constant k_2^{Quino} is less reliable than k_3^{Quino}, since it was calculated using global fits. The non-zero and increasing value of the y-intercept with temperature in the k_{1obs}'^{Quino} vs [O_2] plots of Figure 2.5 indicates that the rate-determining step, i.e., O_2 binding to **1**$^{\mathbf{Quino}}$, is reversible. One can obtain the rate constant associated with the release of O_2 from the intercept of these plots and then calculate the temperature-dependent equilibrium constants, $K_{eq}^{Quino} = k_1^{Quino}/k_{-1}^{Quino}$, summarized in Table 2.7.

Table 2.7. Temperature-dependent rate-constant for O_2 release from **2**$^{\mathbf{Quino}}$, and temperature-dependent equilibrium constant for reversible O_2 binding to **1**$^{\mathbf{Quino}}$.

Temperature (K)	k_{-1}^{Quino} (s^{-1})	K_{eq}^{Quino} (M^{-1})
273.15	9.8 x 10^{-2}	640
263.15	6.1 x 10^{-2}	890
253.15	3.3 x 10^{-2}	1500
243.15	1.9 x 10^{-2}	1900

Previously reported superoxo **2**$^{\mathbf{Mepy}}$, on the other hand, does not release O_2 once O_2 binding occurs.[6] Thermodynamic parameters for O_2 binding to **1**$^{\mathbf{Quino}}$ (ΔH = -20 kJ mol^{-1} and ΔS = -23 J mol^{-1} K^{-1}) were obtained from a Van't Hoff plot (Figure 2.10). The negative entropy value is consistent with an associative process. The activation parameters for O_2 release from **2**$^{\mathbf{Quino}}$ E_a = 30(5) kJ mol^{-1}, $\Delta H^{\ddagger}$ = 28(3) and $\Delta S^{\ddagger}$ = -160(9), were obtained from Arrhenius (Figure 2.11) and Eyring (Figure 2.12) plots, respectively. Although the negative entropy of activation is not what one would expect for a dissociative process, it indicates that the barrier associated with the bond rearrangement required for electron transfer (Mn(III)→Mn(II)) is large enough to offset the entropy gained via O_2 release. The K_{eq} for O_2 binding to **1**$^{\mathbf{Quino}}$ is four orders of magnitude larger than K_{eq} for O_2 binding to [(py)Mn^{II}(TPP)] (K_{eq}(298 K) = 2.3 x 10^{-2} M^{-1}),[41] but comparable to K_{eq} for O_2 binding to [Co^{II}(SalMeDPT)] (**7**, K_{eq}(233 K) = 1.63 x 10^3 M^{-1}).[70] The kinetic barrier to O_2 binding, $\Delta H^{\ddagger}$, is 3.4 kJ mol^{-1} higher than that of **7**[70] but 7 kJ mol^{-1} lower than

O_2 binding to MbFe(II) (Mb = myoglobin).[71] The barrier to O_2 release is 13 kJ mol^{-1} higher than that of **7-O$_2$**,[70] and 9 kJ mol^{-1} higher than that of MbFe-O_2.[71]

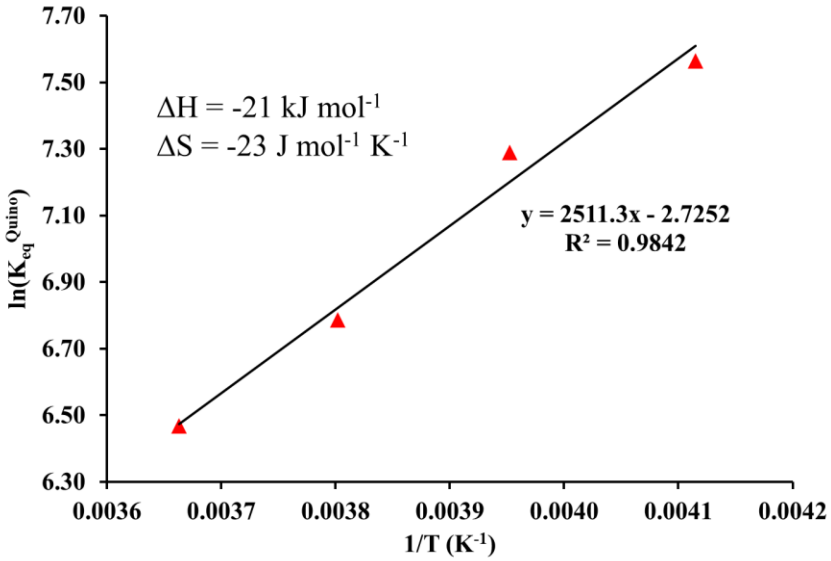

Figure 2.10. Van't Hoff plot for O_2 binding to **1^{Quino}** in MeCN, from which the thermodynamic parameters ΔH_1^{Quino} = -21(2) kJ mol^{-1} and ΔS_1^{Quino} = -23(9) J mol^{-1} K^{-1} were obtained.

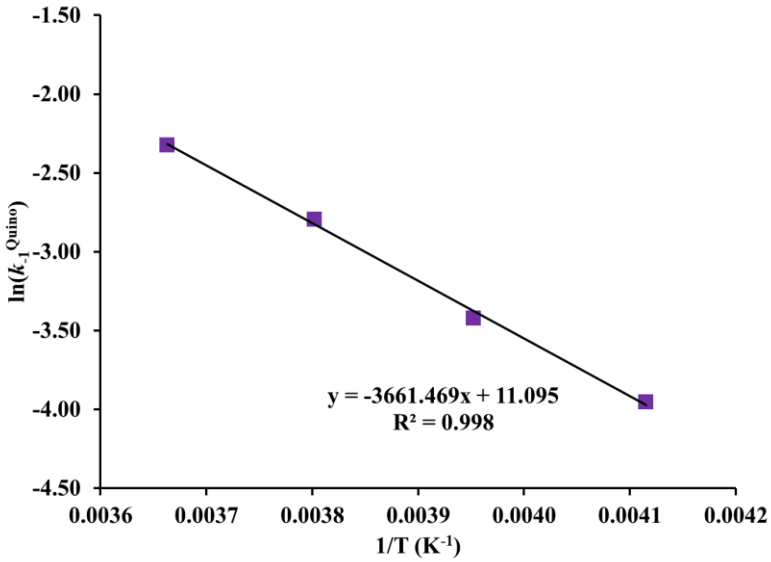

Figure 2.11. Arrhenius plot for O_2 release from **2^{Quino}** in MeCN, from which the activation energy E_a = 30(5) kJ mol^{-1}, was obtained. The rate constants k_{-1}^{Quino} were obtained from the intercepts of the temperature-dependent plots of Figure 6.

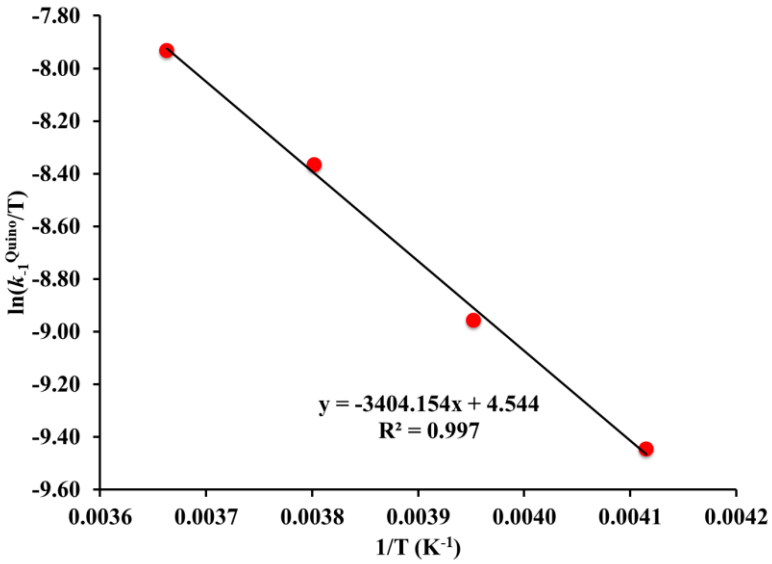

Figure 2.12. Eyring plot for O_2 release from $\mathbf{2^{Quino}}$ in MeCN, from which activation parameters $\Delta H_{-1}^{Quino‡}$ = 28(3) kJ mol^{-1} and $\Delta S_{-1}^{Quino‡}$ = -160(9) J mol^{-1} K^{-1} were obtained. The first-order rate constants k_{-1}^{Quino} were obtained from the intercept of Figure 2.5.

Activation parameters (Tables 2.5 and 2.6) for peroxo $\mathbf{3^{Quino}}$ formation (Figures 2.13 and 2.14), O_2 binding to $\mathbf{1^{Quino}}$ (Figures 2.15 and 2.16), as well as superoxo $\mathbf{2^{Quino}}$ → peroxo $\mathbf{3^{Quino}}$ conversion (Figures 2.17 and 2.18), were obtained from Eyring and Arrhenius plots. The largest errors are associated with the conversion of superoxo $\mathbf{2^{Quino}}$ to peroxo $\mathbf{3^{Quino}}$, since the superoxo intermediate is not directly observed. The enthalpy of activation ($\Delta H_1^{‡Mepy}$) associated with O_2 binding to $\mathbf{1^{Mepy}}$ (26(2) kJ/mol)[6] is 1.6 times greater than that for O_2 binding to $\mathbf{1^{Quino}}$ (16(3) kJ/mol, Table 2.6). A negative entropy of activation ($\Delta S_1^{‡Mepy}$, Table 2.6) is seen with both $\mathbf{1^{Mepy}}$ and $\mathbf{1^{Quino}}$, consistent with an associative process. With the 6-Me-pyridine ligand system, the barrier to the conversion of superoxo $\mathbf{2^{Mepy}}$ to peroxo $\mathbf{3^{Mepy}}$ (E_a = 49 kJ mol^{-1}) is significantly higher than the barrier to O_2 binding (E_a = 26(2) kJ mol^{-1}), explaining why the superoxo intermediate is observed. For the quinoline system, both of these barriers are significantly lower (E_a = 18(3) kJ mol^{-1}, Figure 2.17), and E_a = 17(5) kJ mol^{-1} (Figure 2.18), respectively), and the reaction landscape is relatively flat, explaining why it is more difficult to trap superoxo $\mathbf{2^{Quino}}$.

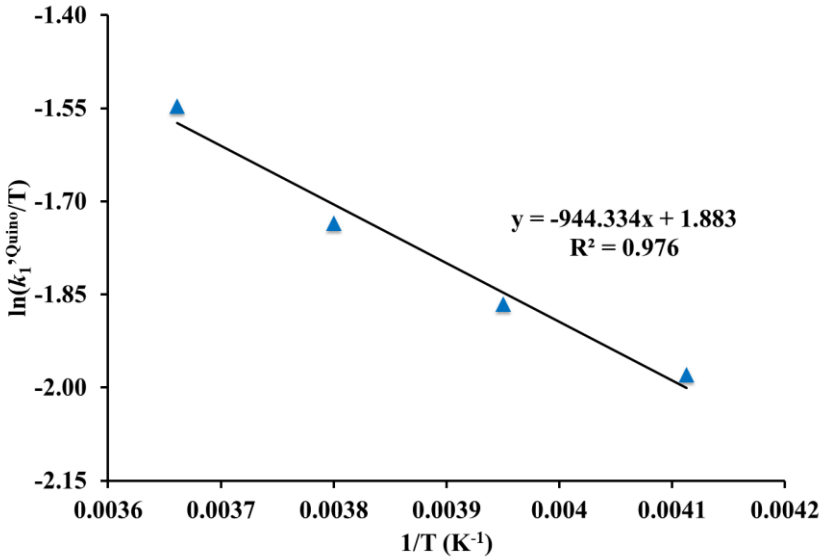

Figure 2.13. Eyring plot for the formation of peroxo-bridged **3^{Quino}** via the addition of O_2 (4.1 mM in MeCN) to **1^{Quino}** (0.30 mM in MeCN), from which activation parameter $\Delta H_1{}'^{Quino‡}$ = 7.8(9) kJ mol^{-1} and $\Delta S_1{}'^{Quino‡}$ = -182(3) J mol^{-1} K^{-1}, were obtained. The second-order rate constants, $k_1{}'^{Quino}$, were experimentally obtained.

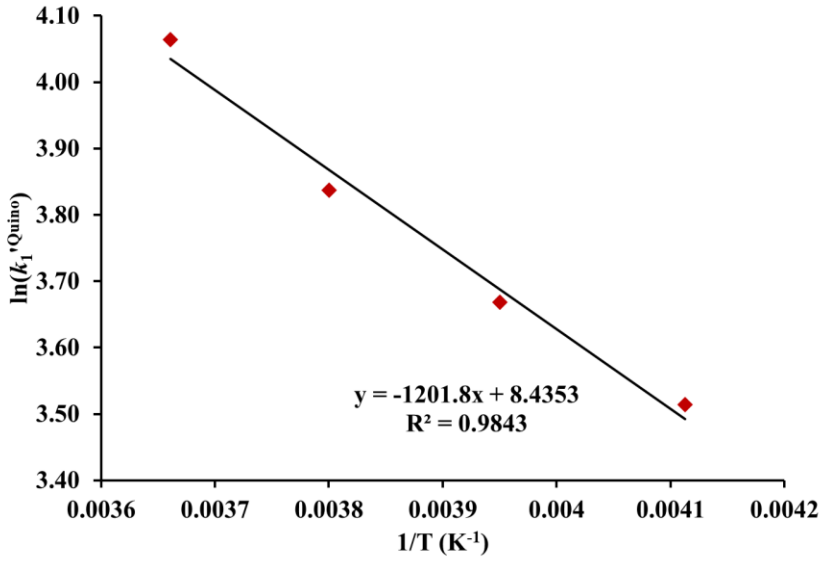

Figure 2.14. Arrhenius plot for the formation of peroxo-bridged **3^{Quino}** via the addition of O_2 (4.1 mM in MeCN) to **1^{Quino}** (0.30 mM in MeCN), from which the activation energy, E_a = 10(1) kJ mol^{-1}, was obtained. The second-order rate constants $k_1{}'^{Quino}$ experimentally obtained.

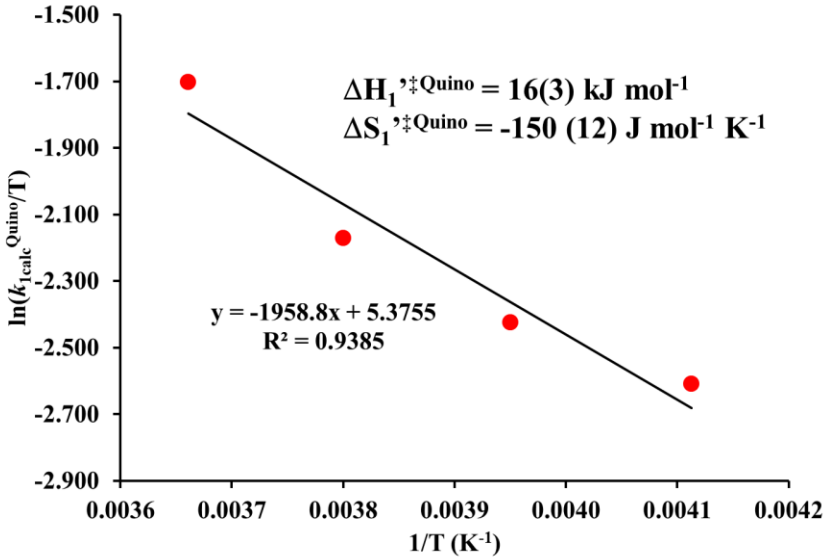

Figure 2.15. Eyring plot for O_2 binding to **1**$^{\mathbf{Quino}}$ to form putative superoxo intermediate **2**$^{\mathbf{Quino}}$ in MeCN, from which activation parameters $\Delta H_1^{Quino‡}$ = 16(3) kJ mol^{-1} and $\Delta S_1^{Quino‡}$ = -150(12) J mol^{-1}K^{-1}, were derived. The calculated second-order rate constants k_{1calc}^{Quino} were obtained from a kinetic model using ReactLab.

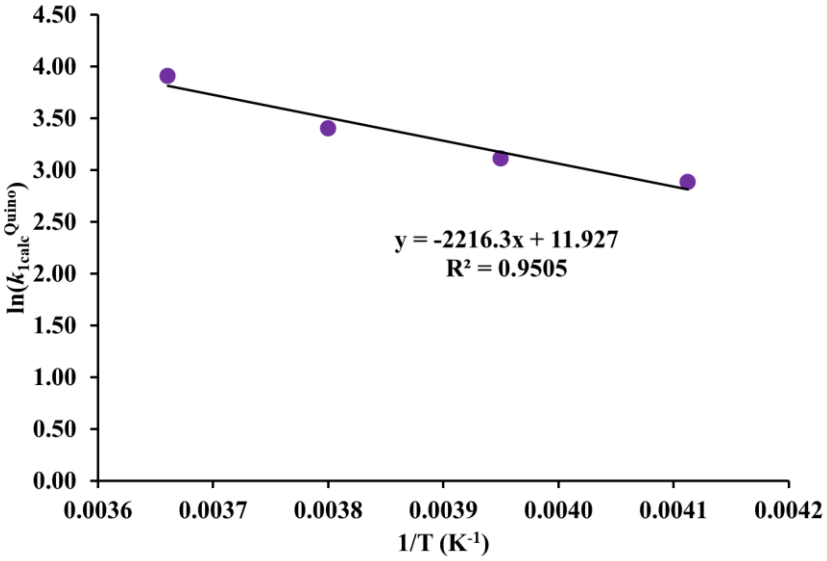

Figure 2.16. Arrhenius plot for O_2 binding to **1**$^{\mathbf{Quino}}$ to form putative superoxo intermediate **2**$^{\mathbf{Quino}}$ in MeCN, from which the activation energy, E_a = 18(3) kJ mol^{-1}, was obtained. The calculated second-order rate constants k_{1calc}^{Quino} were obtained from the kinetic model using ReactLab.

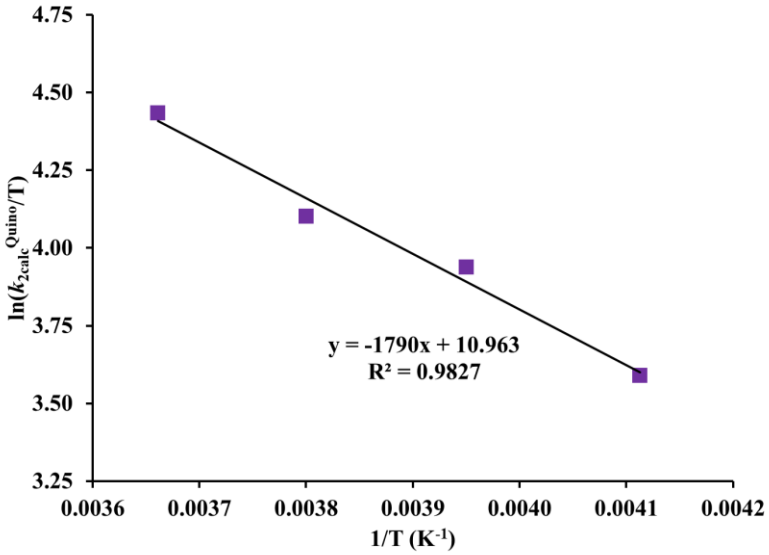

Figure 2.17. Eyring plot for the conversion of superoxo **2**$^{\mathbf{Quino}}$ to peroxo **3**$^{\mathbf{Quino}}$, from which activation parameters $\Delta H_{2,calc}^{Quino‡}$ = 15(6) kJ mol^{-1} and $\Delta S_{2,calc}^{Quino‡}$ = -106(5) J mol^{-1} K^{-1}, were obtained. The calculated second-order rate constants k_{2calc}^{Quino} were obtained from a kinetic model using ReactLab.

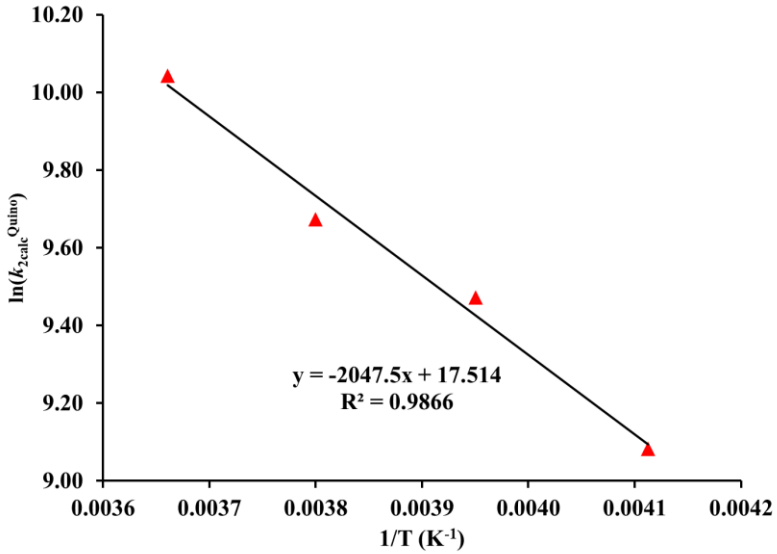

Figure 2.18. Arrhenius plot for the conversion of superoxo **2**$^{\mathbf{Quino}}$ to peroxo **3**$^{\mathbf{Quino}}$ in MeCN, from which the activation energy, E_a = 17(5) kJ mol^{-1}, was obtained. The calculated second-order rate constants k_{2calc}^{Quino} were obtained from a kinetic model using ReactLab.

2.3.4 *The Barrier to Peroxo O-O Bond Cleavage*

With the 6-Me-pyridine ligand scaffold, cleavage of the peroxo O-O bond of $\mathbf{3}^{\mathbf{Mepy}}$ was determined to be slow and rate-limiting, making it difficult to obtain information regarding the mechanism of $\mathbf{3}^{\mathbf{Mepy}}$ to mono oxo-bridged $\mathbf{6}^{\mathbf{Mepy}}$ conversion (Scheme 2.1).[6] In contrast, the rate at which the less stable quinoline peroxo, $\mathbf{3}^{\mathbf{Quino}}$ converts to mono-oxo bridged $\mathbf{6}^{\mathbf{Quino}}$ (Table 2.8) is an order of magnitude faster (*vide infra*), allowing us to obtain stopped-flow kinetics data for this step. Calculated rate constants (k_{3calc}^{Quino}) obtained from global fits (Table 2.6) are in good agreement with the experimentally determined rate constants (k_3^{Quino}, Table 2.5).

Activation parameters (Table 2.5) for peroxo O-O bond cleavage were obtained from Eyring and Arrhenius plots (Figures 2.19-2.22). Although activation parameters are not available for comparison to other Mn-peroxo compounds, the barrier to cleavage of the peroxo O-O bond of $\mathbf{3}^{\mathbf{Quino}}$ of the peroxo O-O bond of $\mathbf{3}^{\mathbf{Quino}}$ is comparable to the barrier to homolytic O-O bond cleavage for a known Fe-hydroperoxo $[(TMC)Fe^{III}\text{-}OOH]^{2+}$.[72]

Table 2.8. Observed pseudo first order rate constants for the peroxo $\mathbf{3}^{\mathbf{Quino}}$ O-O bond cleavage as a function of dioxygen concentration and temperature. Data obtained by monitoring the decay of peroxo $\mathbf{3}^{\mathbf{Quino}}$ at λ = 749 nm, $[Mn^{II}$ ($\mathbf{1}^{\mathbf{Quino}}$)] = 0.3 mM.

Temperature (K)	**$[O_2]$ (mM)**	**k_{3obs}'^{Quino} (s^{-1})**
233.15	2.40	0.01074
	3.12	0.01010
	3.96	0.01021
223.15	1.67	0.01080
	2.39	0.01118
	3.08	0.01118
	4.00	0.01114
213.15	1.64	0.00985
	2.35	0.01060
	3.08	0.01119
	3.96	0.01112
203.15	1.80	0.00932
	2.46	0.01096
	3.27	0.01094
	4.40	0.01150

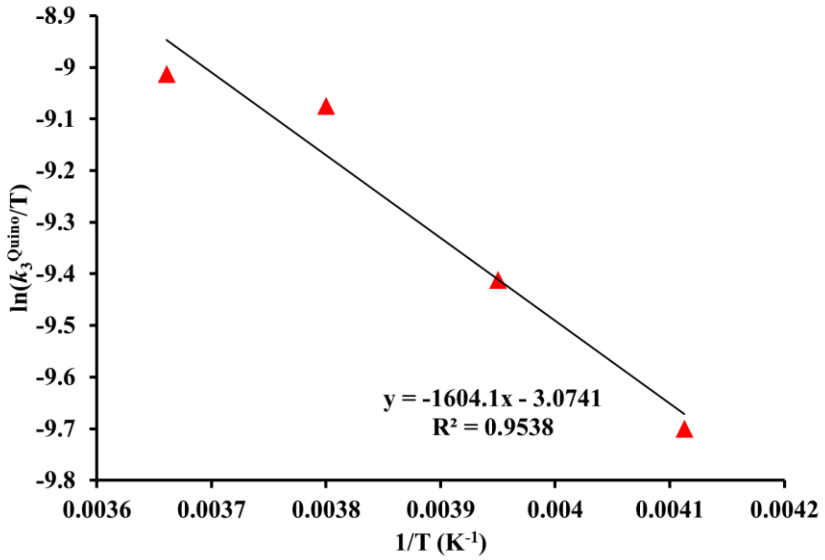

Figure 2.19. Eyring plot for cleavage of the peroxo O-O bond of **3**$^{\mathbf{Quino}}$ and its conversion to mono oxo-bridged **6**$^{\mathbf{Quino}}$ in MeCN, from which activation parameters $\Delta H_3^{\ddagger Quino}$ = 13(1) kJ mol^{-1} and $\Delta S_3^{\ddagger Quino}$ = -220(4) J mol^{-1} K^{-1}, were obtained. First-order rate constants k_3^{Quino} were obtained from stopped-flow experiments.

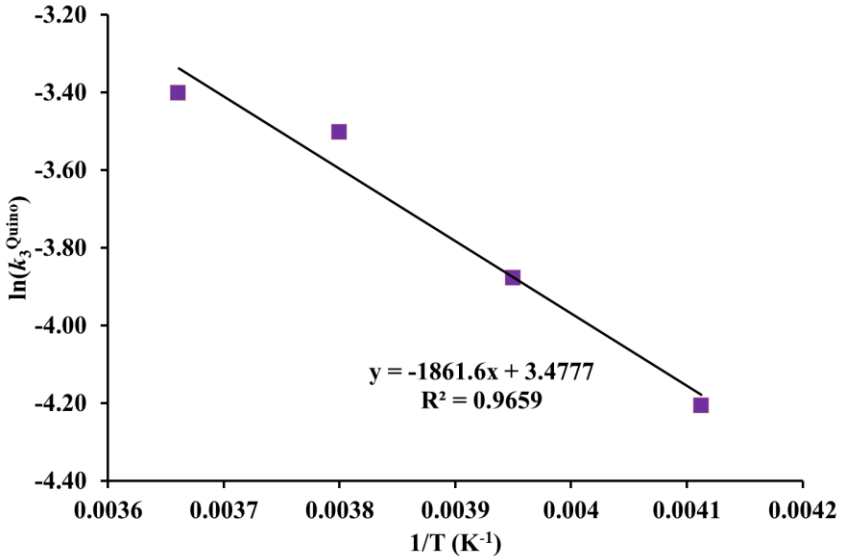

Figure 2.20. Arrhenius plot for O-O bond cleavage of peroxo **3**$^{\mathbf{Quino}}$ in MeCN, from which the activation energy, E_a = 15(1) kJ mol^{-1}, was obtained. The first order rate constants k_3^{Quino} were experimentally obtained by monitoring the disappearance of **3**$^{\mathbf{Quino}}$ at λ = 749 nm.

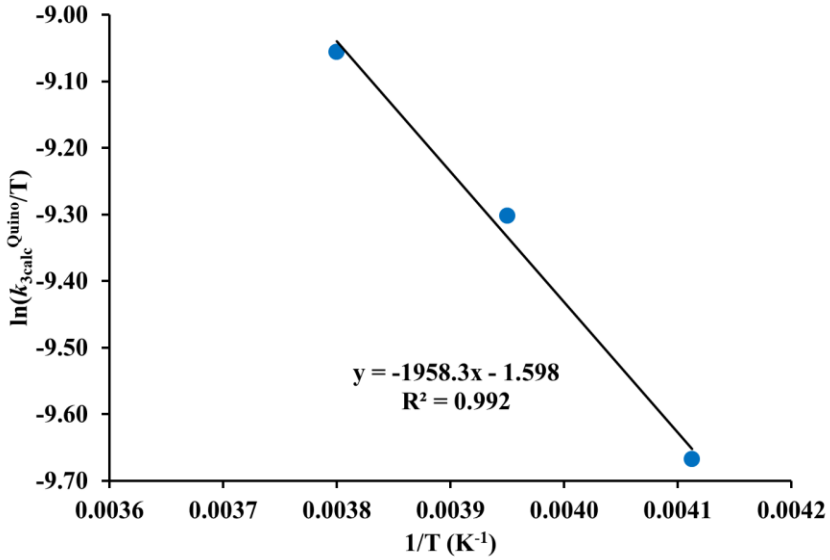

Figure 2.21. Eyring plot for the conversion of peroxo-bridged **3^{Quino}** to mono oxo-bridged **6^{Quino}** via O-O bond cleavage in MeCN, from which activation parameters $\Delta H_3^{\ddagger Quino}$ = 16(2) kJ mol^{-1} and $\Delta S_3^{\ddagger Quino}$ = -211(6) J mol^{-1} K^{-1}, were derived. The calculated second-order rate constants $k_{3calc}{}^{Quino}$ were obtained from a kinetic model using ReactLab.

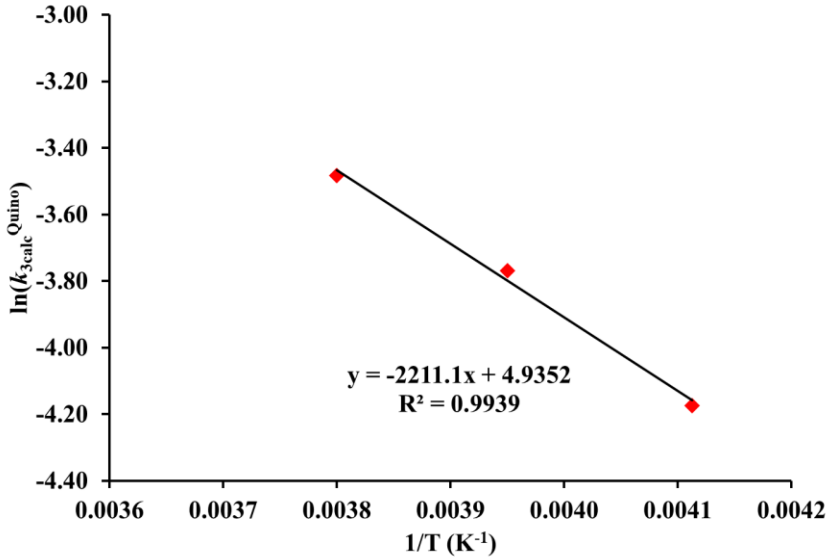

Figure 2.22. Arrhenius plot for the cleavage of the O-O bond of peroxo-bridged **3^{Quino}** in MeCN, from which the activation energy, E_a = 18(1) kJ mol^{-1}, was obtained. The second-order rate constants $k_{3calc}{}^{Quino}$ were obtained from the kinetic model using a global model in ReactLab.

If Mn peroxo **3^{Quino}** follows a pathway (Scheme 2.3) analogous to that of Cu- and Fe-peroxo compounds,[13–19] then homolytic O-O bond cleavage would afford a high-valent bis-oxo-bridged compound, $L^{Quino}Mn^{IV}(\mu\text{-}O)_2Mn^{IV}L^{Quino}$ (**4^{Quino}**). Two electrons, and two protons, or,

two H-atoms, would then be required to convert this high-valent bis-oxo intermediate to mono-oxo bridged $L^{Quino}Mn^{III}_2(\mu\text{-}O)$ (**6^{Quino}**). We were unable to observe intermediates following quinoline peroxo **3^{Quino}**, however, even at temperatures as low as -120 °C (in Me-THF). This implies that O-O bond cleavage is the rate-determining step in this case. In order to increase the stability of high-valent intermediates and increase the likelihood of observing intermediates beyond the peroxo, we synthesized a more electron-rich ligand system, containing a 6-MeO-pyridine substituent, L^{MeOpy}.

2.3.5 *Ligand Design and Synthesis*

The pentadentate ligand L^{MeOpy}, which is a structural derivative of previously reported L^{MePy}, was synthesized according to the procedure outlined in the experimental section. This ligand features a 6-methoxy-pyridine substituent, which is simultaneously more electron-donating and less-sterically-encumbering than L^{MePy} (A-value = 0.6 vs 1.7 for MeO and Me respectively).[73] The synthetic scheme for the N-heterocyclic ligand precursor N,N-bis(6-methoxy-2-pyridinilmethyl)ethane-1,2-diamine (6-MeO-DPEN, **L$_5$**) is shown in Scheme 2.4. The ligand synthesis has an overall yield of 20.9%. The first step involves methylation of alcohol groups of 6-hydroxypyridine-2-carboxylic acid by iodomethane in the presence of silver carbonate to produce methyl 6-methyloxy-2-pyridinecarboxylate (**L$_1$**). Reduction of **L$_1$** using $LiAlH_4$ yield 6-methoxy-2-pyridinemethanol (**L$_2$**). The following ligands were synthesized using similar procedures to that of the quinoline and 6-Me-DPEN ligands with chromatography conditions modified accordingly.[6,52] These ligands were characterized by ^{1}H NMR (Figures 2.23-2.27).

Scheme 2.4. Five-step synthetic scheme to isolate N,N-bis(6-methoxy-2-pyridinilmethyl)ethane-1,2-diamine (6-MeO-DPEN, L_5).

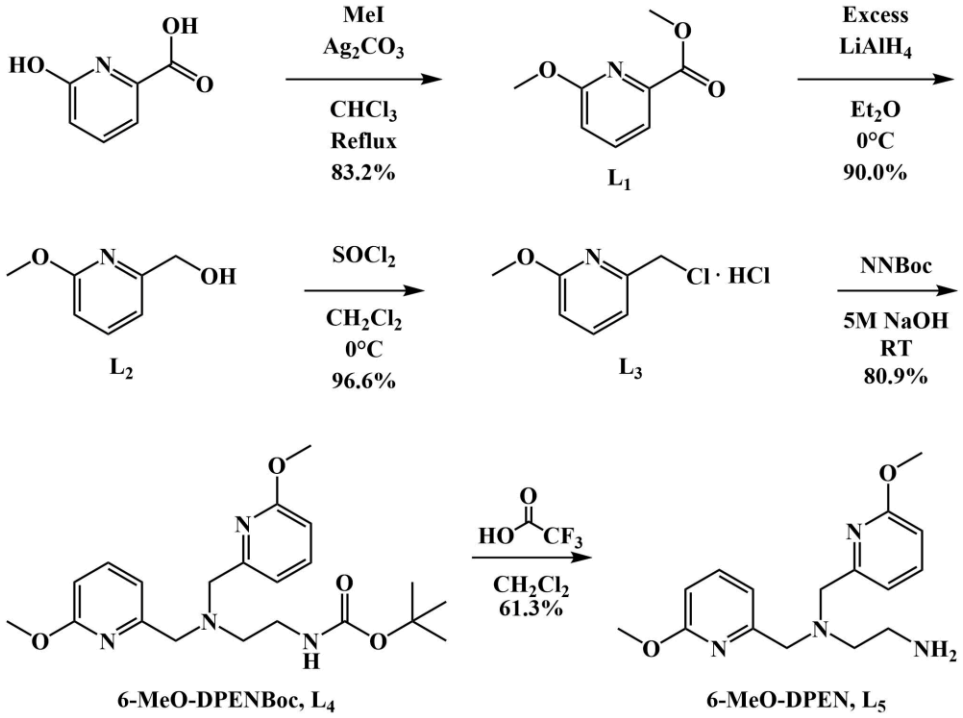

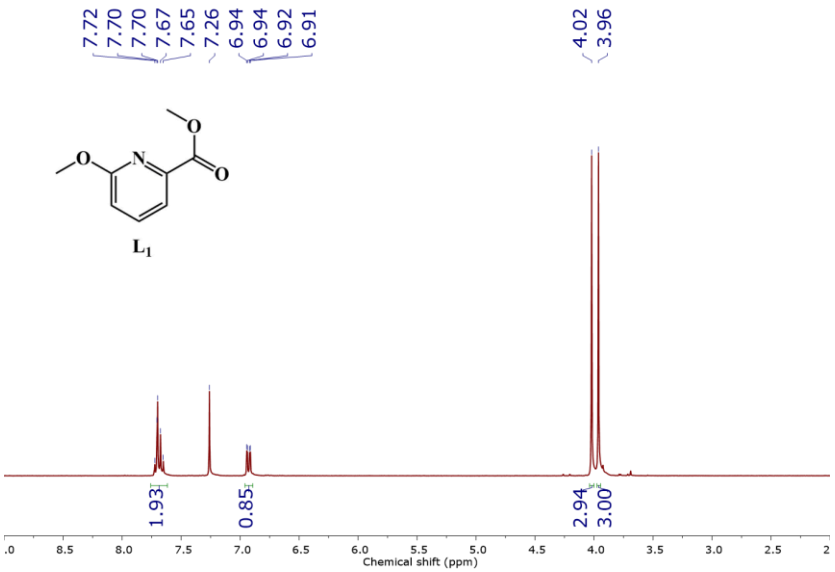

Figure 2.23. ^{1}H NMR of methyl 6-methyloxy-2-pyridinecarboxylate (**L_1**) in $CDCl_3$.

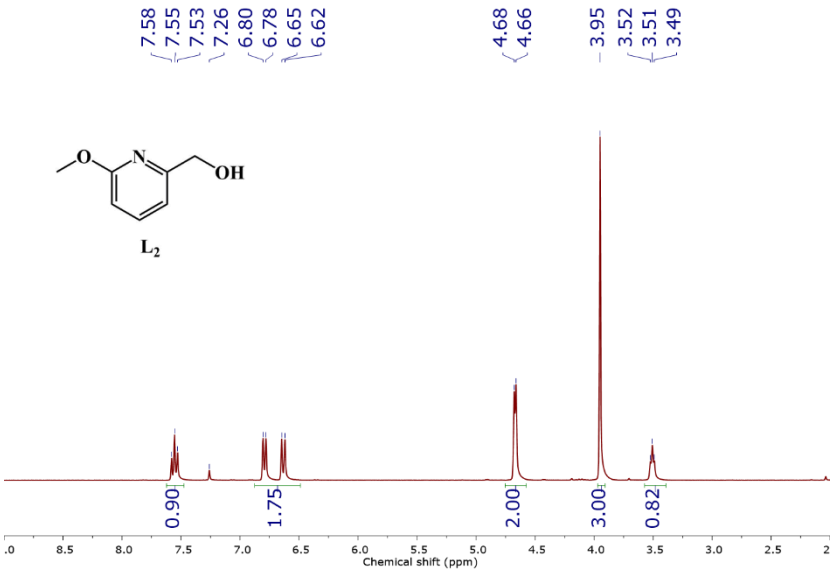

Figure 2.24. ^{1}H NMR of 6-methoxy-2-pyridinemethanol (**L$_2$**) in $CDCl_3$.

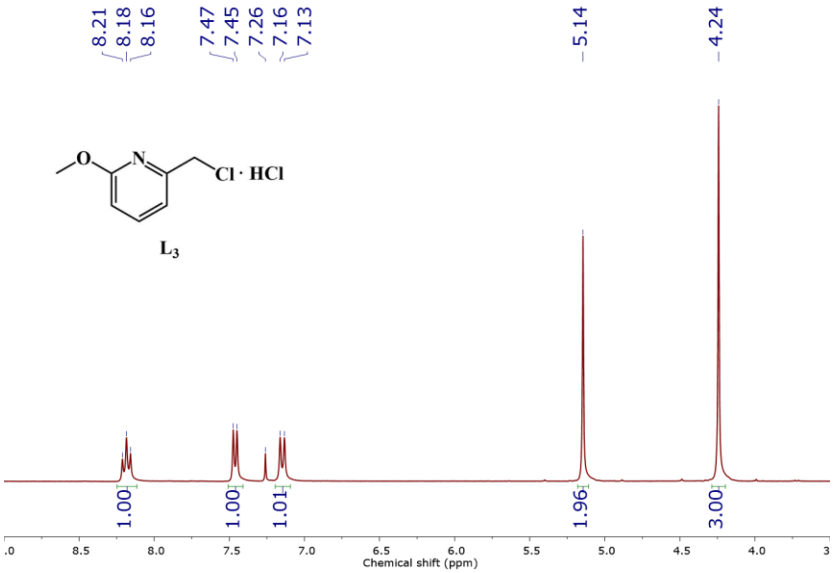

Figure 2.25. ^{1}H NMR of 2-(chloromethyl)-6-methoxypyridine hydrochloride (**L$_3$**) in $CDCl_3$.

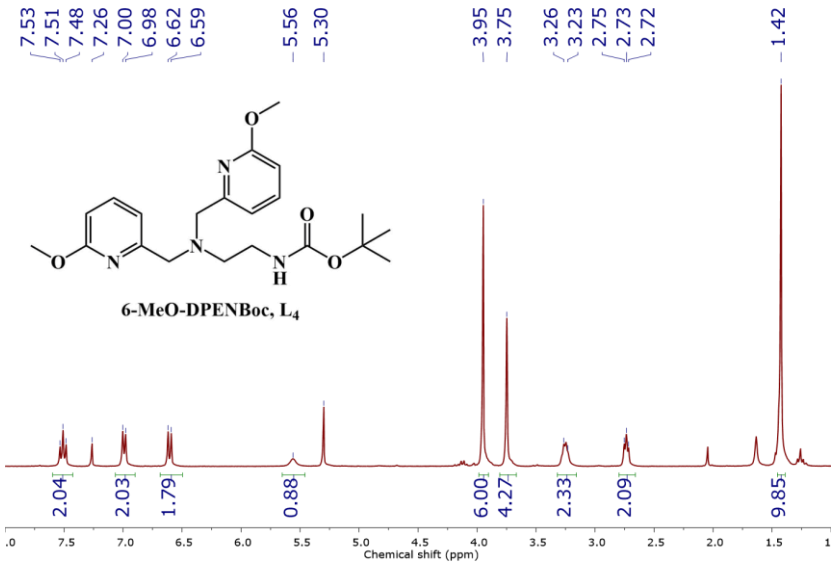

Figure 2.26. ^{1}H NMR of 6-MeO-DPENBoc (**L4**) in $CDCl_3$.

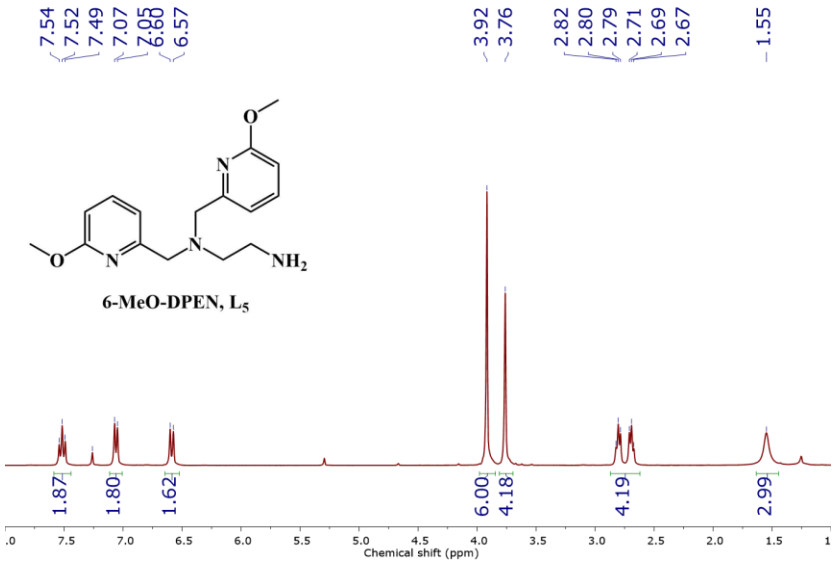

Figure 2.27. ^{1}H NMR of 6-MeO-DPEN (**L5**) in $CDCl_3$.

2.3.6 *Synthesis of a New Mn^{II} Complex Containing a Less Sterically Encumbered, More Electron-Donating Pyridine Substituent*

The corresponding Mn^{II} complex, $[Mn^{II}(L^{MeOpy})]_2^{2+}$ (**1**$^{\mathbf{MeOpy}}$), was synthesized via a metal-templated Schiff-based condensation between N,N-bis(6-methoxy-2-pyridinilmethyl)ethane-1,2-diamine and 3-methyl-3-mercapto-2-butanone, as previously described for **1**$^{\mathbf{Mepy}}$ and **1**$^{\mathbf{Quino}}$.[48] Crystallographic characterization showed that the Mn^{II} complex derived from this ligand, **1**$^{\mathbf{MeOpy}}$, is dimeric in solid state (Figure 2.28). Comparing to the trigonal bipyramidal geometry of **1**$^{\mathbf{Mepy}}$ (τ = 0.59)[48] and **1**$^{\mathbf{Quino}}$ (τ = 0.55)[52], the τ-value for **1**$^{\mathbf{MeOpy}}$ (0.42) reflects the Mn^{II} ion is a more distorted square pyramidal geometry, which is in part due to the bis-μ-thiolate. Instead of a 6-coordinate Mn^{II} center, one of the pyridine ligands is not coordinated to the metal center in the solid-state structure. The flexibility of the ligand framework would provide better stability for high valent bis-μ-oxo species, as the Mn ion would be six-coordinate with the reversible binding pyridine ligand.

Despite the dimeric structure in solid state, the magnetic moment measured by Evans' method[51] (μ_{eff} = 5.88 B.M., MeCN, 298 K), solution-state ESI-MS (Figure 2.29), X-band EPR spectrum (hyperfine splitting 90 G, Figure 2.30), and cyclic voltammogram (Figure 2.31) all indicate that **1**$^{\mathbf{MeOpy}}$ is monomeric in solution. Both solution state magnetic moment and EPR data confirms the complex as high spin Mn^{II} (S = 5/2). The cyclic voltammogram of **1**$^{\mathbf{MeOpy}}$ display a quasi-reversible $Mn^{III/II}$ wave at 0.378 V (vs SCE, in MeCN) that is much lower relative to **1**$^{\mathbf{Mepy}}$ (0.412 V vs SCE)[48] and **1**$^{\mathbf{Quino}}$ (0.452 V vs SCE)[52]. This implies a less Lewis acidic Mn ion for **1**$^{\mathbf{MeOpy}}$ compared to **1**$^{\mathbf{Mepy}}$ and **1**$^{\mathbf{Quino}}$, which was expected for the more electron donating 6-methoxy-pyridine ligand.

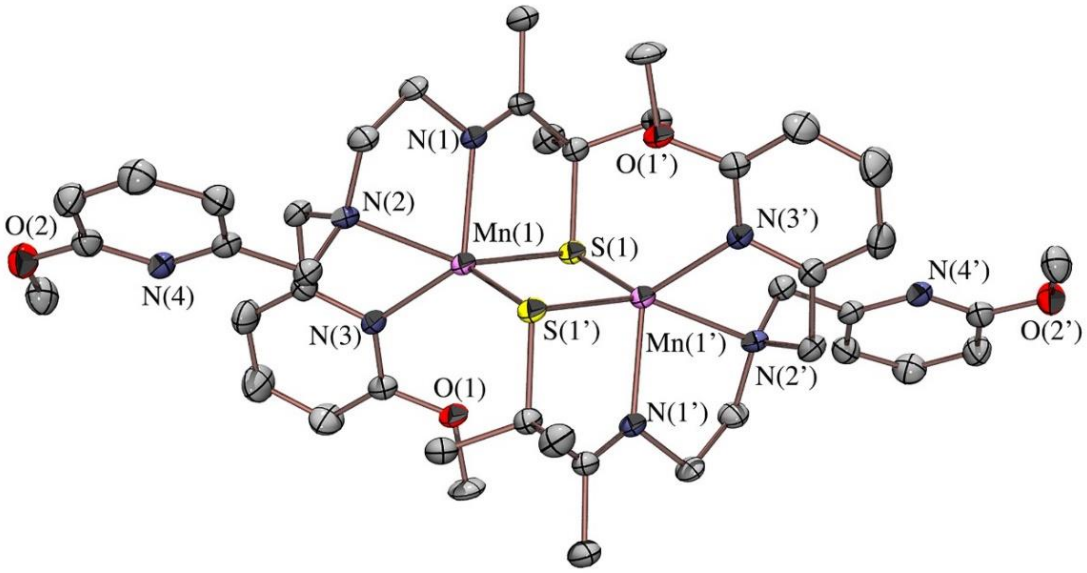

Figure 2.28. ORTEP diagram of $[Mn^{II}(L^{MeOpy})]_2^{2+}$ (**1**$^{\mathbf{MeOpy}}$). Hydrogens and counterions have been omitted for clarity.

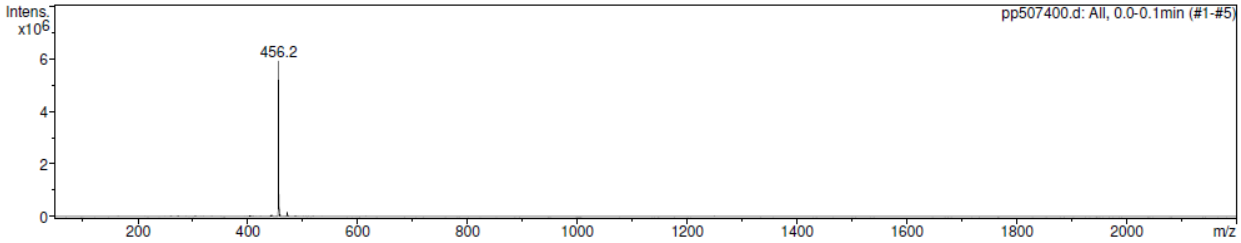

Figure 2.29. ESI-MS of $[Mn^{II}(L^{MeOpy})]_2^{2+}$ (**1**$^{\mathbf{MeOpy}}$) in MeCN with a low skim-voltage, showing that dimeric **1**$^{\mathbf{MeOpy}}$ cleaves into monomeric complex in solution.

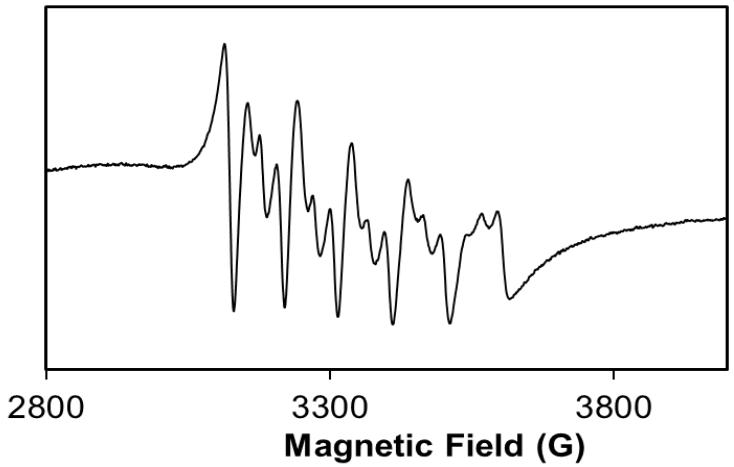

Figure 2.30. X-band (9.64 GHz) EPR spectrum of **1**$^{\mathbf{MeOpy}}$ (perpendicular-mode) in MeOH/EtOH at 6.6 K, and 5 mW power. The hyperfine splitting between the prominent lines is 90 G.

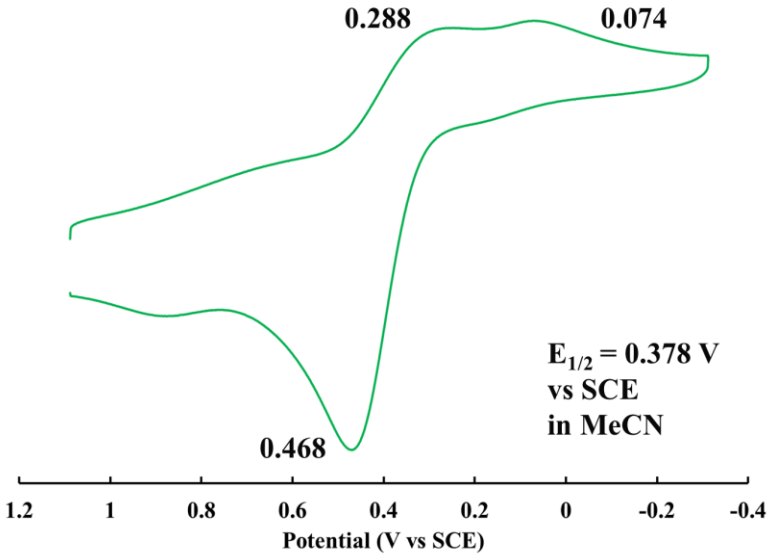

Figure 2.31. Cyclic voltammogram of the monomeric derivative of $[Mn^{II}(L^{MeOpy})]_2^{2+}$ (**1**$^{\mathbf{MeOpy}}$) that forms in MeCN at 298 K. Potentials shown are versus SCE, with 0.1 M Bu_4NPF_6 supporting electrolyte, a glassy carbon electrode, and scan rate of 500 mV/sec.

2.3.7 *Reactivity of 1^{MeOpy} with Dioxygen*

Like Mn^{II} complexes **1**$^{\mathbf{Mepy}}$ and **1**$^{\mathbf{Quino}}$, reduced **1**$^{\mathbf{MeOpy}}$ rapidly reacts with O_2 under ambient conditions to ultimately afford binuclear mono oxo-bridged $\{[Mn^{III}(L^{MeOpy})]_2(\mu\text{-}O)\}^{2+}$ (**6**$^{\mathbf{MeOpy}}$), characterized by its λ_{max} = 565 nm (ε = 1030 M^{-1} cm^{-1}) in the electronic absorption spectrum (Figure 2.32), the ORTEP of which is shown in Figure 2.33.

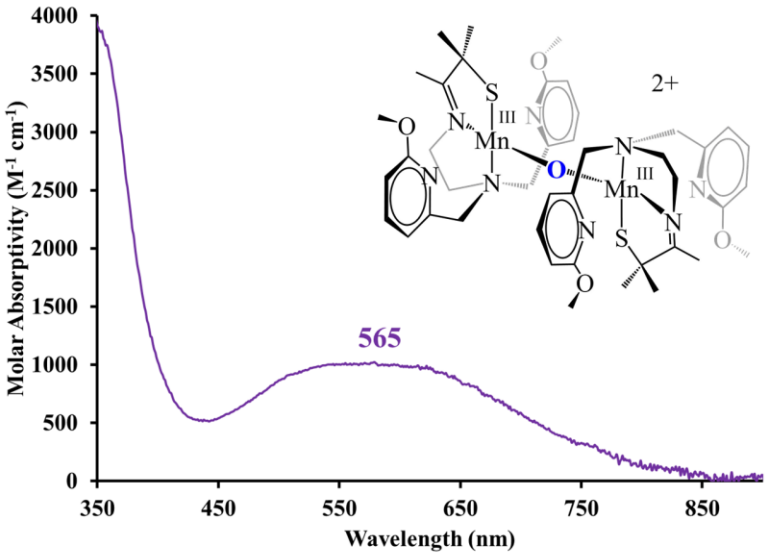

Figure 2.32. Electronic absorption spectrum of $\{[Mn^{III}(L^{MeOpy})]_2(\mu\text{-}O)\}^{2+}$ (**6**$^{\mathbf{MeOpy}}$) in DCM at 25 °C.

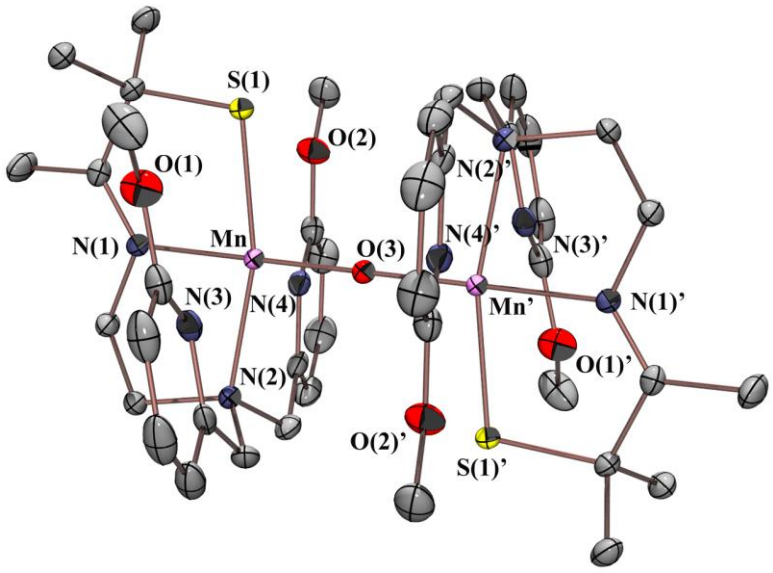

Figure 2.33. ORTEP diagram of mono oxo bridged **6**$^{\mathbf{MeOpy}}$ formed in the reaction between **1**$^{\mathbf{MeOpy}}$ and O_2. Hydrogens have been omitted for clarity.

The mean Mn•••N^{Ar} separation in **6**$^{\mathbf{MeOpy}}$ is 0.15 Å shorter than that of 6-Me-pyridine **6**$^{\mathbf{Mepy}}$, and 0.18 Å longer than that of 6-H-pyridine **6**$^{\mathbf{Py}}$ (Table 2.1), indicating, based on previously established trends,[69] that the corresponding peroxo derivative should have a weaker O-O bond, but will likely be observable (*vide supra*). In addition, the more electron-rich metal

ion should be capable of stabilizing high-valent intermediates (*vide infra*). Consistent with this, four metastable intermediates are observed *en route* to mono oxo-bridged **6**$^{\mathbf{MeOpy}}$. At low temperatures (-73 °C) a metastable green intermediate, **3**$^{\mathbf{MeOpy}}$, (λ_{max} (EtCN) = 612 nm, λ_{max} (DCM) = 630 nm) is observed in the reaction between **1**$^{\mathbf{MeOpy}}$ and O_2 (Figure 2.34). Given the similarity of this spectrum (Figure 2.34) to that of peroxo-bridged **3**$^{\mathbf{Mepy}}$ (λ_{max} = 660 nm, Figure 2.1), this intermediate was tentatively assigned as a peroxo-bridged dimer, $\{[Mn^{III}(L^{MeOpy})]_2(\mu\text{-}O_2)\}^{2+}$ (**3**$^{\mathbf{MeOpy}}$).

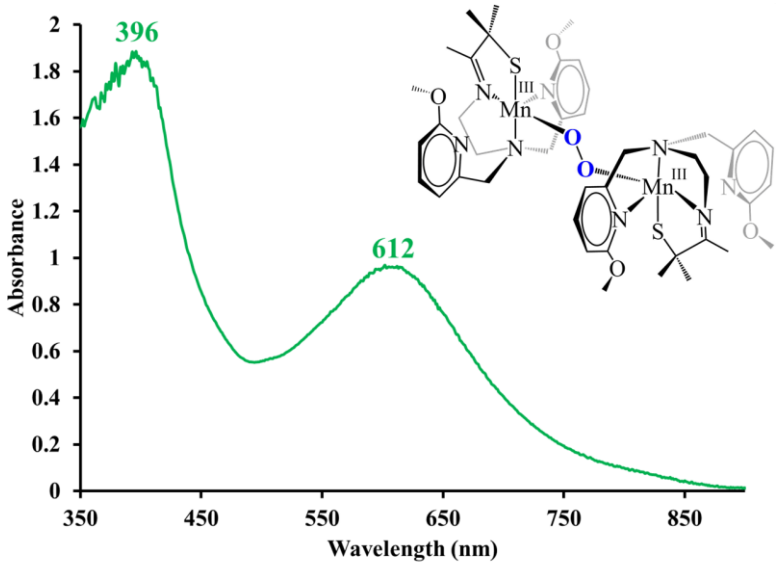

Figure 2.34. Electronic absorption spectrum of peroxo intermediate **3**$^{\mathbf{MeOpy}}$ formed in the reaction between **1**$^{\mathbf{MeOpy}}$ and O_2 (5 mL dry O_2 gas) in EtCN at -73 °C.

DFT and TD-DFT calculations were found to support this assignment. Metrical parameters (Table 2.9) for the DFT optimized structure, calculated using the spin-unrestricted B3LYP hybrid functional and the 6-311G basis set, are consistent with **3**$^{\mathbf{MeOpy}}$ being a trans-μ-1,2-peroxo-bridged Mn^{III} dimer (Figure 2.35), analogous to **3**$^{\mathbf{Mepy}}$ and **3**$^{\mathbf{Quino}}$. The TD-DFT calculated electronic absorption spectrum (Figure 2.36) is in good agreement with the experimental spectrum of Figure 2.29, and the calculated exchange coupling constant, J^{Calc} = -

0.53 cm^{-1}, indicates that the two Mn^{III} ions are essentially uncoupled. The calculated O-O bond length (1.518 Å) is 0.02 Å longer than that of $\mathbf{3}^{\mathbf{Quino}}$, and 0.07 Å longer than that of $\mathbf{3}^{\mathbf{Mepy}}$ (O-O = 1.452(5) Å),[6] indicating that this bond should cleave more readily in $\mathbf{3}^{\mathbf{MeOpy}}$. Consistent with this, $\mathbf{3}^{\mathbf{MeOpy}}$ is less stable than $\mathbf{3}^{\mathbf{Mepy}}$ and $\mathbf{3}^{\mathbf{Quino}}$, and is not readily observed at temperatures above -73 °C unless a stopped-flow instrument is used.

Table 2.9. Selected DFT optimized bond lengths (Å) and angles (°) for peroxo-bridged $[Mn^{III}(L^{MeOpy})]_2(\mu\text{-}O_2)^{2+}$ ($\mathbf{3}^{\mathbf{MeOpy}}$).

Metrical parameters	Calculated distance (Å) and angles (°)
O(1)-O(2)	1.518
Mn(1)-O(1)	1.848
Mn(2)-O(2)	1.866
Mn(1)-S(1)	2.332
Mn(2)-S(2)	2.329
Mn(1)•••Mn(2)	4.361
Mn•••$N(3)_{avg}$	2.455
Mn•••$N(4)_{avg}$	2.310
Mn(1)-O(1)-O(2)	109.5
Mn(2)-O(2)-O(1)	101.5
N(1)-Mn(1)-O(1)	176.7
N(5)-Mn(2)-O(2)	175.7
S(1)-Mn(1)-O(1)	91.6
S(2)-Mn(2)-O(2)	91.7

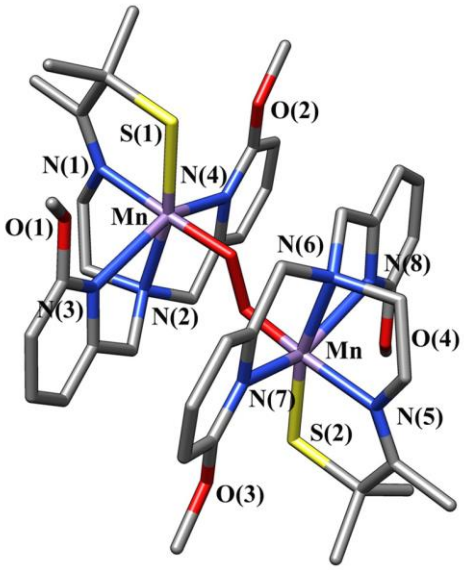

Figure 2.35. DFT optimized structure of peroxo-bridged $\mathbf{3}^{\mathbf{MeOpy}}$.

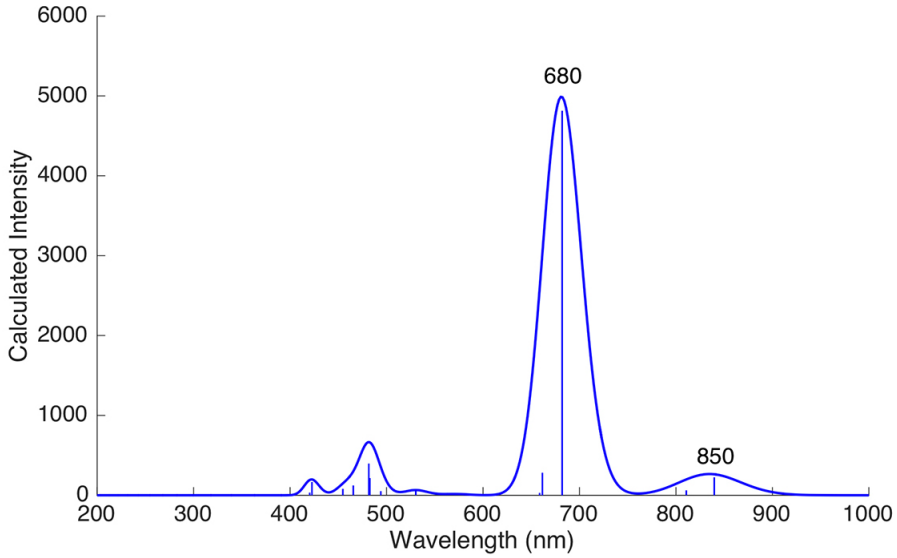

Figure 2.36. TD-DFT calculated electronic absorption spectrum of peroxo-bridged $\{[Mn^{III}(L^{MeOpy})]_2(\mu\text{-}O_2)\}^{2+}$ (**3**$^{\mathbf{MeOpy}}$).

Kinetic data for O_2 binding to Mn^{II} **1**$^{\mathbf{MeOpy}}$ and the formation of putative peroxo **3**$^{\mathbf{MeOpy}}$ were collected at low temperatures using a stopped-flow instrument. The build-up and decay of putative superoxo **2**$^{\mathbf{MeOpy}}$ was followed at 515 nm. As illustrated in the time-resolved electronic absorption spectra of Figure 2.37, **2**$^{\mathbf{MeOpy}}$ forms in approximately 3 s at -80 °C, *en route* to putative peroxo **3**$^{\mathbf{MeOpy}}$ (λ_{max} = 612 nm). The electronic absorption spectrum of **2**$^{\mathbf{MeOpy}}$ is similar to that of our previously reported superoxo, **2**$^{\mathbf{Mepy}}$ (Scheme 2.1, λ_{max} = 515 nm),[6] which forms *en route* to crystallographically characterized **3**$^{\mathbf{Mepy}}$, suggesting that **2**$^{\mathbf{MeOpy}}$ is a superoxo, $[Mn(L^{MeOpy})(O_2)]^+$ (**2**$^{\mathbf{MeOpy}}$). In contrast to **2**$^{\mathbf{Mepy}}$, **2**$^{\mathbf{MeOpy}}$ is only cleanly observed if ≥ 20-fold excess $[O_2]$ (8 mM $[O_2]$ vs 0.375 mM [**1**$^{\mathbf{MeOpy}}$]), and lower temperatures (-80 °C to -62 °C) are used (Table 2.10, Figure 2.38). These conditions are likely required in order to ensure that Mn^{II} **1**$^{\mathbf{MeOpy}}$ is consumed by the excess O_2, thereby slowing down the conversion of **2**$^{\mathbf{MeOpy}}$ to binuclear peroxo-bridged **3**$^{\mathbf{MeOpy}}$ (Scheme 2.5 and Figure 2.38) and increasing its lifetime.

Table 2.10. Observed pseudo first order rate constants for dioxygen binding to Mn^{II} $\mathbf{1^{MeOpy}}$ as a function of dioxygen concentration and temperature. Data collected by monitored at λ = 504 nm using a stopped flow instrument, [Mn^{II} ($\mathbf{1^{MeOpy}}$)] = 0.75 mM.

Temperature (K)	$[O_2]$ (mM)	k_{1obs}^{MeOpy} (s^{-1})
193.15	2.2	0.19759
	4.4	0.29557
	6.6	0.40904
	8.8	0.36095
202.15	8.8	0.58759
211.15	8.8	0.77636
220.15	8.8	1.10650

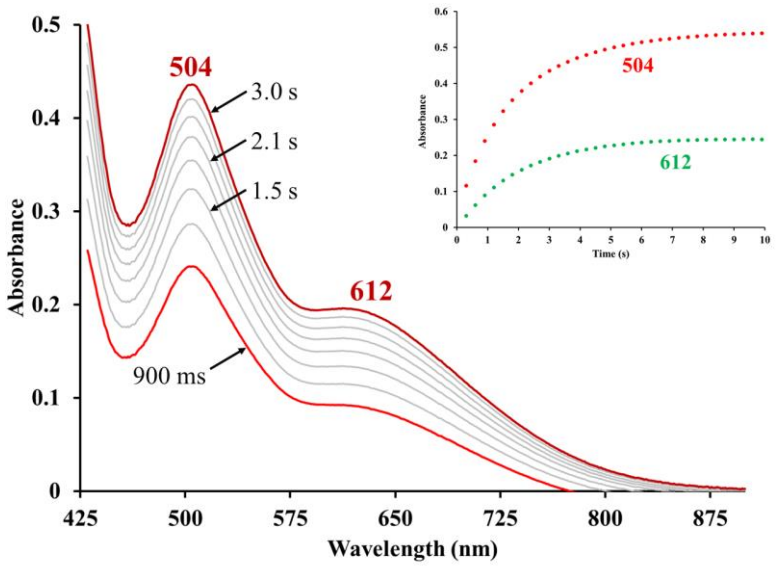

Figure 2.37. Time-resolved electronic absorption spectra, for dioxygen binding to $\mathbf{1^{MeOpy}}$ in EtCN at -80 °C, obtained using a stopped-flow instrument, under pseudo-first-order conditions with excess O_2 ([$\mathbf{1^{MeOpy}}$] = 0.375 mM, $[O_2]$ = 8 mM after mixing). Inset: kinetic trace obtained at λ_{max} = 504 and 612 nm.

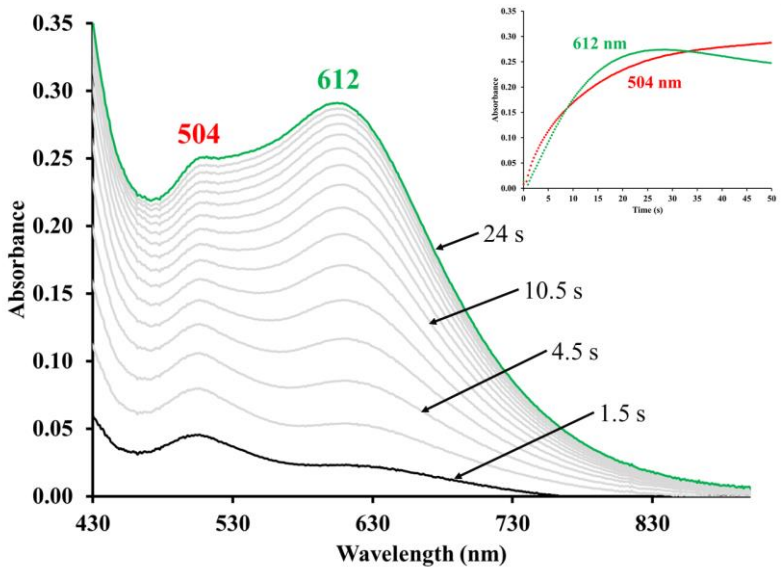

Figure 2.38. Monitoring the growth of putative peroxo **3**$^{\mathbf{MeOpy}}$, and putative superoxo **2**$^{\mathbf{MeOpy}}$ in EtCN at -80 °C ([**1**$^{\mathbf{MeOpy}}$] = 0.75 mM, [O_2] = 0.75 mM).

Scheme 2.5. Dioxygen reactivity of 6-MeO-pyridine **1**$^{\mathbf{MeOpy}}$, showing rate constant labeling scheme, and observed intermediates.

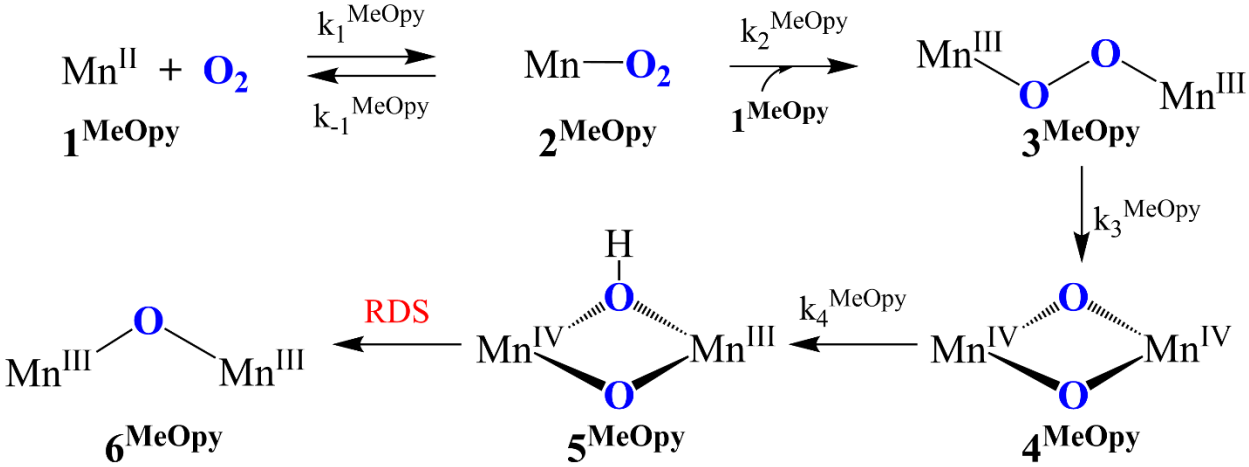

The general kinetic scheme used to analyze the data was the same as that used for **1**$^{\mathbf{Mepy}}$.[6] Reactions were run under pseudo first-order conditions, in the presence of excess O_2. *Psuedo* first-order rate constants, k_{1obs}^{MeOpy} and k_{2obs}^{MeOpy}, as a function of [O_2], temperature, and [**1**$^{\mathbf{MeOpy}}$] are assembled in Tables 2.10-2.12, respectively. The observed rate constant k_{1obs}^{MeOpy} was found to increase linearly (Figure 2.39) with increasing O_2 concentration, indicative of a 1st

order reaction with respect to [O_2]. The second order rate constant for O_2 binding k_1^{MeOpy} was obtained from the slope, and the first order rate constant for O_2 release at -80 °C, k_{-1}^{MeOpy}, was obtained from the intercept of Figure 2.39. Intermediates **2**^{MeOpy} and **3**^{MeOpy} were found to be too unstable at temperatures above -80 °C if lower concentrations of dioxygen (i.e., [O_2] < 8.8 mM) were used, requiring that, at higher temperatures, k_{-1}^{MeOpy} parameters be obtained from global fits. Second order rate constants for the conversion of superoxo **2**^{MeOpy} to peroxo **3**^{MeOpy}, k_2^{MeOpy}, were also obtained from global fits to the [O_2] = 8.8 mM data using ReactLab. Superoxo **2**^{MeOpy} is not observed at temperatures above -62 °C.

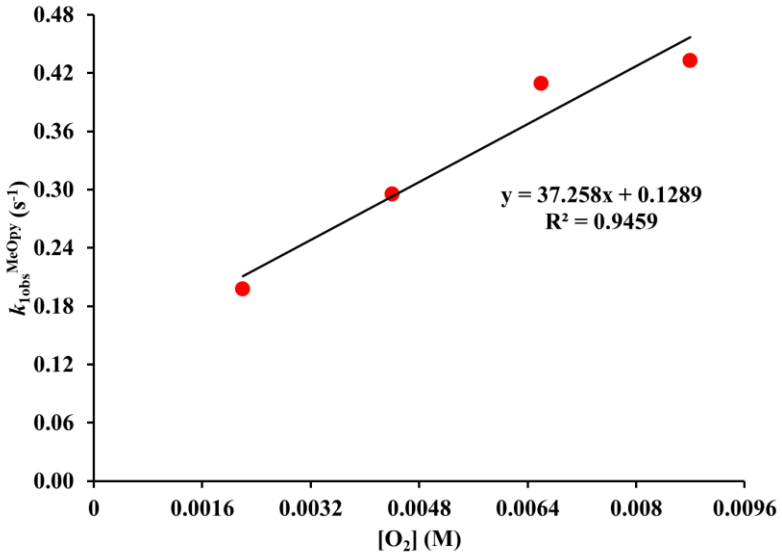

Figure 2.39. Plot of pseudo first order rate constants (k_{1obs}^{MeOpy}) for O_2 binding to **1**^{MeOpy} as a function of [O_2] at -80 °C, from which the second-order rate constant k_1^{MeOpy}, and first-order rate constant k_{-1}^{MeOpy} were obtained.

Table 2.11. Observed pseudo first order rate constants for the conversion of superoxo **2**^{MeOpy} to peroxo **3**^{MeOpy} as a function of dioxygen concentration and temperature. Data obtained by monitoring reaction at λ = 504 nm by stopped-flow, [Mn^{II} (**1**^{MeOpy})] = 0.75 mM.

Temperature (K)	[O_2] (mM)	k_{2obs}^{MeOpy} (s^{-1})
193.15	2.2	0.006417
	4.4	0.007637
	6.6	0.007670
	8.8	0.005773
202.15	8.8	0.01062
211.15	8.8	0.000853
220.15	8.8	0.00944

Table 2.12. Pseudo first order rate constants for the conversion of superoxo $\mathbf{2}^{\mathbf{MeOpy}}$ to peroxo $\mathbf{3}^{\mathbf{MeOpy}}$ as a function of Mn^{II} $\mathbf{1}^{\mathbf{MeOpy}}$ concentration and temperature. Data obtained by monitoring reaction at λ = 630 nm by stopped-flow, $[O_2]$ = 8.8 mM.

Temperature (K)	$[\mathbf{1}^{\mathbf{MeOpy}}]$ (mM)	k_{2obs}^{MeOpy} (s^{-1})
193.15	0.75	0.041
	0.60	0.038
	0.45	0.037
	0.30	0.028

Temperature-dependent rate constants for the reaction between $\mathbf{1}^{\mathbf{MeOpy}}$ and O_2 are summarized in supplemental Tables 2.10-2.11, and Tables 2.13-2.14. The rate constant numbering scheme and observed intermediates are shown in Scheme 2.5. Dioxygen binding to $\mathbf{1}^{\mathbf{MeOpy}}$ (k_1^{MeOpy} (211 K) = 70.9(8) M^{-1} s^{-1}, Table 2.12, Figure 2.39) is two orders of magnitude slower than O_2 binding to $\mathbf{1}^{\mathbf{Mepy}}$ (k_{1calc}^{Quino} (263 K) = 3.8(2) x 10^3 M^{-1} s^{-1}),[6] and approximately twice as fast as O_2 binding to $\mathbf{1}^{\mathbf{Quino}}$ (k_{1calc}^{Quino} (263 K) = 30.0(8) M^{-1} s^{-1}, Table 2.6), albeit, at lower temperatures, where entropy favors an associative binding process. This step is rate determining, with respect to formation of peroxo $\mathbf{3}^{\mathbf{Quino}}$ and $\mathbf{3}^{\mathbf{MeOpy}}$ but not $\mathbf{3}^{\mathbf{Mepy}}$. Dioxygen binds reversibly to $\mathbf{1}^{\mathbf{MeOpy}}$, as well as $\mathbf{1}^{\mathbf{Quino}}$ (*vide supra*), but irreversibly to $\mathbf{1}^{\mathbf{Mepy}}$. Dioxygen release from $\mathbf{2}^{\mathbf{MeOpy}}$ is three orders of magnitude slower (k_{-1}^{MeOpy} = 2.4(2) x 10^{-2} s^{-1}, Table 2.15) than O_2 binding (k_1^{MeOpy} = 70.9(8) M^{-1} s^{-1}) at -80 °C. Due to the instability of superoxo $\mathbf{2}^{\mathbf{MeOpy}}$ at temperatures above -80 °C, and the limitations of the low-temperature stopped-flow instrument, the error associated with the kinetic parameters, k_{-1}^{MeOpy}, for O_2 release is too large to reasonably obtain equilibrium constants. The apparent low affinity for O_2 (based on the intercept of Figure 2.39), and the reversibility of O_2 binding to $\mathbf{1}^{\mathbf{MeOpy}}$ indicates that, consistent with our design, the electron donating L^{MeOpy} ligand decreases the metal ion Lewis acidity of the 6-MeO-pyridine dioxygen derivatives. This is reflected in the $Mn^{II/III}$ redox potentials for $\mathbf{1}^{\mathbf{MeOpy}}$ versus $\mathbf{1}^{\mathbf{Quino}}$ and $\mathbf{1}^{\mathbf{Mepy}}$ (*vide infra*). This is not only an electronic effect, but also a steric effect since the decreased

steric bulk of the 6-MeO-pyridine substituent favors shorter Mn•••N^{Ar} distances, which should increase electron density at the metal ion (*vide supra*, Table 2.1).[11,69]

Table 2.13. Temperature-dependent rate constants for O_2 binding to $\mathbf{1^{MeOpy}}$, O_2 release from $\mathbf{2^{MeOpy}}$, and the conversion of superoxo $\mathbf{2^{MeOpy}}$ to peroxo $\mathbf{3^{MeOpy}}$ in EtCN.

	-80 °C	**-71 °C**	**-62 °C**
$\boldsymbol{k_1^{MeOpy}}$ **(M^{-1} s^{-1})**	34(4)	43.6(5)	70.9(8)
$\boldsymbol{k_{-1}^{MeOpy}}$ **(s^{-1})**	8.4(3) x 10^{-3}	1.8(9) x 10^{-2}	2.4(9) x 10^{-2}
$\boldsymbol{k_2^{MeOpy}}$ **(M^{-1} s^{-1})**	1.1(4) x 10^{3}	9.5(2) x 10^{2}	2.0(3) x 10^{2}

Table 2.14. Rate constants, obtained from global fits for cleavage of the peroxo $\mathbf{3^{MeOpy}}$ O-O bond (k_3^{MeOpy}) and HAT (k_4^{MeOpy}) to the putative $Mn^{IV}Mn^{IV}$ bis oxo $\mathbf{4^{MeOpy}}$ as a function of [O_2]. Data obtained at -80 °C. Rate constants k_1^{MeOpy} = 34 M^{-1} s^{-1}, k_{-1}^{MeOpy} = 0.0084 s^{-1}, and k_2^{MeOpy} = 1070 M^{-1} s^{-1} were obtained from excess-O_2 experiments and used without optimization.

[Mn] (mM)	**[O_2] (mM)**	$\boldsymbol{k_3^{MeOpy}}$	$\boldsymbol{k_4^{MeOpy}}$
0.75	0.375	6.19(6) x 10^{-2}	8(4) x 10^{-3}
	0.75	7.8(6) x 10^{-2}	1.00(4) x 10^{-2}
	1.5	1.39(3) x 10^{-1}	1.3(2) x 10^{-2}
1.5	0.375	3.0(8) x 10^{-2}	1.0(2) x 10^{-2}
	0.75	2.35(4) x 10^{-2}	3.3(4) x 10^{-3}
	1.5	2.8(1) x 10^{-2}	1.5(2) x 10^{-3}

Eyring and Arrhenius plots were used to obtain activation parameters for O_2 binding to $\mathbf{1^{MeOpy}}$ (Figure 2.40-2.41), O_2 release from $\mathbf{2^{MeOpy}}$ (Figure 2.42-2.43), and the conversion of superoxo $\mathbf{2^{MeOpy}}$ to peroxo $\mathbf{3^{MeOpy}}$ (Figure 2.44-2.45), and are compared with the corresponding parameters for $\mathbf{1^{Mepy}}$ and $\mathbf{1^{Quino}}$ in Table 2.15. An analysis of the factors that govern the magnitude of these kinetic barriers shows that both metal ion Lewis acidity and metal ion accessibility play a role. For example, there is a strong correlation (R^2 = 0.999) between the barrier to O_2 binding and the cathodic peak potential, $E_{p,c}$,[48] an experimental parameter that reflects metal ion Lewis acidity: the higher the redox potential, the higher the barrier to O_2 binding (Figure 2.46). This indicates O_2 binding is coupled with the oxidation of the metal ion, as one would expect for a process that converts O_2 to superoxide, $O_2^{\bullet-}$. Peak potentials, as

opposed to $E_{1/2}$ values are compared in Figure 2.46, since the cyclic voltammogram wave associated with the $\mathbf{1}^{\mathbf{Quino}}$ is irreversible.[52]

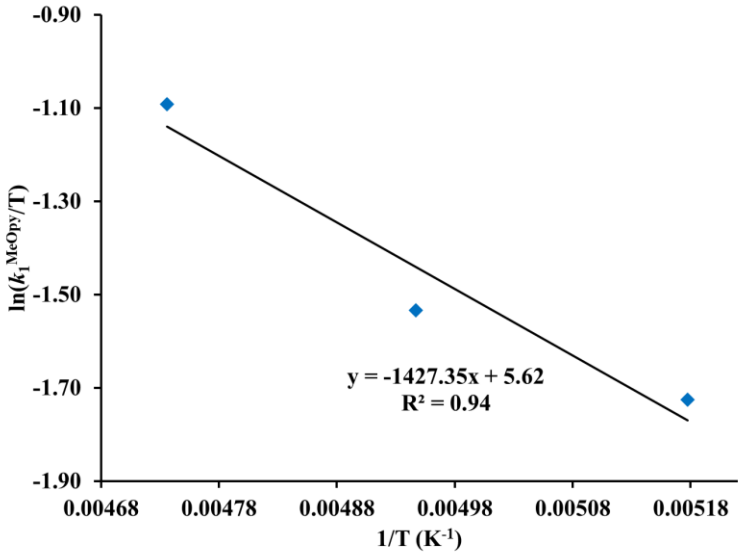

Figure 2.40. Eyring plot for O_2 binding to $\mathbf{1}^{\mathbf{MeOpy}}$ to form putative superoxo intermediate $\mathbf{2}^{\mathbf{MeOpy}}$ in EtCN, from which activation parameters $\Delta H_1^{\ddagger MeOpy}$ = 11.9(8) kJ mol^{-1} and $\Delta S_1^{\ddagger MeOpy}$ = -151(6) J mol^{-1} K^{-1}, were derived. The second-order rate constants k_1^{MeOpy} were experimentally obtained.

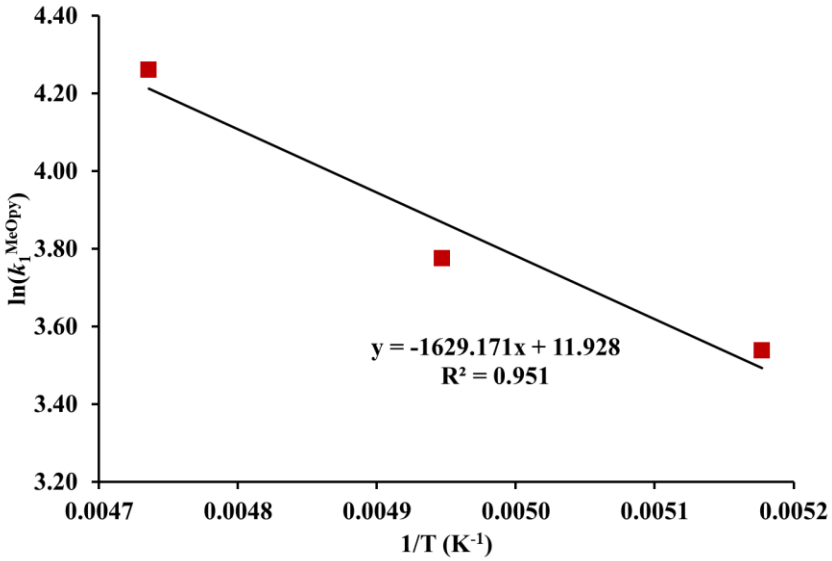

Figure 2.41. Arrhenius plot for O_2 binding to $\mathbf{1}^{\mathbf{MeOpy}}$ to form putative superoxo intermediate $\mathbf{2}^{\mathbf{MeOpy}}$ in EtCN, from which the activation energy, E_a = 14(1) kJ mol^{-1}, was obtained.

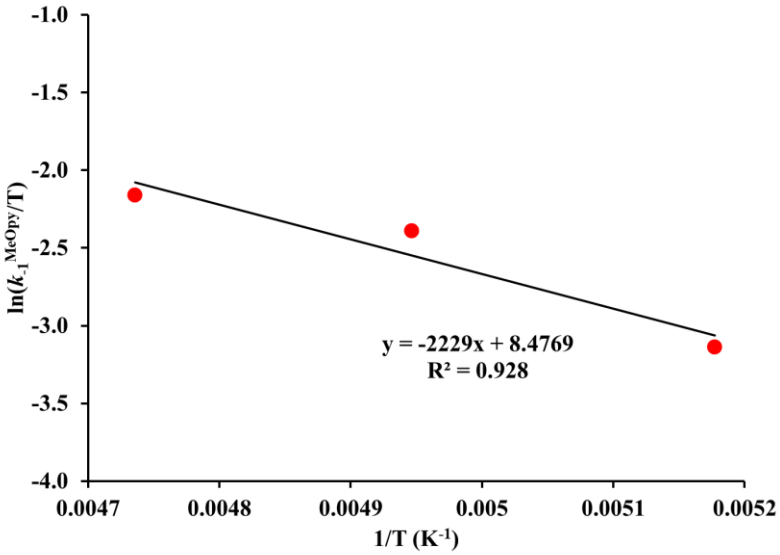

Figure 2.42. Eyring plot for O_2 release from superoxo **2^{MeOpy}** in EtCN, from which activation parameters $\Delta H_{-1}^{\ddagger MeOpy}$ = 18(2) kJ mol^{-1} and $\Delta S_{-1}^{\ddagger MeOpy}$ = -127(9) J mol^{-1} K^{-1}, were derived.

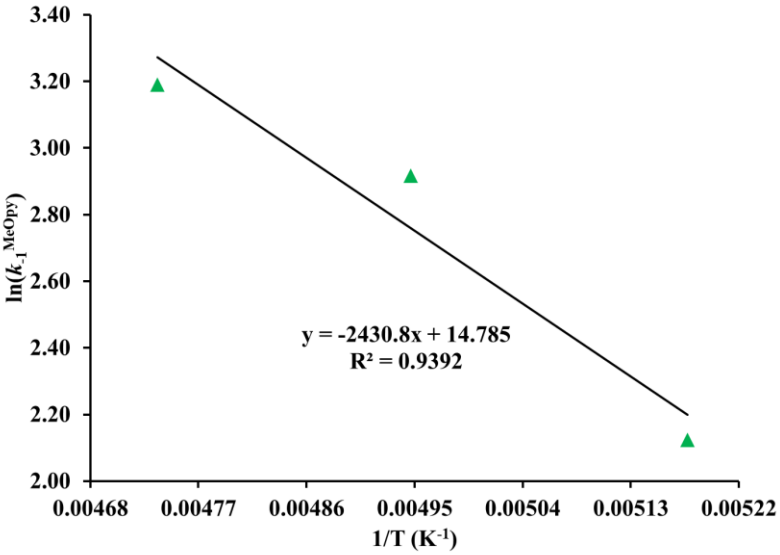

Figure 2.43. Arrhenius plot for O_2 release from superoxo **2^{MeOpy}** in EtCN, from which the activation energy, E_a = 20(1) kJ mol^{-1}, was obtained.

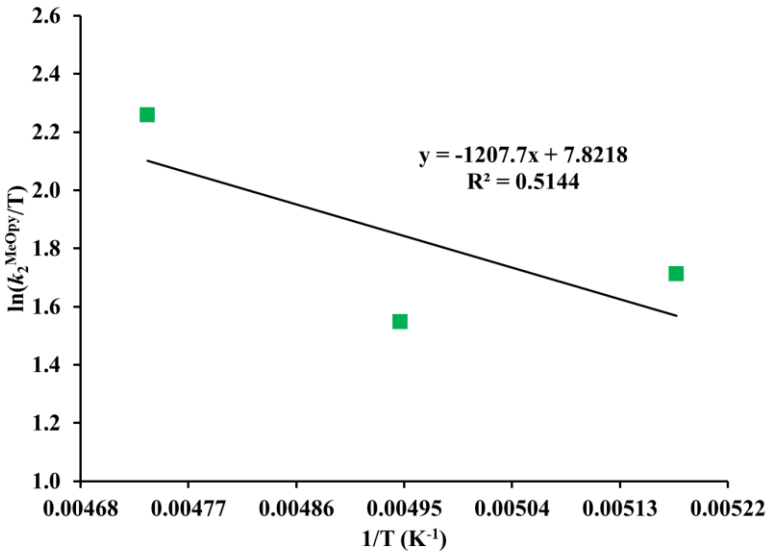

Figure 2.44. Eyring plot for the conversion of superoxo intermediate **2**$^{\mathbf{MeOpy}}$ to peroxo **3**$^{\mathbf{MeOpy}}$ in EtCN, from which activation parameters $\Delta H_2^{\ddagger MeOpy}$ = 10(2) kJ mol^{-1} and $\Delta S_2^{\ddagger MeOpy}$ = -132(3) J mol^{-1} K^{-1}, were derived.

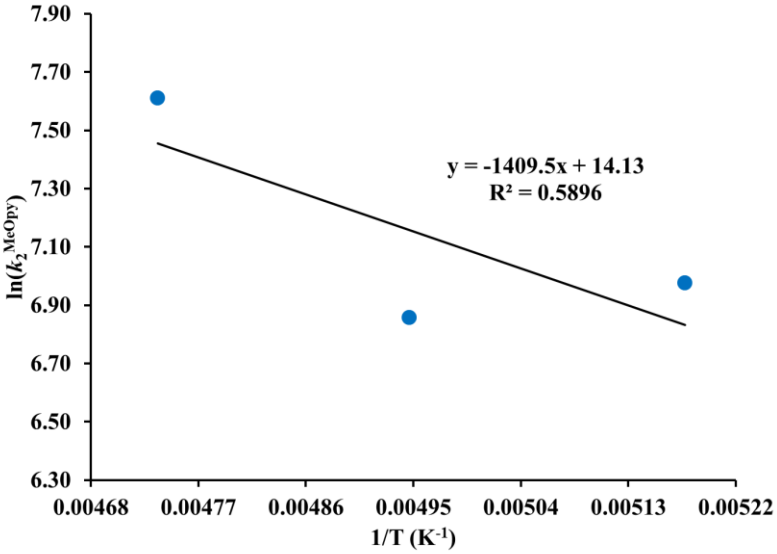

Figure 2.45. Arrhenius plot for the conversion of superoxo intermediate **2**$^{\mathbf{MeOpy}}$ to peroxo **3**$^{\mathbf{MeOpy}}$ in EtCN, from which the activation energy, E_a = 12(6) kJ mol^{-1} was obtained.

Table 2.15. Comparison of the activation barriers to dioxygen binding to **1**$^{\mathbf{MeOpy}}$, **1**$^{\mathbf{Quino}}$, and **1**$^{\mathbf{Mepy}}$, dioxygen release from superoxo **2**$^{\mathbf{MeOpy}}$, superoxo **2**$^{\mathbf{MeOpy}}$ to peroxo **3**$^{\mathbf{MeOpy}}$ conversion, and peroxo **3**$^{\mathbf{MeOpy}}$ O-O bond cleavage.

Ligand Scaffold	Activation Parameter	O_2 binding to 1	O_2 release from 2	Superoxo 2 to peroxo 3	O-O Cleavage	Peroxo Half-life	$E_{p,c}^{MnIII/II}$ (mV vs SCE)
L^{MeOpy}	$\Delta H^{\ddagger}$ (kJ mol^{-1})	11.9	18.5	10.0	N/A	11.5 s (193 K)	+288
	$\Delta S^{\ddagger}$ (J mol^{-1} K^{-1})	-151	-127	-132			
	E_a (kJ mol^{-1})	13.5	20.2	11.7			
L^{Quino}	$\Delta H^{\ddagger}$ (kJ mol^{-1})	16(3)	28(4)	16(2)	16(2)	23s (221 K)	+312
	$\Delta S^{\ddagger}$ (J mol^{-1} K^{-1})	-150(12)	-160 30(5)	-106(6) 17(5)	-211(6) 18(3)		
	E_a (kJ mol^{-1})	18(3)					
L^{Mepy}	$\Delta H^{\ddagger}$ (kJ mol^{-1})	26(2)	N/A	47(1)	N/A	290 s (233 K)	+360
	$\Delta S^{\ddagger}$ (J mol^{-1} K^{-1})	-76(7)		-15(6)			
	E_a (kJ mol^{-1})	28(1)		49(1)			

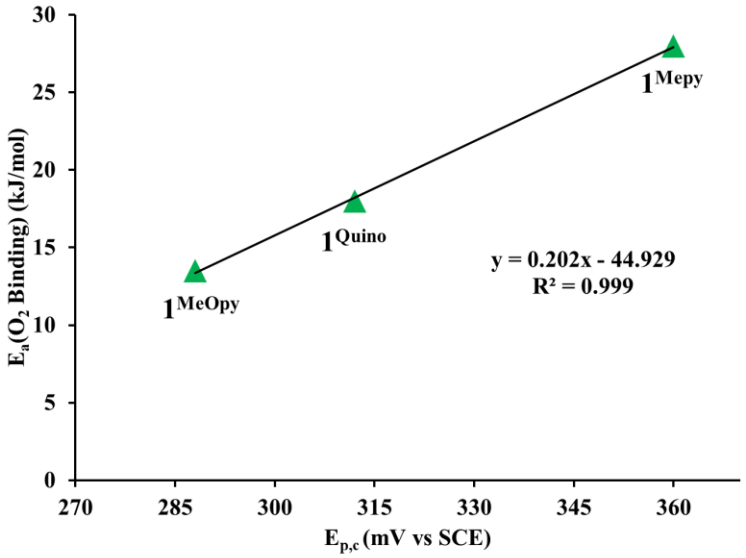

Figure 2.46. Correlation between the activation barrier (E_a) to O_2 binding and the cathodic peak potential, $E_{p,c}$.

In addition, comparison of the steric properties shows that the activation barrier decreases as the metal ion becomes more (Figures 2.47-2.49). The Mn^{II} ion is more accessible in **1**$^{\mathbf{MeOpy}}$, less so in **1**$^{\mathbf{Quino}}$, and less accessible in the more sterically encumbered **1**$^{\mathbf{Mepy}}$. A similar

correlation is observed between the redox potential and the kinetic barrier to the conversion of superoxo **2** to the corresponding peroxo **3** (Figure 2.48).

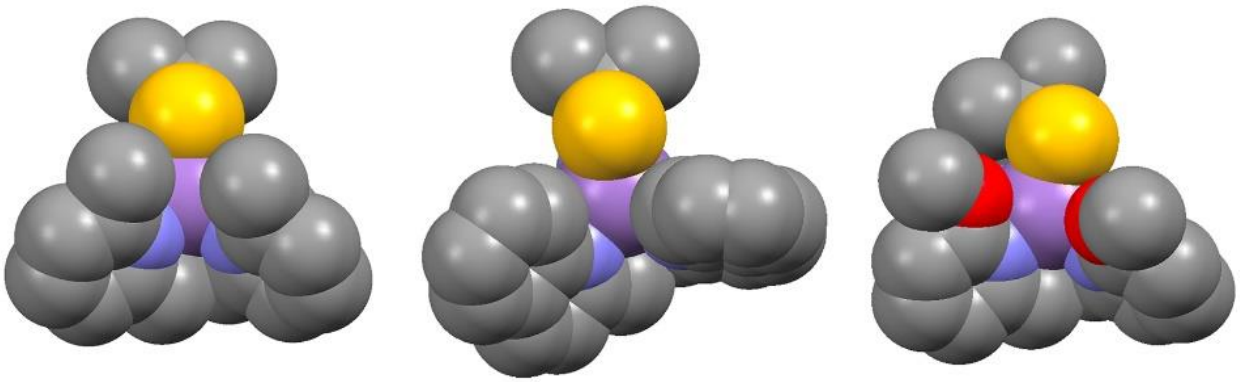

Figure 2.47. Steric properties of the ligand influence metal ion (shown in purple) accessibility, as shown by space filling diagrams of $\mathbf{1}^{\mathbf{Mepy}}$ (left), $\mathbf{1}^{\mathbf{Quino}}$ (center), and $\mathbf{1}^{\mathbf{MeOpy}}$ (right).

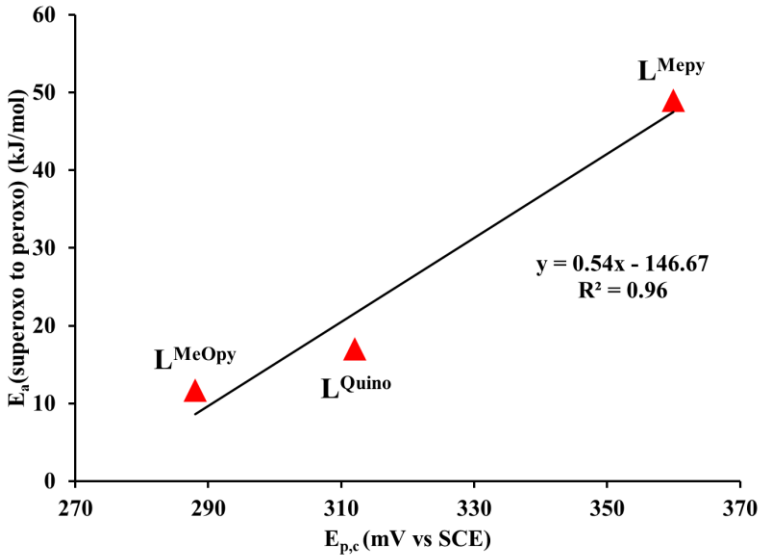

Figure 2.48. Correlation between cathodic peak potential, $E_{p,c}$, and the kinetic barrier to the conversion of superoxo **2** to peroxo **3**.

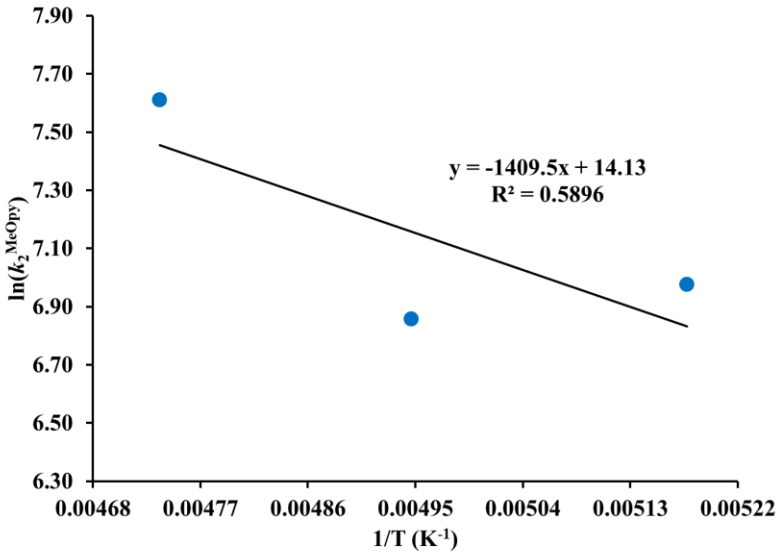

Figure 2.49. Arrhenius plot for the conversion of superoxo intermediate **2**$^{\mathbf{MeOpy}}$ to peroxo **3**$^{\mathbf{MeOpy}}$ in EtCN, from which the activation energy, E_a = 12(6) kJ mol^{-1}, was obtained.

2.3.8 *Barrier to O-O Bond Cleavage and the Observation of Additional Intermediates*

As noted in the introduction, the steric properties of the substituted N-heterocycles differ dramatically, and have been shown to influence the barrier to alkylperoxo O-O bond cleavage.[6] The least sterically encumbered complexes contain shorter Mn•••N^{Ar} distances and weaker alkylperoxo O-O bonds. This is because the metal ion becomes less Lewis acidic as the Mn•••N^{Ar} distance decreases, and this decreases the π-back bonding from the filled peroxo π*(O-O) orbital to the metal ion. X-ray emission (XES) spectroscopically calibrated calculations showed that peroxo **3**$^{\mathbf{Mepy}}$ adheres to this correlation, as well.[11] Presumably this also applies to the other dioxygen-derived peroxos, **3**$^{\mathbf{Quino}}$ and **3**$^{\mathbf{MeOpy}}$, described herein. Kinetic studies were used to determine whether the orbitals followed this correlation.

Observation of peroxo **3**$^{\mathbf{MeOpy}}$, and the metastable intermediates that follow, is optimized when excess amounts of O_2 ([O_2] = 8.8 mM vs [**1**$^{\mathbf{MeOpy}}$] = 0.375 mM) and high temperatures (-44 °C), are used (Figure 2.50). These conditions speed up the formation of superoxo **2**$^{\mathbf{MeOpy}}$ and its

conversion to peroxo **3**$^{\mathbf{MeOpy}}$. Under these conditions, peroxo **3**$^{\mathbf{MeOpy}}$ forms within 1.2 s (Figure 2.50), and then converts to a metastable species, **4**$^{\mathbf{MeOpy}}$, within 21s. There is a clean isosbestic point at 730 nm, indicating that at most two species contribute to the absorbance at higher wavelengths. However, at wavelengths below 525 nm, the isosbestic points are less clear because several species (including superoxo **2**$^{\mathbf{MeOpy}}$, and peroxo **3**$^{\mathbf{MeOpy}}$) contribute to this region of the spectrum. Based on global fits to the data **4**$^{\mathbf{MeOpy}}$ possesses absorption bands at 805 nm and 497 nm, and a shoulder at 532 nm (Figure 2.50).

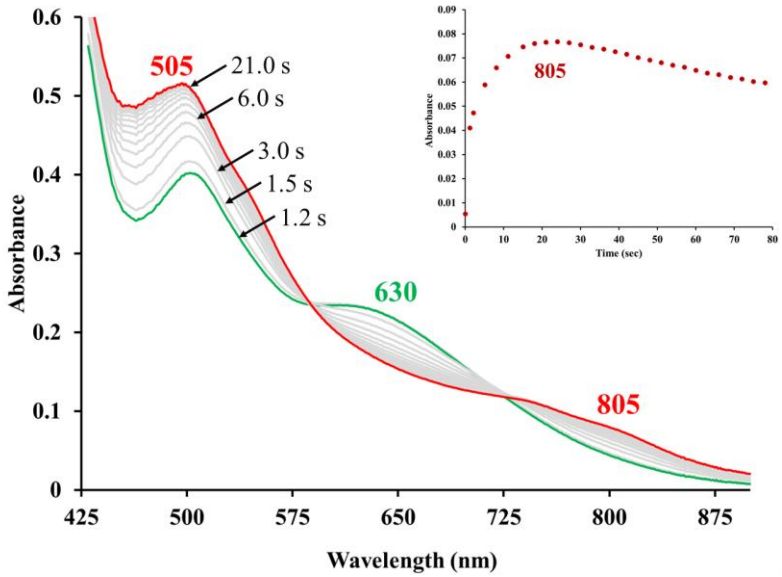

Figure 2.50. Conversion of peroxo **3**$^{\mathbf{MeOpy}}$ to a metastable species, **4**$^{\mathbf{MeOpy}}$, with λ_{max} = 805 nm monitored by transient absorption spectroscopy in EtCN at -44 °C. [O_2] = 8.8 mM, [**1**$^{\mathbf{MeOpy}}$] = 0.375 mM, after mixing.

According to the reaction scheme of Scheme 2.3, the species most likely to form following peroxo **3**$^{\mathbf{MeOpy}}$, would be a high-valent bis μ-oxo, $[((L^{MeOpy})Mn^{IV})_2(\mu^2\text{-}O)_2]^{2+}$ (**4**$^{\mathbf{MeOpy}}$). Conversion of **3**$^{\mathbf{MeOpy}}$ to **4**$^{\mathbf{MeOpy}}$ would involve peroxo O-O bond cleavage, explaining why higher temperatures are required. Rate constants for the conversion of **3**$^{\mathbf{MeOpy}}$ to **4**$^{\mathbf{MeOpy}}$ were obtained from global fits to the data. A comparison of the half-lives of **3**$^{\mathbf{MeOpy}}$ (k_3^{MeOpy} (193 K) = 0.06(3) s^{-1}, $t_{1/2}$ = 11.5 s), **3**$^{\mathbf{Quino}}$ (Table 2.15), and **3**$^{\mathbf{Mepy}}$ (Table 2.15), shows that there is a

correlation between the barrier to peroxo O-O bond cleavage and the experimentally measured redox potential, $E_{p,c}^{MnIII/II}$. This effect is enhanced if one takes into account the fact that these half-lives were measured at different temperatures, due to the fact that peroxo-bridged $\mathbf{3}^{\mathbf{MeOpy}}$ is not observed above 233 K, and temperatures below 233 K were required for an accurate determination of rate constants for $\mathbf{3}^{\mathbf{Quino}}$ due to its instability. The higher the redox potential, the more Lewis acidic the metal ion, and the more π back-donation from the filled peroxo π* orbital is facilitated. Redox potentials for the $Mn^{III/II}$ couple are used, as opposed to the $Mn^{IV/III}$ couple, because our Mn(IV) derivatives are too reactive (*vide infra*) to obtain the latter. The metastable, reactive nature of $\mathbf{4}^{\mathbf{MeOpy}}$ contrasts with the majority of bis-oxo bridged $Mn^{IV}Mn^{IV}$ dimers,[74–76] likely reflecting the electron donating properties of the thiolate.

Following its formation, putative high-valent bis oxo $Mn^{IV}Mn^{IV}$ ($\mathbf{4}^{\mathbf{MeOpy}}$, λ_{max} = 805 nm) converts more slowly (Table 2.12) to metastable red species with λ_{max} = 505 nm, and a reproducibly observed multi-line ⊥-mode EPR signal (Figure 2.51). The spectrum of Figure 2.51 is well simulated with an S = 1/2 system with a rhombic g-tensor with principal values 1.994, 2.004, and 2.016 coupled to two ^{55}Mn nuclei with isotropic hyperfine couplings of 325 MHz and 180 MHz.[49] These values are consistent with an antiferromagnetically coupled $Mn^{III}Mn^{IV}$ bimetallic species, $\mathbf{5}^{\mathbf{MeOpy}}$.[77–83]

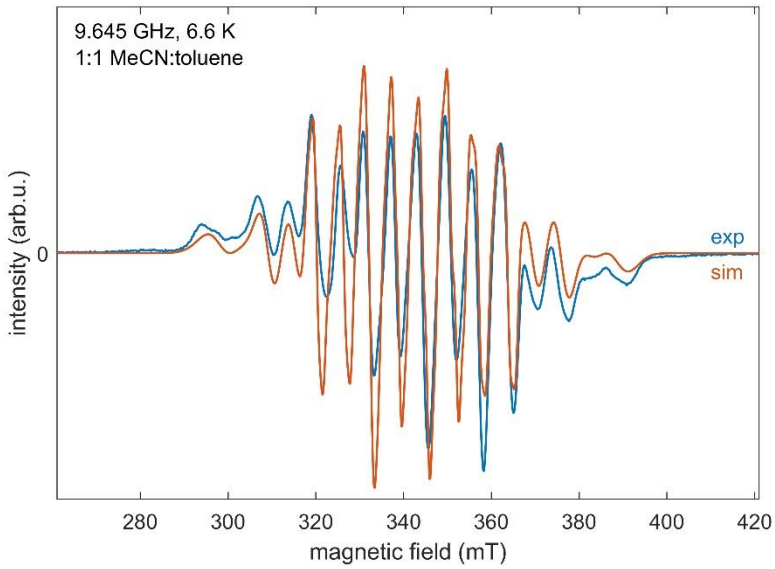

Figure 2.51. Low temperature (6.6 K) perpendicular-mode X-band (9.645 GHz) EPR spectrum of the $Mn^{III}Mn^{IV}$ intermediate $\mathbf{5}^{\mathbf{MeOpy}}$, observed following peroxo $\mathbf{3}^{\mathbf{MeOpy}}$. Microwave power = 0.2 mW, modulation amplitude = 0.75 mT.

2.4 Conclusion

With this study, we have shown that the relative stability of metastable dioxygen intermediates can be tuned by adjusting the supporting ligands. Whereas O_2 binds irreversibly to $\mathbf{1}^{\mathbf{Mepy}}$, kinetics data shows that O_2 binding was less favored for the less Lewis acidic complexes $\mathbf{1}^{\mathbf{Quino}}$ and $\mathbf{1}^{\mathbf{MeOpy}}$, and the microscopic reverse process involving O_2 releasing process involving O_2 release from superoxo $\mathbf{2}^{\mathbf{Quino}}$ and $\mathbf{2}^{\mathbf{Quino}}$, was more favorable. The Mn^{II} complexes $\mathbf{1}^{\mathbf{Mepy}}$ and $\mathbf{1}^{\mathbf{Quino}}$ are complementary in that the initial O_2 binding step to form a superoxo intermediate was observable with $\mathbf{1}^{\mathbf{Mepy}}$, but not with $\mathbf{1}^{\mathbf{Quino}}$. Information regarding the barrier to peroxo O-O bond cleavage can be obtained for peroxo $\mathbf{3}^{\mathbf{Quino}}$, but not for $\mathbf{3}^{\mathbf{Mepy}}$, or $\mathbf{3}^{\mathbf{MeOpy}}$ because the reaction step was too slow, or too fast, respectively. The incorporation of a more electron rich, less sterically encumbered ligand (6-MeO-pyridine) decreases the barrier to O_2 binding and releasee, as well as peroxo O-O bond cleavage, relative to the other derivatives. A strong correlation between the

$Mn^{II/III}$ redox potential and the ligand-dependent activation barrier to O_2 binding and the conversion of superoxo **2** to peroxo **3** is observed. The reaction landscape for the dioxygen chemistry of $\mathbf{1^{Quino}}$ and $\mathbf{1^{MeOpy}}$ is shown to be relatively flat, compared to that of $\mathbf{1^{Mepy}}$, with respect to the barriers separating metastable intermediates. With a more electron-donating, less sterically encumbered 6-MeO-pyridine ligand, a total of four intermediates are observed at low temperatures, including two reactive intermediates following peroxo $\mathbf{3^{MeOpy}}$, *en route* to the final mono oxo-bridged dimer product, $\mathbf{6^{MeOpy}}$. The highly reactive nature of a putative $Mn^{IV}Mn^{IV}$ dimer contrasts with the majority of $Mn^{IV}Mn^{IV}$ dimers, which are stable. The reactivity reflects the electron donating properties of the thiolate ligand. Further investigation on the O_2 activation pathway of $\mathbf{1^{MeOpy}}$, along with hydrogen atom abstraction (HAT) reactivity with $\mathbf{5^{MeOpy}}$, will be discussed I the following chapter, as high-valent metal oxo species are often involved in HAT reactivity.

2.5 References

(1) Askerka, M.; Brudvig, G. W.; Batista, V. S. The O2-Evolving Complex of Photosystem II: Recent Insights from Quantum Mechanics/Molecular Mechanics (QM/MM), Extended X-Ray Absorption Fine Structure (EXAFS), and Femtosecond X-Ray Crystallography Data. *Acc. Chem. Res.* **2017**, *50*, 41–48.

(2) Yano, J.; Yachandra, V. Mn_4Ca Cluster in Photosynthesis: Where and How Water Is Oxidized to Dioxygen. *Chem. Rev.* **2014**, *114*, 4175–4205.

(3) Nocera, D. G. The Artificial Leaf. *Acc. Chem. Res.* **2012**, *45*, 767–776.

(4) Cox, N.; Pantazis, D. A.; Neese, F.; Lubitz, W. Biological Water Oxidation. *Acc. Chem. Res.* **2013**, *46*, 1588–1596.

(5) Park, S.; Shao, Y.; Liu, J.; Wang, Y. Oxygen Electrocatalysts for Water Electrolyzers and Reversible Fuel Cells: Status and Perspective. *Energy Environ. Sci.* **2012**, *5*, 9331–9344.

(6) Coggins, M. K.; Sun, X.; Kwak, Y.; Solomon, E. I.; Rybak-Akimova, E.; Kovacs, J. A. Characterization of Metastable Intermediates Formed in the Reaction between a Mn(II) Complex and Dioxygen, Including a Crystallographic Structure of a Binuclear Mn(III)-Peroxo Species. *J. Am. Chem. Soc.* **2013**, *135*, 5631–5640.

(7) Geiger, R. A.; Wijeratne, G. B.; Day, V. W.; Jackson, T. A. Steric and Electronic Influences on the Structures of Peroxomanganese(III) Complexes Supported by Tetradentate Ligands. *Eur. J. Inorg. Chem.* **2012**, *2012*, 1598–1608.

(8) Chattopadhyay, S.; Geiger, R. A.; Yin, G.; Busch, D. H.; Jackson, T. A. Oxo-and Hydroxomanganese(IV) Adducts: A Comparative Spectroscopic and Computational Study. *Inorg. Chem.* **2010**, *49*, 7530–7535.

(9) Geiger, R. A.; Leto, D. F.; Chattopadhyay, S.; Dorlet, P.; Anxolabéhère-Mallart, E.;

Jackson, T. A. Geometric and Electronic Structures of Peroxomanganese(III) Complexes Supported by Pentadentate Amino-Pyridine and -Imidazole Ligands. *Inorg. Chem.* **2011**, *50*, 10190–10203.

(10) Shook, R. L.; Gunderson, W. A.; Greaves, J.; Ziller, J. W.; Hendrich, M. P.; Borovik, A. S. A Monomeric Mn^{III}-Peroxo Complex Derived Directly from Dioxygen. *J. Am. Chem. Soc.* **2008**, *130*, 8888–8889.

(11) Rees, J. A.; Martin-Diaconescu, V.; Kovacs, J. A.; DeBeer, S. X-Ray Absorption and Emission Study of Dioxygen Activation by a Small-Molecule Manganese Complex. *Inorg. Chem.* **2015**, *54*, 6410–6422.

(12) Bossek, U.; Weyhermiiller, T.; Wieghardt, K.; Nuber, B.; Weiss, J. $[L_2Mn_2(\mu\text{-}O)_2(\mu\text{-}O_2)](ClO_4)_2$: The First Binuclear (μ-Peroxo)Dimanganese(IV) Complex (L = 1,4,7-Trimethyl-1,4,7-Triazacyclononane). A Model for the $S_4 \rightarrow S_0$ Transformation in the Oxygen-Evolving Complex in Photosynthesis. *J. Am. Chem. Soc.* **1990**, *112*, 6387–6388.

(13) Lee, J. Y.; Karlin, K. D. Elaboration of Copper-Oxygen Mediated C-H Activation Chemistry in Consideration of Future Fuel and Feedstock Generation. *Curr. Opin. Chem. Biol.* **2015**, *25*, 184–193.

(14) Lewis, E. A.; Tolman, W. B. Reactivity of Dioxygen-Copper Systems. *Chem. Rev.* **2004**, *104*, 1047–1076.

(15) Tinberg, C. E.; Lippard, S. J. Dioxygen Activation in Soluble Methane Monooxygenase. *Acc. Chem. Res.* **2011**, *44*, 280–288.

(16) Solomon, E. I.; Wong, S. D.; Liu, L. V.; Decker, A.; Chow, M. S. Peroxo and Oxo Intermediates in Mononuclear Nonheme Iron Enzymes and Related Active Sites. *Curr. Opin. Chem. Biol.* **2009**, *13*, 99–113.

(17) Green, M. T. C-H Bond Activation in Heme Proteins: The Role of Thiolate Ligation in Cytochrome P450. *Curr. Opin. Chem. Biol.* **2009**, *13*, 84–88.

(18) Costas, M.; Mehn, M. P.; Jensen, M. P.; Que, L. Dioxygen Activation at Mononuclear Nonheme Iron Active Sites: Enzymes, Models, and Intermediates. *Chem. Rev.* **2004**, *104*, 939–986.

(19) Solomon, E. I.; Heppner, D. E.; Johnston, E. M.; Ginsbach, J. W.; Cirera, J.; Qayyum, M.; Kieber-Emmons, M. T.; Kjaergaard, C. H.; Hadt, R. G.; Tian, L. Copper Active Sites in Biology. *Chem. Rev.* **2014**, *114*, 3659–3853.

(20) Renger, G. Light Induced Oxidative Water Splitting in Photosynthesis: Energetics, Kinetics and Mechanism. *J. Photochem. Photobiol. B Biol.* **2011**, *104*, 35–43.

(21) Retegan, M.; Krewald, V.; Mamedov, F.; Neese, F.; Lubitz, W.; Cox, N.; Pantazis, D. A. A Five-Coordinate Mn(IV) Intermediate in Biological Water Oxidation: Spectroscopic Signature and a Pivot Mechanism for Water Binding. *Chem. Sci.* **2016**, *7*, 72–84.

(22) Cox, N.; Retegan, M.; Neese, F.; Pantazis, D. A.; Boussac, A.; Lubitz, W. Electronic Structure of the Oxygen-Evolving Complex in Photosystem II Prior to O-O Bond Formation. *Science.* **2014**, *345*, 804–808.

(23) Brudvig, G. W. Water Oxidation Chemistry of Photosystem II. *Philos. Trans. R. Soc. B Biol. Sci.* **2008**, *363*, 1211–1219.

(24) Charles Dismukes, G.; Brimblecombe, R.; Felton, G. A. N.; Pryadun, R. S.; Sheats, J. E.; Spiccia, L.; Swiegers, G. F. Development of Bioinspired Mn_4O_4-Cubane Water Oxidation Catalysts: Lessons from Photosynthesis. *Acc. Chem. Res.* **2009**, *42*, 1935–1943.

(25) Betley, T. A.; Wu, Q.; Van Voorhis, T.; Nocera, D. G. Electronic Design Criteria for O-O Bond Formation via Metal-Oxo Complexes. *Inorg. Chem.* **2008**, *47*, 1849–1861.

(26) Armstrong, F. A. Why Did Nature Choose Manganese to Make Oxygen? *Philos. Trans. R. Soc. B Biol. Sci.* **2008**, *363*, 1263–1270.

(27) Shearer, J.; Scarrow, R. C.; Kovacs, J. A. Synthetic Models for the Cysteinate-Ligated Non-Heme Iron Enzyme Superoxide Reductase: Observation and Structural Characterization by XAS of an Fe^{III}-OOH Intermediate. *J. Am. Chem. Soc.* **2002**, *124*, 11709–11717.

(28) Kitagawa, T.; Dey, A.; Lugo-Mas, P.; Benedict, J. B.; Kaminsky, W.; Solomon, E.; Kovacs, J. A. A Functional Model for the Cysteinate-Ligated Non-Heme Iron Enzyme Superoxide Reductase (SOR). *J. Am. Chem. Soc.* **2006**, *128*, 14448–14449.

(29) Nam, E.; Alokolaro, P. E.; Swartz, R. D.; Gleaves, M. C.; Pikul, J.; Kovacs, J. A. Investigation of the Mechanism of Formation of a Thiolate-Ligated Fe(III)-OOH. *Inorg. Chem.* **2011**, *50*, 1592–1602.

(30) Kovacs, J. A.; Brines, L. M. Understanding How the Thiolate Sulfur Contributes to the Function of the Non-Heme Iron Enzyme Superoxide Reductase. *Acc. Chem. Res.* **2007**, *40*, 501–509.

(31) Villar-Acevedo, G.; Nam, E.; Fitch, S.; Benedict, J.; Freudenthal, J.; Kaminsky, W.; Kovacs, J. A. Influence of Thiolate Ligands on Reductive N-O Bond Activation. Probing the O2- Binding Site of a Biomimetic Superoxide Reductase Analogue and Examining the Proton-Dependent Reduction of Nitrite. *J. Am. Chem. Soc.* **2011**, *133*, 1419–1427.

(32) Brown, C. D.; Neidig, M. L.; Neibergall, M. B.; Lipscomb, J. D.; Solomon, E. I. VTVH-MCD and DFT Studies of Thiolate Bonding to $\{FeNO\}^7/\{FeO_2\}^8$ Complexes of Isopenicillin *N* Synthase: Substrate Determination of Oxidase versus Oxygenase Activity in Nonheme Fe Enzymes. *J. Am. Chem. Soc.* **2007**, *129*, 7427–7438.

(33) Blakely, M. N.; Dedushko, M. A.; Poon, P. C. Y.; Villar-Acevedo, G.; Kovacs, J. A. Formation of a Reactive, Alkyl Thiolate-Ligated Fe^{III}-Superoxo Intermediate Derived from Dioxygen. *J. Am. Chem. Soc.* **2019**, *141*, 1867–1870.

(34) Kovacs, J. A. How Iron Activates O2. *Science.* **2003**, *299*, 1024–1025.

(35) Pecoraro, V. L.; Baldwin, M. J.; Gelasco, A. Interaction of Manganese with Dioxygen and Its Reduced Derivatives. *Chem. Rev.* **1994**, *94*, 807–826.

(36) Guo, M.; Lee, Y. M.; Gupta, R.; Seo, M. S.; Ohta, T.; Wang, H. H.; Liu, H. Y.; Dhuri, S. N.; Sarangi, R.; Fukuzumi, S.; Nam, W. Dioxygen Activation and O-O Bond Formation Reactions by Manganese Corroles. *J. Am. Chem. Soc.* **2017**, *139*, 15858–15867.

(37) Crandell, D. W.; Xu, S.; Smith, J. M.; Baik, M. H. Intramolecular Oxyl Radical Coupling Promotes O-O Bond Formation in a Homogeneous Mononuclear Mn-Based Water Oxidation Catalyst: A Computational Mechanistic Investigation. *Inorg. Chem.* **2017**, *56*, 4435–4445.

(38) Liao, R.-Z.; Siegbahn, P. E. M. Quantum Chemical Modeling of Homogeneous Water Oxidation Catalysis. *ChemSusChem* **2017**, *10*, 4236–4263.

(39) Kim, S. H.; Park, H.; Seo, M. S.; Kubo, M.; Ogura, T.; Klajn, J.; Gryko, D. T.; Valentine, J. S.; Nam, W. Reversible O-O Bond Cleavage and Formation between Mn(IV)-Peroxo and Mn(V)-Oxo Corroles. *J. Am. Chem. Soc.* **2010**, *132*, 14030–14032.

(40) Ray, K.; Pfaff, F. F.; Wang, B.; Nam, W. Status of Reactive Non-Heme Metal-Oxygen Intermediates in Chemical and Enzymatic Reactions. *J. Am. Chem. Soc.* **2014**, *136*, 13942–13958.

(41) Jones, R. D.; Summerville, D. A.; Basolo, F. Manganese(II) Porphyrin Oxygen Carriers. Equilibrium Constants for the Reaction of Dioxygen with Para-Substituted Meso-

Tetraphenylporphinatomanganese(II) Complexes. *J. Am. Chem. Soc.* **1978**, *100*, 4416–4424.

(42) Seo, M. S.; Kim, J. Y.; Annaraj, J.; Kim, Y.; Lee, Y. M.; Kim, S. J.; Kim, J.; Nam, W. $[Mn(Tmc)(O_2)]^+$: A Side-on Peroxido Manganese(III) Complex Bearing a Non-Heme Ligand. *Angew. Chemie. Int. Ed.* **2007**, *46*, 377–380.

(43) Vanatta, R. B.; Strouse, C. E.; Hanson, L. K.; Valentine, J. S. [Peroxotetraphenylporphinato] Manganese(III) and [Chlorotetraphenylporphinato]Manganese(II) Anions: Syntheses, Crystal Structures, and Electronic Structures. *J. Am. Chem. Soc.* **1987**, *109*, 1425–1434.

(44) Kitajima, N.; Komatsiizaki, H.; Hikichi, S.; Osawa, M.; Moro-oka, Y. A Monomeric Side-On Peroxo Manganese(III) Complex: $Mn(O_2)(3,5\text{-}IPr_2pzH)(HB(3,5\text{-}iPr_2pz)_3)$. *J. Am. Chem. Soc.* **1994**, *116*, 11596–11597.

(45) Singh, U. P.; Sharma, A. K.; Hikichi, S.; Komatsuzaki, H.; Moro-Oka B, Y.; Akita, M. Hydrogen Bonding Interaction between Imidazolyl N-H Group and Peroxide: Stabilization of Mn(III)-Peroxo Complex $Tp^{IPr2}Mn(\eta^2\text{-}O_2)(im^{Me}H)$ ($im^{Me}H$ = 2-Methylimidazole). *Inorganica Chim. Acta.* **2006**, *359*, 4407–4411.

(46) So, H.; Park, Y. J.; Cho, K. Bin; Lee, Y. M.; Seo, M. S.; Cho, J.; Sarangi, R.; Nam, W. Spectroscopic Characterization and Reactivity Studies of a Mononuclear Nonheme Mn(III)-Hydroperoxo Complex. *J. Am. Chem. Soc.* **2014**, *136*, 12229–12232.

(47) Kovacs, J. A. Tuning the Relative Stability and Reactivity of Manganese Dioxygen and Peroxo Intermediates via Systematic Ligand Modification. *Acc. Chem. Res.* **2015**, *48*, 2744–2753.

(48) Coggins, M. K.; Toledo, S.; Shaffer, E.; Kaminsky, W.; Shearer, J.; Kovacs, J. A.

Characterization and Dioxygen Reactivity of a New Series of Coordinatively Unsaturated Thiolate-Ligated Manganese(II) Complexes. *Inorg. Chem.* **2012**, *51*, 6633–6644.

(49) Stoll, S.; Schweiger, A. EasySpin, a Comprehensive Software Package for Spectral Simulation and Analysis in EPR. *J. Magn. Reson.* **2006**, *178*, 42–55.

(50) Live, D. H.; Chan, S. I. Bulk Susceptibility Corrections in Nuclear Magnetic Resonance Experiments Using Superconducting Solenoids. *Anal. Chem.* **1970**, *42*, 791–792.

(51) Evans, D. F. The Determination of the Paramagnetic Susceptibility of Substances in Solution by Nuclear Magnetic Resonance. *J. Chem. Soc.* **1959**, *81*, 2003–2005.

(52) Coggins, M. K.; Kovacs, J. A. Structural and Spectroscopic Characterization of Metastable Thiolate-Ligated Manganese(III)-Alkylperoxo Species. *J. Am. Chem. Soc.* **2011**, *133*, 12470–12473.

(53) Kryatov, S. V.; Rybak-Akimova, E. V. Kinetics and Mechanisms of Formation and Reactivity of Non-Heme Iron Oxygen Intermediates. *Chem. Rev.* **2005**, *105*, 2175–2226.

(54) Bruker APEX2 (Version 2.1-4), SAINT (Version 7.34A), SADABS (Version 2007), BrukerAXS Inc, Madison, Wisconsin, USA.

(55) Altomare, A.; Cascarano, G.; Giacovazzo, C.; Guagliardi, A. *Completion and Refinement of Crystal Structures with SIR92*. **1993**, *26*, 343-350

(56) Altomare, A.; Burla, M. C.; Camalli, M.; Cascarano, G. L.; Giacovazzo, C.; Guagliardi, A.; Moliterni, A. G. G.; Polidori, G.; Spagna, R. SIR97: A New Tool for Crystal Structure Determination and Refinement. *J. Appl. Cryst* **1999**, *32*, 115–119.

(57) Sheldrick, G M. SHELXL-97: Program for the Refinement of Crystal Structures. **1997**. University of Göttingen, Germany.

(58) Sheldrick, G. M. Crystal Structure Refinement with SHELXL. *Acta. Cryst.* **2015**, *C71*, 3–

8.

(59) Waasmaier, D.; Kirfel, A. New Analytical Scattering-factor Functions for Free Atoms and Ions. *Acta Crystallogr. Sect. A.* **1995**, *51*, 416–431.

(60) Neese, F. The ORCA Program System. *Wiley Interdiscip. Rev. Comput. Mol. Sci.* **2012**, *2*, 73–78.

(61) Grimme, S.; Ehrlich, S.; Goerigk, L. Effect of the Damping Function in Dispersion Corrected Density Functional Theory. *J. Comput. Chem.* **2011**, *32*, 1456–1465.

(62) Barone, V.; Cossi, M. Quantum Calculation of Molecular Energies and Energy Gradients in Solution by a Conductor Solvent Model. *J. Phys. Chem. A* **1998**, *102*, 1995–2001.

(63) Adamo, C.; Barone, V. Toward Reliable Density Functional Methods without Adjustable Parameters: The PBE0 Model. *J. Chem. Phys.* **1999**, *110*, 6158–6170.

(64) Neese, F.; Wennmohs, F.; Hansen, A.; Becker, U. Efficient, Approximate and Parallel Hartree-Fock and Hybrid DFT Calculations. A “chain-of-Spheres” Algorithm for the Hartree-Fock Exchange. *Chem. Phys.* **2008**, *356*, 98–109.

(65) Soda, T.; Kitagawa, Y.; Onishi, T.; Takano, Y.; Shigeta, Y.; Nagao, H.; Yoshioka, Y.; Yamaguchi, K. Ab Initio Computations of Effective Exchange Integrals for H-H, H-He-H and Mn_2O_2 Complex: Comparison of Broken-Symmetry Approaches. *Chem. Phys. Lett.* **2000**, *319*, 223–230.

(66) Hirata, S.; Head-Gordon, M. Time-Dependent Density Functional Theory within the Tamm-Dancoff Approximation. *Chem. Phys. Lett.* **1999**, *314*, 291-299.

(67) Neese, F.; Olbrich, G. Efficient Use of the Resolution of the Identity Approximation in Time-Dependent Density Functional Calculations with Hybrid Density Functionals. *Chem. Phys. Lett.* **2002**, *362*, 170–178.

(68) Pettersen, E. F.; Goddard, T. D.; Huang, C. C.; Couch, G. S.; Greenblatt, D. M.; Meng, E. C.; Ferrin, T. E. UCSF Chimera-A Visualization System for Exploratory Research and Analysis. *J. Comput. Chem.* **2004**, *25*, 1605–1612.

(69) Coggins, M. K.; Martin-Diaconescu, V.; Debeer, S.; Kovacs, J. A. Correlation between Structural, Spectroscopic, and Reactivity Properties within a Series of Structurally Analogous Metastable Manganese(III)-Alkylperoxo Complexes. *J. Am. Chem. Soc.* **2013**, *135*, 4260–4272.

(70) Rybak-Akimova, E. V.; Otto, W.; Deardorf, P.; Roesner, R.; Busch, D. H. Kinetics and Equilibria of Dioxygen Binding to a Vacant Site in Cobalt(II) Complexes with Pentadentate Ligands. *Inorg. Chem.* **1997**, *36*, 2746–2753.

(71) Antonini, E.; Brunori, M. *Hemoglobin and Myoglobin in Their Reactions with Ligands*, North-Holland, Amsterdam. **1971**, Vol. 21.

(72) Liu, L. V.; Hong, S.; Cho, J.; Nam, W.; Solomon, E. I. Comparison of High-Spin and Low-Spin Nonheme Fe^{III}-OOH Complexes in O-O Bond Homolysis and H-Atom Abstraction Reactivities. *J. Am. Chem. Soc.* **2013**, *135*, 3286–3299.

(73) Eliel, E. L.; Wilen, S. H.; Mander, L. N. *Stereochemistry of Organic Compounds*; John Wiley & Sons, Ltd, 1994.

(74) Lassalle-kaiser, B.; Iii, T. T. B.; Krewald, V.; Kern, J.; Beckwith, M. A.; Delgado-jaime, M. U.; Schroeder, H.; Alonso-mori, R.; Nordlund, D.; Weng, T.; Sokaras, D.; Neese, F.; Bergmann, U.; Yachandra, V. K.; Debeer, S.; Pecoraro, V. L.; Yano, J. Experimental and Computational X-Ray Emission Spectroscopy as a Direct Probe of Protonation States in Oxo-Bridged Mn. **2013**.

(75) Larson, E. J.; Pecoraro, V. L. The Peroxide-Dependent μ_2-O Bond Formation of

[Mn^{IV}SALPN(O)]$_2$. *J. Am. Chem. Soc.* **1991**, *113*, 3810–3818.

(76) Tyler Caudle, M.; Kamp, J. W.; Kirk, M. L.; Rasmussen, P. G.; Pecoraro, V. L. The First Binuclear Mn(IV) Complex Containing a Bridging Imidazolate Ligand Exhibits Unique EPR Spectral Features. *J. Am. Chem. Soc.* **1997**, *119*, 9297–9298.

(77) Cotruvo, J. A.; Stich, T. A.; Britt, R. D.; Stubbe, J. Mechanism of Assembly of the Dimanganese-Tyrosyl Radical Cofactor of Class Ib Ribonucleotide Reductase: Enzymatic Generation of Superoxide Is Required for Tyrosine Oxidation via a Mn(III)Mn(IV) Intermediate. *J. Am. Chem. Soc.* **2013**, *135*, 4027–4039.

(78) Triller, M. U.; Hsieh, W. Y.; Pecoraro, V. L.; Rompel, A.; Krebs, B. Preparation of Highly Efficient Manganese Catalase Mimics. *Inorg. Chem.* **2002**, *41*, 5544–5554.

(79) Glerup, J.; Goodson, P. A.; Hazell, A.; Hazell, R.; Hodgson, D. J.; McKenzie, C. J.; Michelsen, K.; Rychlewska, U.; Toftlund, H. Synthesis and Characterization of Bis(μ-Oxo)Dimanganese(III,III), -(III,IV), and -(IV,IV) Complexes with Ligands Related to N,N′-Bis(2-Pyridylmethyl)-1,2-Ethanediamine (Bispicen). *Inorg. Chem.* **1994**, *33*, 4105–4111.

(80) Gupta, R.; Taguchi, T.; Lassalle-Kaiser, B.; Bominaar, E. L.; Yano, J.; Hendrich, M. P.; Borovik, A. S. High-Spin Mn-Oxo Complexes and Their Relevance to the Oxygen-Evolving Complex within Photosystem II. *Proc. Natl. Acad. Sci. U. S. A.* **2015**, *112*, 5319–5324.

(81) Parsell, T. H.; Behan, R. K.; Green, M. T.; Hendrich, M. P.; Borovik, A. S. Preparation and Properties of a Monomeric Mn^{IV}-Oxo Complex. *J. Am. Chem. Soc.* **2006**, *128*, 8728–8729.

(82) Ivancich, A.; Zimmermann, J. L.; Barynin, V. V. Pulsed EPR Studies of the Binuclear

Mn(III)Mn(IV) Center in Catalase from Thermus Thermophilus. *Biochemistry* **1995**, *34*, 6628–6639.

(83) Randall, D. W.; Gelasco, A.; Caudle, M. T.; Pecoraro, V. L.; Britt, R. D. ESE-ENDOR and ESEEM Characterization of Water and Methanol Ligation to a Dinuclear Mn(III)Mn(IV) Complex. *J. Am. Chem. Soc.* **1997**, *119*, 4481–4491.

Chapter 3. Hydrogen Atom Transfer Reactivity with Metastable Thiolate-ligated $Mn^{III}Mn^{IV}$ Intermediate Derived from Dioxygen Activation

Portions of this chapter have been republished or adapted with permission of the Journal of the American Chemical Society from "*How Metal Ion Lewis Acidity and Steric Properties Influence the Barrier to Dioxygen Binding, Peroxo O-O Bond Cleavage, and Reactivity*", Poon, Penny Chaau Yan; Dedushko, Maksym A.; Sun, Xianru; Yang, Guang; Toledo, Santiago; Hayes, Ellen C.; Johansen, Audra; Piquette, Marc C.; Rees, Julian A.; Stoll, Stefan; Rybak-Akimova, Elena; Kovacs, Julie A. *J. Am. Chem. Soc.* **2019**. *141*, 15046-15057.; Copyright 2019 American Chemical Society.

3.1 Introduction

High-valent manganese-oxo species have been proposed to be key intermediates in vital biological processes, such as water oxidation by the oxygen evolving complex (OEC) of photosystem II (PSII) [1–6], and the production of deoxyribonucleotides by ribonucleotide reductases (RNR)[7–9]. In these processes, hydrogen atom transfer (or, transfer of a proton and an electron) takes place to relay electrons and protons through the enzyme. The redox relay between D1-His190 and tyrosine (Y_z) in PSII, which is believed to contribute to the high efficiency of water oxidation by the enzyme, has been shown to go through proton-coupled electron transfer (PCET).[10–12] On the other hand, hydrogen atom transfer (HAT) occurs in ribonucleotide reductase (RNR) as the enzyme utilizes a bimetallic active site to generate a tyrosyl radical (Tyr-$O^{\bullet}$) essential for the reduction of ribonucleotides to deoxyribonucleotides, the building blocks of

DNA. In the Mn-dependent class Ib RNR, superoxide ($O_2^{\bullet-}$) oxidizes the $Mn^{II}Mn^{II}$ active site to $Mn^{III}Mn^{IV}$, which is then reduced to $Mn^{III}Mn^{III}$ by oxidizing a tyrosine residue (Tyr-OH) to a tyrosyl radical (Tyr-O$^{\bullet}$) via HAT.[7,8,13,14] The $Mn^{III}Mn^{IV}$ intermediate, which is proposed to contain a bridging μ-oxo and a bridging μ-hydroxo, has been observed and characterized with stopped-flow UV-vis electronic absorption and EPR spectroscopy.[8,15]

In the previous chapter, dioxygen activation by the MeO-derivative Mn^{II}-thiolate complex $\mathbf{1}^{\mathbf{MeOpy}}$ led to a series of metastable Mn-oxo intermediates, including a $Mn^{III}Mn^{III}$ μ-peroxo ($\mathbf{3}^{\mathbf{MeOpy}}$), $Mn^{IV}Mn^{IV}$ bis-μ-oxo ($\mathbf{4}^{\mathbf{MeOpy}}$), and $Mn^{III}Mn^{IV}$(μ-oxo)(μ-hydroxo) ($\mathbf{5}^{\mathbf{MeOpy}}$). The metastable $Mn^{III}Mn^{IV}$ $\mathbf{5}^{\mathbf{MeOpy}}$, stable at -73 °C within a bench-top UV-vis setup, resembles the $Mn^{III}Mn^{IV}$ intermediate with bridging μ-oxo and μ-hydroxo in class Ib RNR mentioned above. While the O_2 activation mechanism was determined via stopped-flow kinetics and EPR spectroscopy, the extended reactivities of Mn^{II} $\mathbf{1}^{\mathbf{MeOpy}}$ and $Mn^{III}Mn^{IV}$ $\mathbf{5}^{\mathbf{MeOpy}}$ with common HAT substrates have yet to be investigated. In this chapter, hydrogen atom transfer reactivities will be explored with the Mn^{II} species $\mathbf{1}^{\mathbf{MeOpy}}$ and the metastable $Mn^{III}Mn^{IV}$ $\mathbf{5}^{\mathbf{MeOpy}}$.

3.2 Experimental

General Methods. All manipulations were performed using Schlenk techniques or under an N_2 atmosphere in a glovebox. Reagents and solvents were purchased from commercial vendors, were of highest available purity, and were used without further purification unless otherwise noted. Methylene chloride (DCM), tetrahydrofuran (THF), diethyl ether (Et_2O), and acetonitrile (MeCN) were rigorously degassed, and purified using solvent purification columns housed in a custom stainless-steel cabinet, dispensed via a stainless steel Schlenk-line (GlassContour). Methanol (MeOH) was dried over magnesium methoxide and distilled prior to use. ^{1}H NMR spectra were recorded on a Bruker DPX-200 or AV 300 FT NMR spectrometer at ambient temperature and were referenced to residual solvent. Chemical shifts are listed in parts per million (ppm) and coupling constants (*J*) in Hz. EAS spectra were recorded on a Varian Cary 50 or Varian Cary 60 spectrophotometer equipped with a fiber optic cable connected to an ATR "dip" probe (C-technologies). A custom-built two-neck solution sample holder equipped with a threaded glass connector was sized specifically to fit the "dip" probe. Electrospray-ionization mass spectrometry (ESI-MS) data were obtained on a Bruker Esquire Liquid Chromatograph-Ion Trap mass spectrometer. Gas chromatography-mass spectrometry (GC-MS) data were obtained on an Agilent 5973 Gas Chromatograph/Mass spectrometer. Organic ligands, 1-(tert-butyloxycarbonyl)ethyldiamine (NNBoc) and 3-methyl-3-metcapto-2-butanone were synthesized according to published procedures.[16,17] Synthesis of hydrogen atom donor TEMPO-H was synthesized according to a published procedure[18] and D_2O was used in place of H_2O to synthesize the deuterium version TEMPO-D. Synthesis of 6-MeO-DPEN ligand and Mn^{II} complex $\mathbf{1^{MeOpy}}$, as well as generation of putative $Mn^{III}Mn^{IV}$ ($\mathbf{5^{MeOpy}}$) were reported in Chapter 2.

3.2.1. Room Temperature Reaction between 1^{MeOpy} and O_2 in the absence of hydrogen atom donors. A solution of $\mathbf{1}^{MeOpy}$ (3.75 x 10^{-6} mmol) was dissolved in 5 mL DCM, placed in an argon purged dip probe cell at ambient temperature. Dry O_2 addition to the solution resulted in the formation of mono oxo-bridged $\mathbf{6}^{MeOpy}$ (λ_{max} = 575 nm) in 57.4 ± 1.0% yield. The reactions were monitored by EAS.

3.2.2. Room Temperature Reaction between 1^{MeOpy} and O_2 in the presence of 1,4-Cyclohexadiene (CHD). A solution of $\mathbf{1}^{MeOpy}$ (3.75 x 10^{-6} mmol) was dissolved in 5 mL DCM, placed in an argon purged dip probe cell at ambient temperature. A diluted solution of 100 equiv. CHD (100 μL, 3.75 M) was added to $\mathbf{1}^{MeOpy}$. The mixture was then introduced to O_2, resulting in the formation of mono oxo-bridged $\mathbf{6}^{MeOpy}$ (λ_{max} = 575 nm) in 73.0 ± 0.5% yield. The reactions were monitored by EAS.

3.2.3. Room Temperature Reaction between 1^{MeOpy} and O_2 in the presence of TEMPO-H. A solution of $\mathbf{1}^{MeOpy}$ (3.75 x 10^{-6} mmol) was dissolved in 5 mL DCM, placed in an argon purged dip probe cell at ambient temperature. A DCM solution of 100 equiv. TEMPO-H (100 μL, 3.75 M) was added to $\mathbf{1}^{MeOpy}$. The mixture was then introduced to O_2, resulting in the formation of mono oxo-bridged $\mathbf{6}^{MeOpy}$ (λ_{max} = 575 nm) in 98.0 ± 1.5% yield. The reactions were monitored by EAS.

3.2.4. Low Temperature Reaction between Putative $Mn^{III}Mn^{IV}$ ($\mathbf{5}^{MeOpy}$) and 1,4-Cyclohexadiene (CHD). A solution of $\mathbf{1}^{MeOpy}$ (3.75 x 10^{-6} mmol) was dissolved in 5 mL DCM, placed in an argon purged dip probe cell and brought to -73 °C using acetone/dry ice bath. After 10 minutes, the solution was opened to air, resulting in the formation of an EPR-active (in ⊥-mode) red species, putative $Mn^{III}Mn^{IV}$ ($\mathbf{5}^{MeOpy}$), with λ_{max} = 505 nm. Addition of 100 equiv. CHD (100 μL, 3.75 x 10^{-4} mmol) to the resulting solution caused the 505 nm species to slowly

convert to mono oxo-bridged 6^{MeOpy}. The reaction mixture was then filtered through Celite. GC-MS analysis of the reaction mixture confirmed the formation of 0.5(1) equivalents of benzene per equivalent of Mn.

3.2.5. Low Temperature Reaction between $\mathbf{1^{MeOpy}}$ and 1,4-Cyclohexadiene (CHD). A solution of $\mathbf{1^{MeOpy}}$ (3.75×10^{-6} mmol) was dissolved in 5 mL DCM, placed in an argon purged dip probe cell and 100 equiv. of CHD (100 μL, 3.75×10^{-4} mmol) was added. The reaction mixture was brought to -73 °C using acetone/dry ice bath. After 10 minutes, the solution was opened to air. Formation of the mono oxo-bridged 6^{MeOpy} was observed by EAS with λ_{max} = 575 nm. The reaction mixture was then filtered through Celite. GC-MS analysis of the reaction mixture confirmed the formation of 1.0(1) equivalents of benzene per equivalent of Mn.

3.2.6. Low Temperature Kinetics for the Reaction between $\mathbf{Mn^{III}Mn^{IV}}$ ($\mathbf{5^{MeOpy}}$) and TEMPO-H(D). A solution of $\mathbf{1^{MeOpy}}$ (3.75×10^{-6} mmol) was dissolved in 5 mL DCM, placed in an argon purged dip probe cell and cooled to -73 °C. After 10 minutes, the solution was opened to air resulting in the formation of metastable $\mathbf{5^{MeOpy}}$ (505 nm). To this solution, 100 equiv. of TEMPO-H(D) (0.060 g, 3.75×10^{-4} mmol) dissolved in 100 μL DCM was added. The 505 nm species was observed to rapidly convert to $\mathbf{6^{MeOpy}}$ (λ_{max} = 575 nm). Data was collected at regular time intervals, and pseudo first-order kinetics plots were used to obtain k_{obs} values. By varying the concentration of TEMPO-H(D), second order rate constants were obtained from the plot of k_{obs} vs [TEMPO-H(D)].

3.2.7. Low Temperature Kinetics for the Reaction between $\mathbf{Mn^{III}Mn^{IV}}$ ($\mathbf{5^{MeOpy}}$) and Hydrazine. A solution of $\mathbf{1^{MeOpy}}$ (3.75×10^{-6} mmol) was dissolved in 5 mL DCM, placed in an argon purged dip probe cell and cooled to -73 °C. After 10 minutes, dry O_2 gas was introduced to the solution, resulting in the formation of metastable $\mathbf{5^{MeOpy}}$ (λ_{max} = 505 nm). To this solution, a

100 μL solution of 10 equiv. hydrazine (3.75 x 10^{-5} mmol) in DCM was added. The 505 nm species was observed to convert to **6**$^{\mathbf{MeOpy}}$ over 66 minutes. The reactions were monitored by EAS.

3.2.8. Low Temperature Kinetics for the Reaction between $Mn^{III}Mn^{IV}$ (5^{MeOpy}) and Ammonium Hexafluorophosphate. A solution of **1**$^{\mathbf{MeOpy}}$ (3.75 x 10^{-6} mmol) was dissolved in 5 mL DCM, placed in an argon purged dip probe cell and cooled to -73 °C. After 10 minutes, dry O_2 gas was introduced to the solution, resulting in the formation of metastable **5**$^{\mathbf{MeOpy}}$ (λ_{max} = 505 nm). To this solution, a 250 μL solution of 10 equiv. ammonium hexafluorophosphate (6.1 mg, 3.75 x 10^{-5} mmol) in DCM was added. The 505 nm species was observed to convert to **6**$^{\mathbf{MeOpy}}$ over 30+ hours. The reactions were monitored by EAS.

3.2.9. Low Temperature Kinetics for the Reaction between $Mn^{III}Mn^{IV}$ (5^{MeOpy}) and Triethylamine. A solution of **1**$^{\mathbf{MeOpy}}$ (3.75 x 10^{-6} mmol) was dissolved in 5 mL DCM, placed in an argon purged dip probe cell and cooled to -73 °C. After 10 minutes, dry O_2 gas was introduced to the solution, resulting in the formation of metastable **5**$^{\mathbf{MeOpy}}$ (λ_{max} = 505 nm). To this solution, a 100 μL solution of 5 equiv. triethylamine (1.88 x 10^{-5} mmol) in DCM was added. The 505 nm species was observed to convert to **6**$^{\mathbf{MeOpy}}$ over 6.5 hours. The reactions were monitored by EAS.

3.2.10. Low Temperature Kinetics for the Reaction between $Mn^{III}Mn^{IV}$ (5^{MeOpy}) and Tetrabutylammonium Hydroxide. A solution of **1**$^{\mathbf{MeOpy}}$ (3.75 x 10^{-6} mmol) was dissolved in 5 mL DCM, placed in an argon purged dip probe cell and cooled to -73 °C. After 10 minutes, dry O_2 gas was introduced to the solution, resulting in the formation of metastable **5**$^{\mathbf{MeOpy}}$ (λ_{max} = 505 nm). To this solution, a 100 μL solution of 5 equiv. tetrabutylammonium hydroxide (1.88 x 10^{-5}

mmol) in DCM was added. The new species at 515 nm was observed to grow in over 5.42 hours. The reactions were monitored by EAS.

3.3 Results and Discussion

3.3.1 *Reactivity of Mn^{II} 1^{MeOpy} with O_2 in the Presence of Sacrificial Hydrogen Atom Donor at Room Temperature*

In Chapter 2, dioxygen reactivity with Mn^{II} thiolate, $[Mn^{II}(L^{MeOpy})]^+$ (**1**$^{\mathbf{MeOpy}}$, L^{MeOpy}= (6-MeO-DPEN)$N_4{}^{Me2}S^-$), was investigated and four high valent Mn oxo intermediates were observed, including a $Mn^{III}Mn^{IV}$ intermediate, **5**$^{\mathbf{MeOpy}}$ (λ_{max} = 505 nm), *en route* to the thermodynamic product $\{[Mn^{III}(L^{MeOpy})]_2(\mu\text{–}O)\}^{2+}$ (**6**$^{\mathbf{MeOpy}}$). The dioxygen activation pathway from **1**$^{\mathbf{MeOpy}}$ to **6**$^{\mathbf{MeOpy}}$ at ambient temperature was further explored herein for possible hydrogen-atom abstraction reactivities. As shown previously, Mn^{II} complex **1**$^{\mathbf{MeOpy}}$ reacts with O_2 to form mono oxo-bridged **6**$^{\mathbf{MeOpy}}$ at ambient temperature (Scheme 3.1). In the absence of sacrificial H-atom donor, the yield of **6**$^{\mathbf{MeOpy}}$ generated at room temperature by reacting **1**$^{\mathbf{MeOpy}}$ with O_2 was considerably low (57.4 ± 1.0%) when the reaction was carried out in DCM (BDFE = 98 kcal/mol, Scheme 3.1, Figure 3.1-3.2)[19]. Conversely, in DCM, the structural analogues $\{[Mn^{III}(L^{Mepy})]_2(\mu\text{–}O)\}^{2+}$ (**6**$^{\mathbf{Mepy}}$) and $\{[Mn^{III}(L^{Quino})]_2(\mu\text{–}O)\}^{2+}$ (**6**$^{\mathbf{Quino}}$) were found to be at near quantitative yield.[17,20] The yield of **6**$^{\mathbf{MeOpy}}$ was found to significantly increase to 73.0 ± 0.5% and 98.0 ± 1.5% yield when excess sacrificial H-atom donor, 1,4-cyclohexadiene (CHD, 100 equiv., BDFE = 76.0 kcal/mol)[19] or 2,2,6,6-tetramethyl-1-hydroxypiperidine (TEMPO-H, 20 equiv., BDFE = 70.6 kcal/mol)[19] were added, respectively. (Scheme 3.1, Figure 3.2) In the absence of a sacrificial H-atom donor (with a BDFE lower than solvent) , the ligand manifold of the Mn

complex could potentially serve as the sacrificial H-atom donor source *en route* to the O_2 activation product **6**$^{\mathbf{MeOpy}}$, causing the low yield of **6**$^{\mathbf{MeOpy}}$.

Scheme 3.1. Reaction scheme for dioxygen activation reactivity of $[Mn^{II}(L^{MeOpy})]^{+}$ (**1**$^{\mathbf{MeOpy}}$) in the absence or presence of additional hydrogen-atom source at ambient temperature *en route* to $\{[Mn^{III}(L^{MeOpy})]_2(\mu\text{–}O)\}^{2+}$ (**6**$^{\mathbf{MeOpy}}$).

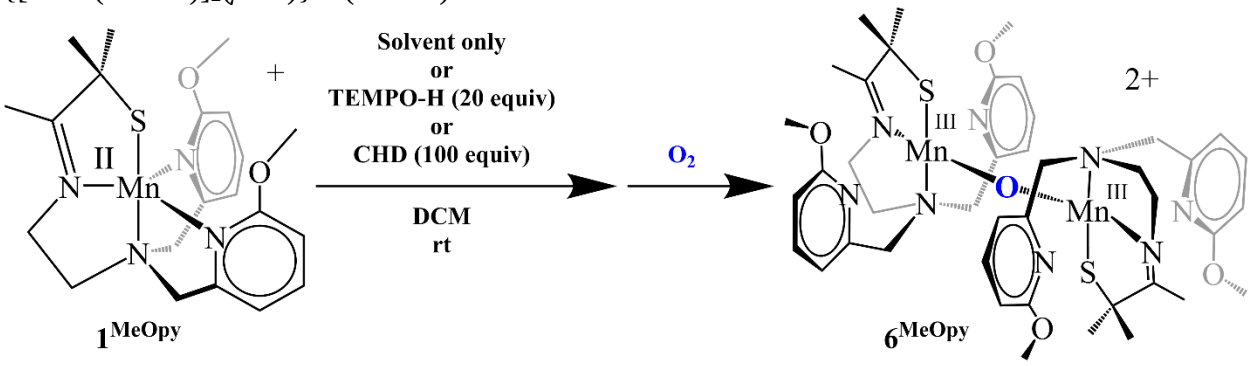

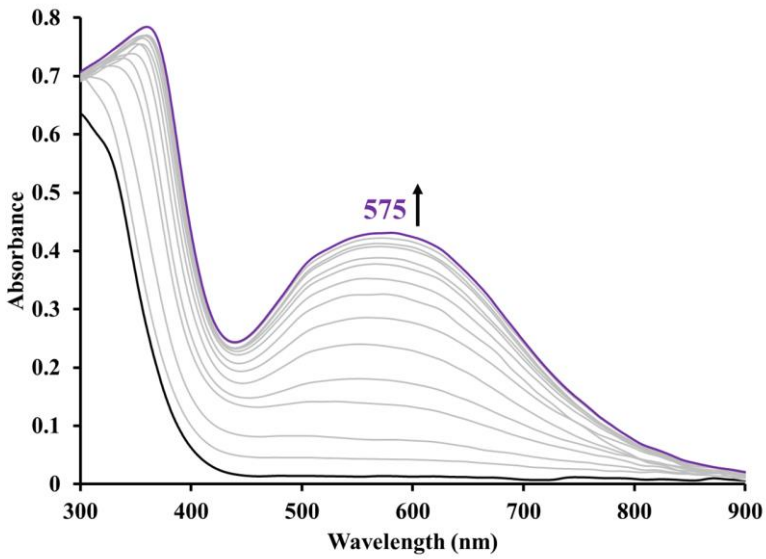

Figure 3.1. EAS spectrum monitoring the growth of **6**$^{\mathbf{MeOpy}}$ (purple) generated by reacting **1**$^{\mathbf{MeOpy}}$ (black) with O_2 at room temperature. Scans recorded at 2.77 minutes intervals. ([**1**$^{\mathbf{MeOpy}}$] = 0.75 mM).

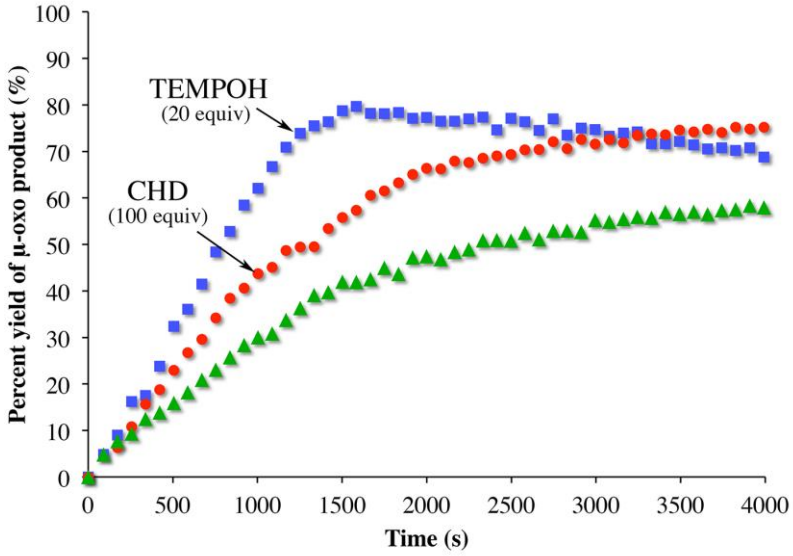

Figure 3.2. Comparison of the rates of formation and yield of $\mathbf{6}^{\mathbf{MeOpy}}$ in DCM, both in the absence (green triangles) and presence of sacrificial H atom donors, 1,4-cyclohexadiene (red circles) or TEMPOH (blue squares).

Reactivities with hydrogen atom donors were further investigated with kinetic experiments. These experiments were performed at ambient temperature under pseudo first order conditions with 100 equiv. TEMPO-H (BDE(O-H) = 70.6 kcal/mol)[19] or CHD (BDE(C-H) = 76.0 kcal/mol)[19]. The rate expressions are provided in equations 3.1 and 3.2 below based on the previously established O_2 activation scheme in Chapter 2 (Scheme 2.5). The observed rate constants (k_{obs}^{MeOpy}) for the formation of $\mathbf{6}^{\mathbf{MeOpy}}$ either in the absence or in the presence of sacrificial hydrogen atom donor (TEMPO-H and CHD) were obtained by monitoring the growth of mono oxo-bridged $\mathbf{6}^{\mathbf{MeOpy}}$ at 575 nm. Rate constants were obtained from first-order plots versus time and are reported in Table 3.1.

$$\text{Rate} = k_1^{MeOpy}[Mn^{II}(\mathbf{1}^{\mathbf{MeOpy}})]^2[O_2][H^{\bullet}] \quad (3.1)$$

$$\text{Rate}_1 = k_{obs}^{MeOpy}[H^{\bullet}], \text{ where } k_{obs}^{MeOpy} = k_1^{MeOpy}[Mn^{II}(\mathbf{1}^{\mathbf{MeOpy}})]^2[O_2] \quad (3.2)$$

The rate of formation of $\mathbf{6^{MeOpy}}$ was shown to increase slightly in the presence of 100 equiv. CHD (k_{obs}^{MeOpy} = 8.70(5) x 10^{-4} s^{-1}), while increasing an order of magnitude with TEMPO-H (k_{obs}^{MeOpy} = 3.30(6) x 10^{-3} s^{-1}). This increase in rate would be consistent with H atom abstraction taking place *en route* to the formation of mono oxo-bridged $\mathbf{6^{MeOpy}}$. The quantification of benzene in the CHD reaction mixture was confirmed by GC-MS, suggesting a total of two equivalents of H atoms were consumed per Mn ion. Further HAT investigations will be discussed in the following section.

Table 3.1. Observed *pseudo* first order rate constants for $\mathbf{6^{MeOpy}}$ formation as a function of sacrificial hydrogen atom concentration. Data obtained at ambient temperature. [Mn^{II}] = 0.75 mM. Concentration of the sacrificial hydrogen atom donor (after mixing) is reported below.

Hydrogen atom source	**[H•] (mM)**	$\boldsymbol{k_{obs}^{MeOpy}}$ **(s^{-1})**
Solvent only	N/A	7.13(3) x 10^{-4}
CHD	75	8.70(5) x 10^{-4}
TEMPO-H	75	3.30(6) x 10^{-3}

Complex $\mathbf{6^{MeOpy}}$, monitored by EAS, was found to be stable over an extended period of time in the absence of H-atom donor source or in the presence of CHD, even when exposed to O_2. However, $\mathbf{6^{MeOpy}}$ was found to decompose in the presence of TEMPO• (λ_{max} = 454 nm), which is the hydrogen atom abstraction radical product of TEMPO-H, as shown in Figure 3.3. Attempts to identify the TEMPO-H reaction mixture composition by mass spectrometry were unsuccessful.

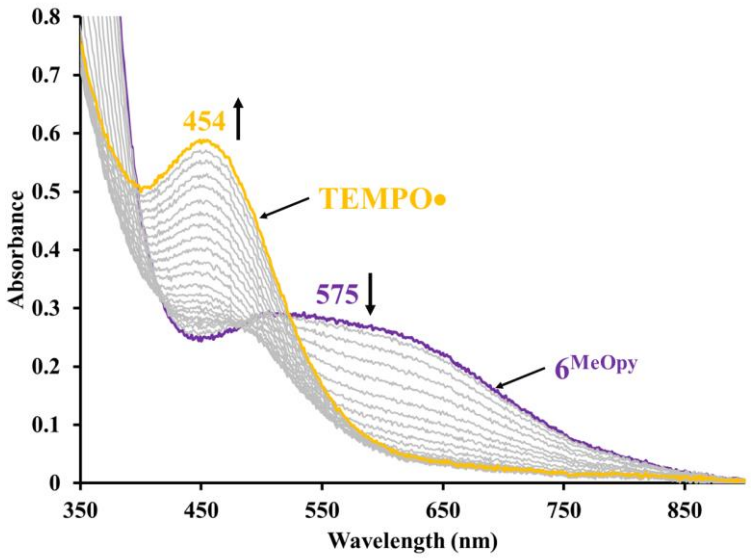

Figure 3.3. EAS spectrum monitoring the decay of $\mathbf{6}^{\mathbf{MeOpy}}$ (purple) driven by TEMPO$^{\bullet}$ (yellow) in the presence of air at room temperature. Scans recorded at 7 minutes intervals. ([$\mathbf{6}^{\mathbf{MeOpy}}$] = 0.375 mM).

3.3.2 *Hydrogen Atom Abstraction Reactivity Study with CHD*

To investigate the placement of the hydrogen atom abstraction in the mechanism, either prior to, or after the formation of the putative $Mn^{III}Mn^{IV}$ ($\mathbf{5}^{\mathbf{MeOpy}}$), reactions between $\mathbf{1}^{\mathbf{MeOpy}}$ and O_2 were carried out in the presence of 100 equiv. 1,4-cyclohexadiene (CHD) at -73 °C, a temperature at which $\mathbf{5}^{\mathbf{MeOpy}}$ can be consistently generated. Quantitative measurement of the yield of benzene, the HAT product of CHD, was measured using GC-MS. The measurement of benzene allowed for the determination of equivalents of H atom transferred in the process. To verify that two equiv. H atom abstraction by $\mathbf{1}^{\mathbf{MeOpy}}$ at ambient temperature (*vida supra*) would also occur at -73 °C, the reaction between $\mathbf{1}^{\mathbf{MeOpy}}$ and O_2 was carried out in the presence of 100 equiv. CHD at the lower temperature. The formation of putative $Mn^{III}Mn^{IV}$ 5^{MeOpy} (λ_{max} = 505 nm) was observed, followed by a 20-hour conversion to mono-oxo bridged $\mathbf{6}^{\mathbf{MeOpy}}$. One equiv. of

benzene was detected in the final reaction mixture, indicating two H atoms abstraction occurred throughout the dioxygen activation by $\mathbf{1}^{\mathbf{MeOpy}}$.

The EPR-active $Mn^{III}Mn^{IV}$ species provides a better handle to determine whether the two H atoms were abstracted prior to, or after the formation of the metastable $\mathbf{5}^{\mathbf{MeOpy}}$,as the complex can be steadily generated by reacting $\mathbf{1}^{\mathbf{MeOpy}}$ with O_2 at -73 °C. Reactions between $\mathbf{1}^{\mathbf{MeOpy}}$ and O_2 were carried out in the presence of 100 equiv. CHD at -73 °C, monitored by EAS. The solution was filtered through silica-packed pipet immediately upon the formation of the red $\mathbf{5}^{\mathbf{MeOpy}}$ and 0.5 equiv. of benzene was detected by GC-MS (Figure 3.4). This indicates one H atom was abstracted along the conversion of Mn^{II} $\mathbf{1}^{\mathbf{MeOpy}}$ to $Mn^{III}Mn^{IV}$ intermediate $\mathbf{5}^{\mathbf{MeOpy}}$.

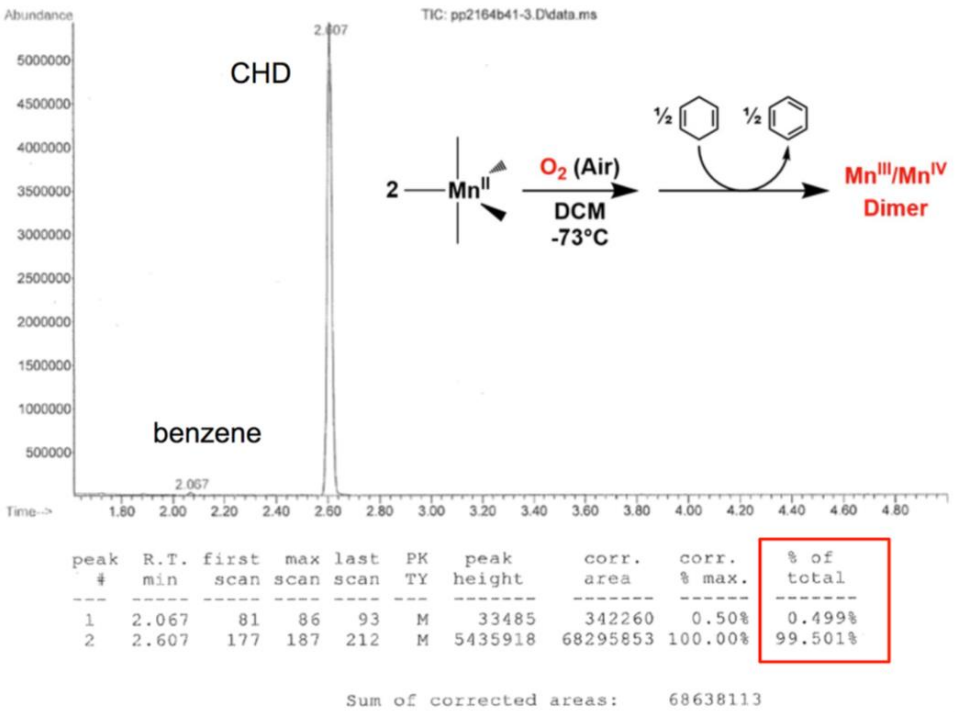

Figure 3.4. GC-MS chromatogram showing that 0.5 equivalent of benzene formed during the formation of the red intermediate $Mn^{III}Mn^{IV}$ $\mathbf{5}^{\mathbf{MeOpy}}$ in the reaction between $\mathbf{1}^{\mathbf{MeOpy}}$ and O_2 in the presence of 100 equivalent of 1,4-cyclohexadiene (CHD). Control experiments show that benzene was not present in the CHD starting material.

To confirm another equiv. of H atom transfer takes place following the formation of the red intermediate $\mathbf{5}^{\mathbf{MeOpy}}$, the experiment was changed with 100 equiv. addition of CHD after

$\mathbf{5}^{\mathbf{MeOpy}}$ was generated. The solution was quenched following the formation of mono oxo-bridged $\mathbf{6}^{\mathbf{MeOpy}}$ and GC-MS data indicates 0.5 equiv. of benzene was formed . (Figure 3.5) This supports another H atom transfer has taken place during the conversion from $Mn^{III}Mn^{IV}$ $\mathbf{5}^{\mathbf{MeOpy}}$ to the thermodynamic product $\mathbf{6}^{\mathbf{MeOpy}}$. With the H atom abstraction reactivity completed, we were able to revise the O_2 activation scheme for $\mathbf{1}^{\mathbf{MeOpy}}$ where one HAT occurs prior to the formation of the red intermediate $\mathbf{5}^{\mathbf{MeOpy}}$ and one after. (Scheme 3.2)

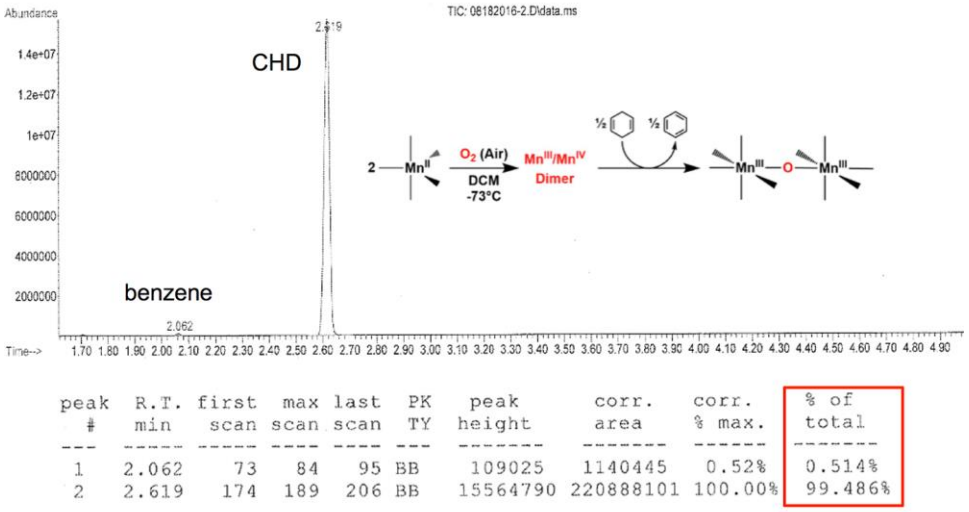

peak #	R.T. min	first scan	max scan	last scan	PK TY	peak height	corr. area	corr. % max.	% of total
1	2.062	73	84	95	BB	109025	1140445	0.52%	0.514%
2	2.619	174	189	206	BB	15564790	220888101	100.00%	99.486%

Figure 3.5. GC-MS chromatogram showing that 0.5 equivalent of benzene formed during the conversion of the red intermediate $Mn^{III}Mn^{IV}$ $\mathbf{5}^{\mathbf{MeOpy}}$ to mono-oxo bridged $\mathbf{6}^{\mathbf{MeOpy}}$ when the reaction is performed in the presence of 100 equivalent of 1,4-cyclohexadiene (CHD). Control experiments show that benzene was not present in the CHD starting material.

Scheme 3.2. Revised scheme of dioxygen reactivity of 6-MeO-pyridine $\mathbf{1}^{\mathbf{MeOpy}}$, showing rate constant, and observed intermediates.

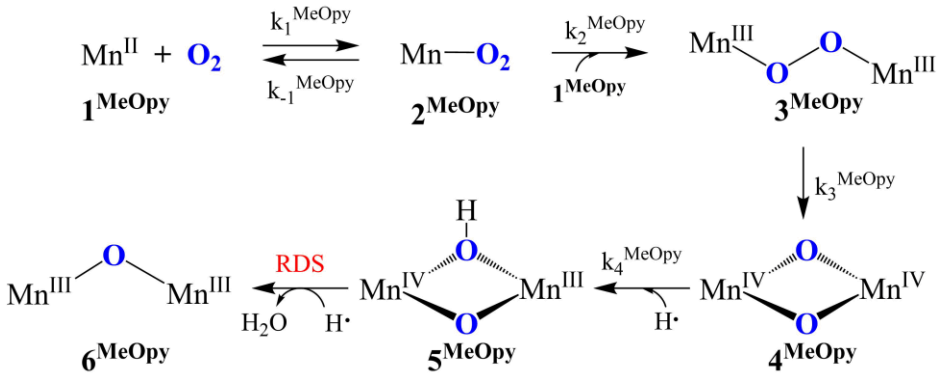

3.3.3 *Kinetic Isotope Study of HAT by 5^{MeOpy} with TEMPO-H*

In order to determine the kinetic isotope effect of the second HAT step, kinetic studies of $\mathbf{5^{MeOpy}}$ with 2,2,6,6-tetramethyl-1-hydroxypiperidine (TEMPO-H) were performed. Since the conversion of $Mn^{III}Mn^{IV}$ $\mathbf{5^{MeOpy}}$ to mono oxo-bridged Mn^{III}_2 $\mathbf{6^{MeOpy}}$ is much slower with 100 equiv. of CHD (half-life of $\mathbf{5^{MeOpy}}$ = 154.5 minutes) comparing to 40 equiv. of TEMPO-H (half-life of $\mathbf{5^{MeOpy}}$ = 1.18 minutes, Figure 3.6) at -73 °C, the latter sacrificial H atom and its deuterium version TEMPO-D (half-life of $\mathbf{5^{MeOpy}}$ in the presence of 40 equiv. TEMPO-D = 4.66 minutes) were used instead.

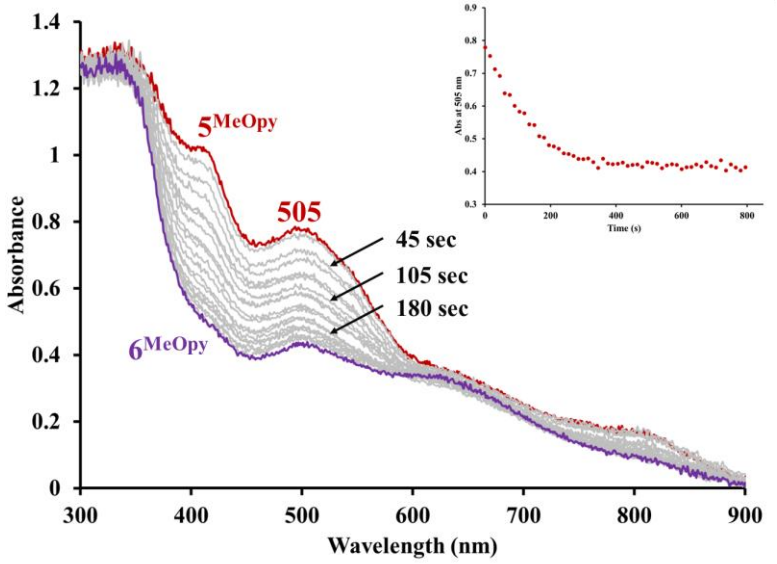

Figure 3.6. Time-resolved EAS spectra for conversion of $Mn^{III}Mn^{IV}$ $\mathbf{5^{MeOpy}}$ to mono oxo-bridged $\mathbf{6^{MeOpy}}$ in the presence of 40 equiv. sacrificial H atom donor TEMPO-H in DCM at -73 °C. ([$\mathbf{1^{MeOpy}}$] = 0.75 mM, [TEMPO-H] = 0.3 M). Inset: kinetic trace obtained at λ_{max} = 505 nm. showing the decay of $Mn^{III}Mn^{IV}$ $\mathbf{5^{MeOpy}}$.

Similar to the CHD reactivity, metastable $\mathbf{5^{MeOpy}}$ was generated by introducing dry O_2 to Mn^{II} $\mathbf{1^{MeOpy}}$ (0.6 mM in DCM) at low temperature, and kinetic studies were performed under pseudo-first order conditions with excess TEMPO-H(D). Observed rate constants (k_{obs}) were obtained from first order plots ($\ln(A_{adjust})$ versus time (s), where $A_{adjust} = (A_f - A_t)/(A_f - A_i)$). The k_{obs} was observed to increase in a linear fashion along with the concentration of TEMPO-H(D),

where the slope gives the second order rate constant for the H atom abstraction by $\mathbf{5}^{\mathbf{MeOpy}}$ *en route* to $\mathbf{6}^{\mathbf{MeOpy}}$. A kinetic isotope effect (k_H/k_D = 3.5) was observed. (Figure 3.7) Kinetic measurements at different temperatures were attempted for activation parameters. However, due to instrumentation limits and the short half-life of the reaction, results were not conclusive.

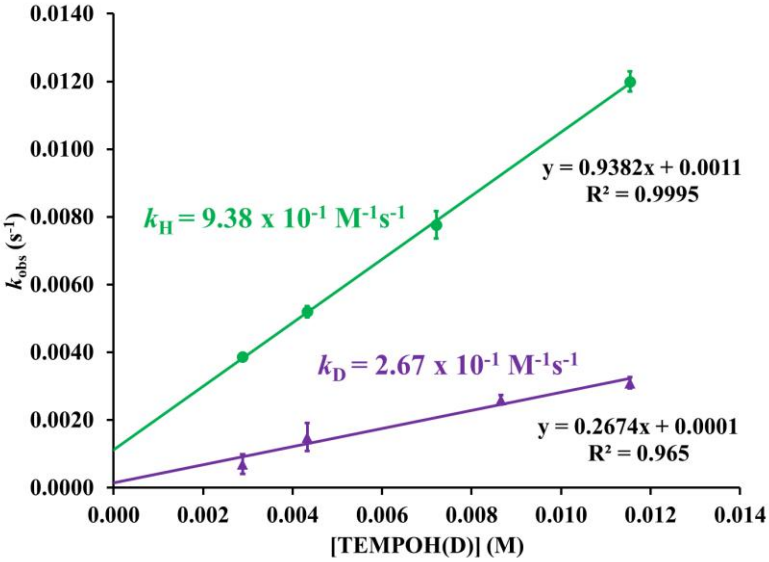

Figure 3.7. Deuterium isotope effect observed when TEMPOH(D) was used as a sacrificial H atom donor for the conversion of $\mathbf{5}^{\mathbf{MeOpy}}$ to $\mathbf{6}^{\mathbf{MeOpy}}$.

Together with the CHD reactivity studies, these results indicated that the O_2-promoted conversion of $\mathbf{1}^{\mathbf{MeOpy}}$ to $\mathbf{6}^{\mathbf{MeOpy}}$ requires two e^- and two H^+ (Scheme 3.2). However, the large difference in half-life ($t_{1/2}$) for the conversion from $\mathbf{5}^{\mathbf{MeOpy}}$ to $\mathbf{6}^{\mathbf{MeOpy}}$ using CHD (C-H BDE: 76.0 kcal/mol) versus TEMPO-H (O-H BDE: 70.6 kcal/mol) could imply different pathways for the H atom abstraction (concerted vs sequential proton and electron transfers). While HAT for CHD is traditionally not concerted step, with some exceptions[21]. The H atom of TEMPO-H is known to transfer via three possible mechanisms[22,23] (Scheme 3.3). These pathways include concerted hydrogen atom transfer (HAT), stepwise proton transfer followed by electron transfer (PT-ET), or the reverse, sequential electron transfer followed by proton transfer (ET-PT).[22,23] However it has been shown that the proton-coupled electron transfer (PCET) of TEMPO/TEMPOH has a

strong preference towards concerted H atom transfer (HAT) from the thermochemical analysis of the three concerted or stepwise mechanisms.[23] Future expanded studies may be able to identify, the H atom abstraction pathway utilized by **5**$^{\mathbf{MeOpy}}$.

Scheme 3.3. Possible pathways for the H atom transfer of TEMPO-H, including concerted H atom transfer (HAT) and sequential proton-electron transfers (PT-ET or ET-PT).

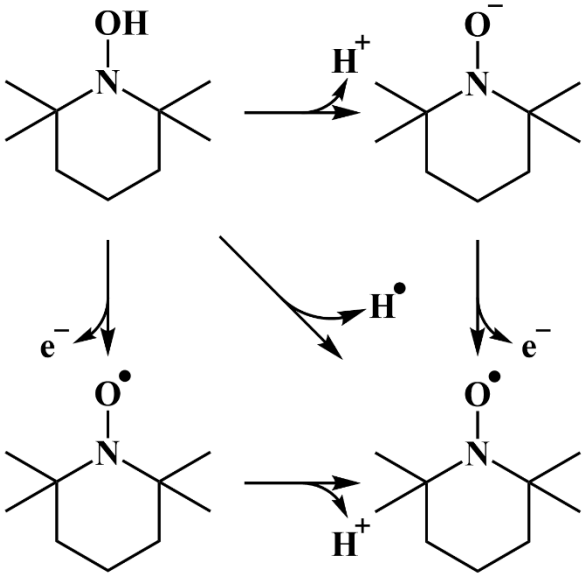

3.3.4 *Preliminary PCET reactivity with 5*^{MeOpy}

The high valent $Mn^{III}Mn^{IV}$ **5**$^{\mathbf{MeOpy}}$ has been shown to abstract a H atom, which is essentially a proton and an electron, from CHD and TEMPO-H. In order to investigate whether **5**$^{\mathbf{MeOpy}}$ could also perform either electron transfer (ET) or proton transfer (PT) separately, the metastable intermediate was reacted with acids and reductants. The exploration of this reactivity might also shine light on the possibility of ET-PT or PT-ET between **5**$^{\mathbf{MeOpy}}$ and TEMPO-H, and determining the rate determining step.

High valent metal-oxo species have been shown as effective oxidants.[24,25] A mild reductant, hydrazine (0.02 V vs SCE, in DMSO)[26] was added to O_2 generated $Mn^{III}Mn^{IV}$ **5**$^{\mathbf{MeOpy}}$. Hydrazine was chosen as the reductant because the reduction byproducts (N_2 and H-containing

species, such as H_2 and H_2O)[26,27] were expected to have little to no effect to the reaction. To ensure complete conversion, a total of 10 equiv. of hydrazine was used and the conversion from **5**$^{\mathbf{MeOpy}}$ to **6**$^{\mathbf{MeOpy}}$ was observed over 66 minutes at -73 °C. (Figure 3.8) The mono oxo-bridged **6**$^{\mathbf{MeOpy}}$ was observed to decompose in the presence of hydrazine at ambient temperature.

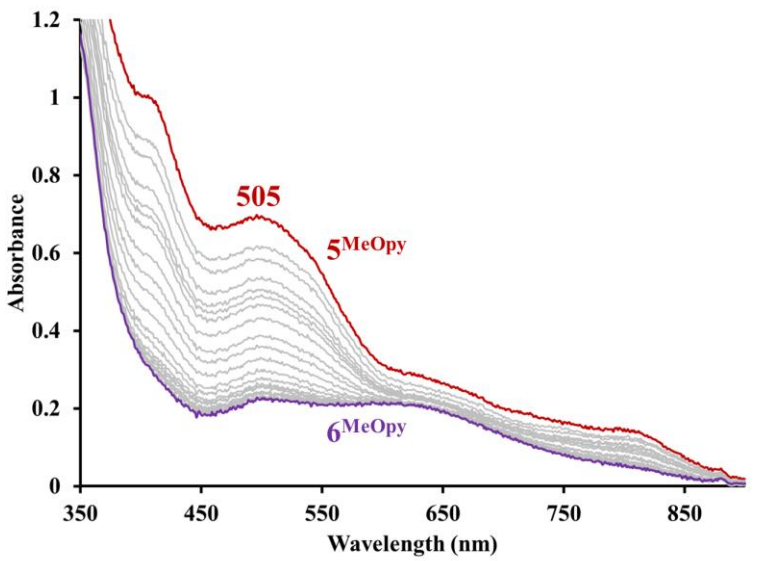

Figure 3.8. EAS spectrum of the addition of 10 equiv. hydrazine to **5**$^{\mathbf{MeOpy}}$ (red trace) in DCM at -73 °C. Conversion to **6**$^{\mathbf{MeOpy}}$ (purple trace) was observed over 66 minutes. Scans recorded at 2.77 minute intervals. Solution of **5**$^{\mathbf{MeOpy}}$ was generated via addition of O_2 to a precooled solution of **1**$^{\mathbf{MeOpy}}$ in DCM. [**1**$^{\mathbf{MeOpy}}$] = 0.75 mM.

The conversion from **5**$^{\mathbf{MeOpy}}$ to **6**$^{\mathbf{MeOpy}}$ was lengthened to more than 30 hours at -73 °C (versus 6.59 hours in the absence of external proton source), when excess ammonium hexafluorophosphate (10 equiv., pK_a = 9.24)[28] was added as an external proton (H^+) source. The change in rate suggests that the $Mn^{III}Mn^{IV}$ intermediate **5**$^{\mathbf{MeOpy}}$ was stabilized by the presence of protons, and conversely the presence of base could destabilize the species. When **5**$^{\mathbf{MeOpy}}$ was reacted with 5 equiv. triethylamine (TEA, pK_a = 18.46)[29], the conversion rate to **6**$^{\mathbf{MeOpy}}$ was not significantly different than the reactivity in the absence of external substances. Another base, tetrabutylammonium hydroxide (Bu_4NOH, pK_a = 15 in H_2O) was employed to investigate the stability of **5**$^{\mathbf{MeOpy}}$. The distinct UV-vis features of the $Mn^{III}Mn^{IV}$ intermediate became rather

featureless upon addition of 5 equiv. tetrabutylammonium hydroxide (Bu_4NOH), (Figure 3.9, left) while a new peak at 515 nm slowly grew after 4.6 hours (Figure 3.9, right). As Bu_4NOH can also act as a hydroxide source, it is possible the species observed at 515 nm was a Mn^{III}-OH species. The 515 nm intermediate was not stable at room temperature and mass spectrometry experiments suggested the Mn species decomposed at ambient temperature.

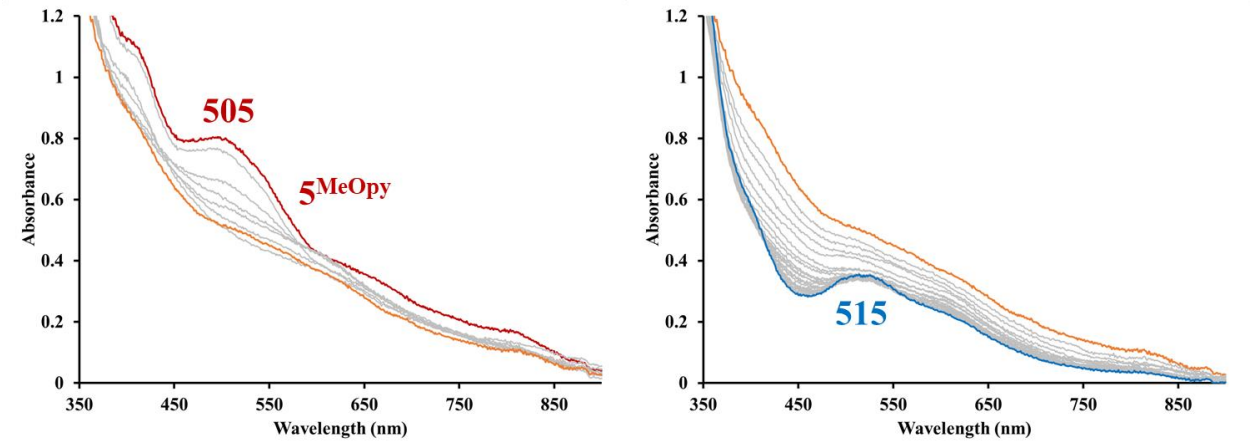

Figure 3.9. EAS spectrum of addition of 5 equiv. tetrabutylammonium hydroxide (Bu_4NOH) to $\mathbf{5^{MeOpy}}$ (red trace) in DCM at -73 °C. Left: Conversion from $\mathbf{5^{MeOpy}}$ to orange trace was observed over 34.5 minutes. Scans recorded at 4.94 minute intervals. Right: Continuous conversion from orange trace to blue trace (λ_{max} = 515 nm) over 5.42 hours. Scans recorded at 13.8 minute intervals. Solution of $\mathbf{5^{MeOpy}}$ was generated via addition of O_2 to precooled solution of $\mathbf{1^{MeOpy}}$ in DCM. [$\mathbf{1^{MeOpy}}$] = 0.75 mM.

From the HAT reactivities with TEMPO-H and CHD shown previously, it was proposed that the H atom abstraction from TEMPO-H could have gone through either an electron transfer (ET), followed by proton transfer (PT), or vice versa. The preliminary ET and PT reactivities with the metastable $Mn^{III}Mn^{IV}$ $\mathbf{5^{MeOpy}}$ suggest that if the H atom transfer were indeed sequential, the electron transfer would likely be the rate determining step, as the high valent $\mathbf{5^{MeOpy}}$ was easily reduced to $Mn^{III}Mn^{III}$ $\mathbf{6^{MeOpy}}$ by hydrazine.

3.4 Conclusion

The hydrogen atom abstraction study in this chapter has further expanded our understanding on the complex dioxygen activation pathway of Mn^{II} $\mathbf{1}^{\mathbf{MeOpy}}$. Two electrons and two protons are shown to be requirements for the O_2-promoted conversion of Mn^{II} $\mathbf{1}^{\mathbf{MeOpy}}$ to $Mn^{III}Mn^{III}$ mono-oxo-bridged $\mathbf{6}^{\mathbf{MeOpy}}$. In the absence of a sacrificial H atom donor, such as 1,4-cyclohexadiene (CHD, BDE(C-H) = 76.0 kcal/mol) or TEMPO-H (BDE(O-H) = 70.6 kcal/mol), this conversion presumably involves the abstraction of H-atoms from solvent, or from the ligand backbone of the complex, which would explain the low yield of $\mathbf{6}^{\mathbf{MeOpy}}$. The quantification of benzene from the CHD experiments showed that one H atom (one electron and one proton) was abstracted *en route* to the formation of $Mn^{III}Mn^{IV}$ $\mathbf{5}^{\mathbf{MeOpy}}$, while another pair transferred during the conversion of $\mathbf{5}^{\mathbf{MeOpy}}$ to thermodynamic product $\mathbf{6}^{\mathbf{MeOpy}}$. With the study using TEMPO-H, a deuterium isotope effect was observed (k_H/k_D = 3.5) for the conversion of $\mathbf{5}^{\mathbf{MeOpy}}$ to $\mathbf{6}^{\mathbf{MeOpy}}$, also implicating a hydrogen atom transfer (HAT) mechanism. Preliminary studies with the mild reductant hydrazine show a quick conversion of $\mathbf{5}^{\mathbf{MeOpy}}$ to $\mathbf{6}^{\mathbf{MeOpy}}$, while additional proton source appeared to stabilize the $Mn^{III}Mn^{IV}$ species.

3.5 References

(1) Umena, Y.; Kawakami, K.; Shen, J. R.; Kamiya, N. Crystal Structure of Oxygen-Evolving Photosystem II at a Resolution of 1.9Å. *Nature* **2011**, *473*, 55–60.

(2) Saito, K.; Mandal, M.; Ishikita, H. Redox Potentials along the Redox-Active Low-Barrier H-Bonds in Electron Transfer Pathways. *Phys. Chem. Chem. Phys.* **2020**, *22*, 25467–25473.

(3) Pantazis, D. A. Missing Pieces in the Puzzle of Biological Water Oxidation. *ACS Catal.* **2018**, *8*, 9477–9507.

(4) Vinyard, D. J.; Brudvig, G. W. Progress Toward a Molecular Mechanism of Water Oxidation in Photosystem II. *Annu. Rev. Phys. Chem.* **2017**, *68*, 101–117.

(5) Yano, J.; Yachandra, V. Mn4Ca Cluster in Photosynthesis: Where and How Water Is Oxidized to Dioxygen. *Chem. Rev.* **2014**, *114*, 4175–4205.

(6) Ghosh, I.; Khan, S.; Banerjee, G.; Dziarski, A.; Vinyard, D. J.; Debus, R. J.; Brudvig, G. W. Insights into Proton-Transfer Pathways during Water Oxidation in Photosystem II. *J. Phys. Chem. B* **2019**, *123*, 8195–8202.

(7) Boal, A. K.; Cotruvo, J. A.; Stubbe, J. A.; Rosenzweig, A. C. Structural Basis for Activation of Class Ib Ribonucleotide Reductase. *Science (80-.).* **2010**, *329*, 1526–1530.

(8) Cotruvo, J. A.; Stich, T. A.; Britt, R. D.; Stubbe, J. Mechanism of Assembly of the Dimanganese-Tyrosyl Radical Cofactor of Class Ib Ribonucleotide Reductase: Enzymatic Generation of Superoxide Is Required for Tyrosine Oxidation via a Mn(III)Mn(IV) Intermediate. *J. Am. Chem. Soc.* **2013**, *135*, 4027–4039.

(9) Greene, B. L.; Kang, G.; Cui, C.; Bennati, M.; Nocera, D. G.; Drennan, C. L.; Stubbe, J. Annual Review of Biochemistry Ribonucleotide Reductases: Structure, Chemistry, and Metabolism Suggest New Therapeutic Targets. *Annu. Rev. Biochem.* **2020**, *89*, 45–75.

(10) Hays, A. M. A.; Vassiliev, I. R.; Golbeck, J. H.; Debus, R. J. Role of D1-His190 in the Proton-Coupled Oxidation of Tyrosine Y(Z) in Manganese-Depleted Photosystem II. *Biochemistry* **1999**, *38*, 11851–11865.

(11) Guerra, W. D.; Odella, E.; Secor, M.; Goings, J. J.; Urrutia, M. N.; Wadsworth, B. L.; Gervaldo, M.; Sereno, L. E.; Moore, T. A.; Moore, G. F.; Hammes-Schiffer, S.; Moore, A. L. Role of Intact Hydrogen-Bond Networks in Multiproton-Coupled Electron Transfer. *J. Am. Chem. Soc.* **2020**, *142*, 21842–21851.

(12) Sirohiwal, A.; Neese, F.; Pantazis, D. A. Microsolvation of the Redox-Active Tyrosine-D in Photosystem II: Correlation of Energetics with EPR Spectroscopy and Oxidation-Induced Proton Transfer. *J. Am. Chem. Soc.* **2019**, *141*, 3217–3231.

(13) Cotruvo, J. A.; Stubbe, J. Metallation and Mismetallation of Iron and Manganese Proteins in Vitro and in Vivo: The Class i Ribonucleotide Reductases as a Case Study. *Metallomics* **2012**, *4*, 1020–1036.

(14) Rose, H. R.; Maggiolo, A. O.; McBride, M. J.; Palowitch, G. M.; Pandelia, M. E.; Davis, K. M.; Yennawar, N. H.; Boal, A. K. Structures of Class Id Ribonucleotide Reductase Catalytic Subunits Reveal a Minimal Architecture for Deoxynucleotide Biosynthesis. *Biochemistry* **2019**, *58*, 1845–1860.

(15) Rose, H. R.; Ghosh, M. K.; Maggiolo, A. O.; Pollock, C. J.; Blaesi, E. J.; Hajj, V.; Wei, Y.; Rajakovich, L. J.; Chang, W. C.; Han, Y.; Hajj, M.; Krebs, C.; Silakov, A.; Pandelia,

M. E.; Bollinger, J. M.; Boal, A. K. Structural Basis for Superoxide Activation of Flavobacterium Johnsoniae Class i Ribonucleotide Reductase and for Radical Initiation by Its Dimanganese Cofactor. *Biochemistry* **2018**, *57*, 2679–2693.

(16) Coggins, M. K.; Kovacs, J. A. Structural and Spectroscopic Characterization of Metastable Thiolate-Ligated Manganese(III)-Alkylperoxo Species. *J. Am. Chem. Soc.* **2011**, *133*, 12470–12473.

(17) Coggins, M. K.; Toledo, S.; Shaffer, E.; Kaminsky, W.; Shearer, J.; Kovacs, J. A. Characterization and Dioxygen Reactivity of a New Series of Coordinatively Unsaturated Thiolate-Ligated Manganese(II) Complexes. *Inorg. Chem.* **2012**, *51*, 6633–6644.

(18) Mader, E. A.; Davidson, E. R.; Mayer, J. M. Large Ground-State Entropy Changes for Hydrogen Atom Transfer Reactions of Iron Complexes. *J. Am. Chem. Soc.* **2007**, *129*, 5153–5166.

(19) Luo, Y.-R. *Comprehensive Handbook of Chemical Bond Energies*, 1st Editio.; Taylor & Francis Group, 2007.

(20) Coggins, M. K. Small Molecule Activation Studies Involving Thiolate-Ligated Manganese(II) Complexes and Biologically-Relevant Oxidants, Univeristy of Washington, Seattle, 2012.

(21) Bím, D.; Maldonado-Domínguez, M.; Rulísek, L.; Srnec, M. Beyond the Classical Thermodynamic Contributions to Hydrogen Atom Abstraction Reactivity. *Proc. Natl. Acad. Sci. U. S. A.* **2018**, *115*, E10287–E10294.

(22) Darcy, J. W.; Koronkiewicz, B.; Parada, G. A.; Mayer, J. M. A Continuum of Proton-

Coupled Electron Transfer Reactivity. *Acc. Chem. Res.* **2018**, *51*, 2391–2399.

(23) J. Warren, J.; A. Tronic, T.; M. Mayer, J. Thermochemistry of Proton-Coupled Electron Transfer Reagents and Its Implications. *Chem. Rev.* **2010**, *110*, 6961–7001.

(24) Fukuzumi, S.; Kojima, T.; Lee, Y. M.; Nam, W. High-Valent Metal-Oxo Complexes Generated in Catalytic Oxidation Reactions Using Water as an Oxygen Source. *Coord. Chem. Rev.* **2017**, *333*, 44–56.

(25) Larson, V. A.; Battistella, B.; Ray, K.; Lehnert, N.; Nam, W. Iron and Manganese Oxo Complexes, Oxo Wall and Beyond. *Nat. Rev. Chem.* **2020**, *4*, 404–419.

(26) Connelly, N. G.; Geiger, W. E. Chemical Redox Agents for Organometallic Chemistry. *Chem. Rev.* **1996**, *96*, 877–910.

(27) Furst, A.; Berlo, R. C.; Hooton, S. Hydrazine as a Reducing Agent for Organic Compounds (Catalytic Hydrazine Reductions). *Chem. Rev.* **1965**, *65*, 51–68.

(28) Luo, S.; Rauchfuss, T. B.; Wilson, S. R. Arene vs Thiophene Reduction in the System (C6R6)Ru(C4R4S)2+ and the Protonation of H4-Thiophene Ligands. *J. Am. Chem. Soc.* **1992**, *114*, 8515–8520.

(29) Izutsu, K. *Acid-Base Dissociation Constants in Dipolar Aprotic Solvents*; Boston : Blackwell Scientific Publications, 1990.

Chapter 4. Tuning a π-Acceptor N-heterocyclic Ligand to Synthesize a More Lewis Acidic Fe^{II} Thiolate Complex and Its Characterization

Components of this chapter have been adapted from: Toledo, S.; Poon, P. C. Y.; Gleaves, M.; Rees, J.; Rogers, D.; Kaminsky, W.; Kovacs, J. A. "Increasing Reactivity by Incorporating π-Acceptor Ligands into Coordinatively Unsaturated Thiolate-Ligated Iron(II) Complex" S*ubmitted*.

4.1 Introduction

Incorporation of a thiolate ligand impacts the function of iron metalloenzymes in a variety of ways. Thiolate ligands have been shown to lower the activation barrier to binding dioxygen,[1] increase the ability of iron superoxo ($Fe\text{-}O_2^{\bullet-}$) compounds to abstract H-atoms from strong C-H bonds,[2] promote peroxo O-O bond cleavage,[3,4] and create potent high-valent metal-oxos capable of activating strong C-H bonds.[5–9] Highly covalent iron thiolate (Fe-SR) bonds stabilize low spin-states due to the nephelauxetic effect,[10,11] and are able to compensate for changes in electron density at the metal ion thereby maintaining a relatively constant reduction potential.[12] The observed compensatory effect reflects the redox non-innocence of thiolate ligands, which facilitates the delocalization of oxidizing equivalents onto the sulfur atoms.[13] This unique property is important to the function of both blue copper electron-transfer proteins,[14] as well as non-heme iron enzymes, such as isopenicilin *N*-synthase (IPNS),[1,15–18] superoxide reductase (SOR),[11,19–24] cysteine dioxygenases (CDO),[25–31] nitrile hydratases (NHase),[32,33] and the heme iron enzyme cytochrome P450.[34–39]

The primary coordination sphere surrounding a transition-metal ion can have a profound influence on the electronic and geometric structure, as well as the magnetic, redox, and reactivity

properties. Even subtle changes to the coordination sphere, involving the replacement of a coordinated ligand[40], or a single H-bond[41], can dramatically alter these properties. For example, if the imidazole of hemoglobin is replaced with a cysteinate, then O_2 activation and reduction, followed by peroxo O-O bond cleavage, are favored as opposed to O_2 transport, and the resulting iron-oxo becomes a potent oxidant capable of cleaving strong C-H bonds.[42] The Kovacs group has shown that thiolate ligands contribute to an accessible low-spin (S = 1/2) Fe even in a non-heme environment[43–45], stabilize Fe^{III} species[43–45], and labilize sites *trans* to the thiolate and promote reactivity by releasing product[21], even with substitutionally inert low-spin Co^{3+} [46,47].

Previously, the Kovacs group showed that five-coordinate $[Fe^{II}(S^{Me2}N_4(tren))]^+$ (**1**$^{\mathbf{Tren}}$) reacts with superoxide in a proton-dependent mechanism to afford a well-characterized metastable hydroperoxo complex, $[Fe^{III}(S^{Me2}N_4(tren))(OOH)]^+$ (**2**$^{\mathbf{Tren}}$), which releases H_2O_2 upon protonation at the proximal oxygen.[48] Two potential mechanisms for the formation of both **2**$^{\mathbf{Tren}}$ (Scheme 4.1) and the SOR enzyme (Scheme 4.2), would involve either (a) the sequential addition of $O_2^{\bullet-}$, to afford an Fe^{II}-$O_2^{\bullet-}$ intermediate, followed by a proton (H^+) abstraction, to afford the corresponding Fe^{III}-OOH, or (b) the concerted addition of HO_2 to the metal ion. Primary amine-ligated **1**$^{\mathbf{Tren}}$, the precursor to hydroperoxo **2**$^{\mathbf{Tren}}$, is colorless and only displays absorption bands in the UV range, due to the high energy of the S→Fe^{II} CT band.[48,49] This makes it difficult to detect Fe^{II}-L (e.g. L = O_2^-) intermediates. The incorporation of π-acceptor N-heterocycles (N^{Ar}) into the ligand scaffold (Figure 4.1) would provide a better spectroscopic handle to monitor reactivity via electronic absorption spectroscopy (EAS) using the M→π-acceptor chromophore. The Kovacs group recently showed that sterically encumbering groups on the pyridine ligand (N^{Ar}) influences the kinetic barriers to O_2 binding and peroxo O-O bond cleavage, and the reactivity of the corresponding high-valent oxo intermediates.[3,50] The Kovacs

group has also shown that the combination of π-acceptor N-heterocycle ligands and π-donor thiolate ligands has a profound effect on the electronic structure, and the nature of the charge transfer (CT) bands, which is reflected in their intense RS-Fe → (α-imino)-N-heterocycle π* CT bands.[13]

Herein, the synthesis of $[Fe^{II}(S^{Me2}N_4(6\text{-H-DPEN}))]^+$ (**1**$^{\mathbf{Py}}$) is reported. The structure, reactivity, and redox properties of **1**$^{\mathbf{Py}}$ will be explored and compared with other structurally related thiolate-ligated Fe^{II} complexes that incorporate both a π-donating thiolate ligand and π-accepting pyridine, $[Fe^{II}(S^{Me2}N_4(6\text{-Me-DPEN}))]^+$ (**1**$^{\mathbf{Mepy}}$), or quinoline, $[Fe^{II}(S^{Me2}N_4(\text{QuinoEN}))]^+$ (**1**$^{\mathbf{Quino}}$), onto their ligands. (Figure 4.1) The results of incorporating π-accepting N-heterocycles in place of the primary amines of **1**$^{\mathbf{Tren}}$ include, (a) the complexes are intensely colored, allowing reactivity to be monitored by electronic absorption spectroscopy (EAS); (b) the binding affinity for a sixth ligand increases; and (c) Fe^{II} ion Lewis acidity increases[51].

Scheme 4.1. Proposed mechanism of superoxide reduction by SOR analogue **1**$^{\mathbf{Tren}}$ via a Fe^{III}-OOH intermediate (**2**$^{\mathbf{Tren}}$). Regeneration of **1**$^{\mathbf{Tren}}$ is completed via proton-promoted H_2O_2 release, followed by reduction by cobaltocene.[48,49]

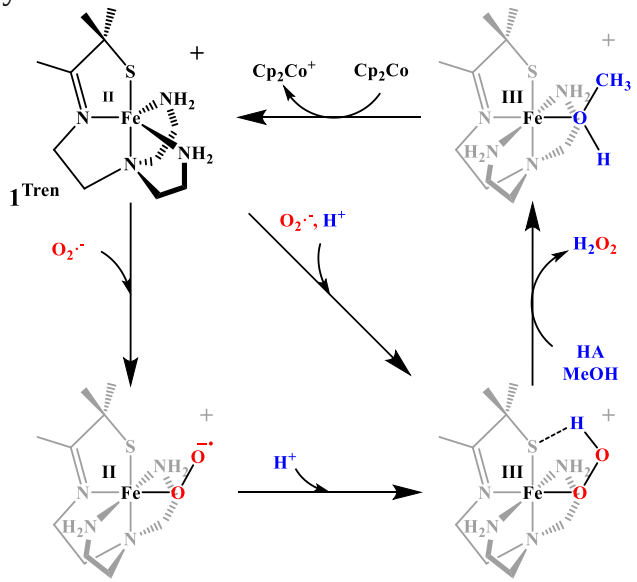

Scheme 4.2. Proposed general scheme of sequential versus concerted addition of HO_2 to Fe^{II} to afford Fe^{III}-OOH for SOR.

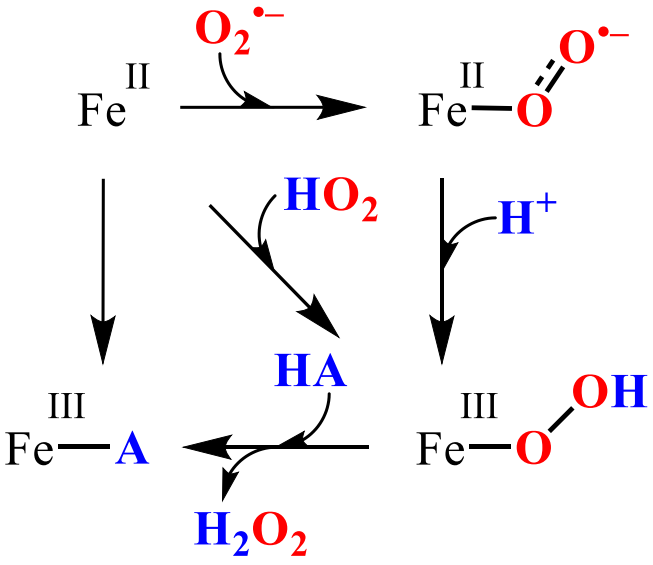

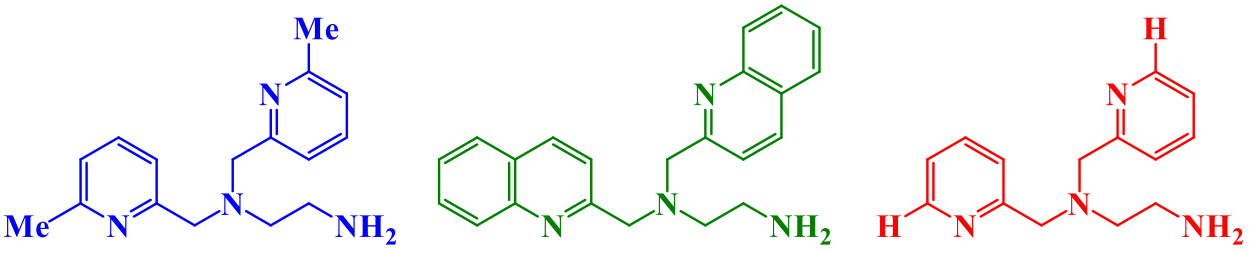

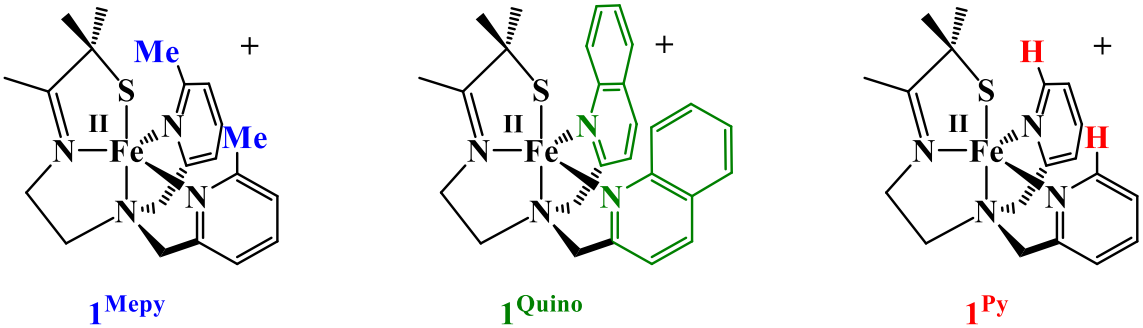

Figure 4.1. ChemDraw representations of $[Fe^{II}(S^{Me2}N_4(6\text{-Me-DPEN}))](PF_6)$ (**1**$^{\mathbf{Mepy}}$, left), $[Fe^{II}(S^{Me2}N_4(\text{QuinoEN}))](PF_6)$ (**1**$^{\mathbf{Quino}}$, middle), proposed monomeric structure of $[Fe^{II}(S^{Me2}N_4(6\text{-H-DPEN}))]^+$ (**1**$^{\mathbf{Py}}$, right), and their respective ligands.

4.2 Experimental

General Methods. All manipulations were performed using Schlenk techniques or under an N_2 atmosphere in a glovebox. Reagents and solvents were purchased from commercial vendors, were of highest available purity, and were used without further purification unless otherwise noted. Methylene chloride (DCM), tetrahydrofuran (THF), diethyl ether (Et_2O), and acetonitrile (MeCN) were rigorously degassed, and purified using solvent purification columns housed in a custom stainless-steel cabinet, dispensed via a stainless steel Schlenk-line (GlassContour). Methanol (MeOH) was dried over magnesium methoxide and distilled prior to use. ^{1}H NMR spectra were recorded on a Bruker AV 300, AV 301, or DRX499 spectrometer at reported temperature and were referenced to residual solvent. Chemical shifts are listed in parts per million (ppm) and coupling constants (*J*) in Hz. UV-vis spectra were recorded on a Varian Cary 50 or Varian Cary 60 spectrophotometer equipped with a fiber optic cable connected to an ATR "dip" probe (C-technologies). A custom-built two-neck solution sample holder equipped with a threaded glass connector was sized specifically to fit the "dip" probe. Spectrums were recorded at either medium scan rate (83 seconds/scan) or fast scan rate (15 seconds/scan). Electrospray-ionization mass spectrometry (ESI-MS) data were obtained on either a Bruker Esquire Liquid Chromatograph-Ion Trap mass spectrometer or a LTQ ion trap mass spectrometer equipped with an HP 1100 capillary inlet. Cyclic voltammograms were recorded in MeCN with $^nBu_4N(PF_6)$ supporting electrolyte (0.100 M) using a CH Instruments (CHI600E) potentiostat with a glassy carbon working electrode, an $Ag^+/AgNO_3$ reference electrode, and a platinum auxiliary electrode. EPR spectra were recorded on a Bruker E580 CW-EPR spectrometer operating at X-band frequency and equipped with an Oxford helium cryostat and dual mode cavity. Simulated fits of EPR spectra were generated with EasySpin.[52] X-ray crystallography data were recorded on

a Bruker APEX II single Crystal X-ray diffractometer with Mo Kα radiation. Magnetic moments (solution state) were obtained using the Evans' method as modified for super-conducting solenoids.[53,54] Organic ligands, 1-(tert-butyloxycarbonyl)ethyldiamine (NNBoc)[55] and 3-methyl-3-metcapto-2-butanone,[44] [N', N'-bis(2-pyridylmethyl)]ethane-1,2-diamine] (6-H-DPEN)[55] were synthesized according to published procedure. Oxidant tri-(ρ-tolyl)-aminium hexafluorophosphate was synthesized using a published modified procedure.[55,56] Complexes $[Fe^{II}(S^{Me2}N_4(6\text{-Me-DPEN}))](PF_6)$ (**1**$^{\mathbf{Mepy}}$) and $[Fe^{II}(S^{Me2}N_4(\text{QuinoEN}))](PF_6)$ (**1**$^{\mathbf{Quino}}$) were synthesized according to a published procedure.[55] Crystal structures for **1**$^{\mathbf{Mepy}}$, **1**$^{\mathbf{Quino}}$, **1**$^{\mathbf{PyPN}}$, **6**$^{\mathbf{Mepy}}$, and **6**$^{\mathbf{Quino}}$ were previously reported.[55,57]

4.2.1. Synthesis of Bimetallic $[Fe^{II}(S^{Me2}N_4(6\text{-H-DPEN}))(\mu\text{-}S^{Me2}N_4(6\text{-H-DPEN})Fe^{II}(MeCN)]^{2+}(PF_6)_2$ (1$^{Py}_2$-MeCN). Sodium methoxide (0.119 g, 2.2 mmol), 3-mercapto-3-methyl-2-butanone (0.260 g, 2.2 mmol), [N', N'-bis(2-pyridylmethyl)]ethane-1,2-diamine] (6-H-DPEN, 0.484 g, 2 mmol), iron(II) acetate (0.348 g, 2 mmol), and sodium hexafluorophosphate (0.336 g, 2 mmol) were each dissolved or slurried in MeOH (2 mL) under an inert atmosphere in a dry box. Each reagent was subsequently added to a 20 mL vial charged with a stir bar. The resulting reaction mixture was stirred at ambient temperature for one day. All volatiles were removed to afford a crude dark red solid. The crude product was redissolved in minimal MeCN (~5 mL) and filtered through a fine fritted filter. The resulting solution was layered with ~15 mL Et_2O and was allowed to crystallize at -30 ºC to afford the product as a red solid in 24 % yield (0.259 g, 0.477 mmol). λ_{max} (nm) (ε (M^{-1} cm^{-1})) at ambient temperature: MeOH: 447(1250); MeCN: 447(1276); THF: 462(1515); DCM: 401(1224). LTQ ion trap MS: MeOH: expected m/z for mononuclear MeO-bound **1**$^{\mathbf{Py}}$**-OMe**: $[FeC_{20}H_{28}N_4OS]^+$ = 428.1, found m/z = 428.1; MeCN: expected m/z for **1**$^{\mathbf{Py}}_{\mathbf{2}}$: $[Fe_2C_{38}H_{50}N_8S_2]^{2+}$ = 397.1, found m/z = 397.1. Solution magnetic moment (298 K): MeOH:

μ_{eff} = 4.92 B.M. per Fe; MeCN: μ_{eff} = 3.60 B.M. per Fe. Reduction potential (MeCN, vs SCE): $E_{1/2}$ = -89 mV.

4.2.2. Synthesis of [($Fe^{III}(S^{Me2}N_4$(6-H-DPEN)))$_2$-(μ-O)](PF_6)$_2$ (6^{Py}). To a 1 mL concentrated orange solution of $\mathbf{1^{Py}}$ (10 mM) in acetonitrile, dry O_2 was bubbled through the solution at room temperature. By layering ether to the deep red solution, a brick red solid was collected in 72% yield. λ_{max} (nm) (ε (M^{-1} cm^{-1}): MeOH: 513(4372); MeCN: 495(7435); THF: 496(7920). LTQ ion trap MS: expected m/z for $[Fe_2C_{38}H_{50}N_8OS_2]^{2+}$ = 405.1, found m/z = 405.1.

4.2.3. Reactivity of Fe^{II} complexes (1) with O_2 at room temperature. Around 2-7 mg of Fe^{II} complex ($\mathbf{1^{Py}}$, $\mathbf{1^{Mepy}}$, or $\mathbf{1^{Quino}}$) was dissolved in selected solvent. The solution (5 mL) was transferred to an argon purged dip probe cell via a gas-tight syringe. A stream of dry O_2 was introduced to the dip probe cell from gas cylinder. The reactions were monitored by EAS.

4.2.4. Reactivity of Fe^{II} complexes with O_2 at low temperature. Around 2-7 mg of Fe^{II} complex ($\mathbf{1^{Py}}$, $\mathbf{1^{Mepy}}$, or $\mathbf{1^{Quino}}$) was dissolved in selected solvent. The solution (5 mL) was transferred to an argon purged dip probe cell via a gas-tight syringe and brought to selected temperature using a cold bath. The solution was left in a positive Ar stream environment for 10-15 minutes for the temperature to equilibrate. A stream of dry O_2 was then introduced to the dip probe cell from gas cylinder. The reactions were monitored by EAS.

4.2.5. Addition of 1^{Py} to O_2-purged DCM at low temperature. Dried solution of DCM (4.5 mL) was placed in an argon purged dip probe cell and brought to -90 °C using cold bath. Once the temperature of the solution is equilibrated, a stream of dry O_2 was introduced to the solution for 15 minutes. At the end of the 15 minutes, O_2 stream was removed and Ar gas was introduced into the headspace of the dip probe cell to remove excess O_2. After 15 seconds, a 0.5 mL chilled

solution of $\mathbf{1^{Py}}$ (2 mM) was quickly injected into the DCM solution. The reactions were monitored by EAS with fast scan rates (15 s/scan).

4.2.6. Oxidation of $\mathbf{1^{Py}}$ with ferrocenium hexafluorophosphate. Around 2 mg of $\mathbf{1^{Py}}$ was dissolved in 20 mL MeCN. A 5 mL of the 0.2 mM solution was placed in an argon purged dip probe cell. Titration of 1.0 equiv. ferrocenium hexafluorophosphate (0.01 M in MeCN) to $\mathbf{1^{Py}}$ was added in an 0.1 equiv. (10 μL) increment, for a total of 100 μL. Additional equiv. of oxidant was added to ensure complete conversion of $\mathbf{1^{Py}}$ to $\mathbf{4^{Py}}$. The reactions were monitored by EAS at ambient temperature.

4.2.7. Oxidation of $\mathbf{1^{Mepy}}$ and $\mathbf{1^{Quino}}$ with tri-ρ-tolyl-aminium hexafluorophosphate. Around 1.5-5 mg of $\mathbf{1^{Mepy}}$ or $\mathbf{1^{Quino}}$ was dissolved in 20 mL THF. A 5 mL solution ($\mathbf{1^{Mepy}}$: 0.2 mM; $\mathbf{1^{Quino}}$: 0.5 mM) was placed in an argon purged dip probe cell. The solution was brought to -73 °C using acetone/dry ice bath. Titration of 1.0 equiv. tri-ρ-tolyl-aminium hexafluorophosphate in THF ($\mathbf{1^{Py}}$: 0.01 M; $\mathbf{1^{Quino}}$: 0.025 M) to the Fe^{II} solution was added in a 10 μL increment, for a total of 100 μL. Extra equiv. of oxidant was added to ensure complete conversion to $\mathbf{4^{Mepy}}$ and $\mathbf{4^{Quino}}$. The reactions were monitored by EAS.

4.2.8. Reactivity of $\mathbf{Fe^{II}}$ complexes with Azide. A 5 mL solution of Fe^{II} complexes in THF($\mathbf{1^{Py}}$: 0.2 mM, $\mathbf{1^{Mepy}}$ or $\mathbf{1^{Quino}}$: 0.5 mM) was cooled to -73 °C using acetone/dry ice bath. A 200 μL solution of 10 equiv. tetrabutylammonium azide in THF ($\mathbf{1^{Py}}$: 0.05 mM; $\mathbf{1^{Mepy}}$ or $\mathbf{1^{Quino}}$: 0.125 mM) was added to the chilled Fe^{II} solution. The reactions were monitored by EAS.

4.2.9. Reactivity of $\mathbf{Fe^{III}}$ complexes with Azide. A 5 mL solution of Fe^{III} complexes in THF($\mathbf{4^{Py}}$: 0.2 mM, $\mathbf{4^{Mepy}}$ or $\mathbf{4^{Quino}}$: 0.5 mM) was prepared with 1.0 equiv. oxidant following the protocol above. The Fe^{III} solution was kept at -73 °C using acetone/dry ice bath. A 200 μL

solution of 10 equiv. tetrabutylammonium azide in THF ($\mathbf{4^{Py}}$: 0.05 mM; $\mathbf{4^{Mepy}}$ or $\mathbf{4^{Quino}}$: 0.125 mM) was added to the chilled Fe^{III} solution. The reactions were monitored by EAS.

4.2.10. X-ray Crystallography.

A red plate of $\mathbf{1^{Py}}$, measuring 0.14 x 0.09 x 0.08 mm^3 was mounted on a loop with oil. Data was collected at -173°C on a Bruker APEX II single crystal X-ray diffractometer, Mo-radiation. Crystal-to-detector distance was 40 mm and exposure time was 60 seconds per frame for all sets. The scan width was 1°. Data collection was 99.9% complete to 25° in ϑ. A total of 19221 reflections were collected covering the indices, -10<=h<=10, -50<=k<=50, -17<=l<=17. 9698 reflections were symmetry independent and the R_{int} = 0.0565 indicated that the data was of better than average quality (0.07). Indexing and unit cell refinement indicated a primitive monoclinic lattice. The space group was found to be P 2_1/c (No. 13).

The data was integrated and scaled using SAINT, SADABS within the APEX2 software package by Bruker. Solution by direct methods (SHELXT[58] or SIR97[59,60]) produced a complete heavy atom phasing model consistent with the proposed structure. The structure was completed by difference Fourier synthesis with SHELXL[58,61,62]. Scattering factors are from Waasmair and Kirfel.[63] Hydrogen atoms were placed in geometrically idealized positions and constrained to ride on their parent atoms with C---H distances in the range 0.95-1.00 Angstrom. Isotropic thermal parameters U_{eq} were fixed such that they were 1.2Ueq of their parent atom U_{eq} for CH's and 1.5U_{eq} of their parent atom U_{eq} in case of methyl groups. All non-hydrogen atoms were refined anisotropically by full-matrix least-squares. Crystallographic data for $\mathbf{1^{Py}}$ is presented in Table 4.1.

Table 4.1. Crystal data, intensity collections[a], and structure refinement for $[Fe^{II}(S^{Me2}N_4(6\text{-H-DPEN}))(\mu\text{-}S^{Me2}N_4(6\text{-H-DPEN})Fe^{II}(MeCN)](PF_6)_2$ (**$1^{Py}{}_2$-MeCN**).

	$1^{Py}{}_2$-MeCN
Empirical formula	$C_{44}H_{59}F_{12}Fe_2N_{11}P_2S_2$
MW	1207.78
Temperature (K)	100(2)
Crystal system	Monoclinic
a (Å)	8.8322(5)
b (Å)	41.798(3)
c (Å)	14.4591(7)
α (°)	90
β (°)	97.514(3)
γ (°)	90
Volume ($Å^3$)	5292.0(5)
Z	4
Density (calculated, Mg/m^3)	1.516
Space group	P $2_{1/c}$
R	0.0639[b]
R_w	0.1003[c]
GOF	1.102

[a] Mo Kα (λ = 0.71073 Å) radiation; graphite monochromator; -90 °C. [b] $R = \Sigma ||F_o| - |F_c|| / \Sigma |F_o|$. [c] $R_w = [\Sigma w(|F_o| - |F_o|)^2/\Sigma w F_o^2]^{1/2}$, where $w = 1/[\sigma^2(F_o^2) + 19.6516P]$, $P = (F_o^2 + 2F_c^2)/3$.

4.3 Results and Discussion

4.3.1 *Synthesis and Solid-State Characterization of [$Fe^{II}(S^{Me2}N_4$(6-H-DPEN))(μ-$S^{Me2}N_4$(6-H-DPEN)Fe^{II}(MeCN)]$(PF_6)_2$ ($1^{Py}{}_2$-MeCN)*

Novel iron complexes, $[Fe^{II}(S^{Me2}N_4(6\text{-Me-DPEN}))](PF_6)$ (**1^{Mepy}**) and $[Fe^{II}(S^{Me2}N_4(\text{QuinoEN}))](PF_6)$ (**1^{Quino}**) results in a more Lewis acidic complex due to the π-accepting ligands. The new complex has been synthesized with ligand 6-H-DPEN (**L_1**) by adapting the established synthesis previously reported in the Kovacs group.[55,64] The ligand **L_1** and 3-methyl-3-mercapto-2-butanone were condensed using Fe^{II} as a metal template for the Schiff-base condensation in attempts to yield the proposed 5-coordinate monomeric Fe^{II} complex, $[Fe^{II}(S^{Me2}N_4(6\text{-H-DPEN}))]^+$, similar to the two crystallographically characterized Fe^{II} DPEN complexes, **1^{Mepy}** and **1^{Quino}**.[55] (Figure 4.1) Previous attempts to synthesize this complex in the Kovacs group have resulted in the isolation of a series of bimetallic complexes, $[(Fe^{II}(6\text{-H-DPEN}))_2\text{-bis-μ-Cl}](PF_6)$, $[(Fe^{II}N_4(6\text{-H-DPEN}))_2\text{-bis-μ-(OAc)}](PF_6)$, and $[Fe^{II}(S^{Me2}N_4(6\text{-H-DPEN}))]_2(OAc)(PF_6)$.[55] To ensure the incorporation of the thiolate, excess 3-methyl-3-mercapto-2-butanone and sodium methoxide (1.1 equiv. each) were used in the synthesis. The crude solid was washed thoroughly with MeCN and DCM in order to remove salt from the Fe source and prevent the formation of either bis-μ-Cl or bis-μ-(OAc).

A new bimetallic species was isolated from attempts to synthesize monomeric **1^{Py}**. Obtained by solvent diffusion of Et_2O onto a MeCN solution of **1^{Py}**, the intensely red complex **1^{Py}** was shown to be a Fe^{II} μ-thiolate bimetallic species, $[Fe^{II}(S^{Me2}N_4(6\text{-H-DPEN}))(\mu\text{-}S^{Me2}N_4(6\text{-H-DPEN})Fe^{II}(MeCN)]^{2+}$ $(PF_6)_2$ (**$1^{Py}{}_2$-MeCN**, Figure 4.2) via single X-ray crystallography. The solid-state structure shows that both Fe^{II} centers are coordinatively saturated and 6-coordinate. Complex **$1^{Py}{}_2$-MeCN** dimerizes via a bridging thiolate sulfur to form an asymmetric molecule

with only one solvent (MeCN) bound to one of the Fe ions, Fe(2).(Figure 4.2 and 4.3) The two halves of the bimetallic complex are rotated approximately 90° relative to one another. The crystallographic details as well as selected bond distances and bond angles in comparison to other Fe^{II} DPEN complexes (**1**$^{\mathbf{Mepy}}$ and **1**$^{\mathbf{Quino}}$) and a 6-coordinate propyl(Pr)-linked $[Fe^{II}(S^{Me2}N_4(6\text{-H-DPPN}))(MeOH)](PF_6)$ (**1**$^{\mathbf{PyPN}}$) are reported in Tables 4.1 and 4.2.[55] Bond lengths of **1**$^{\mathbf{Py}}$ is consistent with high spin Fe^{II}.

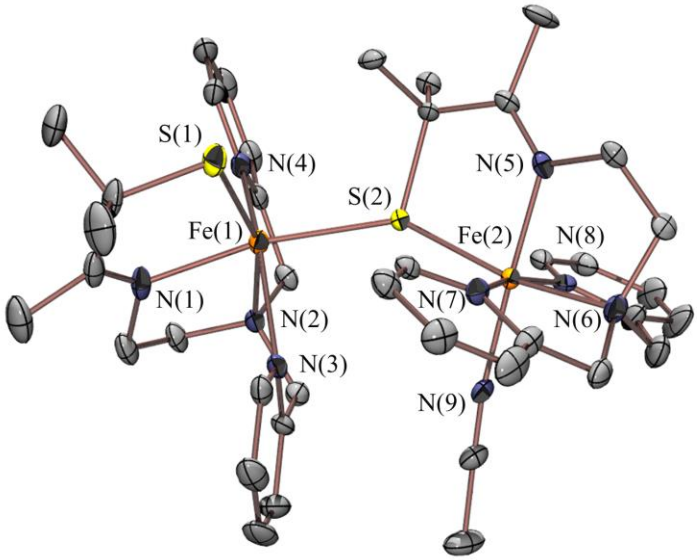

Figure 4.2. ORTEP diagram of binuclear $[Fe^{II}(S^{Me2}N_4(6\text{-H-DPEN}))(\mu\text{-}S^{Me2}N_4(6\text{-H-DPEN})Fe^{II}(MeCN)](PF_6)_2$ (**1**$^{\mathbf{Py}}$**$_2$-MeCN**) with thermal ellipsoids at 50% probability level. Counter-ions, disorder, solvent molecules, and hydrogen atoms have been omitted for clarity.

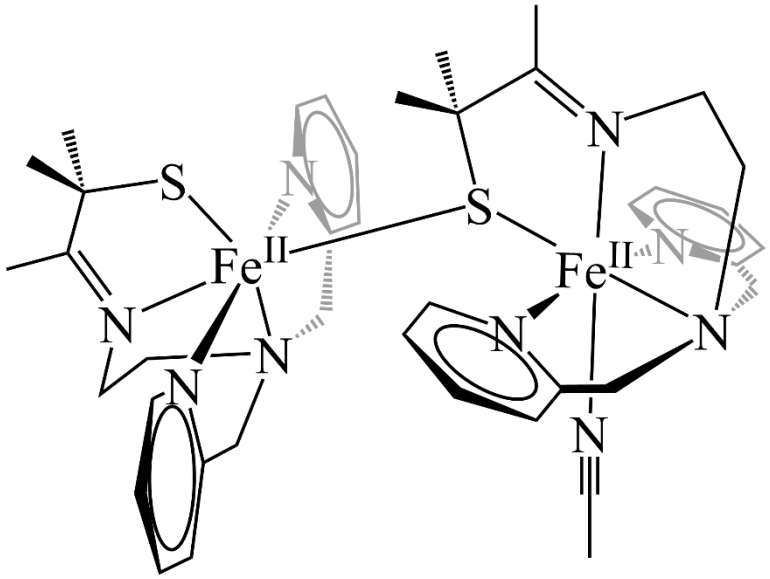

Figure 4.3. ChemDraw representation of binuclear $[Fe^{II}(S^{Me2}N_4(6\text{-H-DPEN}))(\mu\text{-}S^{Me2}N_4(6\text{-H-DPEN})Fe^{II}(MeCN)]^{2+}$ (**$1^{Py}{}_2$-MeCN**).

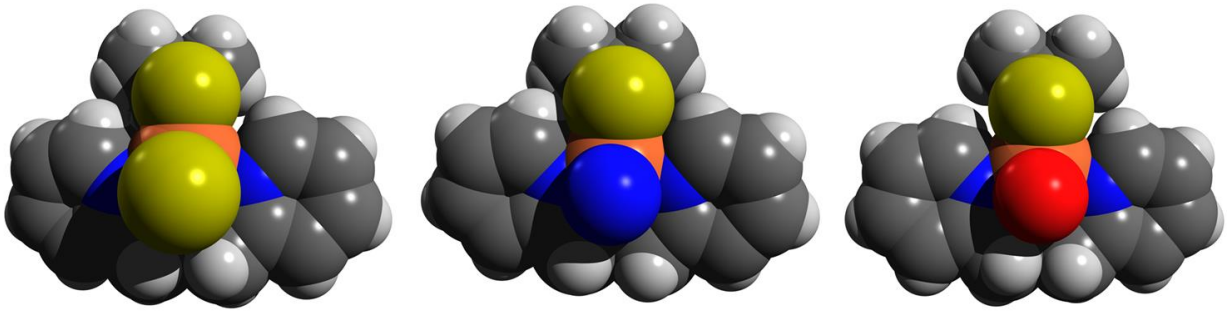

Figure 4.4. Space filling models of Fe(1) (left) and Fe(2) (middle) ions of $[Fe^{II}(S^{Me2}N_4(6\text{-H-DPEN}))(\mu\text{-}S^{Me2}N_4(6\text{-H-DPEN})Fe^{II}(MeCN)]^{2+}$ (**$1^{Py}{}_2$-MeCN**), and $[Fe^{II}(S^{Me2}N_4(6\text{-H-DPPN}))(MeOH)]^{+}$ (**1^{PyPN}**, right)[55]. Portions of the MeCN (Fe(2)) and MeOH (**1^{PyPN}**) have been omitted for clarity. Fe^{II} ions are shown in orange, sulfur atoms are shown in yellow, oxygen and nitrogen atoms are shown in red and blue, respectively.

As the two halves of **$1^{Py}{}_2$-MeCN** are both 6-coordinate, the structural parameters are not directly comparable to the 5-coordinate **1^{Mepy}** and **1^{Quino}**. However, this does suggest that either the open sites of the Fe^{II} ions of **$1^{Py}{}_2$-MeCN** are more accessible due to less steric bulk on the ligand scaffold, or that the metal ions are more Lewis acidic for 6-H-pyridine derivative. As the propyl-linked analogue of **1^{Py}** was previously synthesized and crystallographically characterized

as a solvent-bound 6-coordinate [$Fe^{II}(S^{Me2}N_4$(6-H-DPPN))(MeOH)](PF_6) (**1^{PyPN}**), the structural parameters of **1$^{Py}{}_2$-MeCN** were compared to **1^{PyPN}** to establish context on how the difference in ligand constraints (ethyl-linker versus propyl-linker) contributed to structural change. (Table 4.2) The octahedral angle variance ($\sigma_{\theta(oct)}{}^2$) was calculated using equation 4.1 to compare the distortions from an ideal octahedral geometry of the Fe ions. An $\sigma_{\theta(oct)}{}^2$ value closer to 0 represents a more ideal octahedral geometry at the metal center while higher values corresponds to a more distorted 6-coordinate metal center.[65] The Fe(2) ion for **1$^{Py}{}_2$-MeCN** ($\sigma_{\theta(oct)}{}^2$ = 5.859) was the least distorted compared to the Fe(1) center of **1$^{Py}{}_2$-MeCN** ($\sigma_{\theta(oct)}{}^2$ = 11.393) and **1^{PyPN}** ($\sigma_{\theta(oct)}{}^2$ = 9.382). (Table 4.2) Since the Fe centers of Fe(2) (**1$^{Py}{}_2$-MeCN**) and **1^{PyPN}** are both solvent bound (Fe(2) of **1$^{Py}{}_2$-MeCN**: MeCN; **1^{PyPN}**: MeOH), while Fe(1) has two thiolates coordinated, the comparison between the former two Fe centers would be more appropriate. (Figure 4.4) The covalent nature of the bridging thiolate of Fe(1) is expected to significantly contribute to the distortion reflected by the octahedral variance. As the octahedral variance values suggest the Et-linker Fe(2) of **1$^{Py}{}_2$-MeCN** is closer to an ideal octahedral geometry (where angles are closer to 90°) versus Pr-linker **1^{PyPN}**, better orbital overlap between metal d-orbitals and the ligands would be expected for the Fe(2) center. The degree of orbital overlap is also reflected in the spacing-filling diagram (Figure 4.4) and the Fe-S and Fe-$N^{Ar}{}_{avg}$ bond lengths.

$$\sigma_{\theta(oct)}{}^2 = \sum_{i=1}^{12}(\theta_i - 90°)^2/11 \qquad (4.1)^{65}$$

The Fe-S bond lengths of **1$^{Py}{}_2$-MeCN** and **1^{PyPN}**, with the exception of Fe(1)-S(2), are comparable to the reported 5-coordinate **1^{Mepy}** and **1^{Quino}**.[55] The shortest Fe-S bond of the Fe(2) ion of **1$^{Py}{}_2$-MeCN** (2.3125(13) Å) is consistent with a better orbital overlap, and a more covalent Fe-S bond. The bond distance between the bridging thiolate and Fe(1) ion of **1$^{Py}{}_2$-MeCN** (Fe(1)-

S(2) = 2.5286(12) Å) is much longer than Fe(1)-S(1) (2.3597(14) Å) and Fe(2)-S(2) (2.3125(13) Å) but is still within their covalent radii (2.62 Å).[66] The covalent natural of the bridging thiolate contributes to the elongated Fe(1)-S(1), and therefore worse orbital overlap and a stronger octahedral distortion.

The shorter Fe-N^{Ar} bonds of the Fe(2) ion (Fe(2)-N^{Ar}_{avg} = 1.995(4) Å), are likely due to the lowered steric constraints of the ligand backbone, suggesting the Fe^{II} ion is less Lewis acidic than in $\mathbf{1^{PyPN}}$ (Fe-N^{Ar}_{avg} = 2.155(3) Å), which has also been illustrated in the structurally analogous Mn^{II} derivatives.[3] A more accessible N^{Ar}-Fe-N^{Ar} angle (Fe(2) of $\mathbf{1^{Py_2}}$**-MeCN** = 164.68(15)°, $\mathbf{1^{PyPN}}$ = 151.33(10)°) was also present and is shown in the space filling diagrams (Figure 4.4). The difference in angle implies the ligand constraint from the Pr-linker of $\mathbf{1^{PyPN}}$ restricts the structural rearrangement to achieve a better overlap between the metal ion d-orbitals and the ligand backbone, as well as a more accessible Fe^{II} ion.

Table 4.2. Selected Bond Distances (Å) and Bond Angles (deg) for $[Fe^{II}(S^{Me2}N_4(6\text{-Me-DPEN}))](PF_6)$ (**1^{Mepy}**)[55], $[Fe^{II}(S^{Me2}N_4(QuinoEN))](PF_6)$ (**1^{Quino}**)[55], $[Fe^{II}(S^{Me2}N_4(6\text{-H-DPEN}))(\mu\text{-}S^{Me2}N_4(6\text{-H-DPEN})Fe^{II}(MeCN)](PF_6)_2$ (**1^{Py}$_2$-MeCN**), and $[Fe^{II}(S^{Me2}N_4(6\text{-H-DPPN}))(MeOH)](PF_6)$ (**1^{PyPN}**)[55,57].

	1^{Mepy}	**1^{Quino}**	**1^{Py} (Fe(1))**	**1^{PyPN}**		**1^{Py} (Fe(2))**
Fe(1)-N(1)	2.132(4)	2.111(2)	2.176(4)	2.169(3)	**Fe(2)-N(5)**	1.939(4)
Fe(1)-N(2)	2.253(4)	2.226(2)	2.236(4)	2.273(3)	**Fe(2)-N(6)**	2.003(4)
Fe(1)-N(3)	2.165(4)	2.152(2)	2.213(4)	2.152(3)	**Fe(2)-N(7)**	1.988(4)
Fe(1)-N(4)	2.191(4)	2.159(2)	2.198(4)	2.158(3)	**Fe(2)-N(8)**	2.002(4)
Fe(1)-N^{Ar}$_{avg}$	2.178(4)	2.156(2)	2.206(4)	2.155(3)	**Fe(2)-N^{Ar}$_{avg}$**	1.995(4)
Fe(1)-S(1)	2.326(1)	2.3357(9)	2.3597 (14)	2.3351(9)	**Fe(2)-S(2)**	2.3125(13)
Fe(1)-X	N/A	N/A	2.5286(12)[a]	2.210(2)[b]	**Fe(2)-N(9)**	1.931(4)
S(1)-Fe(1)-N(1)	81.5(1)	82.91(7)	80.31(12)	82.13(7)	**S(2)-Fe(2)-N(5)**	83.30(11)
S(1)-Fe(1)-N(2)	158.7(1)	157.80(6)	159.48(10)	178.58(8)	**S(2)-Fe(2)-N(6)**	169.14(12)
S(1)-Fe(1)-N(3)	116.1(1)	106.98(7)	104.69(11)	104.03(8)	**S(2)-Fe(2)-N(7)**	97.40(11)
S(1)-Fe(1)-N(4)	115.0(1)	121.74(7)	103.42(11)	104.11(8)	**S(2)-Fe(2)-N(8)**	97.78(12)
S(1)-Fe(1)-X	N/A	N/A	105.35(5)[a]	91.94(7)[b]	**S(2)-Fe(2)-N(9)**	97.97(11)
N(1)-Fe(1)-N(3)	123.1(1)	120.28(9)	80.25(14)	93.00(11)	**N(5)-Fe(2)-N(7)**	93.71(16)
N(1)-Fe(1)-N(4)	121.0(1)	119.21(9)	94.88(14)	96.16(11)	**N(5)-Fe(2)-N(8)**	90.13(15)
N(3)-Fe(1)-N(4)	100.5(1)	104.91(9)	150.16(15)	151.33(10)	**N(7)-Fe(2)-N(8)**	164.68(15)
τ-value	0.59	0.60	N/A	N/A	**τ-value**	N/A
$\sigma_{\theta(oct)}^2$	N/A	N/A	11.393	9.382	**$\sigma_{\theta(oct)}^2$**	5.859

Note: [a]X = S(2), [b]X = O(1)

4.3.2 *Characterization of $1^{Py}{}_2$-MeCN in Solution State*

In order to investigate the nuclearity of **$1^{Py}{}_2$-MeCN** in solution, magnetic susceptibility of **$1^{Py}{}_2$-MeCN** was obtained using Evans' method.[54] While the bimetallic $Fe^{II}{}_2$ species would likely be diamagnetic (S = 0) due to antiferromagnetic coupling between the Fe^{II} centers, a high spin monomeric Fe^{II} species would be expected to be high spin (S = 2). The magnetic susceptibility of **$1^{Py}{}_2$-MeCN** was obtained in two commonly used solvents, MeOD-d_4 (μ_{eff} = 4.92 B.M. at 298K, Figure 4.5 top, Table 4.3) and MeCN-d_3 (μ_{eff} = 3.60 B.M. at 298K, Figure 4.5 bottom, Table 4.3). Both spectra show paramagnetic signals, which would not be expected for a bimetallic $Fe^{II}{}_2$ species in solution.

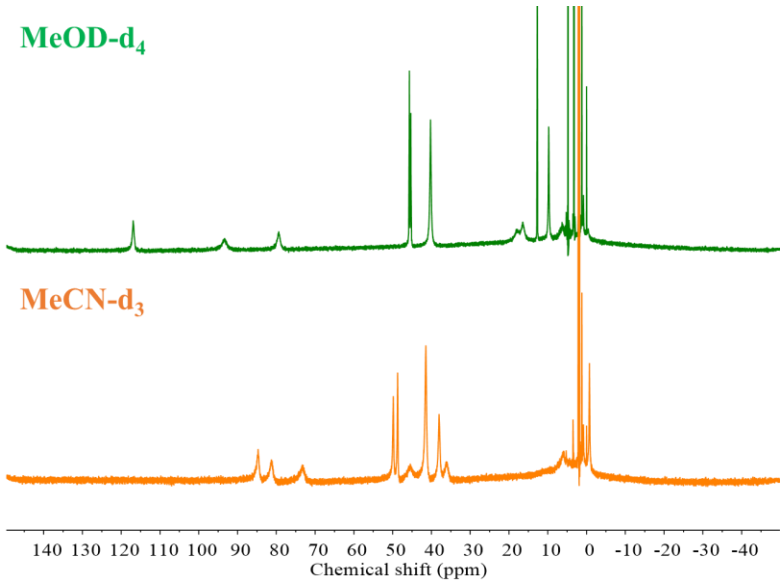

Figure 4.5. ^{1}H NMR spectrum of **$1^{Py}{}_2$-MeCN** in MeOD-d_4 (green, top) and MeCN-d_3 (orange, bottom) at 298 K.

The magnetic susceptibility of **$1^{Py}{}_2$-MeCN** in MeOD-d_4 suggests a monomeric high spin S = 2 Fe^{II} species at 298 K (μ_{eff} = 4.92 B.M.). The assignment of high spin is further demonstrated with evidence from high resolution Linear Trap Quadropole (LTQ) Orbitrap mass spectrometry. The detected isotopomers differs by single mass units, as opposed to half mass

units. (Figure 4.7, top) The experimental mass spectrum matches the calculated isotope pattern (Figure 4.7, bottom) for a monocationic, 6-coordinate solvent bound $[Fe^{II}(S^{Me2}N_4(6\text{-H-DPEN}))(OMe)]^+$ (**1^{Py}-OMe**) with a primary mass peak detected at 428.13 m/z (M+31). Additional temperature-dependent Evans' method experiments of **1^{Py}-OMe** in MeOD-d_4 show a decrease in μ_{eff} per Fe (from 4.92 B.M. to 3.96 B.M., Figure 4.6, right, Table 4.3) as the temperature increases (298 to 323 K). A temperature dependent dimerization process could explain the decrease in μ_{eff} due to an increase in the concentration of spin-coupled dimers. However, one would expect dimerization to be less favored at higher temperatures, given that entropy effects become more important at higher temperatures. Therefore, the more likely explanation is that a coordinated solvent molecule dissociates as the temperature increases, resulting in the formation of a monomeric 5-coordinate Fe^{II} species with an intermediate spin S = 1 (μ_{eff} = 2.83 B.M.).

Table 4.3. Temperature-dependent magnetic moments (μ_{eff} per Fe) of **1^{Py}_2-MeCN** in MeCN-d_3 and MeOD-d_4 using Evans' method. Temperature ranges from 298 K to 323 K (5 K increments).

Temperature (K)	μ_{eff} per Fe in MeCN	μ_{eff} per Fe in MeOH
298	3.60	4.92
303	3.97	4.51
308	4.31	4.43
313	4.55	4.39
318	4.75	4.23
323	4.98	3.96

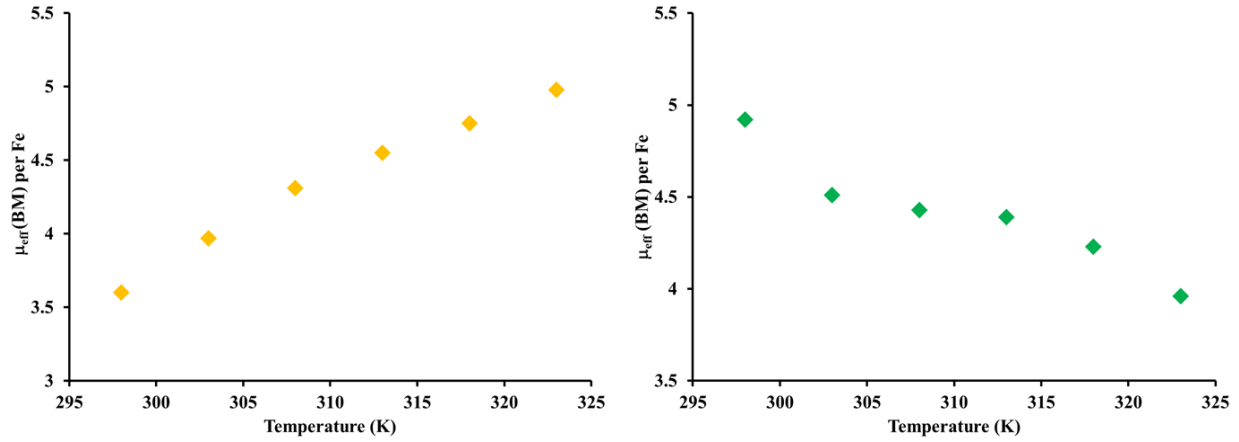

Figure 4.6. Temperature-dependent magnetic moments (μ_{eff} per Fe) of $\mathbf{1^{Py}_2}$**-MeCN** in MeCN-d_3 (left) vs MeOD-d_4 (right) using Evans' method. Temperature ranges from 298 K to 323 K (5 K increments).

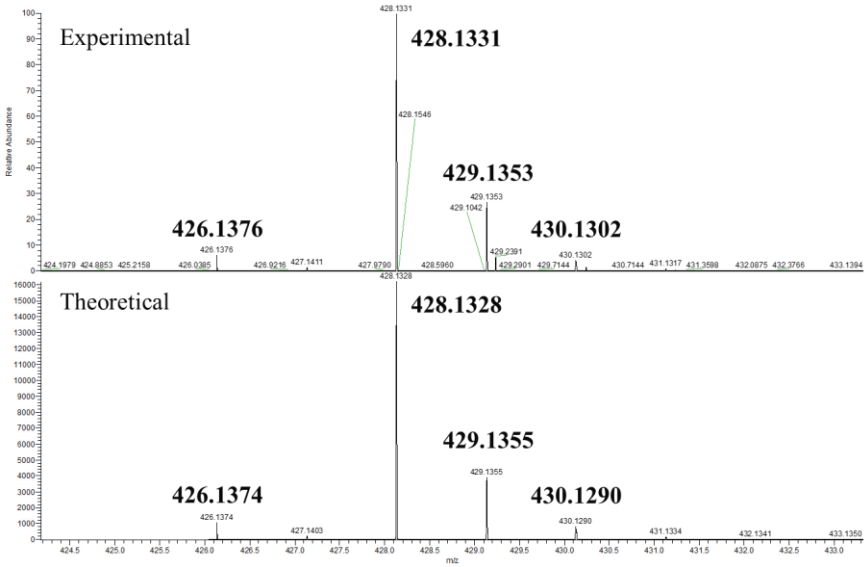

Figure 4.7. LTQ ion trap mass spectrum of $\mathbf{1^{Py}}$ in MeOH (top) and theoretical mass spectrum of MeO-bound monocationic monomer $\mathbf{1^{Py}}$**-OMe** (bottom). Isotopomers suggest that the majority of $\mathbf{1^{Py}}$ in MeOH is in a monocationic monomer form with MeOH bound at ambient temperature.

The opposite trend was observed in MeCN-d_4 (Figure 4.6, left, and Table 4.3). The μ_{eff} per Fe increases (from 3.6 B.M. to 4.98 B.M.) as temperature increases (298 to 323 K). This observation suggests the possibility of temperature-dependent equilibrium between a monomeric (high spin, S = 1) and a bimetallic species (S = 0). The high-resolution mass spectrum of $\mathbf{1^{Py}_2}$**-MeCN** provides further evidence with isotopomers observed that differed by both half and single

mass units, without MeCN coordinating.(Figure 4.8, top) This is consistent with an equilibrium between a monomeric and a dimeric species at room temperature. As shown previously by the Kovacs group,[13] the ratio μ_{eff}^2(experimental)/μ_{eff}^2(theoretical), obtained by equations 4.2-4.5, would provide the percentage of monomeric species in solution at a given temperature. This analysis suggests that **$1^{Py}{}_2$-MeCN** exists as a mixture of 52.3% monomeric **1^{Py}** and 47.7% bimetallic **$1^{Py}{}_2$** in MeCN at 298 K.

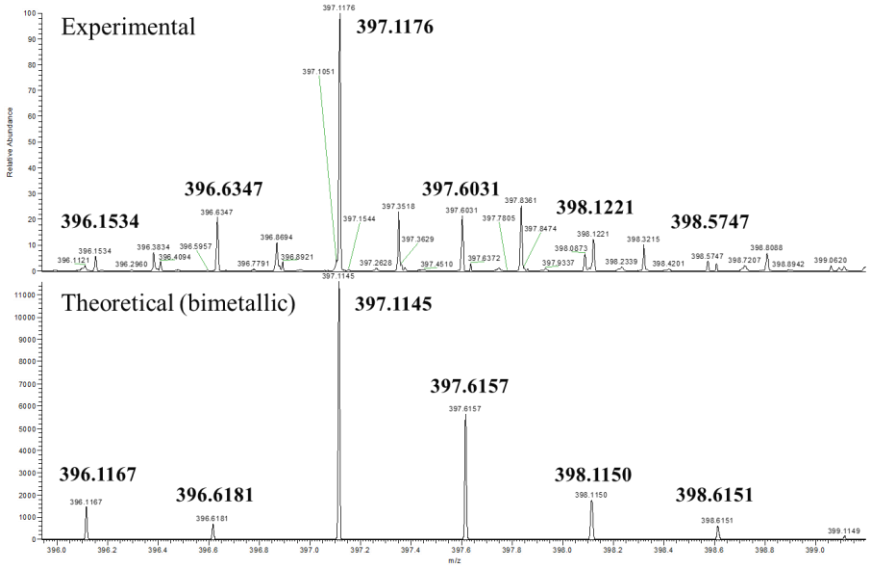

Figure 4.8. LTQ ion trap mass spectrum of **1^{Py}** in MeCN (top) and theoretical mass spectrum of dicationic bimetallic species (bottom). Isotopomers suggest a mixture of bimetallic and monomer in MeCN solution at ambient temperature.

$$2[Monometallic] \rightleftarrows [Bimetallic] \qquad (4.2)$$

$$K_{eq} = \frac{[Monometallic]^2}{[Bimetallic]} \qquad (4.3)$$

$$\mu_{eff} = 2.84\sqrt{\chi_p \cdot T} \qquad (4.4)$$

$$\%\, Monometallic = \frac{{\mu_{eff}}^2(Experimental)}{{\mu_{eff}}^2(Theoretical)} \qquad (4.5)$$

4.3.3 *Electronic Absorption Spectroscopy of* 1^{Py}

In contrast to $\mathbf{1}^{\mathbf{Tren}}$, the π-donating thiolate and π-accepting pyridine ligands contained in complexes $\mathbf{1}^{\mathbf{Py}}$, $\mathbf{1}^{\mathbf{Mepy}}$, and $\mathbf{1}^{\mathbf{Quino}}$ result in intensely colored solutions, allowing for Fe^{II} reactivity to be monitored via electronic absorption spectroscopy. All three complexes of the Fe DPEN series show intense charge transfer (CT) bands in the visible region of the EAS spectra (λ_{max} (nm) (ε (M^{-1} cm^{-1})): $\mathbf{1}^{\mathbf{Py}}$: 474 (2174); $\mathbf{1}^{\mathbf{Mepy}}$: 394 (1328); $\mathbf{1}^{\mathbf{Quino}}$: 502 (777), Figure 4.9). The energy bands are proposed to involve Fe-S → N-heterocycle π* MLCT transition. As shown previously by the π-donating thiolate and π-accepting α-imino-N-heterocycle $[Fe^{II}(tame\text{-}N_2S(py)_2)]_2^{2+}$ (λ_{max} = 580, 650 nm) and $[Fe^{II}(tame\text{-}N_2S(quino)_2)]_2^{2+}$ (λ_{max} = 607, 719 nm), the lowest-energy bands red shifts as the N-heterocycle ring size increases from pyridine to quinoline.[13] A similar trend is observed with the Fe DPEN series, where the CT energy band red shifts comparing $\mathbf{1}^{\mathbf{Py}}$ to $\mathbf{1}^{\mathbf{Quino}}$, which would support its assignment as a Fe-S → N-heterocycle π* MLCT transition.

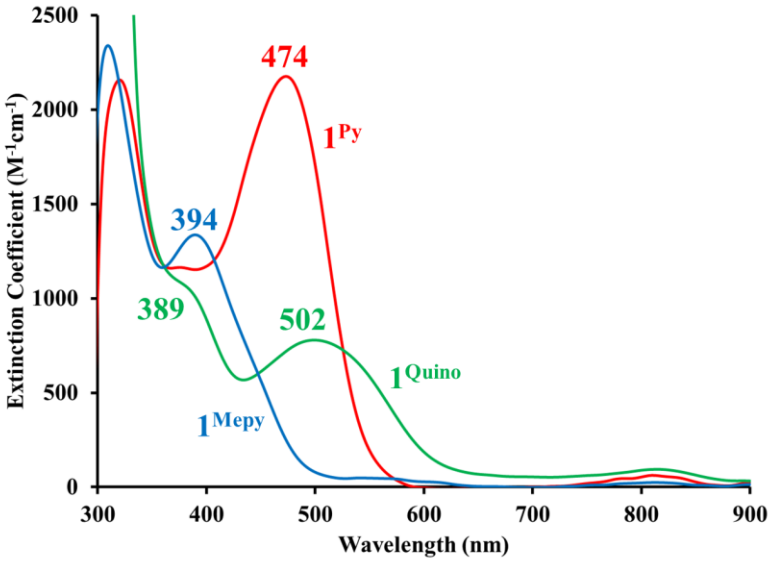

Figure 4.9. EAS spectrum of Fe DPEN complexes $\mathbf{1}^{\mathbf{Py}}$, $\mathbf{1}^{\mathbf{Mepy}}$, and $\mathbf{1}^{\mathbf{Quino}}$ at room temperature. [$\mathbf{1}^{\mathbf{Py}}$], [$\mathbf{1}^{\mathbf{Mepy}}$], [$\mathbf{1}^{\mathbf{Quino}}$] = 0.2 mM in THF.

The more constrained Pr-linker analogue of $\mathbf{1}^{\mathbf{Py}}$, complex $\mathbf{1}^{\mathbf{PyPN}}$, was shown to have coordinating solvents (MeCN, MeOH, THF) reversibly bind to the open coordination site in place of the MeOH ligand present in the solid state structure.[57] The electronic absorption spectra of $\mathbf{1}^{\mathbf{Py}}$ obtained in various solvents at both room temperature (λ_{max} (nm) (ε (M^{-1} cm $^{-1}$)): MeCN: 447 (1276); DCM: 401 (1224); MeOH: 447 (1250); THF: 458 (1515), Figure 4.10) and low temperatures (-73 °C) (λ_{max} (nm) (ε (M^{-1} cm $^{-1}$)): DCM: 407 (1565); MeOH: 449 (1562); THF: 480 (2283), Figure 4.11) suggest coordinating solvents are reversibly binding to the open coordination site of $\mathbf{1}^{\mathbf{Py}}$, similar to $\mathbf{1}^{\mathbf{PyPN}}$ [57]. The Fe-S → N-heterocycle π^* MLCT energy band red shifts in coordinating solvents comparing to non-coordinating solvent (DCM). (Figure 4.10) As solvent binds to the open site, electron density increases at the metal center and leads to a decrease in Fe^{II} ion Lewis acidity. The red shift could also indicate a better overlap between the metal and pyridine π^* orbitals (6-coordinate versus 5-coordinate).

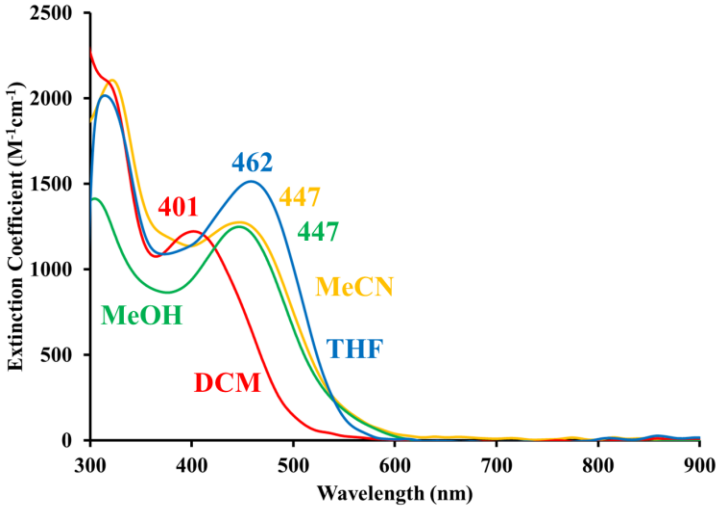

Figure 4.10. EAS spectrum of $\mathbf{1}^{\mathbf{Py}}$ in different solvents, MeCN (yellow), DCM (red), MeOH (green), and THF (blue). Spectra recorded at room temperature. [$\mathbf{1}^{\mathbf{Py}}$] = 0.2 mM.

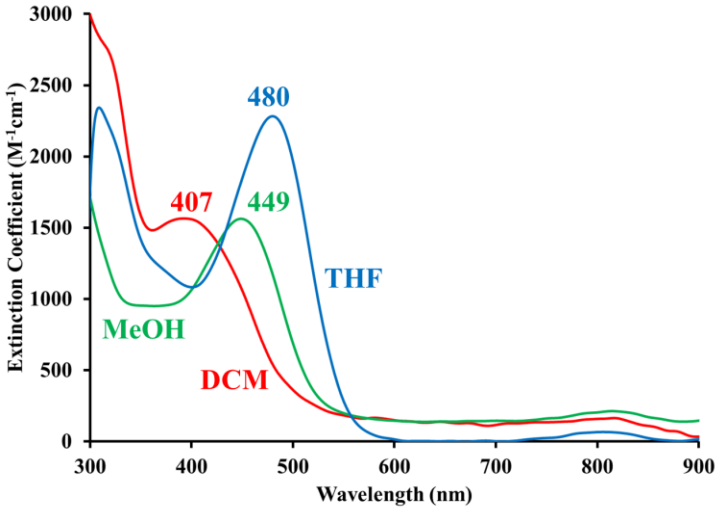

Figure 4.11. EAS spectra of $\mathbf{1^{Py}}$ in different solvents, DCM (red), MeOH (green), and THF (blue). Spectrum recorded at -73 °C. [$\mathbf{1^{Py}}$] = 0.2 mM.

4.3.4 *Oxidation-Reduction Behavior of Fe^{II} DPEN Complexes*

Complex $\mathbf{1^{Py}}$ (Fe(2) ion) was shown to be less Lewis acidic than $\mathbf{1^{PyPN}}$ as evidenced from the solid-state structures. As $\mathbf{1^{Mepy}}$ and $\mathbf{1^{Quino}}$ are both 5-coordinate and cannot be directly structurally compared to the 6-coordinate $\mathbf{1^{Py}}$, reduction potentials would be a more useful parameter for the evaluation of the Lewis acidity of each Fe ion. The cyclic voltammogram (CV) of $\mathbf{1^{Py}}$ was obtained in MeCN and was referenced to SCE using ferrocene (-380 mV vs SCE) as a standard. (Figure 4.12) The CV of $\mathbf{1^{Py}}$ contained a reversible $Fe^{III/II}$ couple at $E_{1/2}$ = -89 mV (vs SCE) with ΔE = 66 mV. Peak potentials ($E_{p,c}$ and $E_{p,a}$) did not change with variations of the scan rates, indicating the wave is reversible versus quasi-reversible or irreversible. The difference between $E_{p,c}$ and $E_{p,a}$ (ΔE) is consistent for the wave representing a one-electron transfer. Reduction potentials of $\mathbf{1^{Py}}$, along with $\mathbf{1^{PyPN}}$, $\mathbf{1^{Mepy}}$, and $\mathbf{1^{Quino}}$, are reported in Table 4.4.

Complex $\mathbf{1^{Py}}$ is more easily oxidized with the lowest $E_{1/2}$ = -89 mV vs SCE , compared to $\mathbf{1^{PyPN}}$ and the other two Fe^{II} DPEN complexes $\mathbf{1^{Mepy}}$ and $\mathbf{1^{Quino}}$. The less positive potential of the

$Fe^{III/II}$ couple implies the highest occupied molecular orbitals (HOMOs) are higher in energy than the other three N-heterocyclic complexes, making the oxidized Fe^{III}-$\mathbf{1^{Py}}$ the most accessible. The reduction potential of $\mathbf{1^{Py}}$ reflects a less Lewis acidic Fe^{II} ion than $\mathbf{1^{PyPN}}$ (+66 mV), which is consistent with their structural data. The positive shift in potential (+156 mV) suggests the added ligand constraints of the Pr-linker plays an important role in the metal ion Lewis acidity.

As shown with the structurally analogous Mn^{II} derivatives, the reduction potential of $M^{III/II}$ and the O_2 activation barrier increase as the metal ion becomes less accessible.[3] Both of the 6-coordinate Fe complexes containing the pyridine amines have significantly lower potentials (as much as -496 mV) than the 5-coordinate $\mathbf{1^{Mepy}}$ (+407 mV) and $\mathbf{1^{Quino}}$ (+401 mV). This difference is consistent with more electron density around the metal center for the solvent bound $\mathbf{1^{Py}}$ and $\mathbf{1^{PyPN}}$. The more sterically encumbered N^{Ar} ligand scaffolds of $\mathbf{1^{Mepy}}$ and $\mathbf{1^{Quino}}$ contribute to the less stable Fe^{III} species of their corresponding complexes.

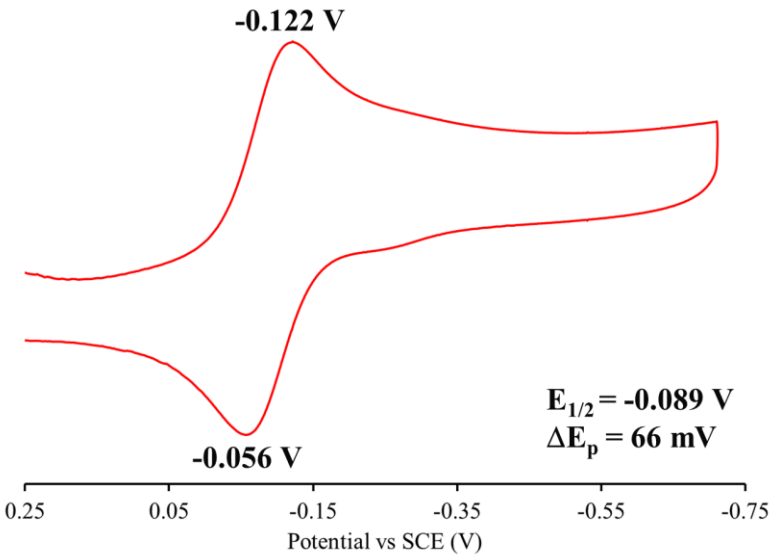

Figure 4.12. Cyclic voltammogram of $\mathbf{1^{Py}}$ in MeCN at room temperature. Potentials shown are in V vs SCE, recorded with glassy carbon working electrode, $Ag/AgNO_3$ reference electrode, and Bu_4NPF_6 as supporting electrolyte. [$\mathbf{1^{Py}}$] = 0.2 mM. Scan rate: 100 mV/s.

Table 4.4. Reduction potentials (mV vs SCE) of $[Fe^{II}(S^{Me2}N_4(6\text{-H-DPEN}))(\mu\text{-}S^{Me2}N_4(6\text{-H-DPEN})Fe^{II}(MeCN)]^{2+}$ (**1^{Py}-MeCN**), $[Fe^{II}(S^{Me2}N_4(6\text{-H-DPPN}))(MeCN)]^{+}$ (**1^{PyPN}-MeCN**)[55], $[Fe^{II}(S^{Me2}N_4(QuinoEN))]^{+}$ (**1^{Quino}**)[55], and $[Fe^{II}(S^{Me2}N_4(6\text{-Me-DPEN}))]^{+}$ (**1^{Mepy}**)[55]. All potentials recorded in MeCN at room temperature.

Complex	$E_{1/2}$ (vs SCE)
1^{Py}-MeCN	-89 mV
1^{PyPN}-MeCN	+66 mV
1^{Quino}	401 mV
1^{Mepy}	407 mV

4.3.5 *Correlation between Structural and Spectroscopic Properties for the Fe^{II} DPEN Series*

The Kovacs group has previously shown that the changes to the N-heterocyclic amine ligand scaffold of the Mn analogue led to strong correlations between the metal-ligand bond distances and angles of Mn^{III}-alkylperoxo compounds, and their electronic structures.[50] Despite the crystal structure of **$1^{Py}{}_2$-MeCN** (Figure 4.2) indicating a 6-coodinate bimetallic nuclearity in solid-state and that fact that the difference in orbital overlap for 6-coodinate versus 5-coordinate would contribute to major differences in the Fe-S → N-heterocycle π* MLCT band, correlations between the structural (Fe-N bond lengths and angles) and spectroscopic parameters (reduction potential of Fe^{II} (**1**) and Fe-S → N-heterocycle π* MLCT band) were observed with the Fe^{II} DPEN series (**1^{Py}**, **1^{Mepy}**, and **1^{Quino}**). The parameters found for the Fe(2) ion of **$1^{py}{}_2$-MeCN** were used for comparison instead of Fe(1), since Fe(2), similar to **1^{Mepy}** and **1^{Quino}**, only had one thiolate in the coordination sphere. The structural parameters of all three complexes are reported in Table 4.2.

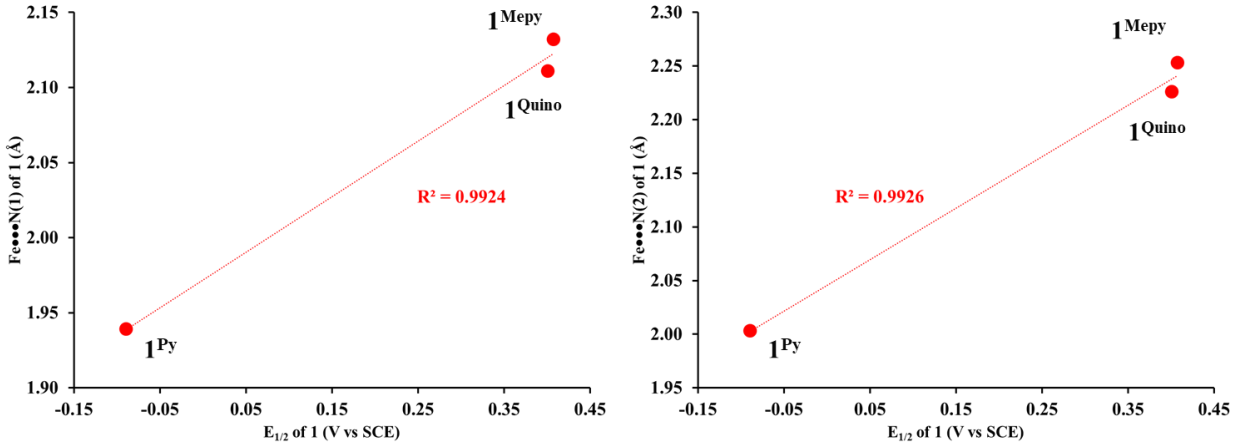

Figure 4.13. Correlation plots of Fe-N(1,2) bond lengths (Left: Fe-N(1), right: Fe-N(2)) versus reduction potential of $Fe^{III/II}$ of $\mathbf{1}^{\mathbf{Py}}$, $\mathbf{1}^{\mathbf{Mepy}}$, and $\mathbf{1}^{\mathbf{Quino}}$.

As shown in Figure 4.13 and 4.14, there are some correlations between the Fe-N bond lengths and the reduction potentials, where the longer the Fe-N bonds, the more positive the reduction potentials of the Fe^{II}. However, one would expect the opposite trend, where the more Lewis acidic the metal ion, the shorter the metal-ligand bonds would be observed. While this is indeed comparing 5- versus 6-coordinated Fe^{II} complexes, this opposite trend also shows how steric effect of the N-heterocyclic amines is possibly playing a role. The average distances between the Fe ion and N-heterocyclic amine nitrogens (N(3,4)) suggests the least sterically bulky 6-H-pyridine ligand of $\mathbf{1}^{\mathbf{Py}}$ allows shorter observed Fe-N^{Ar}_{avg} bonds. (Figure 4.14), despite a least Lewis acidic 6-coordinate Fe^{II} center.

A strong correlation between λ_{max} and Fe-N bond lengths of $\mathbf{1}^{\mathbf{Py}}$, $\mathbf{1}^{\mathbf{Mepy}}$, and $\mathbf{1}^{\mathbf{Quino}}$ (Figure 4.15 and 4.16) were also observed, wherein the energy of the bands red-shift as the Fe-N distances decrease and as the size of the pyridine ring decreases. The correlation implies these observed bands indeed involve the Fe-S → N-heterocycle π* MLCT transitions.

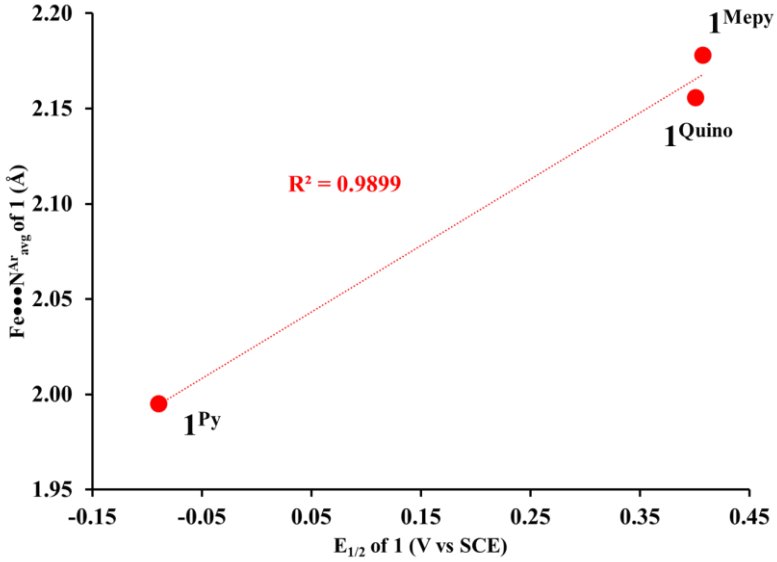

Figure 4.14. Plot illustrating the correlation of average Fe-N^{Ar}(3,4) bond length versus reduction potential of Fe$^{III/II}$ of **1^{Py}**, **1^{Mepy}**, and **1^{Quino}**.

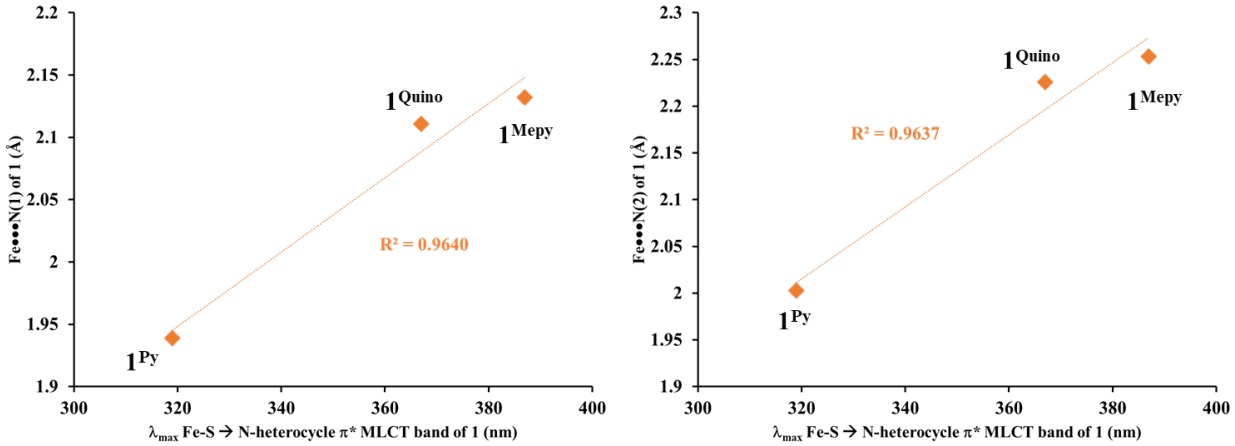

Figure 4.15. Correlation between Fe-N(1,2) bond lengths (Left: Fe-N(1), right: Fe-N(2)) and the Fe-S → N-heterocycle π* MLCT band of **1^{Py}**, **1^{Mepy}**, and **1^{Quino}**.

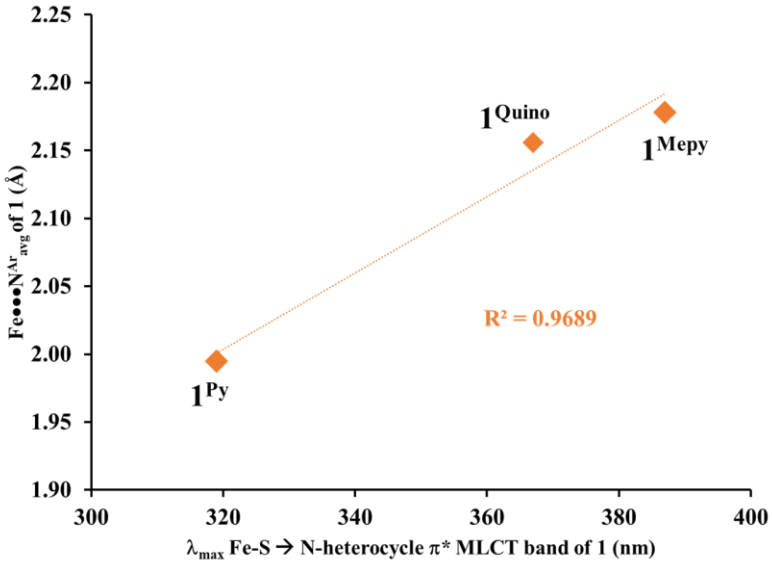

Figure 4.16. Correlation between average Fe-N^{Ar}(3,4) bond length and the Fe-S → N-heterocycle π* MLCT band of $\mathbf{1}^{\mathbf{Py}}$, $\mathbf{1}^{\mathbf{Mepy}}$, and $\mathbf{1}^{\mathbf{Quino}}$.

Correlations between the key angles N(1)-Fe-N(3)/N(4) versus reduction potential, as well as λ_{max} were also explored for another perspective on how the steric properties of the pyridine ligand scaffold might affect the Lewis acidity of the Fe^{II} ion. The 6th ligand (MeCN) coordinated to the Fe^{II} in the crystal structure of $\mathbf{1^{Py}_2}$**-MeCN**, results in N(1)-Fe-N(3,4) angles close to what is expected for an octahedral geometry (93.71° and 90.13° respectively for Fe(2) of $\mathbf{1^{Py}_2}$**-MeCN**), The key angles show a slight decrease when the 6-Me-pyridine ring is substituted with the less sterically intrusive quinoline (Table 4.2). The narrower angles show a correlation with the $Fe^{III/II}$ reduction potentials and λ_{max} of Fe^{II} complexes (Figure 4.17 and 4.18). As the angle decrease between the imine and N-heterocyclic amines, moving closer to 90°, the orbital overlap between the metal d-orbital and the π-acceptor ligands would be more efficient, which in turn would result in a less Lewis acidic Fe^{II} (Figure 4.17) and red shifts of the key EAS bands (Figure 4.18).

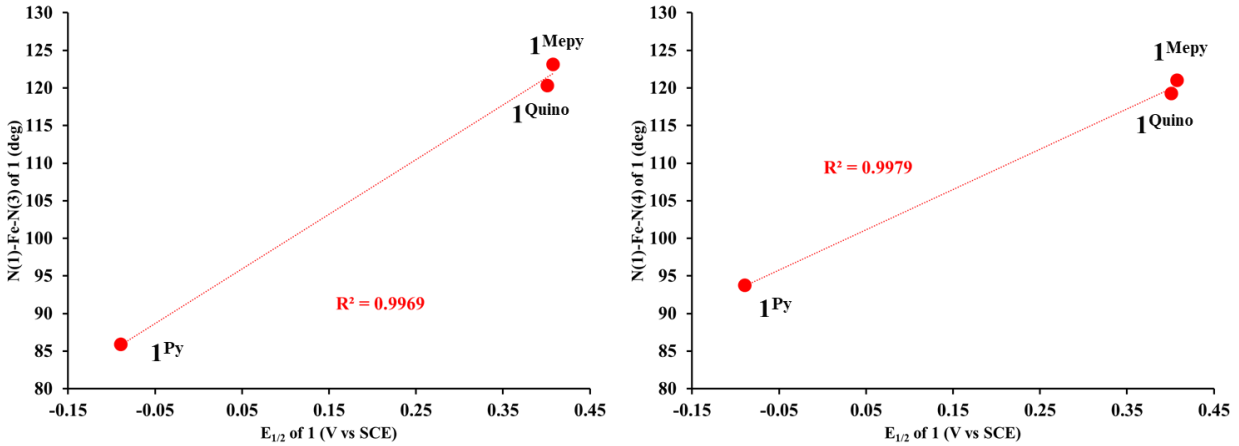

Figure 4.17. Correlation plots of N(1)-Fe-N(3,4) bond angles (Left: N(1)-Fe-N(3), right: N(1)-Fe-N(4)) versus reduction potential of $Fe^{III/II}$ of $\mathbf{1^{Py}}$, $\mathbf{1^{Mepy}}$, and $\mathbf{1^{Quino}}$.

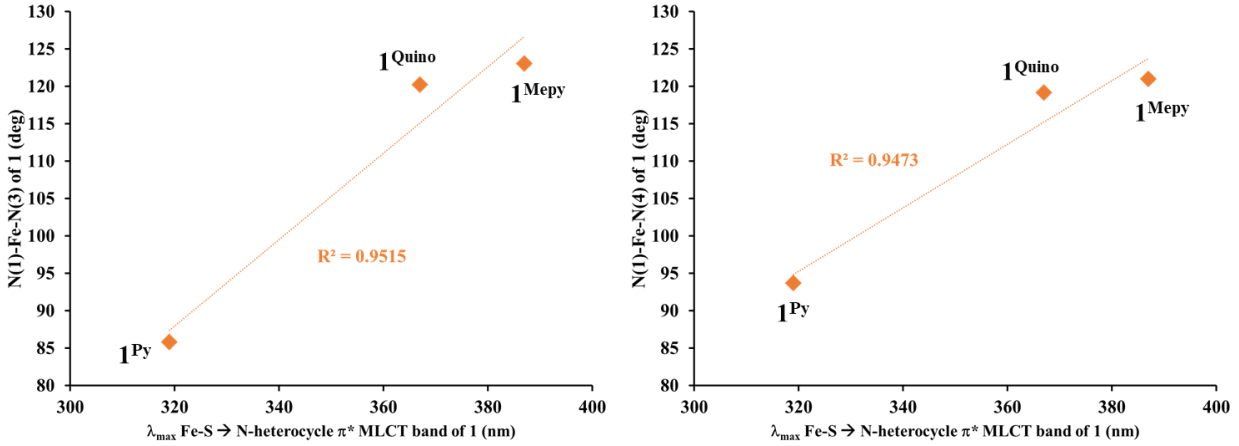

Figure 4.18. Correlation between N(1)-Fe-N(3,4) bond angles (Left: N(1)-Fe-N(3), right: N(1)-Fe-N(4)) and the Fe-S → N-heterocycle π* MLCT band of $\mathbf{1^{Py}}$, $\mathbf{1^{Mepy}}$, and $\mathbf{1^{Quino}}$.

Interesting correlations between the observed structural and spectroscopic parameters of the Fe^{II} DPEN series were observed despite the different coordination environments of the Fe^{II} centers. Even though the 6-H-pyridine ligand of $\mathbf{1^{Py}}$ had less electron donating abilities, the less steric bulk ligand is believed to be the reason for the observation of the shorter Fe-N bonds in the series, despite the lower Lewis acidity reflected in the significantly more negative reduction potential. All together, these experiments suggest the steric effects of the ligand play a strong role in the metal Lewis acidity compared to the electronic effects of the ligand. Previously with

the Mn analogues of the DPEN series, a strong correlation between the Lewis acidity of the metal ion and the activation barrier to O_2 binding was established, where the least Lewis acidic Mn complex with a more electron rich, less sterically encumbering ligand (6-MeO-pyridine) provided a flatter dioxygen activation reaction landscape, and allowed for the observation of more intermediates than in the case of more sterically bulky quinoline and 6-Me-DPEN ligands.[3] Dioxygen reactivity with $\mathbf{1}^{\mathbf{Py}}$, $\mathbf{1}^{\mathbf{Mepy}}$, and $\mathbf{1}^{\mathbf{Quino}}$ will be explored in further sections.

4.3.6 *Reactivity of Fe^{II} DPEN Complexes with Azide*

Previous studies showed solvent reversibly binding to the Pr-linker version $\mathbf{1}^{\mathbf{PyPN}}$,[57] while $\mathbf{1}^{\mathbf{Mepy}}$ and $\mathbf{1}^{\mathbf{Quino}}$ were found to be solvent independent[55]. Solvent binding was observed for the less sterically hindered $\mathbf{1}^{\mathbf{Py}}$ by X-ray crystallography, Evans' method, and mass spectrometry experiments. In order to determine whether an open site is available for small molecules, such as dioxygen (O_2) and superoxide ($O_2^{\bullet-}$), to bind to the Fe^{II} DPEN complexes, the reactivity with anionic small molecule, tetrabutylammonium azide, was performed. Azide (N_3^-) is known to possess the same charge and similar frontier orbitals as superoxide ($O_2^{\bullet-}$) and is often used an analogue to study superoxide reactivity in enzymes and biomimetic models.[44,67–70]

The incorporation of the N-heterocyclic amines allowed for the detection of 6-coordinate small molecule bound-Fe^{II} species resulting from the addition of azide by EAS spectroscopy. As shown in Figure 4.19 (left), when reacted with excess azide (10 equiv.), the energy band associated with Fe-S → N-heterocycle π* MLCT transition of $\mathbf{1}^{\mathbf{Py}}$ red shifted to 554 nm from 474 nm. This is consistent with either the binding of a sixth ligand or the displacement of a solvent molecule bound to Fe^{II} with azide. Both cases would result in the elevation of the metal d-orbital energy level. Excess azide (10 equiv.) was required for full formation of the putative

$[Fe^{II}(S^{Me2}N_4(6\text{-H-DPEN}))(N_3)]^+$ (**3^{Py}**) complex. This species was found to be unstable at ambient temperature. Upon exposure to dioxygen, an immediate irreversible conversion of the 554 nm peak to 413 nm was observed (Figure 4.19, right), with two isosbestic points at 522 nm and 622 nm. One possible explanation is an outer-sphere oxidation of the **3^{Py}** to a Fe^{III}-N_3 species, $[Fe^{III}(S^{Me2}N_4(6\text{-H-DPEN}))(N_3)]^+$ (**5^{Py}**). Mass spectrometry experiments at ambient temperature did not provide further characterization of the thermally unstable species.

Complexes **1^{Mepy}** and **1^{Quino}** were also reacted with excess azide under the same conditions. (Figure 4.20 and 4.21) Both spectra show a similar red shift of the lower energy band as observed with **1^{Py}**, presumably with the azide binding to both of the complexes to afford putative 6-coordinate azide bound Fe^{II} species, $[Fe^{II}(S^{Me2}N_4(6\text{-Me-DPEN}))(N_3)]^+$ (**3^{Mepy}**) and $[Fe^{II}(S^{Me2}N_4(\text{QuinoEN}))(N_3)]^+$ (**3^{Quino}**). The key transition band of putative **3^{Mepy}** red shifted to 471 nm (Figure 4.20) from 389 nm, while the band associated with **3^{Quino}** red shifted to 595 nm from 494 nm (Figure 4.21). The addition of another equivalent of azide did not further increase the absorbance of either species. Both intermediates were also found to be thermally unstable and decomposed upon warming, making further characterization challenging. The consistent red shift of the Fe-S → N-heterocycle π* MLCT transition upon the addition of azide suggests an open site is available for small molecules to bind for all three of the Fe^{II} DPEN complexes.

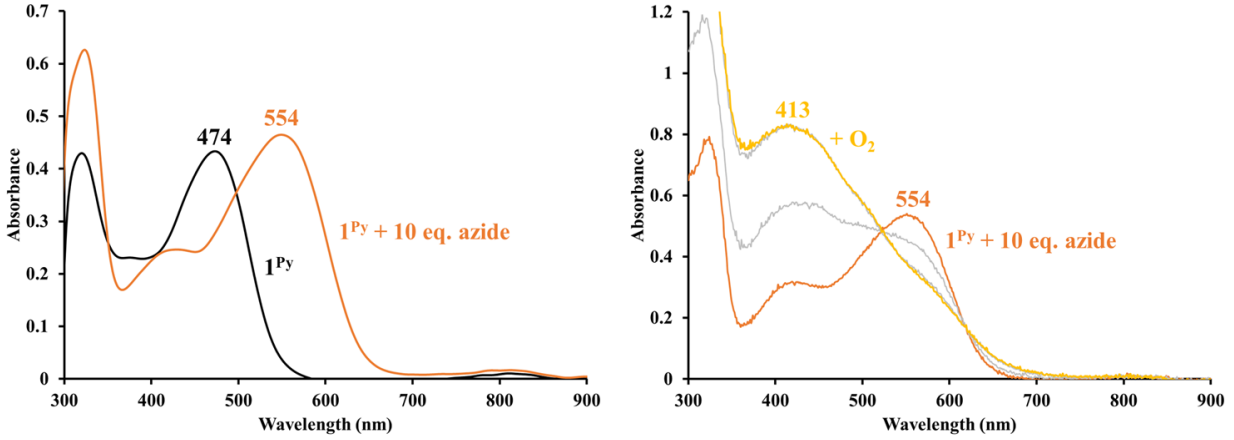

Figure 4.19. Left: EAS spectrum of the addition of 10 equiv. tetrabutylammonium azide (N_3^-) (orange trace) to $\mathbf{1^{Py}}$ (black trace) in THF at -73 °C. Right: EAS spectrum of the addition of O_2 (yellow trace) to solution of azide-bound $\mathbf{1^{Py}}$ (orange trace) at -73 °C. Scans recorded at 0.25 minutes intervals. Isosbestic points observed at 522 nm and 622 nm. [$\mathbf{1^{Py}}$] = 0.2 mM.

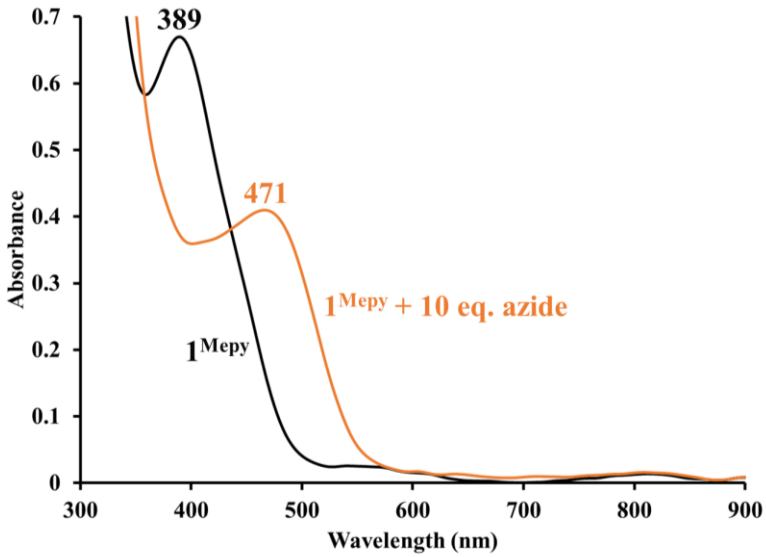

Figure 4.20. EAS spectrum of the addition of 10 equiv. tetrabutylammonium azide (N_3^-) (orange trace) to $\mathbf{1^{Mepy}}$ (black trace) in THF at -73 °C. [$\mathbf{1^{Mepy}}$] = 0.5 mM.

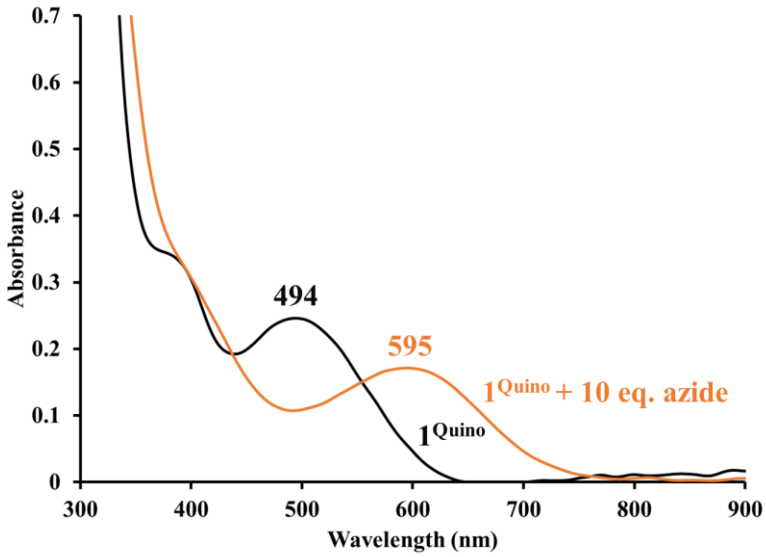

Figure 4.21. EAS spectrum of the addition of 10 equiv. tetrabutylammonium azide (N_3^-) (orange trace) to $\mathbf{1}^{\mathbf{Quino}}$ (black trace) in THF at -73 °C. [$\mathbf{1}^{\mathbf{Quino}}$] = 0.5 mM.

4.3.7 *Oxidation of Fe^{II} DPEN Complexes*

As established previously, one would expect a more stable ferric species for the least Lewis acidic $\mathbf{1}^{\mathbf{Py}}$, compared to $\mathbf{1}^{\mathbf{Mepy}}$ and $\mathbf{1}^{\mathbf{Quino}}$, due to the much lower reduction potential. The spectra of the generation of oxidized complexes, $[Fe^{III}(S^{Me2}N_4(6\text{-H-DPEN}))]^{2+}$ ($\mathbf{4}^{\mathbf{Py}}$), $[Fe^{III}(S^{Me2}N_4(6\text{-Me-DPEN}))]^{2+}$ ($\mathbf{4}^{\mathbf{Mepy}}$), and $[Fe^{III}(S^{Me2}N_4(\text{QuinoEN}))]^{2+}$ ($\mathbf{4}^{\mathbf{Quino}}$) by addition of corresponding oxidants, ferrocenium and tri-(ρ-tolyl)-aminium are shown in Figures 4.22 to 4.25.

The oxidized $\mathbf{4}^{\mathbf{Py}}$ was obtained by the addition of 1.0 equiv. ferrocenium hexafluorophosphate at room temperature (Figure 4.22). Two bands increasing in intensity at λ_{max} = 478 nm and 619 nm were observed for the green species. No change to the 478 nm and 619 nm bands was observed with further addition of oxidant, indicating a one-electron oxidation process and complete conversion of the Fe^{III} species. The red-shift of the energy bands would be more consistent with a S to metal charge transition (LMCT) for the new absorption features, as

opposed to the MLCT transition observed for the Fe^{II} species. Monitored by EAS, no sign of decomposition was observed when $\mathbf{4^{Py}}$ was exposed to O_2 for at least 5.5 hours at ambient temperature. An EPR spectrum with rhombic signal (g = 2.18, 2.15, 2.01) was obtained for $\mathbf{4^{Py}}$ at 77 K and was simulated with EasySpin[52] (Figure 4.23). The g-values were consistent with a low spin Fe^{III}, S = 1/2 system.

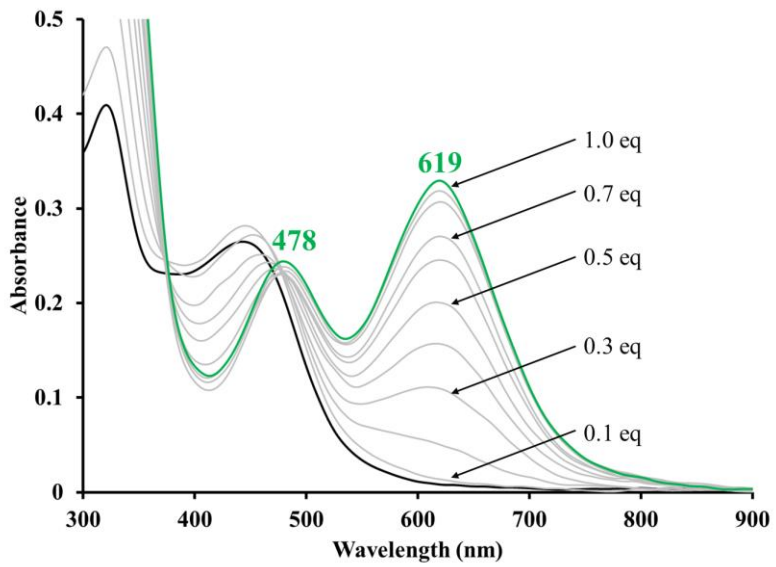

Figure 4.22. EAS spectrum of the oxidation of $\mathbf{1^{Py}}$ (black trace) using ferrocenium hexafluorophosphate in 0.1 equiv. aliquots in MeCN at room temperature. The growth of oxidized species $\mathbf{4^{Py}}$ (green trace) stopped after the addition of 1.0 equiv. of fc^+. [$\mathbf{1^{Py}}$] = 0.2 mM.

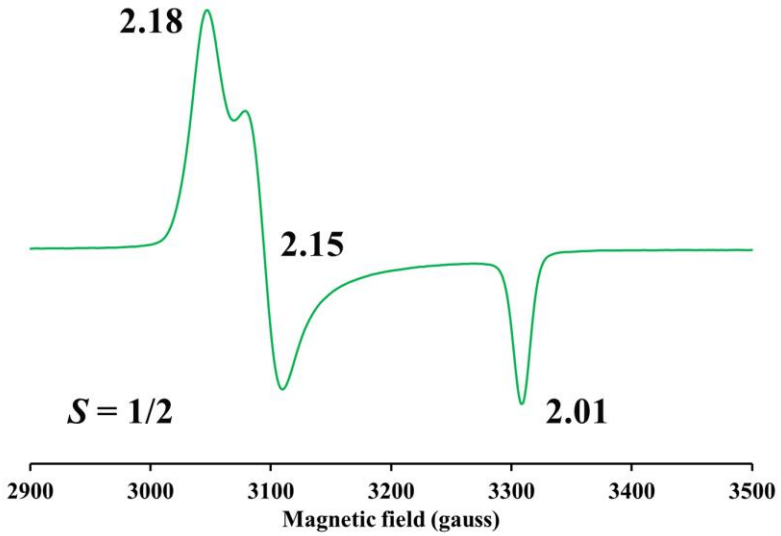

Figure 4.23. ⊥-mode, continuous-wave 9.30 GHz EPR spectrum of $\mathbf{4}^{\mathbf{Py}}$ in THF. Sample generated by addition of 1.0 equiv. ferrocenium hexafluorophosphate (in MeCN) to 1.0 mM $\mathbf{1}^{\mathbf{Py}}$ at room temperature. Spectrum was recorded at 77 K.

The more positive reduction potentials of complex $\mathbf{1}^{\mathbf{Mepy}}$ (+401 mV vs SCE) and $\mathbf{1}^{\mathbf{Quino}}$ (+407 mV vs SCE) compared to $\mathbf{1}^{\mathbf{Py}}$, required a stronger one-electron oxidant, tri-(ρ-tolyl)-aminium hexafluorophosphate (E°' = 780 mV vs SCE)[71]. Growth of similar LMCT bands to $\mathbf{4}^{\mathbf{Py}}$ were observed at 488 nm and 637 nm after the titration of 1.0 equiv. tri-(ρ-tolyl)-aminium hexafluorophosphate to $\mathbf{1}^{\mathbf{Mepy}}$, forming a green species (Figure 4.24). The presumed Fe^{III} species $\mathbf{4}^{\mathbf{Mepy}}$ was less stable than $\mathbf{4}^{\mathbf{Py}}$, as was predicted by the more positive reduction potential (an increase of +496 mV). Oxidized $\mathbf{4}^{\mathbf{Mepy}}$ decomposed immediately when generated at ambient temperature, therefore, the reactivity was performed at -40 °C. Decomposition of $\mathbf{4}^{\mathbf{Mepy}}$ was observed upon warming to room temperature. Similar reactivity was observed with $\mathbf{1}^{\mathbf{Quino}}$ and tri-(ρ-tolyl)-aminium hexafluorophosphate (Figure 4.25). LMCT bands of the green $\mathbf{4}^{\mathbf{Quino}}$ grew in at 467 nm and 643 nm upon addition of 1.0 equiv. of the oxidant. As in the case of $\mathbf{4}^{\mathbf{Mepy}}$, complex $\mathbf{4}^{\mathbf{Quino}}$ was only stable at lower temperatures, which created difficulty in further characterizations of the oxidized species.

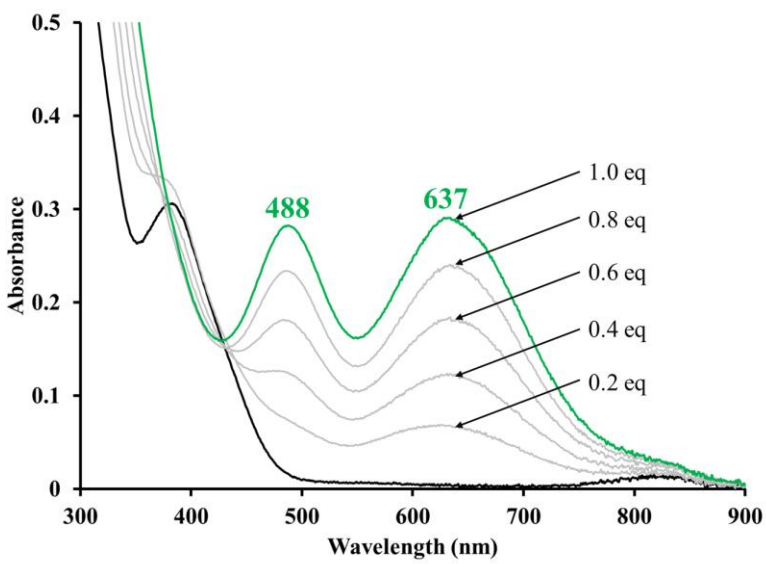

Figure 4.24. EAS spectrum of oxidation of $\mathbf{1}^{\mathbf{Mepy}}$ (black trace) using tri-(ρ-tolyl)-aminium hexafluorophosphate in 0.2 equiv. aliquots in MeCN at -40 °C. The growth of oxidized species $\mathbf{4}^{\mathbf{Mepy}}$ (green trace) stopped after the addition of 1.0 equiv. of oxidant. [$\mathbf{1}^{\mathbf{Mepy}}$] = 0.2 mM.

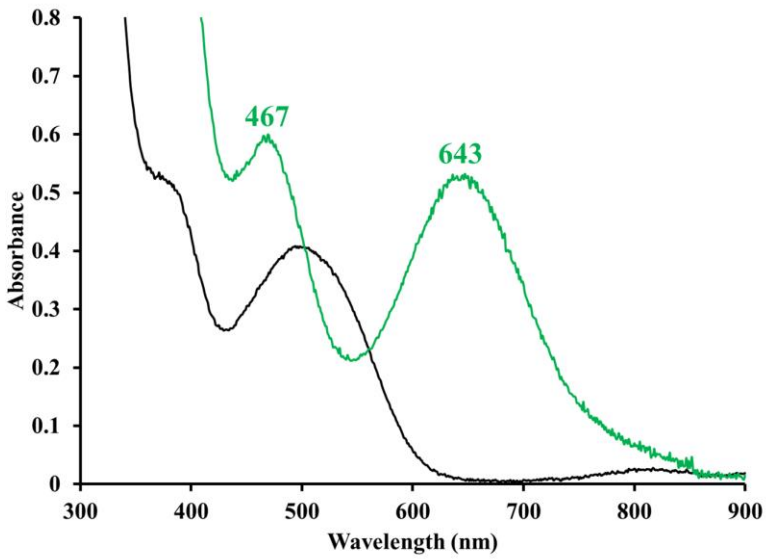

Figure 4.25. EAS spectrum of oxidation of $\mathbf{1}^{\mathbf{Quino}}$ (black trace) using 1.0 equiv. tri-(ρ-tolyl)-aminium hexafluorophosphate in THF at -73 °C. The oxidized species $\mathbf{4}^{\mathbf{Quino}}$ (green trace) was observed immediately upon the addition of 1.0 equiv. of oxidant. [$\mathbf{1}^{\mathbf{Quino}}$] = 0.5 mM.

4.3.8 *Reactivity of Fe^{III} DPEN Complexes with Azide*

Since the Fe^{II} complex $\mathbf{1^{Py}}$ has been shown to be solvent dependent, one would expect a more Lewis acidic Fe^{III} $\mathbf{4^{Py}}$ to have a higher affinity for a sixth ligand to coordinate. In order to determine if an open site is available for small molecules to bind to the oxidized Fe^{III} species, reactivity with the anionic ligand, azide (N_3^-), was performed with $\mathbf{4^{Py}}$, $\mathbf{4^{Mepy}}$, and $\mathbf{4^{Quino}}$. Acetonitrile was avoided as a solvent due to the fact that is known as a strongly coordinating solvent to the oxidized $[Fe^{III}(S^{Me2}N_4(tren))(MeCN)]^{2+}$ ($\mathbf{4^{Tren}}$),[72] and has a higher freezing point compared to other organic solvents. The Fe^{III} solutions were generated by adding 1 equiv. of oxidant to a precooled Fe^{II} solution. Immediate changes to the two Fe^{III} bands were observed upon the addition of 10 equiv. of azide to $\mathbf{4^{Py}}$ via EAS. The two bands for $\mathbf{4^{Py}}$ (492 nm and 606 nm) blue-shifted to 451 nm and 582 nm (Figure 4.26). The previously reported $[Fe^{III}(S^{Me2}N_4(tren))(N_3)]^+$ ($\mathbf{5^{Tren}}$) has shown a similar blue shift to the LMCT bands (from 585 nm ($\mathbf{4^{Tren}}$) to 425 nm and 535 nm).[72] The oxidized $\mathbf{4^{Py}}$ species is stable for more than 9 hours; no immediate change to the EAS spectrum was observed when the reaction mixture was warmed to room temperature or exposed to air.

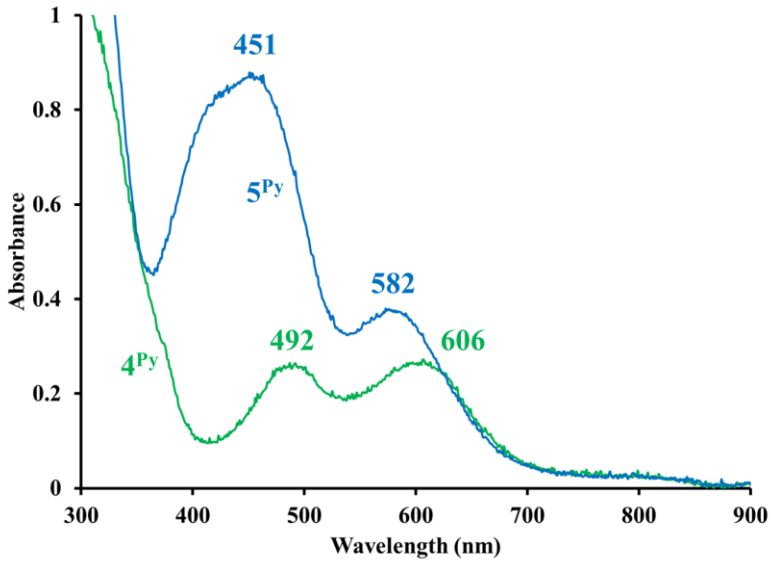

Figure 4.26. EAS spectrum of addition of 10 equiv. tetrabutylammonium azide (N_3^-) to oxidized $\mathbf{4^{Py}}$ in THF at -73 °C (blue trace). Solution of $\mathbf{4^{Py}}$ (green trace) generated by addition of 1 equiv. ferrocenium hexafluorophosphate (in MeCN) in THF at -73 °C. [$\mathbf{1^{Py}}$] = 0.2 mM.

Putative $[Fe^{III}(S^{Me2}N_4(6\text{-Me-DPEN}))(N_3)]^+$ ($\mathbf{5^{Mepy}}$) was generated by addition of 10 equiv. tetrabutylammonium azide to $\mathbf{4^{Mepy}}$, forming a thermally unstable species with similar low energy LMCT bands (λ_{max} = 459 nm and 600 nm) to $\mathbf{5^{Py}}$ (Figure 4.27). The azide bound Fe^{III} converts to a new species (λ_{max} = 409 nm) upon warming to ambient temperature. Putative $\mathbf{5^{Mepy}}$ (λ_{max} = 600 nm) could be regenerated by cooling the solution to -73 °C again, but with a slight residual feature at 409 nm (Figure 4.28). The regeneration suggests a temperature-dependent equilibrium between the azide bound species $\mathbf{5^{Mepy}}$ and the 409 nm species in the solution. This reversible binding effect could be a result of the Lewis acidity of the metal ion or the steric contribution from the 6-Me-pyridine ligand scaffold.

Temperature-dependent reactivity was also performed with putative $[Fe^{III}(S^{Me2}N_4(\text{QuinoEN}))(N_3)]^+$ ($\mathbf{5^{Quino}}$), which has a Lewis acidity of $\mathbf{1^{Quino}}$ (401 mV) comparable to 6-methyl $\mathbf{1^{Mepy}}$ (407 mV). The oxidized species was generated using a similar method to that of $\mathbf{5^{Py}}$ and $\mathbf{5^{Mepy}}$. The lowest energy LMCT band for $\mathbf{5^{Quino}}$ (λ_{max} = 409 nm and

474 nm) was much further blue-shifted (-173 nm) compared to $\mathbf{5}^{\mathbf{Py}}$ (-24 nm) and $\mathbf{5}^{\mathbf{Mepy}}$ (-43 nm) (Figure 4.29). The spectral features remain the same regardless of temperature or exposure to ambient atmosphere. The stability suggests azide binding is irreversible to $\mathbf{5}^{\mathbf{Quino}}$. The steric effect from the ligand scaffold seems to play a more significant role than electronic effect for the anionic ligand binding, i.e., the open site of the quinoline ligated complex is more accessible for small molecule binding, as the Lewis acidity of the Fe^{II} ions was similar ($Fe^{III/II}$ potentials of $\mathbf{1}^{\mathbf{Mepy}}$ and $\mathbf{1}^{\mathbf{Quino}}$ differs by only 6 mV).

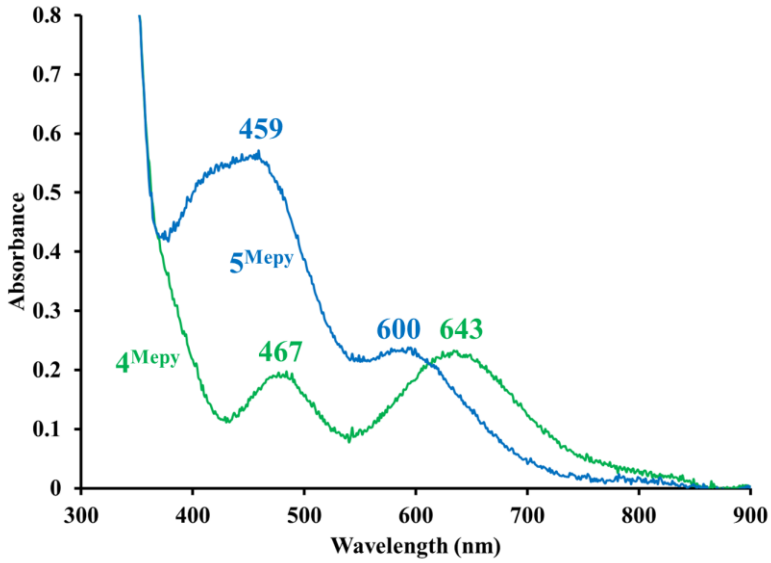

Figure 4.27. EAS spectrum of the addition of 10 equiv. tetrabutylammonium azide (N_3^-) to oxidized $\mathbf{4}^{\mathbf{Mepy}}$ in THF at -73 °C (blue trace). Solution of $\mathbf{4}^{\mathbf{Mepy}}$ (green trace) generated by addition of 1 equiv. tri-(ρ-tolyl)-aminium hexafluorophosphate in THF at -73 °C. [$\mathbf{1}^{\mathbf{Mepy}}$] = 0.2 mM.

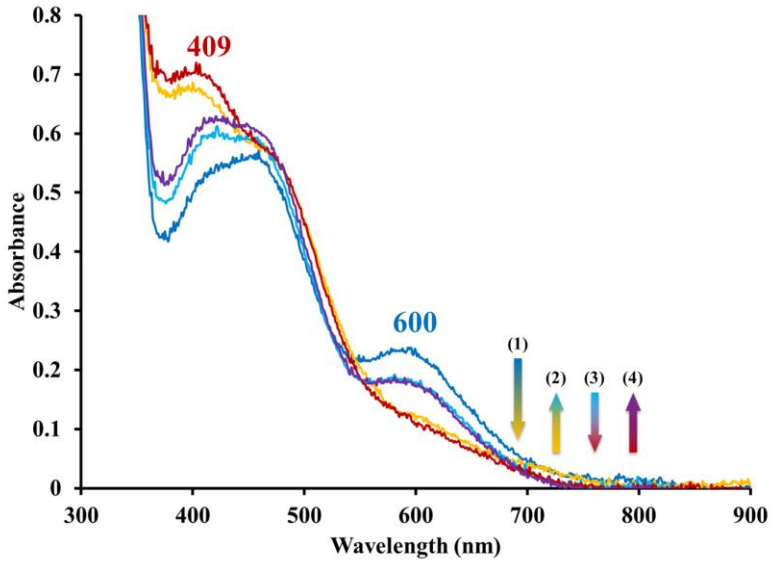

Figure 4.28. EAS spectrum of $\mathbf{5}^{\mathbf{Mepy}}$, generated by addition of 10 equiv. to $\mathbf{4}^{\mathbf{Mepy}}$ in THF at -73 °C (deep blue trace). (1) The solution was warmed to room temperature first (yellow trace), (2) then cooled to -73 °C (aqua blue trace). The warming/cooling process was repeated once again ((3): room temperature, maroon red trace, (4): -73 °C, purple trace). Solution of $\mathbf{4}^{\mathbf{Mepy}}$ generated by addition of 1 equiv. tri-(ρ-tolyl)-aminium hexafluorophosphate in THF at -73 °C. [$\mathbf{1}^{\mathbf{Mepy}}$] = 0.2 mM.

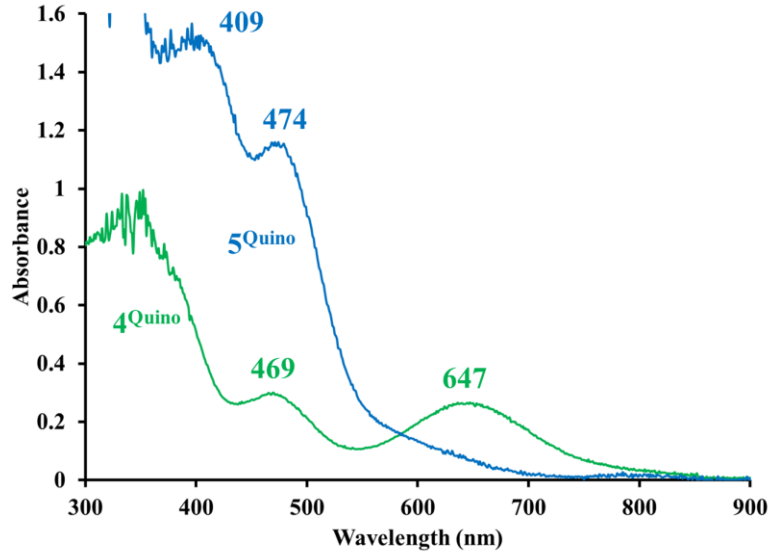

Figure 4.29. EAS spectrum of addition of 10 equiv. tetrabutylammonium azide (N_3^-) to oxidized $\mathbf{4}^{\mathbf{Quino}}$ in THF at -73 °C (blue trace). Solution of $\mathbf{4}^{\mathbf{Quino}}$ (green trace) generated by addition of 1 equiv. tri-(ρ-tolyl)-aminium hexafluorophosphate in THF at -73 °C. [$\mathbf{1}^{\mathbf{Quino}}$] = 0.5 mM.

4.3.9 *Reactivity of 1^{Py} with O_2 at Room Temperature*

Similarly to the Mn analogues of the DPEN series, the addition of dry O_2 to solution of complexes **1^{Py}**, **1^{Mepy}**, and **1^{Quino}** at room temperature leads to the formation of purple-colored thermodynamic products, $[Fe^{III}(S^{Me2}N_4(6\text{-H-DPEN}))]_2(\mu\text{-O})(PF_6)_2$ (**6^{Py}**, Scheme 4.3), $[Fe^{III}(S^{Me2}N_4(6\text{-Me-DPEN}))]_2(\mu\text{-O})(PF_6)_2$ (**6^{Mepy}**), and $[Fe^{III}(S^{Me2}N_4(QuinoEN))]_2(\mu\text{-O})(PF_6)_2$ (**6^{Quino}**) (Scheme 4.3). These mono oxo-bridged Fe^{III}_2 species were previously crystallographically characterized[55], which demonstrates the ability to break an O-O bond by complexes **1^{Py}**, **1^{Mepy}**, and **1^{Quino}**. Dioxygen chemistry with complexes **1^{Mepy}** and **1^{Quino}** were studied previously and reproduced herein. As shown in Figure 4.30, both **1^{Mepy}** (left) and **1^{Quino}** (right) converted to mono oxo-bridged species, **6^{Mepy}** (λ_{max}(DCM) = 587 nm) and **6^{Quino}** (λ_{max}(DCM) = 584 nm), with no intermediates observed with EAS at ambient temperature.

Scheme 4.3. Room temperature reaction between **1^{Py}** and O_2 affording $[Fe^{III}(S^{Me2}N_4(6\text{-H-DPEN}))]_2(\mu\text{-O})(PF_6)_2$ (**6^{Py}**).

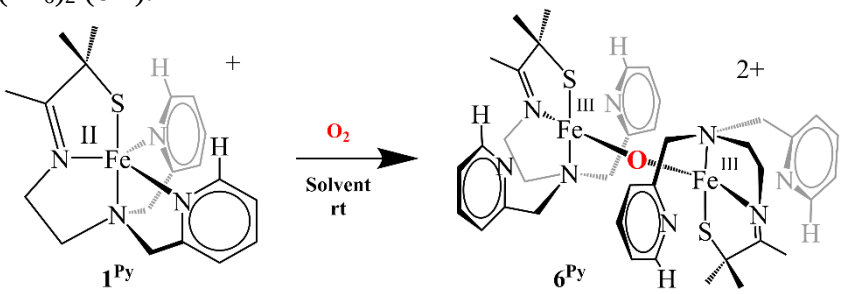

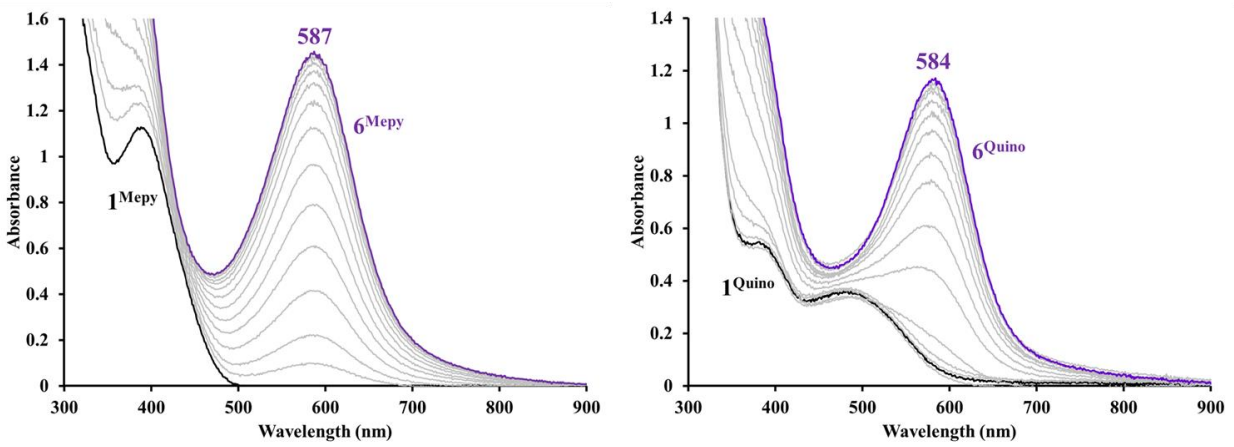

Figure 4.30. Left: EAS spectrum of O_2 addition to $\mathbf{1}^{\mathbf{Mepy}}$ (black trace) in DCM at ambient temperature, formation of $\mathbf{6}^{\mathbf{Mepy}}$ (purple trace) was observed over 36 minutes. Scans recorded at 166 seconds intervals. [$\mathbf{1}^{\mathbf{Mepy}}$] = 0.75 mM. Right: EAS spectrum of O_2 addition to $\mathbf{1}^{\mathbf{Quino}}$ (black trace) in DCM at ambient temperature, formation of $\mathbf{6}^{\mathbf{Quino}}$ (purple trace) was observed over 21 minutes. Scans recorded at 83 seconds intervals. [$\mathbf{1}^{\mathbf{Quino}}$] = 0.5 mM.

Oxidative addition of O_2 to complex $\mathbf{1}^{\mathbf{Py}}$ (-89 mV vs SCE in MeCN) is expected to be more readily due to the much less positive reduction potential. Complex $\mathbf{1}^{\mathbf{Py}}$ is comparatively much more sensitive to O_2 in solution than $\mathbf{1}^{\mathbf{Mepy}}$ and $\mathbf{1}^{\mathbf{Quino}}$. Upon introduction of trace amounts of O_2, the orange solution of $\mathbf{1}^{\mathbf{Py}}$ immediately turned deep red in color. Mass spectrometry measurements obtained using LTQ Orbitrap showed a major peak at m/z = 405.1 (Figure 4.31), which was consistent with expected half-mass for $[Fe^{III}(S^{Me2}N_4(6\text{-H-DPEN}))]_2(\mu\text{-O})^{2+}$ (m/z = 405.1). The isotope pattern of the mentioned peak also matches the calculated isotope pattern for Fe^{III}_2-μ-oxo species $\mathbf{6}^{\mathbf{Py}}$ (Figure 4.32).

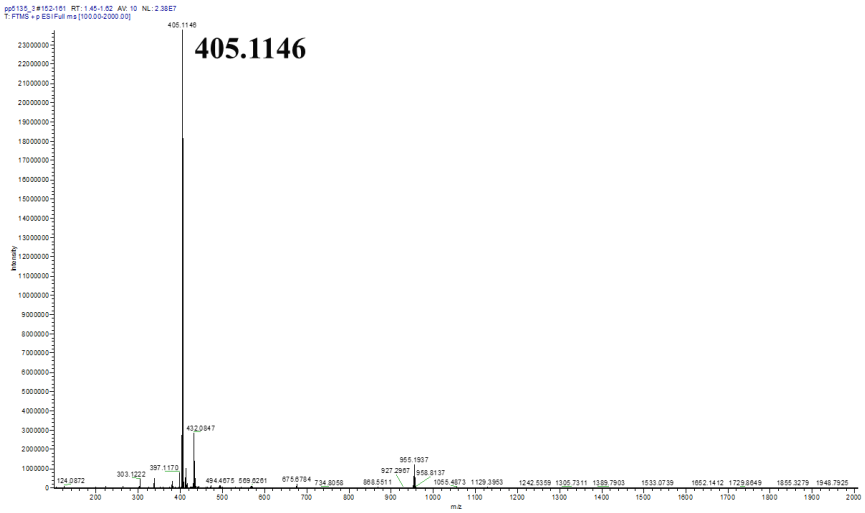

Figure 4.31. LTQ ion trap mass spectrum of **6^{Py}** in MeCN, with major mass peak m/z = 405.1146.

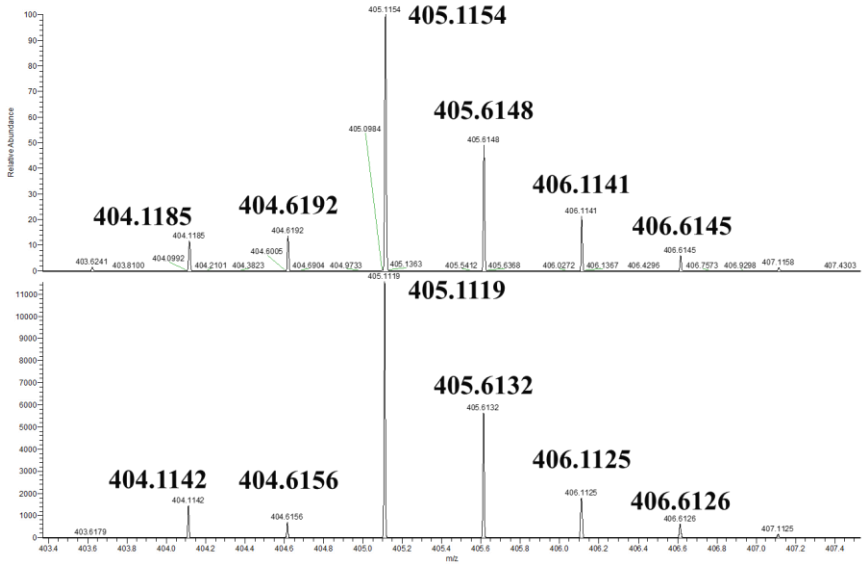

Figure 4.32. LTQ ion trap mass spectrum of **6^{Py}**, focused on m/z 405.1 (top) and the theoretical mass spectrum of $[Fe^{III}(S^{Me2}N_4(6\text{-H-DPEN}))]_2(\mu\text{-O})^{2+}$ (**6^{Py}**) (bottom).

Dioxygen reactivity with **1^{Py}** was explored in various solvents due to their different H-bonding properties, C-H bond strengths (C-H BDE: MeOH: 96 kcal/mol; MeCN: 93 kcal/mol; THF: 92 kcal/mol)[73], and freezing points (f.p.: MeOH: -98 °C; MeCN: -43.8 °C; THF: -108.4 °C). As mentioned previously, **1^{Py}** reacts instantly when exposed to O_2, this behavior was monitored in MeOH, MeCN, and THF at ambient temperature (Figures 4.33-4.35). A new peak

was observed (λ_{max}: MeOH: 513 nm; MeCN: 495 nm; THF: 496 nm) replacing the Fe-S → N-heterocycle π* MLCT transition band of $\mathbf{1}^{\mathbf{Py}}$ in the respective solvents, with no intermediate species observed by EAS. The EAS spectra, along with LTQ MS data, are consistent with the previously crystallographically characterized $[Fe^{III}(S^{Me2}N_4(6\text{-H-DPEN}))]_2(\mu\text{-O})^{2+}$ ($\mathbf{6}^{\mathbf{Py}}$). The rapid formation of $\mathbf{6}^{\mathbf{Py}}$ compared to $\mathbf{6}^{\mathbf{Mepy}}$ and $\mathbf{6}^{\mathbf{Quino}}$ is consistent with the reduction potential of $\mathbf{1}^{\mathbf{Py}}$ being relatively negative versus $\mathbf{1}^{\mathbf{Mepy}}$ and $\mathbf{1}^{\mathbf{Quino}}$. The conversion of $\mathbf{6}^{\mathbf{Py}}$ was found to be close to 100% yield in all three solvents. Monitored by EAS, complex $\mathbf{6}^{\mathbf{Py}}$ was found to be stable at ambient temperature and atmosphere for a minimum of 24 hours. The stable μ-oxo $\mathbf{6}^{\mathbf{Py}}$ is EPR silent (⊥-mode), as expected for an antiferromagnetically coupled Fe^{III}_2 species.

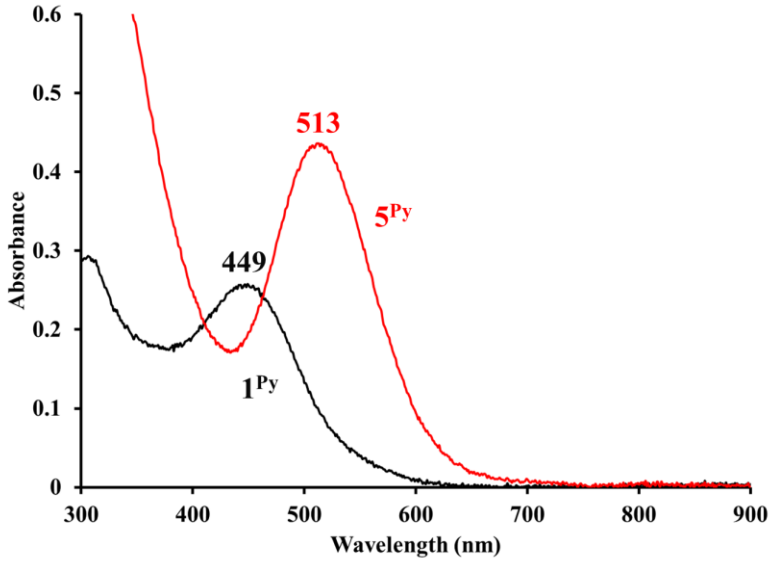

Figure 4.33. EAS spectrum of O_2 addition to $\mathbf{1}^{\mathbf{Py}}$ (black trace) in MeOH at ambient temperature, formation of $\mathbf{6}^{\mathbf{Py}}$ (red trace) was observed immediately. Scans recorded at 15 seconds intervals. [$\mathbf{1}^{\mathbf{Py}}$] = 0.2 mM.

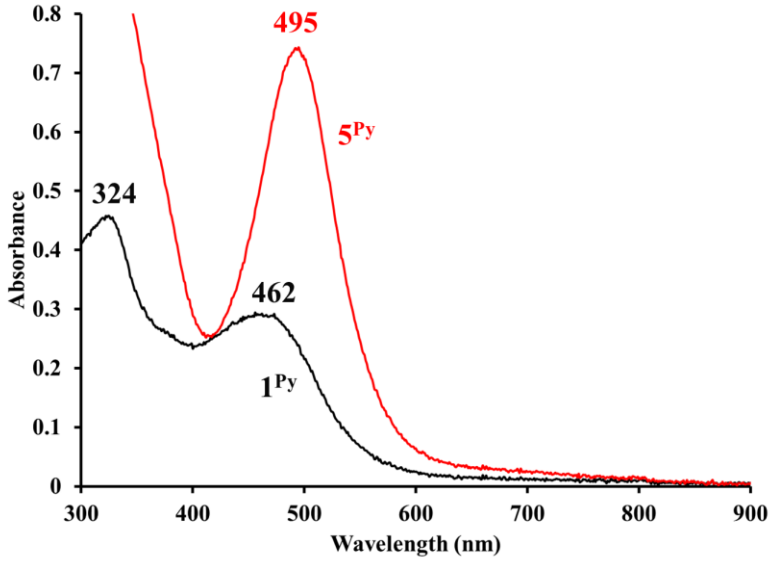

Figure 4.34. EAS spectrum of O_2 addition to **1^{Py}** (black trace) in MeCN at ambient temperature, formation of **6^{Py}** (red trace) was observed immediately. Scans recorded at 15 seconds intervals. [**1^{Py}**] = 0.2 mM.

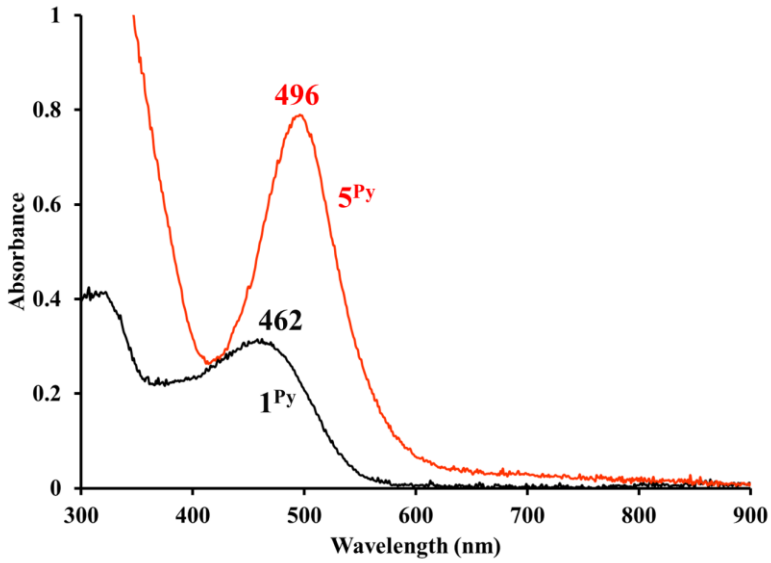

Figure 4.35. EAS spectrum of O_2 addition to **1^{Py}** (black trace) in THF at ambient temperature, formation of **6^{Py}** (red trace) was observed immediately. Scans recorded at 15 seconds intervals. [**1^{Py}**] = 0.2 mM.

4.3.10 *Comparison of Mono Oxo-bridged 6^{Py}, 6^{Mepy}, and 6^{Quino}*

As illustrated in this chapter, the N-heterocyclic amines provide an excellent opportunity for, not only tuning the electron density at the Fe center, but also tuning the steric constraints, which limit the Fe^{II} complexes' capability as reducing agents. This effect was demonstrated by plotting the Fe^{II} structural parameters against their respective reduction potentials. However, one could argue that comparison between 5- and 6-coordinate structures would not be appropriate, as the orbital overlap would be quite different for 5- versus 6-coordinte Fe^{II} centers. In order to better investigate the correlation between the steric effects of the ligand scaffold and the Lewis acidity of the Fe complexes, the Fe-N bond lengths of thermodynamic products of O_2 activation, mono oxo-bridged $[Fe^{III}(S^{Me2}N_4(6\text{-H-DPEN}))]_2(\mu\text{-O})(PF_6)_2$ (**6^{Py}**), $[Fe^{III}(S^{Me2}N_4(6\text{-Me-DPEN}))]_2(\mu\text{-O})(PF_6)_2$ (**6^{Mepy}**), and $[Fe^{III}(S^{Me2}N_4(\text{QuinoEN}))]_2(\mu\text{-O})(PF_6)_2$ (**6^{Quino}**) were compared and plotted against their spectroscopic parameters. As established previously, for the Mn analogue of the mono oxo-bridged species, $\{[Mn^{III}(S^{Me2}N_4(6\text{-H-DPEN}))]_2(\mu\text{-O})\}^{2+}$, $\{[Mn^{III}(S^{Me2}N_4(6\text{-MeO-DPEN}))]_2(\mu\text{-O})\}^{2+}$, $\{[Mn^{III}(S^{Me2}N_4(6\text{-Me-DPEN}))]_2(\mu\text{-O})\}^{2+}$, and $\{[Mn^{III}(S^{Me2}N_4(\text{Quino}))]_2(\mu\text{-O})\}^{2+}$, the Mn•••$N^{Ar}_{avg}$ distances were shown to provide a predictive metric that reflected both the steric properties of the N^{Ar} ligand scaffold, and the Lewis acidity of the Mn^{III} center.[3]

As all three of the Fe^{III} centers are 6-coordinate with an oxo bridge, the steric and electronic effects of the ligand should be reflected in their solid-state structures. For the Fe complexes discussed herein, the Fe-N^{Ar}_{avg} bond lengths (**6^{Py}**: 2.164(4) Å; **6^{Quino}**: 2.337(3) Å; **6^{Mepy}**: 2.410(4) Å, Table 4.5) suggest the Fe^{III} center of 6-H-pyridine derivative would be the least Lewis acidic. This is in agreement with the discussion between the corresponding Fe^{II} complexes and their spectroscopic properties (reduction potential of Fe^{II} (**1**) and Fe-S → N-

heterocycle π* MLCT band). The space filling diagrams of **6**$^{\mathbf{Py}}$, **6**$^{\mathbf{Mepy}}$, and **6**$^{\mathbf{Quino}}$ in Figure 4.36 illustrate that the pyridine ligand of **6**$^{\mathbf{Py}}$ would provide the most flexibility for a wider oxo coordination site. The flexibility is also reflected with the systematically narrower N(3)-Fe-N(4) angles (**6**$^{\mathbf{Py}}$: 152.71(12)°; **6**$^{\mathbf{Quino}}$: 150.57(12)°; **6**$^{\mathbf{Mepy}}$: 148.74(15)°, Table 4.5) The octahedral variance calculated for ($\sigma_{\theta(oct)}^2$) the Fe^{III} centers indicate **6**$^{\mathbf{Py}}$ ($\sigma_{\theta(oct)}^2$ = 10.664) would have better orbital overlap between the metal d-orbitals and the ligand orbitals as the Fe^{III} center is closer to an ideal octahedral geometry versus **6**$^{\mathbf{Quino}}$ ($\sigma_{\theta(oct)}^2$ = 11.306), and **6**$^{\mathbf{Mepy}}$ ($\sigma_{\theta(oct)}^2$ = 11.871). (Table 4.5) The comparison of structural parameters across the products (**6**$^{\mathbf{Py}}$, **6**$^{\mathbf{Mepy}}$, and **6**$^{\mathbf{Quino}}$) show the less sterically bulky, 6-H-pyridine, allows for a sterically more accessible Fe center with shorter Fe-Ligand bonds and better orbital overlap, despite the less electron-donating character.

A strong correlation (R^2 = 1) between the Fe-N^{Ar}_{avg} bond lengths of **6**$^{\mathbf{Py}}$, **6**$^{\mathbf{Mepy}}$, and **6**$^{\mathbf{Quino}}$ and λ_{max} of their corresponding Fe^{II} complexes was observed (Figure 4.37). The Fe-N^{Ar}_{avg} bond is indicative of the Lewis acidity of Fe center, while the λ_{max} of Fe^{II} complexes, which has been assigned as the Fe-S → N-heterocycle π* MLCT band, reflects the degree of orbital overlap between metal d-orbitals and ligand orbital. As the Fe-N^{Ar}_{avg} distance shortens and electron density at the metal center increases, a decrease in the Lewis acidity of the Fe center is observed, and the corresponding energy band would be expected to red shift. This correlation demonstrates the correlation between the Fe center Lewis acidity and the transition band energy, where a red-shift of λ_{max} is observed from the most Lewis acidic 6-Me-pyridine derivative to the least Lewis acidic 6-H-pyridine derivative (Figure 4.37). In the Mn analogue study, the least Lewis acidic Mn complex was shown to have a relatively flat reaction landscape for the O_2 activation chemistry, contributing to the observation of a total of four intermediates *en route* to the mono

oxo-bridged thermodynamic product.[3] A similar reaction landscape is proposed for the least Lewis acidic $\mathbf{1^{Py}}$ and its reactivity with O_2 in comparison to $\mathbf{1^{Mepy}}$ and $\mathbf{1^{Quino}}$.

Table 4.5. Selected Bond Distances (Å) and Bond Angles (deg) for $[Fe^{III}(S^{Me2}N_4(6\text{-H-DPEN}))]_2\text{-}(\mu\text{-O})(PF_6)_2$ ($\mathbf{6^{Py}}$)[55], $[Fe^{III}(S^{Me2}N_4(6\text{-Me-DPEN}))]_2\text{-}(\mu\text{-O})(PF_6)_2$ ($\mathbf{6^{Mepy}}$)[55], and $[Fe^{III}(S^{Me2}N_4(\text{QuinoEN}))]_2\text{-}(\mu\text{-O})(PF_6)_2$ ($\mathbf{6^{Quino}}$)[55].

	$\mathbf{6^{Py}}$	$\mathbf{6^{Quino}}$	$\mathbf{6^{MePy}}$
Fe(1)-S(1)	2.3058(11)	2.3053(13)	2.303(1)
Fe(1)-N(1)	2.155(3)	2.174(3)	2.163(4)
Fe(1)-N(2)	2.222(3)	2.175(3)	2.208(4)
Fe(1)-N(3)	2.160(3)	2.303(3)	2.390(4)
Fe(1)-N(4)	2.168(4)	2.371(3)	2.429(4)
Fe(1)-N^{Ar}_{Avg}	2.164(4)	2.337(3)	2.410(4)
Fe(1)-O	1.787(3)	1.778(3)	1.7816(7)
S(1)-Fe(1)-N(1)	81.75(9)	80.54(9)	80.31(11)
S(1)-Fe(1)-N(2)	159.17(9)	158.49(9)	158.76(12)
S(1)-Fe(1)-N(3)	104.78(9)	104.00(9)	103.63(11)
S(1)-Fe(1)-N(4)	101.35(9)	104.64(8)	106.86(12)
N(1)-Fe(1)-N(3)	82.67(13)	83.02(11)	98.10(15)
N(1)-Fe(1)-N(4)	93.49(12)	95.10(11)	80.52(15)
N(3)-Fe(1)-N(4)	152.71(12)	150.57(12)	148.74(15)
Fe(1)-O-Fe(2)	175.95(17)	174.02(14)	180.00(3)
$\sigma_{\theta(oct)}{}^2$	10.664	11.306	11.871

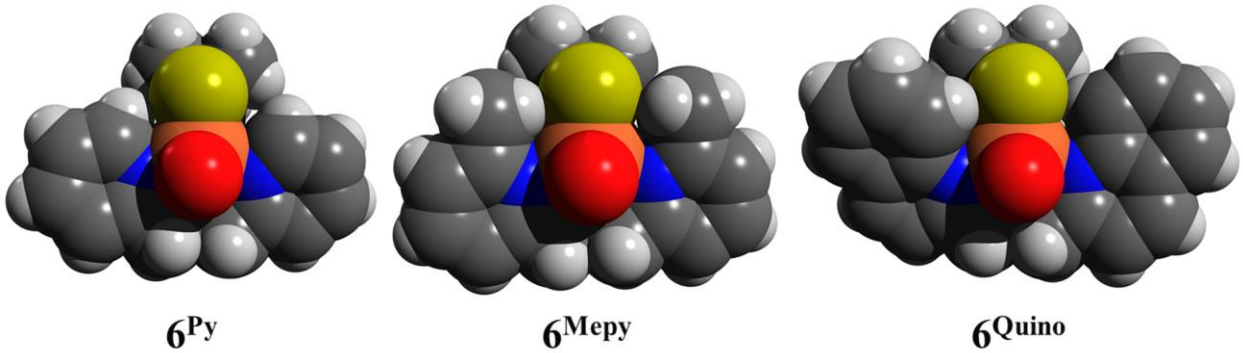

Figure 4.36. Space filling diagrams of mono oxo-bridged $\mathbf{6^{Py}}$ (left), $\mathbf{6^{Mepy}}$ (middle), and $\mathbf{6^{Quino}}$ (right). One half (Fe(2)) of the dimeric structures have been omitted for clarity.

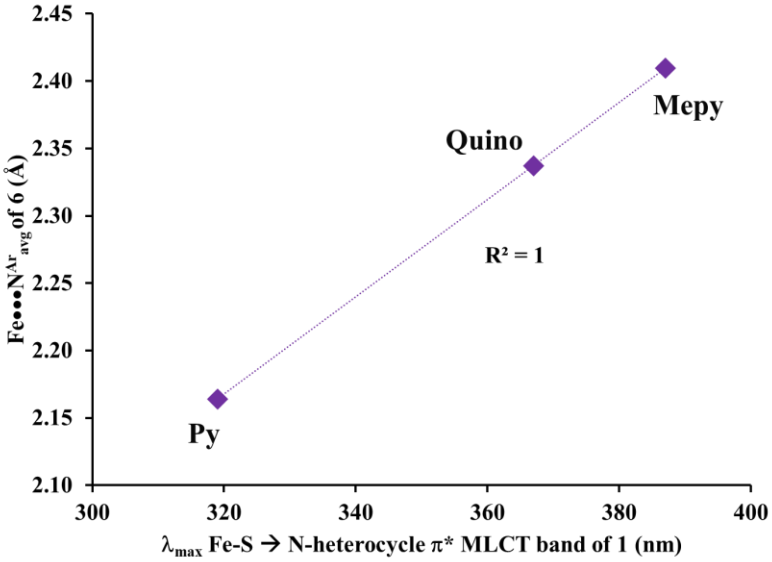

Figure 4.37. Correlation between the average Fe-N^{Ar}(3,4) bond length of mono oxo-bridged Fe^{III}_2 **6** and the Fe-S → N-heterocycle π* MLCT band of Fe^{II} $\mathbf{1^{Py}}$, $\mathbf{1^{Mepy}}$, and $\mathbf{1^{Quino}}$.

4.3.11 *Preliminary Reactivity of 1^{Py} with O_2 at Low Temperature*

Dioxygen activation with Mn analogue of the DPEN series at low temperatures has resulted in various intermediates observed, including a Mn^{III}_2-μ-peroxo and a bis-μ-oxo Mn^{IV}_2.[3,74] A strong correlation between the $Mn^{III/II}$ reduction potential and the activation barriers to O_2 binding was demonstrated, wherein a less Lewis acidic metal ion favored reversible O_2 binding. The reaction landscape for O_2 activation with respect to the energetic barriers separating metastable O_2 intermediates was shown to be relatively flat with a more electron-donating, but less sterically encumbered ligand scaffold.[3] Unlike with the dioxygen activation study of the Mn analogues, no intermediates were observed prior to the formation of $\mathbf{6^{Mepy}}$ or $\mathbf{6^{Quino}}$ for both complexes $\mathbf{1^{Mepy}}$ and $\mathbf{1^{Quino}}$ at temperatures as low as -90 °C in DCM. Preliminary stopped-flow UV-vis spectroscopy experiments were performed with $\mathbf{1^{Mepy}}$ demonstrated no spectroscopic evidence of intermediates *en route* to the final μ-oxo Fe^{III}_2 species $\mathbf{6^{Mepy}}$.

Based on the relative Lewis acidities of $\mathbf{1}^{\mathbf{Py}}$, $\mathbf{1}^{\mathbf{Mepy}}$ and $\mathbf{1}^{\mathbf{Quino}}$, metastable intermediates of O_2 activation would be more likely to be observed with the least Lewis acidic Fe^{II} $\mathbf{1}^{\mathbf{Py}}$, along with its less sterically encumbered 6-H-pyridine ligand. However, no intermediates were observed upon exposure to O_2 with $\mathbf{1}^{\mathbf{Py}}$ in MeCN (f.p. = -43.8 °C, Figure 4.38), MeOH (f.p. = -98 °C, Figure 4.39), and THF (f.p. = -108.4 °C, Figure 4.40) at the lowest temperatures available for each solvent. Isosbestic points were observed in both spectra for MeOH and THF solutions, suggesting a one-to-one conversion from $\mathbf{1}^{\mathbf{Py}}$ to $\mathbf{6}^{\mathbf{Py}}$. Since the C-H bond strength of the solvent is often shown to affect the O_2 reactivity pathway,[2,3] another attempt in observing key Fe O_2 intermediates was performed using aprotic solvent, DCM with a much stronger C-H bond (C-H BDE: 98 kcal/mol, f.p. = -95 °C).

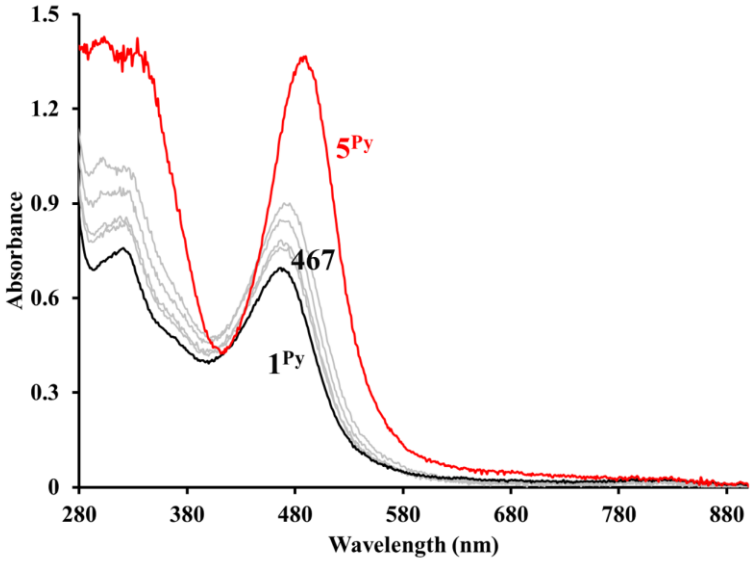

Figure 4.38. EAS spectrum of O_2 addition to $\mathbf{1}^{\mathbf{Py}}$ (black trace) in MeCN at -43 °C, formation of $\mathbf{6}^{\mathbf{Py}}$ (red trace) was observed over 2.5 minutes. Scans recorded at 30 seconds intervals. [$\mathbf{1}^{\mathbf{Py}}$] = 0.2 mM.

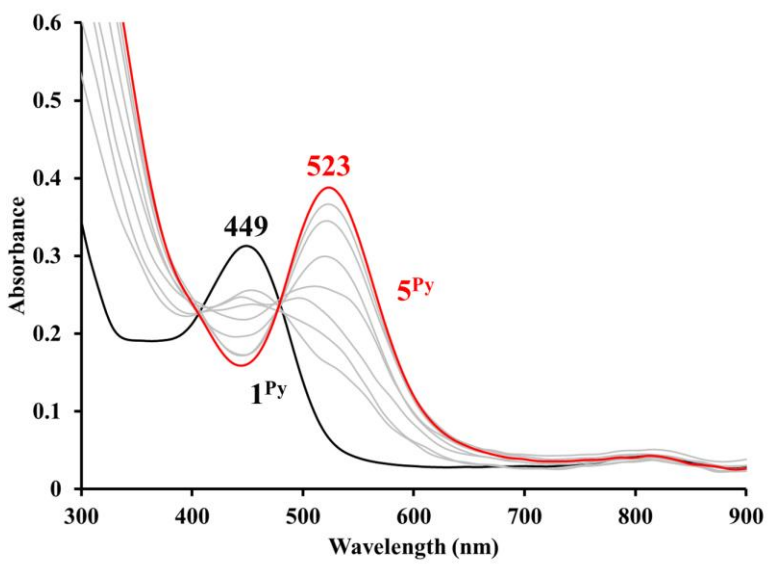

Figure 4.39. EAS spectrum of O_2 addition to $\mathbf{1}^{Py}$ (black trace) in MeOH at -73 °C. Formation of $\mathbf{6}^{Py}$ (red trace) was observed over 2.5 minutes. Scans recorded at 15 seconds intervals. [$\mathbf{1}^{Py}$] = 0.2 mM. Isosbestic points observed at 409 nm and 479 nm.

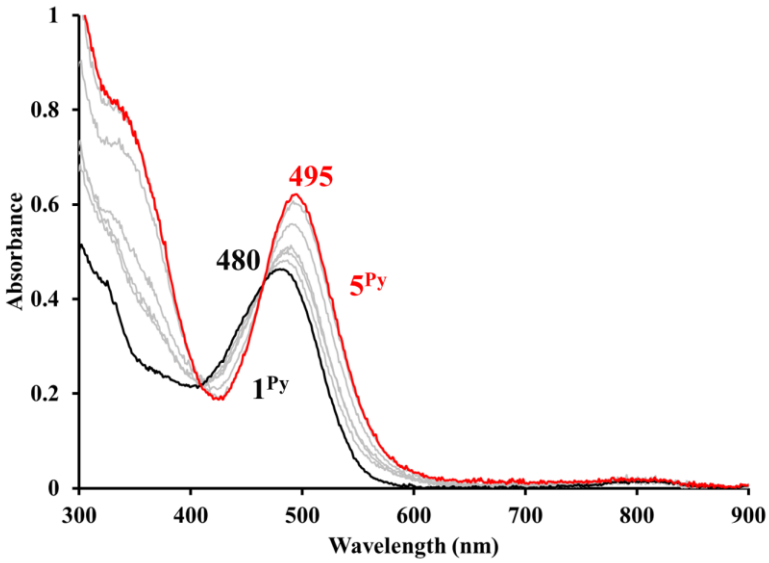

Figure 4.40. EAS spectrum of O_2 addition to $\mathbf{1}^{Py}$ (black trace) in THF at -73 °C. Formation of $\mathbf{6}^{Py}$ (red trace) was observed over 1.5 minutes. Scans recorded at 15 seconds intervals. [$\mathbf{1}^{Py}$] = 0.2 mM. Isosbestic points observed at 410 nm and 465 nm.

As O_2 was introduced to a DCM solution of $\mathbf{1}^{Py}$ at -73 °C, a shoulder peak at 564 nm was observed to simultaneously grow in along with the mono oxo-bridged $\mathbf{6}^{Py}$ (495 nm) (Figure 4.41, Left). The feature then fully converted to $\mathbf{6}^{Py}$ over the following minute (Figure 4.41, Right).

Further characterization of this short-lived 564 nm species would be extremely difficult without the ability to better isolate or lengthen the lifetime of the intermediate. The O_2 reactivity was repeated at -90 °C in attempts to establish a better spectroscopic handle on the metastable species. At the lower temperature, a relatively slower growth of the mixture of $\mathbf{6^{Py}}$ and 564 nm species was observed over 1 minute (as opposed to 15 seconds at -73 °C), followed by the complete conversion to $\mathbf{6^{Py}}$ (Figure 4.42). Isosbestic points were observed at 441 nm and 540 nm for this conversion and indicate no other species or intermediates were present in the reaction mixture.

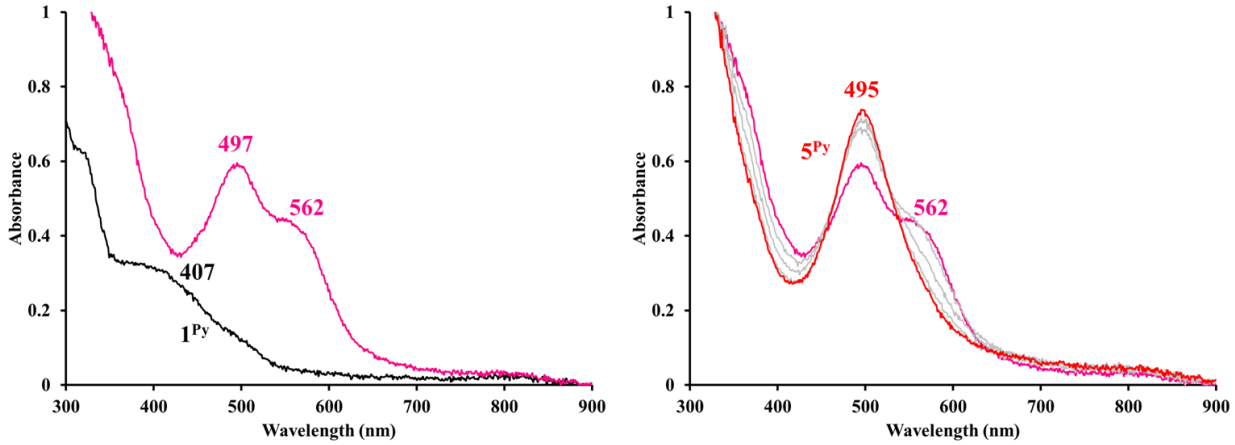

Figure 4.41. EAS spectrum of O_2 addition to $\mathbf{1^{Py}}$ (black trace) in DCM at -73 °C. Left: Growth observed 15 sec after O_2 addition (pink trace). Right: Complete conversion to $\mathbf{6^{Py}}$ (red trace) over 1.25 minutes. Scans recorded at 15 seconds intervals. [$\mathbf{1^{Py}}$] = 0.2 mM.

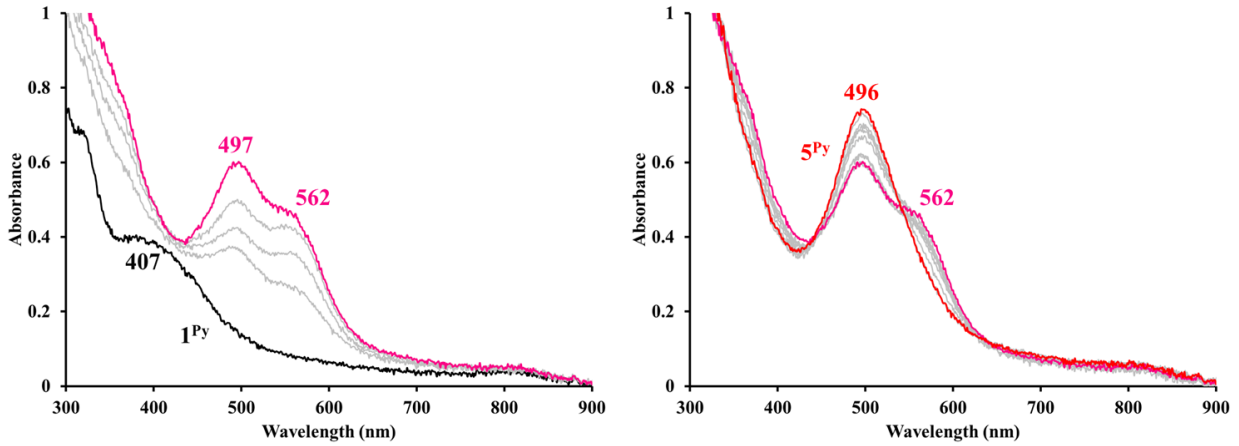

Figure 4.42. EAS spectrum of O_2 addition to $\mathbf{1^{Py}}$ (black trace) in DCM at -95 °C. Left: Growth observed at 497nm and 562 nm over 60 sec after O_2 addition (pink trace). Right: Complete conversion to $\mathbf{6^{Py}}$ (red trace) over 4.25 minutes. Isosbestic point observed at 441 nm and 540 nm for the conversion to $\mathbf{6^{Py}}$. Scans recorded at 15 seconds intervals. [$\mathbf{1^{Py}}$] = 0.2 mM.

The initial O2 binding step could be slowed as an effect of the rate of O2 diffusion caused by the headspace of the experimental set up. Experiments were also performed by adding a chilled concentrated solution of $\mathbf{1^{Py}}$ to an O_2 saturated solution of DCM ([O_2] in DCM at 20 °C = 5.8 mM)[75] at -90 °C (Figure 4.43). The headspace of the dip probe cell was quickly flushed with argon prior to the addition of $\mathbf{1^{Py}}$ to limit the O_2 exposure of the Fe^{II} solution prior to mixing with O_2 saturated DCM solution. As shown in Figure 4.43, no additional species were observed. However, the growth of the intermediate feature and the overall conversion to the mono oxo-bridged species were limited as indicated by their lower absorbance values. Further characterization of this short-lived intermediate has proven to be difficult without a better approach to isolate the intermediate. However, the observation of a new intermediate suggests that the 6-H-pyridine 1^{Py} could serve as a good model for understanding iron dioxygen chemistry, as the intermediate demonstrates a flatter reaction landscape, and it has been shown to support a more stable Fe^{III} state versus $\mathbf{1^{Mepy}}$ and $\mathbf{1^{Quino}}$.

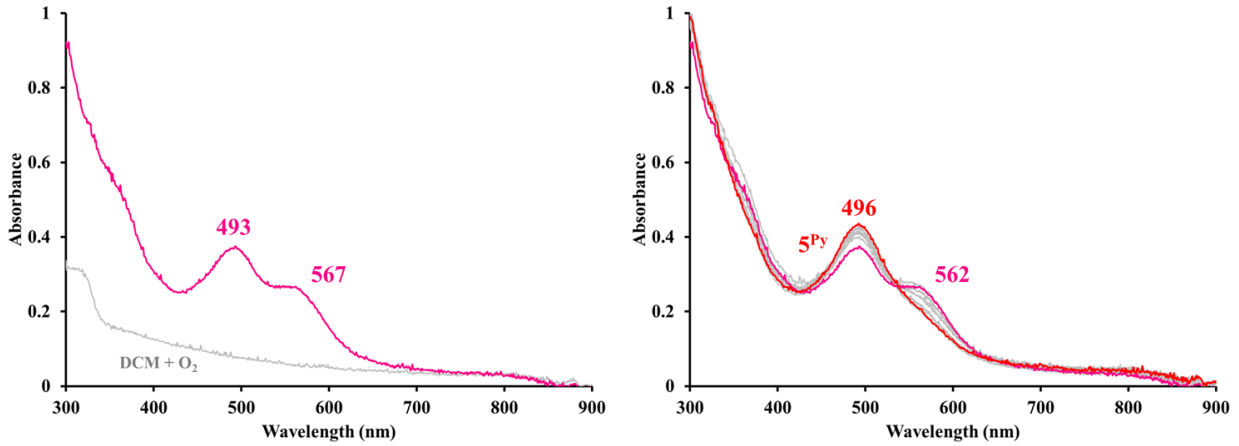

Figure 4.43. EAS spectrum of the addition of 0.5 mL $\mathbf{1^{Py}}$ (2 mM) to 4.5 mL O_2-purged DCM (grey trace) at -90 °C. Left: Growth observed at 493 nm and 567 nm 15 sec after concentrated Fe^{II} solution (pink trace). Right: Complete conversion to $\mathbf{6^{Py}}$ (red trace) over 8.25 minutes. Scans reported at 60 seconds intervals.

4.4 Summary

In this chapter, the structural and spectroscopic properties of a less Lewis acidic Fe-thiolate complex $[Fe^{II}(S^{Me2}N_4(6\text{-H-DPEN}))]^+$ ($\mathbf{1^{Py}}$) have been discussed and compared to complexes with similar but more sterically encumbered ligand scaffolds, $[Fe^{II}(S^{Me2}N_4(6\text{-Me-DPEN}))]^+$ ($\mathbf{1^{Mepy}}$) and $[Fe^{II}(S^{Me2}N_4(\text{QuinoEN}))]^+$ ($\mathbf{1^{Quino}}$). With the incorporation of the π-acceptor N-heterocyclic pyridine or quinoline ligand, all three complexes display features in the UV-visible range, providing a better spectroscopic handle for monitoring Fe^{II} reactivity via electronic absorption spectroscopy. Both solid-state and solution-state characteristics of $\mathbf{1^{Py}}$ were investigated. While the complex was crystallized as a bimetallic Fe^{II}_2 species, $\mathbf{1^{Py}}$ is either in monomeric form (in MeOH) or in a mixture of bimetallic and monomeric species (in MeCN). The comparison of structural parameters of $\mathbf{1^{Py}_2}$**-MeCN** with the 6-coordinate $\mathbf{1^{PyPN}}$, showed the less constrained Et-linker of $\mathbf{1^{Py}_2}$**-MeCN** allowed for a more flexible Fe^{II} center with better orbital overlap, and thereby, a less Lewis acidic Fe^{II} ion. . The dioxygen reactivity was investigated with the expectation that the least Lewis acidic Fe^{II} is that of $\mathbf{1^{Py}}$, compared to the

Er-linker $\mathbf{1^{Mepy}}$ and $\mathbf{1^{Quino}}$. A new metastable intermediate (λ_{max} = 562 nm) was observed at -90 °C in DCM with a maximum lifetime of 8 minutes observed. However, without a better method to isolate the species, the identity remains unknown *en route* to the mono oxo-bridged $\mathbf{6^{Py}}$ product. Upon inspection of the structural parameters of $\mathbf{6^{Py}}$, $\mathbf{6^{Mepy}}$, and $\mathbf{6^{Quino}}$, a correlation between the ligand's steric effects and the Lewis acidity of the Fe^{II} center was observed. The less Lewis acidic, yet less electron donating 6-H-pyridine derivative is proposed to have a flatter dioxygen activation landscape, with respect to the energetic barriers separating Fe-O_2 intermediates, leading to the spectroscopic observation of a new metastable intermediate along the O_2 activation pathway.

4.5 References

(1) Brown, C. D.; Neidig, M. L.; Neibergall, M. B.; Lipscomb, J. D.; Solomon, E. I. VTVH-MCD and DFT Studies of Thiolate Bonding to $\{FeNO\}^7$/ $\{FeO_2\}^8$ Complexes of Isopenicillin N Synthase: Substrate Determination of Oxidase versus Oxygenase Activity in Nonheme Fe Enzymes. *J. Am. Chem. Soc.* **2007**, *129*, 7427–7438.

(2) Blakely, M. N.; Dedushko, M. A.; Poon, P. C. Y.; Villar-Acevedo, G.; Kovacs, J. A. Formation of a Reactive, Alkyl Thiolate-Ligated Fe^{III}-Superoxo Intermediate Derived from Dioxygen. *J. Am. Chem. Soc.* **2019**, *141*, 1867–1870.

(3) Poon, P. C. Y.; Dedushko, M. A.; Sun, X.; Yang, G.; Toledo, S.; Hayes, E. C.; Johansen, A.; Piquette, M. C.; Rees, J. A.; Stoll, S.; Rybak-Akimova, E.; Kovacs, J. A. How Metal Ion Lewis Acidity and Steric Properties Influence the Barrier to Dioxygen Binding, Peroxo O-O Bond Cleavage, and Reactivity. *J. Am. Chem. Soc.* **2019**, *141*, 15046–15057.

(4) Kovacs, J. A. Tuning the Relative Stability and Reactivity of Manganese Dioxygen and Peroxo Intermediates via Systematic Ligand Modification. *Acc. Chem. Res.* **2015**, *48*, 2744–2753.

(5) Green, M. T. C-H Bond Activation in Heme Proteins: The Role of Thiolate Ligation in Cytochrome P450. *Curr. Opin. Chem. Biol.* **2009**, *13*, 84–88.

(6) Yosca, T. H.; Rittle, J.; Krest, C. M.; Onderko, E. L.; Silakov, A.; Calixto, J. C.; Behan, R. K.; Green, M. T. *Iron(IV)Hydroxide PKa and the Role of Thiolate Ligation in C-H Bond Activation by Cytochrome P450*; American Association for the Advancement of Science, **2013**; *342*, 825–829.

(7) Ansari, M.; Senthilnathan, D.; Rajaraman, G. Deciphering the Origin of Million-Fold Reactivity Observed for the Open Core Diiron [HO-FeIII-O-FeIVO]2+species towards C-H Bond Activation: Role of Spin-States, Spin-Coupling, and Spin-Cooperation. *Chem. Sci.* **2020**, *11*, 10669–10687.

(8) Bollinger, J. M.; Broderick, J. B. Frontiers in Enzymatic C-H-Bond Activation. *Curr. Opin. Chem. Biol.* **2009**, *13*, 51–57.

(9) Yosca, T. H.; Ledray, A. P.; Ngo, J.; Green, M. T. A New Look at the Role of Thiolate Ligation in Cytochrome P450. *J. Biol. Inorg. Chem.* **2017**, *22*, 209–220.

(10) Kennepohl, P.; Neese, F.; Schweltzer, D.; Jackson, H. L.; Kovacs, J. A.; Solomon, E. I. Spectroscopy of Non-Heme Iron Thiolate Complexes: Insight into the Electronic Structure of the Low-Spin Active Site of Nitrile Hydratase. *Inorg. Chem.* **2005**, *44*, 1826–1836.

(11) Kovacs, J. A.; Brines, L. M. Understanding How the Thiolate Sulfur Contributes to the Function of the Non-Heme Iron Enzyme Superoxide Reductase. *Acc. Chem. Res.* **2007**, *40*, 501–509.

(12) Lugo-Mas, P.; Dey, A.; Xu, L.; Davin, S. D.; Benedict, J.; Kaminsky, W.; Hodgson, K. O.; Hedman, B.; Solomon, E. I.; Kovacs, J. A. How Does Single Oxygen Atom Addition Affect the Properties of an Fe-Nitrile Hydratase Analogue? The Compensatory Role of the Unmodified Thiolate. *J. Am. Chem. Soc.* **2006**, *128*, 11211–11221.

(13) Leipzig, B. K.; Rees, J. A.; Kowalska, J. K.; Theisen, R. M.; Kavčič, M.; Poon, P. C. Y.; Kaminsky, W.; DeBeer, S.; Bill, E.; Kovacs, J. A. How Do Ring Size and π-Donating Thiolate Ligands Affect Redox-Active, α-Imino-N-Heterocycle Ligand Activation? *Inorg. Chem.* **2018**, *57*, 1935–1949.

(14) Solomon, E. I.; Szilagyi, R. K.; DeBeer George, S.; Basumallick, L. Electronic Structures of Metal Sites in Proteins and Models: Contributions to Function in Blue Copper Proteins. *Chem. Rev.* **2004**, *104*, 419–458.

(15) Baldwin, J. E.; Bradley, M. Isopenicillin N Synthase: Mechanistic Studies. *Chem. Rev.* **1990**, *90*, 1079–1088.

(16) Roach, P. L.; Clifton, I. J.; Hensgens, C. M. H.; Shibata, N.; Schofield, C. J.; Hajdu, J.; Baldwin, J. E. Structure of Isopenicillin N Synthase Complexed with Substrate and the Mechanism of Penicillin Formation. *Nature* **1997**, *387*, 827–830.

(17) Cohen, G.; Shiffman, D.; Mevarech, M.; Aharonowitz, Y. Microbial Isopenicillin N Synthase Genes: Structure, Function, Diversity and Evolution. *Trends Biotechnol.* **1990**, *8*, 105–111.

(18) Tamanaha, E.; Zhang, B.; Guo, Y.; Chang, W. C.; Barr, E. W.; Xing, G.; St Clair, J.; Ye, S.; Neese, F.; Bollinger, J. M.; Krebs, C. Spectroscopic Evidence for the Two C-H-Cleaving Intermediates of Aspergillus Nidulans Isopenicillin N Synthase. *J. Am. Chem. Soc.* **2016**, *138*, 8862–8874.

(19) Fiedler, A. T.; Halfen, H. L.; Halfen, J. A.; Brunold, T. C. Synthesis, Structure Determination, and Spectroscopic/Computational Characterization of a Series of Fe(II)-Thiolate Model Complexes: Implications for Fe-S Bonding in Superoxide Reductases. *J. Am. Chem. Soc.* **2005**, *127*, 1675–1689.

(20) Bukowski, M. R.; Halfen, H. L.; van den Berg, T. A.; Halfen, J. A.; Que, L. Spin-State Rationale for the Peroxo-Stabilizing Role of the Thiolate Ligand in Superoxide Reductase. *Angew. Chemie Int. Ed.* **2005**, *44*, 584–587.

(21) Kitagawa, T.; Dey, A.; Lugo-Mas, P.; Benedict, J. B.; Kaminsky, W.; Solomon, E.; Kovacs, J. A. A Functional Model for the Cysteinate-Ligated Non-Heme Iron Enzyme Superoxide Reductase (SOR). *J. Am. Chem. Soc.* **2006**, *128*, 14448–14449.

(22) Dey, A.; Jenney, F. E.; Adams, M. W. W.; Johnson, M. K.; Hodgson, K. O.; Hedman, B.; Solomon, E. I. Sulfur K-Edge X-Ray Absorption Spectroscopy and Density Functional Theory Calculations on Superoxide Reductase: Role of the Axial Thiolate in Reactivity. *J. Am. Chem. Soc.* **2007**, *129*, 12418–12431.

(23) Mathé, C.; Weill, C. O.; Mattioli, T. A.; Berthomieu, C.; Houée-Levin, C.; Tremey, E.; Nivière, V. Assessing the Role of the Active-Site Cysteine Ligand in the Superoxide Reductase from Desulfoarculus Baarsii. *J. Biol. Chem.* **2007**, *282*, 22207–22216.

(24) Namuswe, F.; Kasper, G. D.; Narducci Sarjeant, A. A.; Hayashi, T.; Krest, C. M.; Green, M. T.; Moënne-Loccoz, P.; Goldberg, D. P. Rational Tuning of the Thiolate Donor in Model Complexes of Superoxide Reductase: Direct Evidence for a Trans Influence in FeIII-OOR Complexes. *J. Am. Chem. Soc.* **2008**, *130*, 14189–14200.

(25) Kumar, D.; Thiel, W.; De Visser, S. P. Theoretical Study on the Mechanism of the Oxygen Activation Process in Cysteine Dioxygenase Enzymes. *J. Am. Chem. Soc.* **2011**, *133*, 3869–3882.

(26) Kumar, D.; Sastry, G. N.; Goldberg, D. P.; De Visser, S. P. Mechanism of S-Oxygenation by a Cysteine Dioxygenase Model Complex. *J. Phys. Chem. A* **2012**, *116*, 582–591.

(27) Che, X.; Gao, J.; Zhang, D.; Liu, C. How Do the Thiolate Ligand and Its Relative Position Control the Oxygen Activation in the Cysteine Dioxygenase Model? *J. Phys. Chem. A* **2012**, *116*, 5510–5517.

(28) Simmons, C. R.; Krishnamoorthy, K.; Granett, S. L.; Schuller, D. J.; Dominy, J. E.; Begley, T. P.; Stipanuk, M. H.; Karplus, P. A. A Putative Fe2+-Bound Persulfenate Intermediate in Cysteine Dioxygenase. *Biochemistry* **2008**, *47*, 11390–11392.

(29) Ray, K.; Pfaff, F. F.; Wang, B.; Nam, W. Status of Reactive Non-Heme Metal-Oxygen Intermediates in Chemical and Enzymatic Reactions. *J. Am. Chem. Soc.* **2014**, *136*, 13942–13958.

(30) Aluri, S.; De Visser, S. P. The Mechanism of Cysteine Oxygenation by Cysteine Dioxygenase Enzymes. *J. Am. Chem. Soc.* **2007**, *129*, 14846–14847.

(31) Faponle, A. S.; Seebeck, F. P.; De Visser, S. P. Sulfoxide Synthase versus Cysteine Dioxygenase Reactivity in a Nonheme Iron Enzyme. *J. Am. Chem. Soc.* **2017**, *139*, 9259–9270.

(32) Light, K. M.; Yamanaka, Y.; Odaka, M.; Solomon, E. I. Spectroscopic and Computational Studies of Nitrile Hydratase: Insights into Geometric and Electronic Structure and the Mechanism of Amide Synthesis. *Chem. Sci.* **2015**, *6*, 6280–6294.

(33) Martinez, S.; Wu, R.; Sanishvili, R.; Liu, D.; Holz, R. The Active Site Sulfenic Acid Ligand in Nitrile Hydratases Can Function as a Nucleophile. *J. Am. Chem. Soc.* **2014**, *136*, 1186–1189.

(34) Auclair, K.; Moënne-Loccoz, P.; Ortiz de Montellano, P. R. Roles of the Proximal Heme Thiolate Ligand in Cytochrome P450cam. *J. Am. Chem. Soc.* **2001**, *123*, 4877–4885.

(35) Sivaramakrishnan, S.; Ouellet, H.; Matsumura, H.; Guan, S.; Moënne-Loccoz, P.; Burlingame, A. L.; Ortiz De Montellano, P. R. Proximal Ligand Electron Donation and

Reactivity of the Cytochrome P450 Ferric-Peroxo Anion. *J. Am. Chem. Soc.* **2012**, *134*, 6673–6684.

(36) Denisov, I. G.; Makris, T. M.; Sligar, S. G.; Schlichting, I. Structure and Chemistry of Cytochrome P450. *Chem. Rev.* **2005**, *105*, 2253–2277.

(37) Schlichting, I.; Berendzen, J.; Chu, K.; Stock, A. M.; Maves, S. A.; Benson, D. E.; Sweet, R. M.; Ringe, D.; Petsko, G. A.; Sligar, S. G. *The Catalytic Pathway of Cytochrome P450cam at Atomic Resolution*; American Association for the Advancement of Science, 2000; Vol. 287, pp 1615–1622.

(38) Krest, C. M.; Onderko, E. L.; Yosca, T. H.; Calixto, J. C.; Karp, R. F.; Livada, J.; Rittle, J.; Green, M. T. Reactive Intermediates in Cytochrome P450 Catalysis. *J. Biol. Chem.* **2013**, *288*, 17074–17081.

(39) Groves, J. T. Enzymatic C-H Bond Activation: Using Push to Get Pull. *Nat. Chem.* **2014**, *6*, 89–91.

(40) Kovacs, J. A. How Iron Activates O2. *Science (80-.).* **2003**, *299*, 1024–1025.

(41) Shook, R. L.; Borovik, A. S. Role of the Secondary Coordination Sphere in Metal-Mediated Dioxygen Activation. *Inorg. Chem.* **2010**, *49*, 3646–3660.

(42) Adachi, S. I.; Nagano, S.; Ishimori, K.; Watanabe, Y.; Morishima, I.; Egawa, T.; Kitagawa, T.; Makino, R. Roles of Proximal Ligand in Heme Proteins: Replacement of Proximal Histidine of Human Myoglobin with Cysteine and Tyrosine by Site-Directed Mutagenesis as Models for P-450, Chloroperoxidase, and Catalase. *Biochemistry* **1993**, *32*, 241–252.

(43) Shoner, S. C.; Barnhart, D.; Kovacs, J. A. A Model for the Low-Spin, Non-Heme, Thiolate-Ligated Iron Site of Nitrile Hydratase. *Inorg. Chem.* **1995**, *34*, 4517–4518.

(44) Ellison, J. J.; Nienstedt, A.; Shoner, S. C.; Barnhart, D.; Cowen, J. A.; Kovacs, J. A. Reactivity of Five-Coordinate Models for the Thiolate-Ligated Fe Site of Nitrile Hydratase. *J. Am. Chem. Soc.* **1998**, *120*, 5691–5700.

(45) Jackson, H. L.; Shoner, S. C.; Rittenberg, D.; Cowen, J. A.; Lovell, S.; Barnhart, D.; Kovacs, J. A. Probing the Influence of Local Coordination Environment on the Properties of Fe-Type Nitrile Hydratase Model Complexes. *Inorg. Chem.* **2001**, *40*, 1646–1653.

(46) Shearer, J.; Kung, I. Y.; Lovell, S.; Kaminsky, W.; Kovacs, J. A. Why Is There an "Inert" Metal Center in the Active Site of Nitrile Hydratase? Reactivity and Ligand Dissociation from a Five-Coordinate Co(III) Nitrile Hydratase Model. *J. Am. Chem. Soc.* **2001**, *123*, 463–468.

(47) Shearer, J.; Jackson, H. L.; Schweitzer, D.; Rittenberg, D. K.; Leavy, T. M.; Kaminsky, W.; Scarrow, R. C.; Kovacs, J. A. The First Example of a Nitrile Hydratase Model Complex That Reversibly Binds Nitriles. *J. Am. Chem. Soc.* **2002**, *124*, 11417–11428.

(48) Shearer, J.; Scarrow, R. C.; Kovacs, J. A. Synthetic Models for the Cysteinate-Ligated Non-Heme Iron Enzyme Superoxide Reductase: Observation and Structural Characterization by XAS of an FeIII-OOH Intermediate. *J. Am. Chem. Soc.* **2002**, *124*, 11709–11717.

(49) Shearer, J.; Nehring, J.; Lovell, S.; Kaminsky, W.; Kovacs, J. A. Modeling the Reactivity of Superoxide Reducing Metalloenzymes with a Nitrogen and Sulfur Coordinated Iron Complex. *Inorg. Chem.* **2001**, *40*, 5483–5484.

(50) Coggins, M. K.; Martin-Diaconescu, V.; Debeer, S.; Kovacs, J. A. Correlation between Structural, Spectroscopic, and Reactivity Properties within a Series of Structurally Analogous Metastable Manganese(III)-Alkylperoxo Complexes. *J. Am. Chem. Soc.* **2013**, *135*, 4260–4272.

(51) Zang, Y.; Kim, J.; Dong, Y.; Wilkinson, E. C.; Appelman, E. H.; Que, L. Models for Nonheme Iron Intermediates: Structural Basis for Tuning the Spin States of Fe(TPA) Complexes. *J. Am. Chem. Soc.* **1997**, *119*, 4197–4205.

(52) Stoll, S.; Schweiger, A. EasySpin, a Comprehensive Software Package for Spectral Simulation and Analysis in EPR. *J. Magn. Reson.* **2006**, *178*, 42–55.

(53) Live, D. H.; Chan, S. I. Bulk Susceptibility Corrections in Nuclear Magnetic Resonance Experiments Using Superconducting Solenoids. *Anal. Chem.* **1970**, *42*, 791–792.

(54) Evans, D. F. The Determination of the Paramagnetic Susceptibility of Substances in Solution by Nuclear Magnetic Resonance. *J. Chem. Soc.* **1959**, *81*, 2003–2005.

(55) Toledo, S. Synthesis and Reactivity of an Expanded Family of Superoxide Reductase (SOR) Model Complexes Using N-Heterocyclic, Thiolate Containing Ligands: Towards a Better Understanding of Structural-Functional Relationships, University of Washington, Seattle, 2009.

(56) Bandlish, B. K.; Shine, H. J. Ion Radicals. 37. Preparation and Isolation of Cation Radical Tetrafluoroborates by the Use of Nitrosonium Tetrafluoroborate. *J. Org. Chem.* **1977**, *42*, 561–563.

(57) Gleaves, M. Thiolate Containing N-Heterocyclic Amine Based Ligands; Investigations

into Intermediates of O – 2 and O 2 Reactivity and Application towards New Ligand Design for Modelling the Active Site of Superoxide Reductase, University of Washington, 2012.

(58) Sheldrick, G. M. SHELXT - Integrated Space-Group and Crystal-Structure Determination. *Acta Crystallogr. Sect. A Found. Crystallogr.* **2015**, *71*, 3–8.

(59) Altomare, A.; Burla, M. C.; Camalli, M.; Cascarano, G. L.; Giacovazzo, C.; Guagliardi, A.; Moliterni, A. G. G.; Polidori, G.; Spagna, R. SIR97: A New Tool for Crystal Structure Determination and Refinement. *J. Appl. Cryst* **1999**, *32*, 115–119.

(60) Altomare, A.; Cascarano, G.; Giacovazzo, C.; Guagliardi, A. *Completion and Refinement of Crystal Structures with SIR92*; 1993; Vol. 26.

(61) Sheldrick, G. M. SHELXL97, Program for the Refinement of Crystal Structures, University of Göttingen, Germany, 1997. University of G ttingen 2000.

(62) Mackay, S.; Edwards, C.; Henderson, A.; Gilmore, C.; Stewart, N.; Shankland, K.; Donald, A. MaXus: A Computer Program for the Solution and Refinement of Crystal Structures from Diffraction Data. University of Glasgow, Scotland 1997.

(63) Waasmaier, D.; Kirfel, A. New Analytical Scattering-factor Functions for Free Atoms and Ions. *Acta Crystallogr. Sect. A* **1995**, *51*, 416–431.

(64) Coggins, M. K. Small Molecule Activation Studies Involving Thiolate-Ligated Manganese(II) Complexes and Biologically-Relevant Oxidants, Univeristy of Washington, Seattle, 2012.

(65) Robinson, K.; Gibbs, G. V; Ribbe, P. H. Quadratic Elongation: A Quantitative Measure of

Distortion in Coordination Polyhedra. *Science (80-.).* **1971**, *172*, 567–570.

(66) Shannon, R. D. Revised Effective Ionic Radii and Systematic Studies of Interatomie Distances in Halides and Chaleogenides. *Acta Crystallogr. Sect. A* **1976**, *32*, 751–767.

(67) Grove, L. E.; Hallman, J. K.; Emerson, J. P.; Halfen, J. A.; Brunold, T. C. Synthesis, X-Ray Crystallographic Characterization, and Electronic Structure Studies of a Di-Azide Iron(III) Complex: Implications for the Azide Adducts of Iron(III) Superoxide Dismutase. *Inorg. Chem.* **2008**, *47*, 5762–5774.

(68) Gutman, C. T.; Guzei, I. A.; Brunold, T. C. Structural, Spectroscopic, and Computational Characterization of the Azide Adduct of FeIII(2,6-Diacetylpyridinebis(Semioxamazide)), a Functional Analogue of Iron Superoxide Dismutase. *Inorg. Chem.* **2013**, *52*, 8909–8918.

(69) Blaesi, E. J.; Fox, B. G.; Brunold, T. C. Spectroscopic and Computational Investigation of Iron(III) Cysteine Dioxygenase: Implications for the Nature of the Putative Superoxo-Fe(III) Intermediate. *Biochemistry* **2014**, *53*, 5759–5770.

(70) Chai, S. C.; Bruyere, J. R.; Maroney, M. J. Probes of the Catalytic Site of Cysteine Dioxygenase. *J. Biol. Chem.* **2006**, *281*, 15774–15779.

(71) Connelly, N. G.; Geiger, W. E. Chemical Redox Agents for Organometallic Chemistry. *Chem. Rev.* **1996**, *96*, 877–910.

(72) Shearer, J.; Fitch, S. B.; Kaminsky, W.; Benedict, J.; Scarrow, R. C.; Kovacs, J. A. How Does Cyanide Inhibit Superoxide Reductase? Insight from Synthetic Fe III N 4 S Model Complexes. *Proc. Natl. Acad. Sci. U. S. A.* **2003**, *100*, 3671–3676.

(73) Luo, Y.-R. *Comprehensive Handbook of Chemical Bond Energies*, 1st Editio.; Taylor &

Francis Group, 2007.

(74) Coggins, M. K.; Sun, X.; Kwak, Y.; Solomon, E. I.; Rybak-Akimova, E.; Kovacs, J. A. Characterization of Metastable Intermediates Formed in the Reaction between a Mn(II) Complex and Dioxygen, Including a Crystallographic Structure of a Binuclear Mn(III)-Peroxo Species. *J. Am. Chem. Soc.* **2013**, *135*, 5631–5640.

(75) Kryatov, S. V.; Rybak-Akimova, E. V.; Schindler, S. Kinetics and Mechanisms of Formation and Reactivity of Non-Heme Iron Oxygen Intermediates. *Chem. Rev.* **2005**, *105*, 2175–2226.

Chapter 5. Influence of Thiolate versus Alkoxide Ligands on the Stability of Crystallographically Characterized Mn^{III}-Alkylperoxo Complexes

Portions of this chapter have been adapted from "Influence of Thiolate versus Alkoxide Ligands on the Stability of Crystallographically Characterized Mn^{III}-Alkylperoxo Complexes", Downing, Alexandra N.‡; Coggins, Michael‡; Poon, Penny Chaau Yan‡; Kovacs, Julie A. *In Review*.

5.1 Introduction

Nature utilizes manganese ions to promote a wide variety of oxidative transformations, many of which involve metastable Mn-peroxo species as key intermediates.[1–18] The majority of which have yet to be spectroscopically characterized. For example, lipoxygenase (MnLO) oxidize fatty acids via a Mn-OOR intermediate,[3,4,9,18] superoxide dismutases (MnSOD)[19,20] break down superoxide radicals, a toxic reactive oxygen species (ROS) associated with Alzheimer's[21,22] and Parkinson's[23] disease, via a Mn-OOH intermediate, and catalases[16] break down H_2O_2, another toxic ROS. A Mn-peroxo intermediate is also involved as an intermediate in photosynthetic H_2O oxidation.[11,24–26] The catalyst involved in these enzymatic reactions contain oxygen/nitrogen ligands in the manganese ion's primary coordination sphere. Why cysteinates are not incorporated in these enzyme active sites has yet to be investigated.

The inherent instability of metastable transition-metal peroxo intermediates precludes their structural characterization in most cases, and despite their significant role, very few well-characterized Mn-peroxo compounds have been reported,[8,27–38] and how the primary coordination affects reactivity properties has yet to be investigated. Previously we reported the

first crystallographically characterized examples of Mn^{III}-alkylperoxo compounds, Mn^{III}-OOR (R = ^{t}Bu, Cm),[27,31] and showed that there are distinct correlations between their geometric and electronic structures and the kinetic barrier to peroxo O-O bond cleavage.[27] Ligand substituents and the carbon backbone were varied, while maintaining a constant N_4S^- inner coordination sphere. Herein, we report the synthesis and structure of a metastable alkoxide derivative of our previously reported alkylperoxo compound, $[Mn^{III}(S^{Me2}N_4(6\text{-Me-DPEN})(OO^{t}Bu))^+$ (**1**, Figure 5.1),[27] in which we maintain an identical ligand framework and molecular charge, but vary the inner coordination sphere. Replacement of the monoanionic thiolate with a monoanionic alkoxide ($RS^- \rightarrow RO^-$) allows for a meaningful comparison of their structures and reactivity.

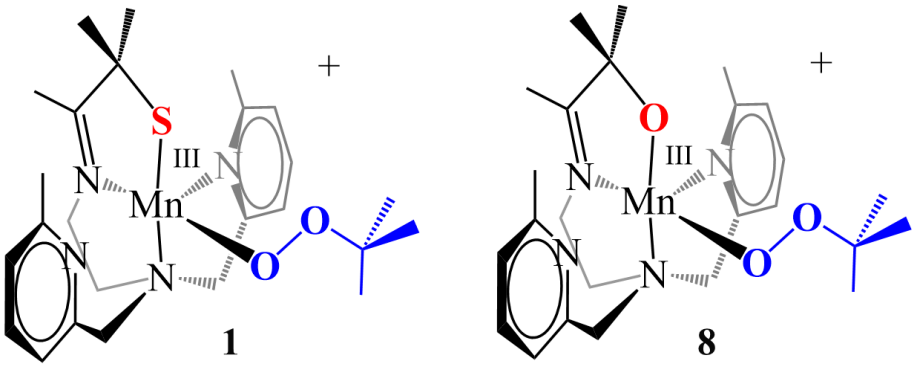

Figure 5.1. Chemdraw representation of $[Mn^{III}(S^{Me2}N_4(6\text{-Me-DPEN}))(OO^{t}Bu)]^+$ (**1**) and $[Mn^{III}(O^{Me2}N_4(6\text{-Me-DPEN}))(OO^{t}Bu)]^+$ (**8**).

5.2 Experimental

General methods. All manipulations were performed using Schlenk techniques or under an N_2 atmosphere in a glovebox. Reagents and solvents were purchased from commercial vendors, were of highest available purity, and were used without further purification unless otherwise noted. Methylene chloride (DCM), tetrahydrofuran (THF), diethyl ether (Et_2O), and acetonitrile (MeCN) were rigorously degassed, and purified using solvent purification columns housed in a custom stainless-steel cabinet, dispensed via a stainless steel Schlenk-line (GlassContour). Methanol (MeOH) was dried over magnesium methoxide and distilled prior to use. ^{1}H NMR spectra was recorded on a Bruker AV 300 and AV 301 FT NMR spectrometer at ambient temperature and were referenced to residual solvent. Chemical shifts are listed in parts per million (ppm), and coupling constants (*J*) in Hz. UV-vis spectra were recorded on a Varian Cary 50 spectrophotometer or Varian Cary 60 spectrophotometer equipped with a fiber optic cable connected to an ATR "dip" probe (C-technologies). A custom-built two-neck solution sample holder equipped with a threaded glass connector was sized specifically to fit the "dip" probe. Electrospray-ionization mass spectrometry (ESI-MS) data were obtained on a Bruker Esquire Liquid Chromatograph-Ion Trap mass spectrometer. Cyclic voltammograms were recorded in MeCN with $^nBu_4N(PF_6)$ supporting electrolyte (0.100 M) using a CH instruments (CHI600E) potentiostat with a glassy carbon working electrode, an $Ag^+/AgNO_3$ reference electrode, and a platinum auxiliary electrode. X-ray crystallography data were recorded on a Bruker APEX II single Crystal X-ray diffractometer with Mo Kα radiation. Magnetic moments (solution state) were obtained using the Evans' method as modified for super-conducting solenoids. The ligand precursors, N,N-Bis(6-methyl-2-pyridilmethyl)propane-1,3-diamine (6-Me-DPPN) and N,N-Bis(6-methyl-2-pyridilmethyl)ethane-1,2-diamine (6-Me-DPEN), complexes [$Mn^{II}(O^{Me2}N_4$(6-

Me-DPPN))](BPh$_4$) (**5**), [Mn^{II}(HO^{Me2}N$_4$(6-Me-DPEN)(MeCN))](BPh$_4$)$_2$ (**6**), and [Mn^{II}(HO^{Me2}N$_4$(6-Me-DPEN))(CHO$_2$)](BPh$_4$)•MeCN•Et$_2$O (**7-BPh$_4$**) were synthesized as previously described.[39,40]

5.2.1. Synthesis of [Mn^{II}(HO^{Me2}N$_4$(6-Me-DPEN))(CHO$_2$)](BPh$_4$)•MeCN (7-PF$_6$). Sodium methoxide (0.22 g, 4.4 mmol), 3-hydroxy-3-methyl-2-butanone (0.45 g, 4.4 mmol), 6-Me-DPEN (1.16 g, 4.0 mmol)[39], manganese(II) formate (0.58 g, 4.0 mmol), and sodium hexafluorophosphate (0.67 g, 4.0 mmol) were each individually dissolved or slurried in MeOH (5 mL) in the glovebox. Each reagent was subsequently added to a vial charged with a stir bar. After gently stirring the resulting reaction mixture at room temperature for two days, all volatiles were removed to afford a crude pale solid. The crude product was redissolved in minimal MeCN and filtered through Celite in a fine fritted filter. The resulting MeCN solution was layered with an equal volume of Et$_2$O and allowed to crystallize at -30 °C to afford **7-PF$_6$** as a white solid in 16% yield (0.35 g, 0.63 mmol). ESI-MS: Expected *m/z* for [C$_{19}$H$_{30}$N$_4$OMn]$^+$ = 408.8, found *m/z* = 408.1.

5.2.2. Monitoring the Formation of Alkyl Peroxo 8 via Electronic Absorption Spectroscopy. In a typical reaction, a 1 mM solution of [Mn^{II}(HO^{Me2}N$_4$(6-Me-DPEN))(CHO$_2$)](BPh$_4$)•MeCN (7-PF$_6$) was prepared in CH$_2$Cl$_2$ (5 mL) inside a glovebox. The resulting solution was transferred via gas-tight syringe to a custom-made two-neck vial equipped with a stir bar that has been purged with argon. *Tert*-butyl hydroperoxide (^{t}BuOOH, 1.5 equiv.) and triethylamine (TEA, 1.5 equiv.) were added to the Mn^{II} solution at ambient temperature. The reactions were monitored by EAS spectroscopy.

5.2.3. Computational Details.

All calculations were performed using the ORCA v.4.1.1 quantum chemistry package developed by Neese and coworkers,[41] and employed the def2-TZVP basis set and the def2/J auxiliary basis set for Coulomb fitting, the atom-pairwise dispersion correction of Grimme (D3BJ).[42] Tight convergence criteria, together with Grid5 (GridX5) and FinalGrid6 (FinalGridX6) integration grid size, were required for self-consistent field (SCF) solutions. Geometry optimization were performed using B3LYP hybrid functional, with the resolution of identity (RI) chain-of-spheres (RIJCOSX) approximation,[43,44] and initiated from the crystallographic coordinates when available. Analytical frequency calculations were performed on all optimized structures to determine whether the obtained stationary points correspond to local minima. Hybrid time-dependent DFT (TD-DFT) calculations employed the RIJCOSX and the Tamm-Dancoff approximations (TDA).[45,46] Excited states from TD-DFT calculations were analyzed using Natural Transition Orbitals (NTOs) and by visualizing their difference densities between the ground and excited states. Canonical molecular orbital isosurfaces and natural transition orbitals in the TD-DFT were visualized at an isovalue of 0.03 a_0^3 using UCSF Chimera software.[47]

5.2.4. X-ray Crystallography.

A clear prism of **7-PF$_6$**, measuring 0.49 x 0.10 x 0.08 mm^3 was mounted on a loop with oil. Data was collected at -173°C on a Bruker APEX II single crystal X-ray diffractometer, Mo-radiation. Crystal-to-detector distance was 40 mm and exposure time was 10 seconds per frame for all sets. The scan width was 0.5°. Data collection was 100% complete to 25° in ϑ. A total of 14099 reflections were collected covering the indices, -13<=h<=13, -15<=k<=15, -16<=l<=16. 7106 reflections were symmetry independent and the R_{int} = 0.0180 indicated that the data was of

excellent than average quality (0.07). Indexing and unit cell refinement indicated a monoclinic primitive lattice. The space group was found to be P 2_1 (No.4).

The data was integrated and scaled using SAINT, SADABS within the APEX2 software package by Bruker.[48] Solution by direct methods (SHELXT[49] or SIR97[50,51]) produced a complete heavy atom phasing model consistent with the proposed structure. The structure was completed by difference Fourier synthesis with SHELXL.[49,52,53] Scattering factors are from Waasmair and Kirfel[54]. Hydrogen atoms were placed in geometrically idealized positions and constrained to ride on their parent atoms with C---H distances in the range 0.95-1.00 Angstrom. Isotropic thermal parameters U_{eq} were fixed such that they were $1.2U_{eq}$ of their parent atom U_{eq} for CH's and $1.5U_{eq}$ of their parent atom U_{eq} in case of methyl groups. All non-hydrogen atoms were refined anisotropically by full-matrix least-squares.

Table 5.1. Crystal data, intensity collections[a], and structure refinement for [Mn^{II}($HO^{Me2}N_4$(6-Me-DPEN))(CHO_2)](BPh_4)•MeCN (**7-PF_6**).

	7-PF_6
Empirical formula	$C_{24}H_{34}F_6MnN_5O_3P$
MW	640.47
Temperature (K)	100(2)
Crystal system	Monoclinic
a (Å)	10.3246(6)
b (Å)	11.7292(6)
c (Å)	12.0296(6)
α (°)	90
β (°)	102.7390(10)
γ (°)	90
Volume ($Å^3$)	1420.92(13)
Z	2
Density (calculated, Mg/m^3)	1.497
Space group	P 2_1
R	0.0180[b]
R_w	0.0205[c]
GOF	1.021

[a] Mo Kα (λ = 0.71073 Å) radiation; graphite monochromator; -90 °C. [b] $R = \Sigma ||F_o|- |F_c|| / \Sigma |F_o|$. [c] $R_w = [\Sigma w(|F_o| - |F_o|)^2/\Sigma wF_o^2]^{1/2}$, where $w = 1/[\sigma^2(F_o^2) + (0.0241P)^2 + 0.2296P]$, $P = (F_o^2 + 2F_c^2)/3$.

5.3 Result and Discussion

5.3.1 *Synthesis and Structure of Mn^{II} Alkoxide Complexes*

In order to determine how the primary coordination sphere influences the electronic, redox, and reactivity properties of previously reported $[Mn^{II}(S^{Me2}N_4(6\text{-Me-DPEN}))]^+$ (**2**) and $[Mn^{II}(S^{Me2}N_4(6\text{-MeDPPN}))]^+$ (**3**, Figure 5.2)[39], we report herein the synthesis and characterization of the corresponding alkoxide derivatives. Thiolate-ligated **2** and **3** are precursors to rare examples of structurally characterized alkylperoxo complexes $[Mn^{III}(S^{Me2}N_4(6\text{-Me-DPEN})(OO^tBu))^+$ (**1**, Figure 5.1) and $[Mn^{III}(S^{Me2}N_4(6\text{-Me-DPPN})(OO^tBu))^+$ (**4**).[27] The corresponding alkoxide or alcohol-ligated derivatives, **5**-**7** (Figure 5.2) were synthesized using a strategy identical to that used to prepare **2** and **3**,[39] except that 3-hydroxy-3-methyl-2-butanone was used in place of 3-mercapto-3-methyl-2-butanone, and in the case of **7** (Figure 5.2), manganese(II) bis-formate, $Mn^{II}(OC(H)O)_2$, was used in place of $[Mn^{II}(H_2O)_6](SO_4)$. The yield of MeCN-ligated **6** (Figure 5.2) was low (7%), making it inconvenient to interrogate its spectroscopic properties or explore its reactivity. Thus, the remainder of the discussion, with the exception of crystallographic characterization, will focus on complexes **5** and **7.** (Figures 5.2 and 5.3)

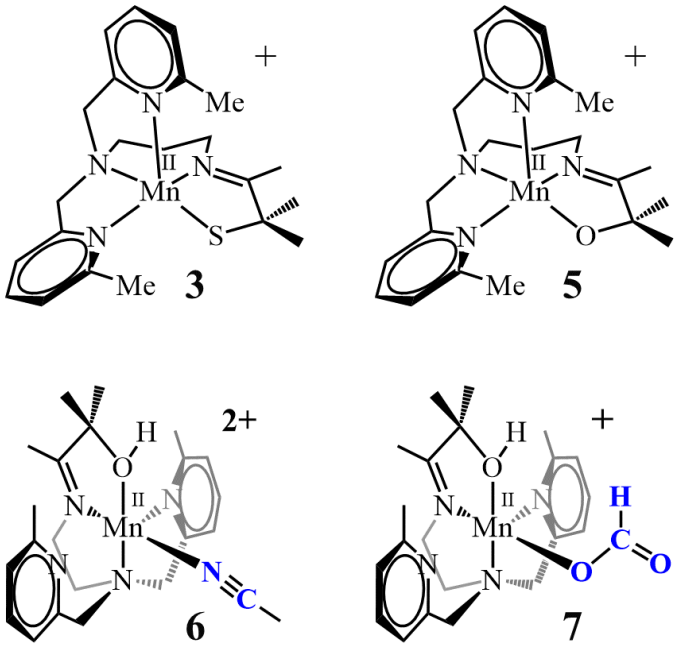

Figure 5.2. Chemdraw representations of $[Mn^{II}(S^{Me2}N_4(6\text{-Me-DPPN}))]^+$ (**3**), $[Mn^{II}(O^{Me2}N_4(6\text{-Me-DPPN}))]^+$ (**5**), $[Mn^{II}(HO^{Me2}N_4(6\text{-Me-DPEN})(MeCN))]^{2+}$ (**6**), and $[Mn^{II}(HO^{Me2}N_4(6\text{-Me-DPEN})(CHO_2))]^+$ (**7**).

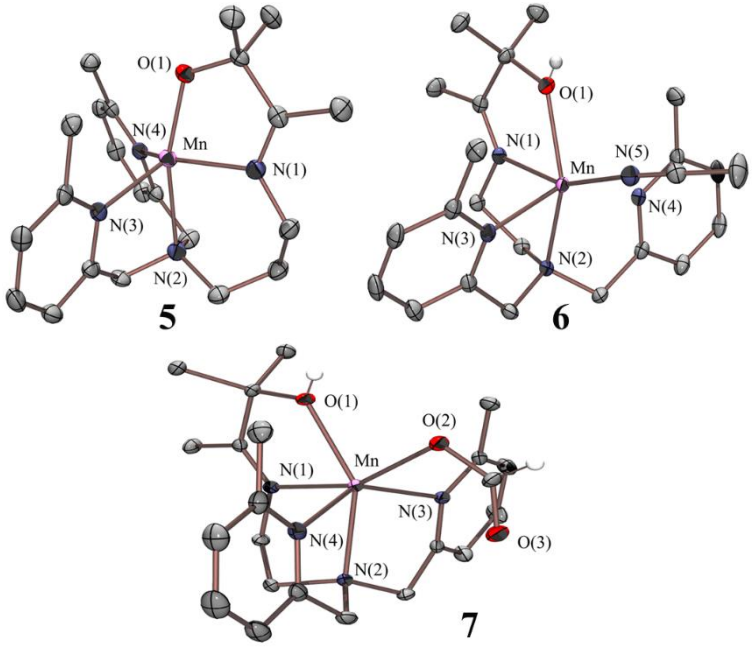

Figure 5.3. ORTEP diagram of $[Mn^{II}(O^{Me2}N_4(6\text{-Me-DPPN}))]^+$ (**5**)[40], $[Mn^{II}(HO^{Me2}N_4(6\text{-Me-DPEN})(MeCN))]^{2+}$ (**6**)[40], and $[Mn^{II}(HO^{Me2}N_4(6\text{-Me-DPEN})(CHO_2))]^+$ (**7**), 50% probability ellipsoids, with hydrogen atoms, with the exception of alcohol protons, counterions, and solvents of crystallization omitted for clarity.

Single crystals of **5-7** suitable were grown by layering Et_2O onto a concentrated MeCN solution of the corresponding Mn^{II} complex. As shown in the ORTEP diagrams of Figure 5.3, $[Mn^{II}(O^{Me2}N_4(6\text{-Me-DPPN}))](BPh_4)$ (**5**) is five-coordinate and contains an alkoxide in place of the thiolate of **3**. The carbon backbone and ligand scaffold are identical. Selected metrical parameters and crystal data for **5-7** are compiled in Table 5.2. Complexes **6** and **7** were shown to reproducibly contain a proton on the alkoxide oxygen (Figure 5.3). Evidence to support this is based on their relative Mn-O bond distances, the number of associated counterions, and observed H-bonding network. By replacing the BPh_4^- with a PF_6^- counterion, a higher resolution structure of **7** (R = 2.0% for **7-PF$_6$** versus R = 6.8% for **7-BPh$_4$**) was obtained and was also shown to contain a proton on the alkoxide oxygen, O(1). The Mn-O(1) bonds of 5-coordinate alkoxide-ligated **5** are 0.24 Å, and 0.21 Å shorter than the corresponding distance in 6-coordinate alcohol-ligated **6** and **7**, respectively (Table 5.2, Figure 5.3), which contain a protonated alkoxide. The hydrogen bonded network shown in the packing diagram of **7** (Figure 5.4) provides additional evidence to indicate that a proton resides on O(1). Bond distances for all three structures (Table 5.2) are more consistent with Mn^{II} than Mn^{III}, ruling this out as an explanation for the extra counterion of **6** and **7**. The Mn^{II} ions of **6** and **7** are each six-coordinate, with either MeCN (**6**) or formate (**7**) coordinated *trans* to the imine nitrogen. Alkoxide-ligated **5** and thiolate-ligated **3** are both mononuclear, monocationic 5-coordinate Mn^{II} complexes and constructed from an identical ligand scaffold, therefore a comparison of their metrical parameters (Table 5.2) should provide the best insight into the structural influence of the thiolate versus alkoxide. Three of the four Mn-N bond lengths (Mn-N(1), Mn-N(2), and Mn-N(3)) in alkoxide-ligated **5** are noticeably longer than the corresponding distances in thiolate-ligated **3** (Table 5.2). This in part reflects the more distorted square pyramidal geometry (τ = 0.47) of alkoxide-ligated **5** relative to thiolate-ligated **3**

(τ = 0.22), a geometry which provides optimum orbital overlap is favored by the highly covalent M-SR bonds.[55,56]

Table 5.2. Selected bond distances (Å) and angles (deg) for thiolate-ligated [$Mn^{II}(S^{Me2}N_4$(6-Me-DPPN))](BPh_4) (**3**)[39], alkoxide-ligated [$Mn^{II}(O^{Me2}N_4$(6-Me-DPPN))](BPh_4) (**5**)[40], alkoxide-ligated [$Mn^{II}(HO^{Me2}N_4$(6-Me-DPEN)(MeCN))](BPh_4)$_2$ (**6**)[40], [$Mn^{II}(HO^{Me2}N_4$(6-Me-DPEN)(CHO_2))](BPh_4)•MeCN•Et_2O (**7-BPh_4**)[40], and [$Mn^{II}(HO^{Me2}N_4$(6-Me-DPEN)(CHO_2))](PF_6)•MeCN (**7-PF_6**).

	3	**5**	**6**	**7-BPh_4**	**7-PF_6**
Mn-X	2.3742(3)[b]	1.9585(14)[a]	2.203(10)[c]	2.172(4)[c]	2.233(1)[c]
Mn-N(1)	2.1909(10)	2.2184(19)	2.2027(9)	2.248(3)	2.246(1)
Mn-N(2)	2.2476(10)	2.2962(17)	2.2798(9)	2.329(3)	2.308(2)
Mn-N(3)	2.1830(10)	2.2293(18)	2.3157(10)	2.267(3)	2.306(2)
Mn-N(4)	2.2787(10)	2.1931(18)	2.2784(10)	2.275(3)	2.291(2)
Mn-N(5)	N/A	N/A	2.2254(10)	N/A	N/A
Mn-O(2)	N/A	N/A	N/A	2.118(3)	2.120(1)
X-Mn-N(1)	82.03(3)	77.95(6)	69.95(3)	69.68(9)	68.65(5)
X-Mn-N(2)	154.06(3)	162.39(7)	147.53(3)	144.13(9)	144.03(9)
X-Mn-N(3)	127.47(3)	118.62(6)	105.39(3)	109.39(9)	106.10(5)
X-Mn-N(4)	93.97(3)	105.96(6)	108.30(4)	113.6(1)	110.51(5)
X-Mn-O(2)	N/A	N/A	N/A	84.0(1)	87.12(5)
N(1)-Mn-N(3)	114.15(4)	112.41(7)	102.24(3)	100.8(1)	86.63(5)
N(1)-Mn-N(4)	140.58(4)	133.98(7)	86.94(3)	99.0(1)	106.37(5)
N(3)-Mn-N(4)	99.40(4)	105.51(6)	146.22(3)	136.6(1)	143.38(5)
O(2)-Mn-N(1)	N/A	N/A	N/A	158.6(1)	154.53(5)
O(2)-Mn-N(2)	N/A	N/A	N/A	126.6(1)	128.85(5)
O(2)-Mn-N(3)	N/A	N/A	N/A	89.22(11)	92.98(5)
O(2)-Mn-N(4)	N/A	N/A	N/A	85.98(11)	88.98(5)
τ	0.22	0.47	N/A	N/A	N/A

Note: [a]X = O, [b]X = S, [c]X = OH.

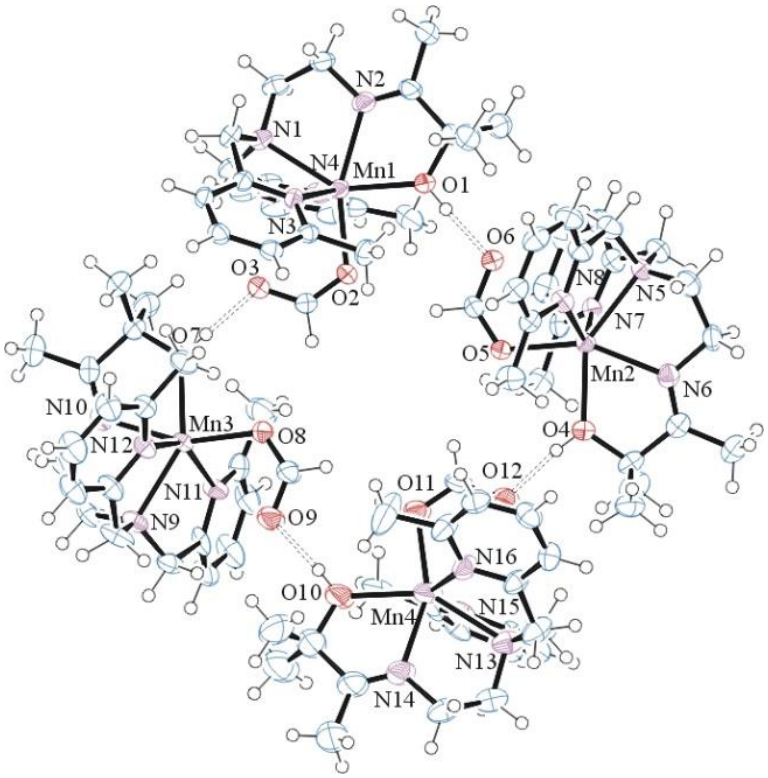

Figure 5.4. Packing diagram of **7**, which shows a hydrogen bonded tetramer involving the coordinated alcohol proton and the distal formate oxygen.

5.3.2 *Magnetic and Redox Properties*

As is true for the majority of Mn^{II} complexes, complexes **5** and **7** are both high-spin S = 5/2, as shown by their solution magnetic moment (μ_{eff}(**5**) = 6.00 B.M.; μ_{eff}(**7**) = 5.93 B.M.), determined using the Evans' method. The ideal Curie behavior in the $1/\chi$ versus temperature plot (range: 5-298 K, Figure 5.5)[40], indicates that the H-bonding network, observed in the crystal structure of **7** does not affect its magnetic properties in the solid state (μ_{eff} = 5.84 μ_B). The thiolate ligand does not affect the spin-state either, as shown by both the solution (μ_{eff} = 5.78 μ_B) and solid-state (μ_{eff} = 5.57 μ_B) magnetic moment of thiolate-ligated **3** (Figure 5.2).

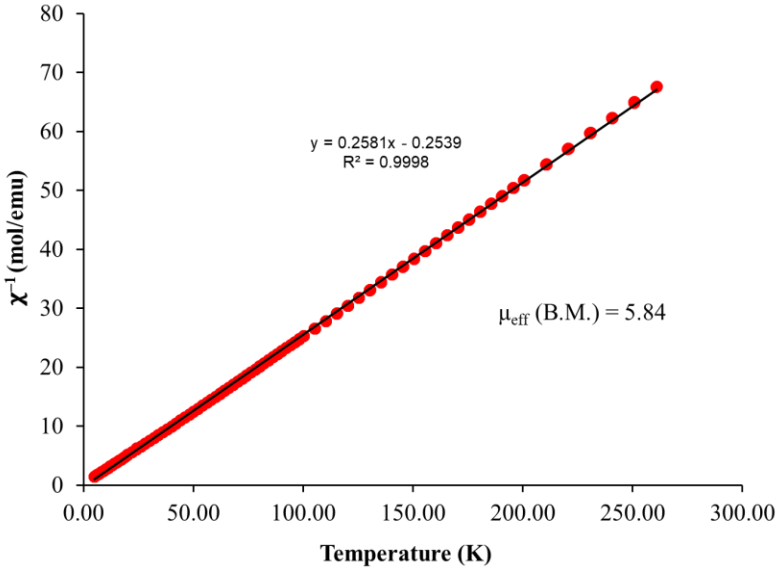

Figure 5.5. Inverse molar magnetic susceptibility (χ_M^{-1}) versus temperature (K) for [Mn^{II}($HO^{Me2}N_4$(6-Me-DPEN)(CHO_2))](BPh_4)•MeCN•Et_2O (**7-BPh$_4$**, solid state), from which the magnetic moment, μ_{eff} = 5.84 B.M. was obtained, consistent with a monomeric high-spin (*S* = 5/2) Mn^{II} ion.[40]

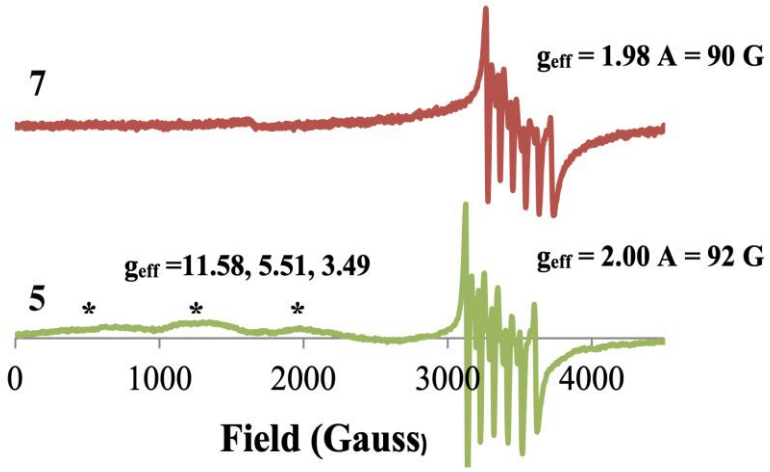

Figure 5.6. X-band (9.4 GHz) perpendicular mode EPR spectra of [Mn^{II}($HO^{Me2}N_4$(6-Me-DPEN)(CHO_2))](BPh_4)•MeCN•Et_2O (**7-BPh$_4$**, top red trace), and [Mn^{II}($O^{Me2}N_4$(6-Me-DPPN))](BPh_4) (**5**, bottom trace). Low-field resonances discussed in the text are identified with an asterisk (*).[40]

The X-band EPR spectrum of **5** and **7** each display features typical of high-spin Mn^{II} (Figure 5.6) with a multi-line signal at g_{eff} = 1.98 (**7**), and 2.00 (**5**), and hyperfine coupling (*A* = 90 G (**7**), 92 G (**5**)) to the ^{55}Mn (*I* = 5/2) nucleus.[40] The coupling constants are consistent with

monometic structures for each. Three weak broad low-field signals, at g = 3.49, 5.51, 11.58 (Figure 5.6), are observed in the EPR spectrum of alkoxide-ligated **5**, in addition to the multiline signal near g ~2, suggesting that there is significant zero-field splitting. These low-field signals are not observed with thiolate-ligated **3**, indicating that the alkoxide perturbs the ligand-field. The electronic absorption spectra of **5** and **7** are featureless, since the d→d transitions are spin-forbidden, and the RO → Mn^{II} charge transfer transitions fall in the UV region of the spectrum.

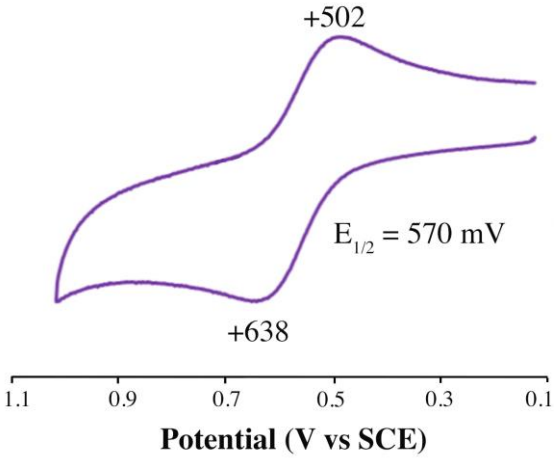

Figure 5.7. Cyclic voltammogram of [Mn^{II}($O^{Me2}N_4$(6-Me-DPPN))](BPh_4) (**5**) in MeCN. 0.1 M $^nBu_4NPF_6$ supporting electrolyte, 120 mV/s scan rate. Potentials listed are versus SCE.[40]

As shown in the cyclic voltammogram of Figure 5.7, alkoxide-ligated **5** is oxidized at a potential of +570 mV vs SCE in MeCN.[40] This potential is cathodically shifted by 58 mV, relative to structurally analogous thiolate-ligated **3** ($E_{p,a}$ = +580 mV vs SCE), indicating that the thiolate ligand provides slightly more stability to the Mn^{III} oxidation state, and that the metal ion of **5** is slightly more Lewis acidic than that of **3**. Alcohol-ligated **7** is oxidized at a slightly higher potential of $E_{p,a}$ = +605 mV vs SCE in MeCN (Figure 5.8). The irreversibility of the latter (ΔE_p = 310 mV) likely reflects the fact that the alcohol deprotonates upon oxidation to Mn^{III}.

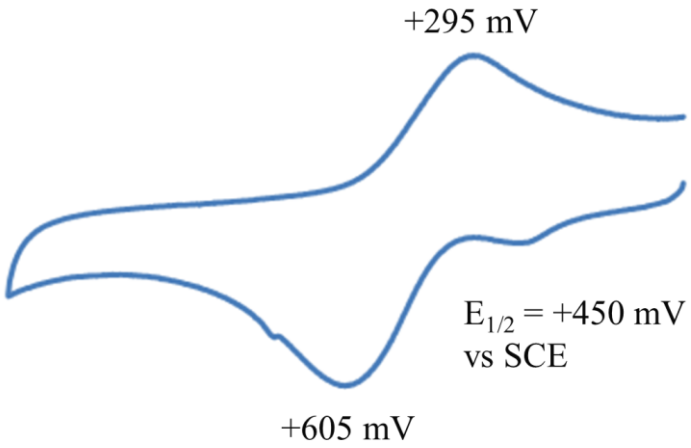

Figure 5.8. Cyclic voltammogram of **7** in MeCN at ambient temperature. Scan rate = 120 mV/s, Ag/AgCl reference electrode, Et_4NPF_6 supporting electrode. Potentials are reported versus SCE.

5.3.3 *Reactivity of 5 and 7 with ^{t}BuOOH*

The addition of *tert*-butyl hydroperoxide (^{t}BuOOH) to **5** and **7** in the presence of Et_3N causes a color change from colorless to blue accompanied by the growth of an intense absorption band at λ_{max} = 650 nm (ε = 1010 $M^{-1}cm^{-1}$) (Figure 5.9 and 5.10). This band is noticeably red-shifted relative to thiolate-ligated Mn^{III}-OOR (**1**, Figure 5.1, λ_{max} = 603(600) nm).[27] It is also lower in energy than all of our other thiolate-ligated Mn^{III}-OO^{t}Bu compounds (λ_{max} = 585-600 nm, Table 5.3),[27,31] but closer in energy to that of carboxamide-ligated $[Mn^{III}(dpaq^{2Me})(OO^tBu)]^+$ (**9**, λ_{max} = 690(115) nm).[38] The latter contains Mn^{III} in an N_5^- coordination sphere.[38] The intensity of the 650 nm band associated with metastable, alkoxide-ligated **8** maximizes once 1.6 equivalents of ^{t}BuOOH have been added Mn^{II}-**7** (Figure 5.9), a stoichiometry that is consistent with a mechanism involving the initial oxidation of Mn^{II}, to afford an unobserved Mn^{III} intermediate, possibly a Mn^{III}-OH (equation 5.1),[38,57] followed by proton-induced release of H_2O (equation 5.2), or ROH (equation 5.3) and ^{t}BuOO$^-$ binding. Support for this mechanism was provided previously via a titration between $[Mn^{II}(dpaq^{2Me})]^+$ and 0-1.0 equiv. of ^{t}BuOOH to

initially afford $[Mn^{III}(dpaq^{2Me})(OH)]^+$, followed by the addition of 50 equiv. of ^{t}BuOOH to afford $[Mn^{III}(dpaq^{2Me})(OO^tBu)]^+$ (**9**).[38]

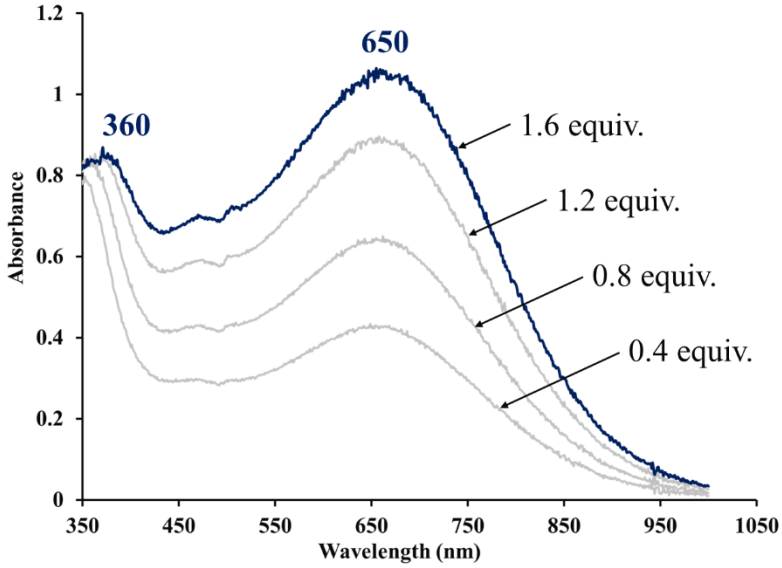

Figure 5.9. EAS spectrum of monitoring the titration of 1.6 equiv. ^{t}BuOOH to Mn^{II} **7** in DCM at -40 °C.[40]

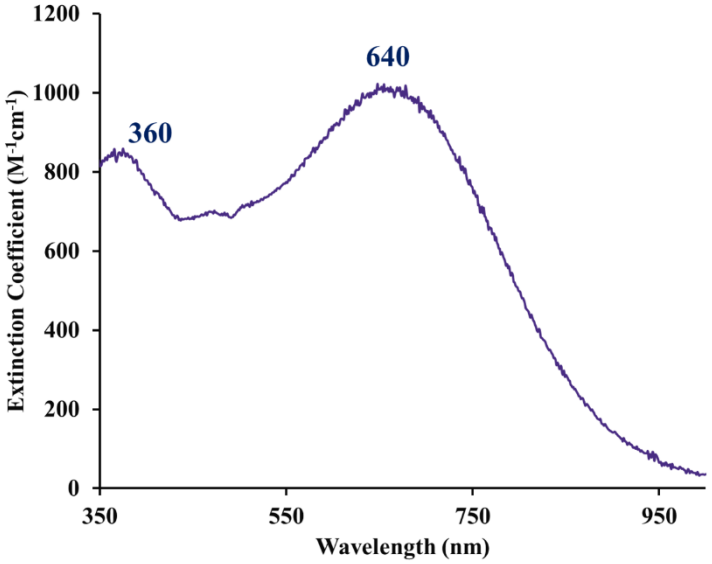

Figure 5.10. Quantitative electronic absorption spectrum of $[Mn^{III}(O^{Me2}N_4$(6-Me-DPEN))$(OO^tBu)]]^+$ (**8**) in DCM at ambient temperature.

$$2Mn^{II} + ROOH \rightarrow Mn^{III}\text{-}OH + Mn^{III}\text{-}OR \quad (5.1)$$

$$Mn^{III}\text{-}OH + ROOH \rightarrow Mn^{III}\text{-}OOR + H_2O \quad (5.2)$$

$$Mn^{III}\text{-}OR + ROOH \rightarrow Mn^{III}\text{-}OOR + ROH \quad (5.3)$$

5.3.4 *Vibrational Spectrum of 8*

The FT-IR spectrum of **8** displays an isotopically sensitive stretch is observed at 850 cm^{-1}, which shifts to 816 cm^{-1} when $^{t}Bu^{18}O^{18}OH$ is used in place of $^{t}Bu^{16}O^{16}OH$. (Figure 5.11) Both the $\nu_{O\text{-}O}$ stretching frequency and isotopic shifts (34 cm^{-1}), provides evidence to support the formation of an alkylperoxo intermediate $[Mn^{III}(O^{Me2}N_4(6\text{-Me-DPEN}))(OO^{t}Bu)](BPh_4)$ (**8**). The isotopic shift is close to that predicted (44 cm^{-1}) based on a harmonic oscillator and Hooke's law. The $\nu(^{16}O\text{-}^{16}O)$ stretching frequency of **8** is close to that of **1** (875 cm^{-1}), both of which are the lowest reported stretches for any vibrationally characterized Mn^{III}-alkylperoxo compounds (range: 875-896 cm^{-1}),[37,58,59] including our previously reported thiolate-ligated peroxo compounds,[27,31] complexes **1**, **4**, $[Mn^{III}(S^{Me2}N_4(\text{quinoEN}))(OO^{t}Bu)]^{+}$ (**10**), and $[Mn^{III}(S^{Me2N}{}_4(\text{quinoPN}))(OO^{t}Bu)]^{+}$ (**11**), but is closer to that of carboxamide-ligated **9** (872 cm^{-1})[38] (Table 5.3). The only reported Mn^{III}-peroxo with a lower $\nu(^{16}O\text{-}^{16}O)$ stretching frequency ($\nu_{O\text{-}O}$ = 819 cm^{-1}), $[Mn^{III}(S^{Me2}N_4(6\text{-Me-DPEN}))]_2(\textit{trans}\text{-}\mu\text{-}1,2\text{-}O_2)(BPh_4)_2$, contains a bridging peroxo.[32] Badger's rule[60,61] is roughly adhered to for alkoxide-ligated **8** as well as thiolate-ligated **1**, **4**, **10**, and **11** (Figure 5.12). Deviations from linearity (R^2 = 0.71) likely reflect perturbations introduced by perturbing the ligand scaffold, replacing the thiolate with an alkoxide, and more likely, are a result of a more complex vibration mode that involves other portions of the moledule (*vide infra*). As we showed previously, the $\nu_{O\text{-}O}$ stretching frequency for our previously

reported thiolate-ligated complexes **1**, **4**, **10**, and **11**,[27] decrease as the O-O bond length increases (Figure 5.13). The data point for alkoxide-ligated **8** falls off of this trend line (Figure 5.13), however, indicating that the $\nu_{O\text{-}O}$ vibrational mode involves the alkoxide and other portions of the molecule. This is supported by density functional theory (DFT) calculations (*vide infra*).

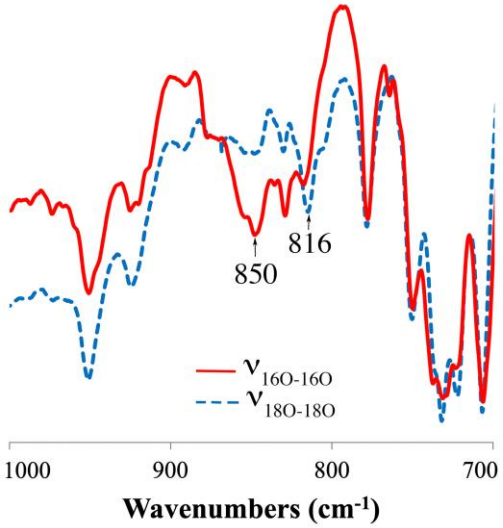

Figure 5.11. FT-IR spectrum of alkoxide-ligated ^{t}butyl peroxo compound **8**.[40]

Table 5.3. Comparison of Vibrational and Electronic Absorption Parameters, and Half-life of Thiolate- (**1**, **4**, **10**, and **11**), Alkoxide- (**8**), and carboxamide- (**9**) Ligated Alkylperoxo Compounds.

Peroxo Compound	O-O (Å)	$\nu_{16O\text{-}16O}$ (cm^{-1})	$\nu_{18O\text{-}18O}$ (cm^{-1})	λ_{max} (nm)	λ_{max} (nm)	Mn•••N^{Ar}_{avg} (Å)	$t_{1/2}$ (T, K) (sec)
8	1.473(1)	850	816	360	650	2.39	6730(298)
9	1.48[a]	872	N/A	~475	690	N/A	3200(253)[b]
1	1.468(7)	875	816	355	600	2.41	249(293)
10	1.457(7)	888	831	385	590	2.44	367(293)
4	1.431(5)	893	835	420	585	2.510	147(293)
11	1.438(5)	895	831	415	590	2.48	136(293)

Note: [a]DFT calculated distance. [b] Parham, J. D.; Wijeratne, G. B.; Rice, D. B.; Jackson, T. A. *Inorg. Chem.* **2018**, *57*, 2489–2502. (Ref 27)

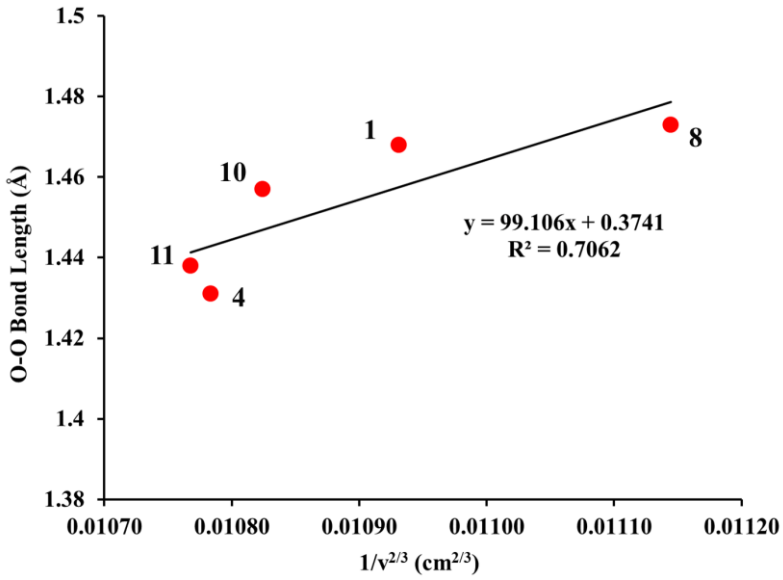

Figure 5.12. Badger's rule[60,61] plot.

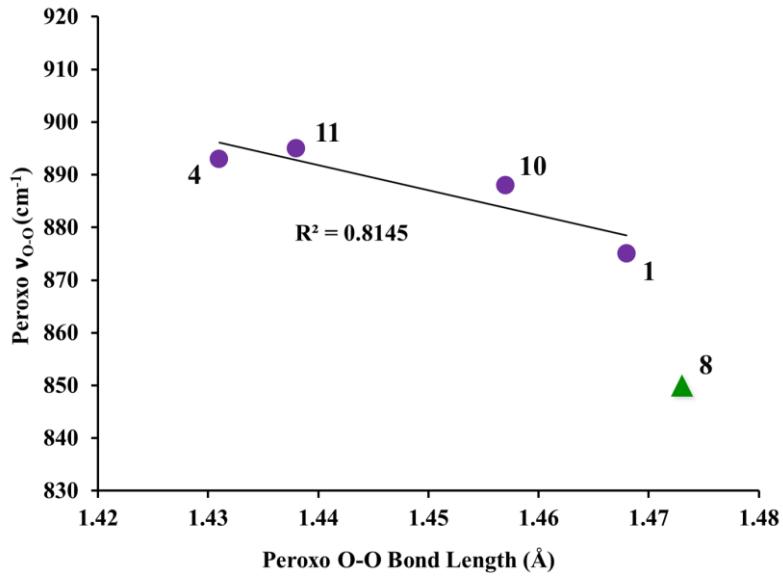

Figure 5.13. Correlation between peroxo O-O stretching frequency and peroxo O-O bond length, showing alkoxide-ligated **8** (green triangle) vs thiolate-ligated **1**, **4**, **10**, and **11** (purple circles).

In contrast to **7**, no intermediates are observed in the reaction between ^{t}BuOOH and five-coordinate **5**. Instead, direct conversion to a stable, crystallographically characterized bis-oxo $Mn^{IV}Mn^{IV}$ dimer was observed,[62] implying that the rate-determining step involves ^{t}BuOOH binding with **5**. The final product in the reaction between **7** ^{t}BuOOH binding to **5** is also a bis-oxo $Mn^{IV}Mn^{IV}$ dimer. Although the rate at which metastable **8** forms (Figure 5.14) is slow

(k_{obs}^{298K} = 4.4 x 10^{-4} s^{-1}, Figure 5.15), it decays four times more slowly (*vide infra*) under the same conditions, thereby facilitating its observation. The slow rate at which **8** forms likely reflects the fact that formic acid must dissociate in order for a reaction to occur.

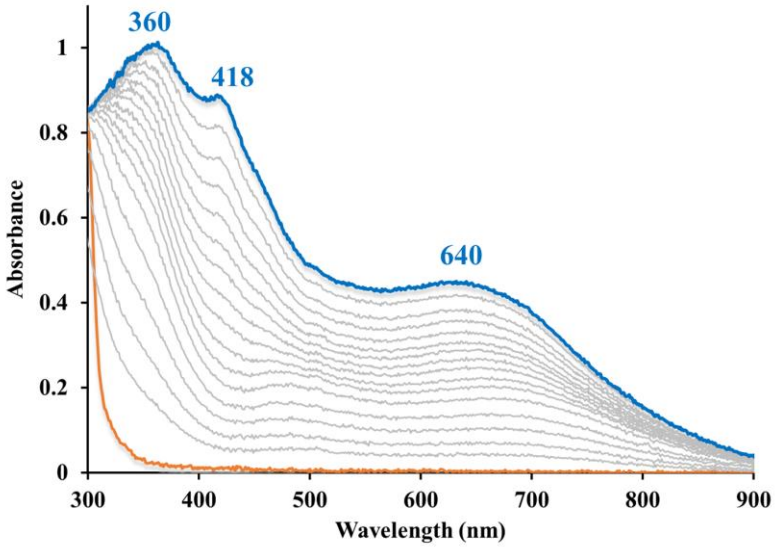

Figure 5.14. EAS spectrum monitoring the formation of alkoxide-ligated Mn^{III}-OO^{t}Bu (**8**, blue trace) by addition of 2.5 equiv. ^{t}BuOOH and 2.5 equiv. TEA to DCM solution of Mn^{II} (**7**, orange trace) at 298 K. Spectrum recorded in 13.8 minutes interval. Growth was monitored over 3.23 hours. [Mn^{II} (**7**)] = 1.0 mM.

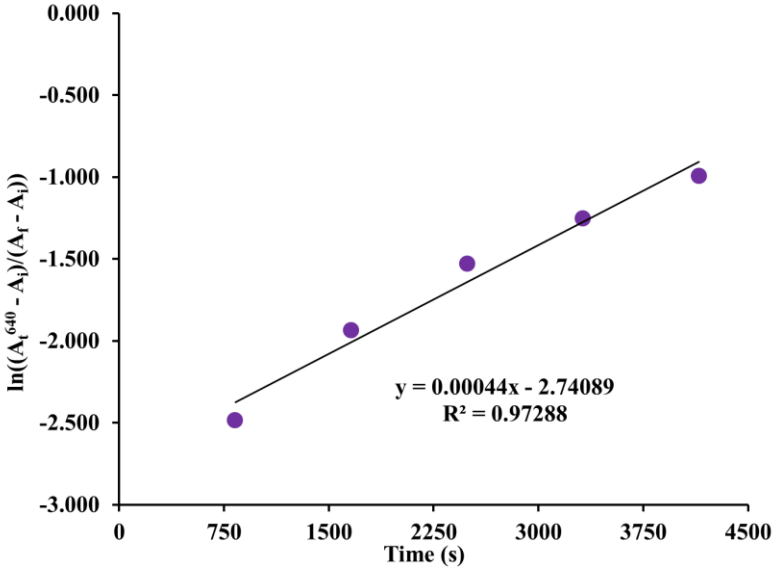

Figure 5.15. First order kinetics plot for the growth of alkoxide-ligated Mn^{III}-OO^{t}Bu (**8**) in DCM at 298 K. [Mn^{II} (**7**)] = 1 mM, [^{t}BuOOH] = 3 mM, [Et_3N] = 3 mM.

5.3.5 *X-ray Structure of Alkoxide-Ligated Alkylperoxo 8*

Dark blue single crystals of $[Mn^{III}(O^{Me2}N_4(6\text{-Me-DPEN}))(OO^tBu)](BPh_4)$ (**8**) was previously obtained[40] and the ORTEP diagram of which is shown in Figure 5.16. Selected metrical parameters for alkoxide-ligated **8** are compared with those of thiolate-ligated $[Mn^{III}(S^{Me2}N_4(6\text{-Me-DPEN}))(OO^tBu)]^+$ (**1**) in Table 5.4.

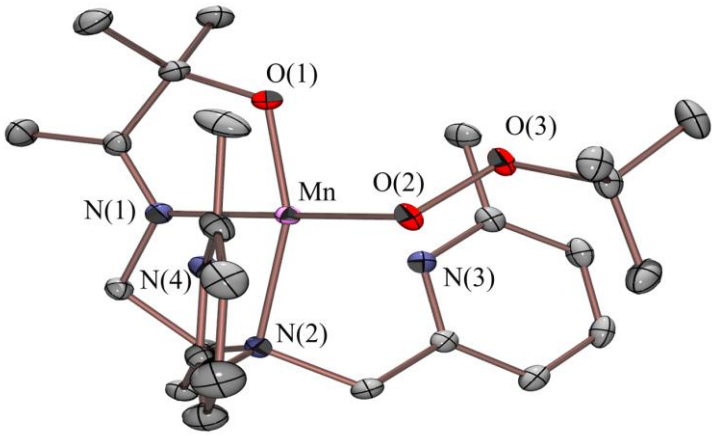

Figure 5.16. ORTEP diagram of $[Mn^{III}(O^{Me2}N_4(6\text{-Me-DPEN}))(OO^tBu)](BPh_4)\bullet Et_2O$ (**8**). Hydrogen atoms, counterion, and solvent of crystallization have been omitted for clarity.

As shown in Figure 5.8, ^{t}BuOO$^-$ binds *cis* to the alkoxide oxygen, and *trans* to the imine nitrogen and is coordinated in an end-on η^1-OOR fashion. A similar *cis*-orientation of the alkylperoxo is seen with thiolate-ligated **1**, as well as all of our previously reported thiolate-ligated RS-Mn-OOR complexes.[27,31] The separation between the Mn^{III} ion and the distal oxygen, O(2), in **8** (2.743 Å) is significantly longer than the sum of the covalent radii (2.01 Å),[63] and approximately the same (Table 5.4) as that of **1**,[27] ruling out a side-on η^2-OO(R) binding mode. The peroxo O-O bond of **8** is significantly longer than reported side-on η^2-coordinated Mn^{III}-peroxo compounds (O-O bond range = 1.403(4)-1.428(7) Å).[27,31,58,59,64,65] The presence of a single BPh_4^- counterion (per Mn) confirms that the manganese ion is in the Mn^{III} oxidation state.

The distance between the Mn ion of **8**, and each of the pyridine nitrogens, N(3) and N(4) (Table 5.4), is significantly longer than the sum of the covalent radii (2.10 Å). This is also the case with thiolate-ligated **1** (Table 5.4), as well as the other three crystallographically characterized thiolate-ligated Mn^{III}-OOR complexes reported by our group.[27,31] The average Mn•••N^{Ar} distance (2.39(4) Å) in **8** is within error of that (2.41(6) Å) of **1**. The peroxo O-O and Mn-O bond lengths in **8** (1.473(1) Å and 1.856(1) Å, respectively) are also within error of the corresponding bond lengths in **1** (1.468(7) Å and 1.853(6) Å, respectively).

Table 5.4. Comparison of Selected Bond Distances (Å) and Angles (deg) for Thiolate-ligated ^{t}Butyl Peroxo Compound $[Mn^{III}(S^{Me2}N_4$(6-Me-DPEN))$(OO^{t}Bu)]^+$ (**1**)[27] and Alkoxide-Ligated ^{t}Butyl Peroxo Compound $[Mn^{III}(O^{Me2}N_4$(6-Me-DPEN))$(OO^{t}Bu)]^+$ (**8**)[40].

	1	**8**
Mn(1)-X	2.241(3)[a]	1.8535(9)[b])
Mn(1)-N(1)	2.015(8)	2.004(1)
Mn(1)-N(2)	2.163(7)	2.161(1)
Mn(1)-N(3)	2.354(8)	2.355(1)
Mn(1)-N(4)	2.471(7)	2.431(1)
Mn(1)-O^{peroxo}	1.853(6)	1.856(1)
O-O^{peroxo}	1.468(7)	1.473(1)
Mn(1)•••O^{peroxo}	2.769	2.743
Mn(1)-O(1)-O(2)	112.4(4)	110.41(7)
O(1)-Mn(1)-X	94.9(2)[a]	98.26(4)[b]
O(1)-Mn(1)-N(1)	175.7(3)	176.10(5)
X-Mn-N(2)	162.6(2)[a]	159.67(4)[b]
X-Mn-N(3)	112.4(2)[a]	113.08(4)[b]
X-Mn-N(4)	109.13(18)[a]	107.98(4)[b]
N(3)-Mn-N(4)	133.3(3)	134.84(4)

Note: [a]X = S(1), [b]X = O(3)

5.3.6 *Correlation Between Metrical and Spectroscopic Parameters for 8*

Previously we showed that there is a strong correlation between the π^*(O-O)→Mn charge transfer (CT) bands of thiolate-ligated Mn^{III}-OOR compounds and the alkylperoxo O-O bond length.[27] As shown in Figure 5.17, the CT band systematically blue-shifts as the O-O bond length increases, a trend which also holds for alkoxide-ligated **8** (green triangle). One can explain this trend as follows. If we first consider the peroxo orbitals prior to interaction with the metal ion, the energy of the π_v^*(O-O) orbital should increase as the O-O bond length decreases, since, in general, the separation between bonding and antibonding orbitals increases as a bond becomes stronger. This would push the π_v^*(O-O) orbital closer to the metal ion d-orbitals thereby decreasing the energy of the π_v^*(O-O)→Mn transition which is in agreement with the experimental data of Figure 5.17. It is surprising, however, that the alkoxide complex **8** adheres to this trend, given that perturbations to the inner coordination sphere should change the energy of the metal acceptor orbitals. There is also a correlation between the energy of the low energy charge transfer band and the peroxo υ_{O-O} stretching frequency (Figure 5.18), as well as the Mn•••N^{Ar} distance and the peroxo O-O bond length (Figure 5.19).[27] Replacement of thiolate ligand with an alkoxide moiety does not, therefore, appear to influence the empirical relationship between Mn(1)•••N^{Ar} distance, π_υ^*(O-O) → Mn CT band, and peroxo O(1)-O(2) bond length.

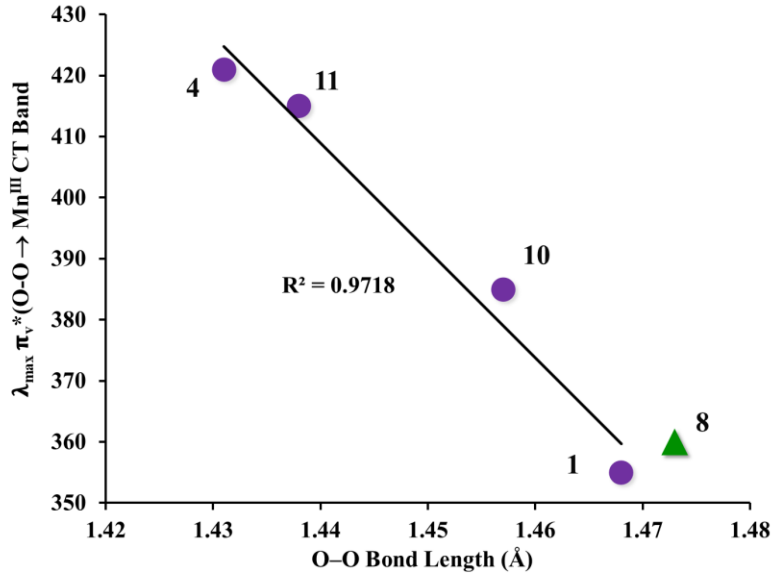

Figure 5.17. Correlation between peroxo π*(O-O)→Mn charge transfer band and peroxo bond length, showing the thiolate-ligated compounds (purple circles) vs the alkoxide compound **8** (green triangle).

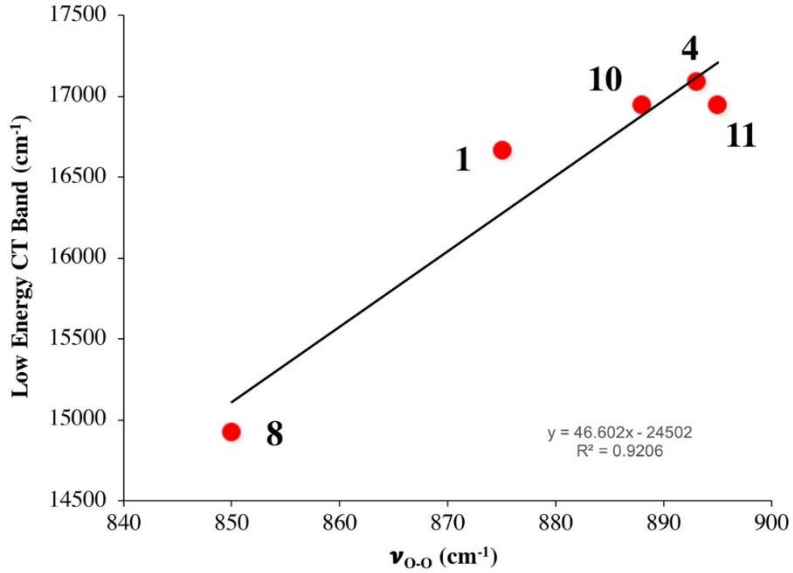

Figure 5.18. Correlation between the low energy charge transfer (CT) band and the peroxo O-O stretching frequency.

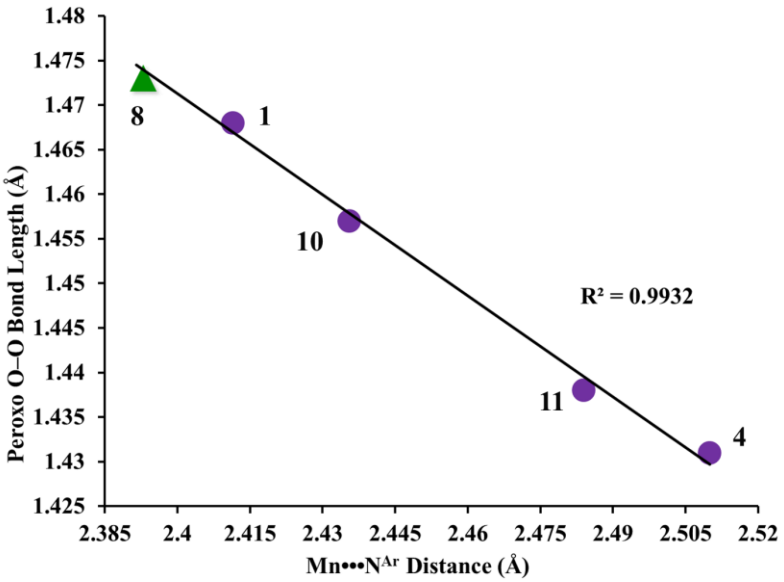

Figure 5.19. Correlation between peroxo O-O bond length and the mean Mn•••N^{Ar} separation showing the thiolate-ligated compounds (purple circles) vs alkoxide ligated **8** (green triangle).

5.3.7 *Stability of Alkoxide Alkylperoxo 8 Relative to the Thiolate Derivative 1*

One might expect the stability of a peroxo to be primarily dictated by the $\nu_{O\text{-}O}$ and O-O bond strength, the latter of which is reflected in the distance. Based on these parameters alone, one would therefore predict that alkoxide-ligated Mn^{III}-OOR **8** and thiolate-ligated Mn^{III}-OOR **1** would have similar stabilities (Table 5.3). However, despite the similarities, alkoxide-ligated Mn^{III}-OOR **8** is considerably more stable (Figure 5.20 and 5.21) than the corresponding thiolate derivative **1**. At 20 °C, DCM solutions of thiolate-ligated **1** are stable for ~30 minutes ($t_{1/2}^{293K}$ = 249 sec, k_1^{293K} = 2.78 x 10^{-3} sec^{-1}),[27] whereas DCM solution of **8**, are stable for several hours at 25 °C ($t_{1/2}^{298K}$ = 6730 sec, k_{obs}^{298K} = 1.03 x 10^{-4} = 1.03 x 10^{-4} sec^{-1}, Figure 5.20, Table 5.3) Alkoxide-ligated **8** is not only more stable than thiolate-ligated *tert*-butylperoxo-**1**, but it is also more stable than thiolate-ligated $[Mn^{III}(S^{Me2}N_4(6\text{-Me-DPPN}))(OO^tBu)]^+$ (**4**), $[Mn^{III}(S^{Me2}N_4(quinoEN))(OO^tBu)]^+$ (**10**), and $[Mn^{III}(S^{Me2}N_4(quinoPN))(OO^tBu)]^+$ (**11**) (Table 5.3), demonstrating a consistent trend.[27] Carboxamide-ligated $[Mn^{III}(OO^tBu)(dpaq^{2Me})]^+$ (**9**) also

decays at a slower rate ($t_{1/2}^{258K}$ = 3200 sec, k^{258K} = 2.17 x 10^{-4} s^{-1}),[38] relative to the thiolate-ligated **1**, **4**, **10**, and **11**.

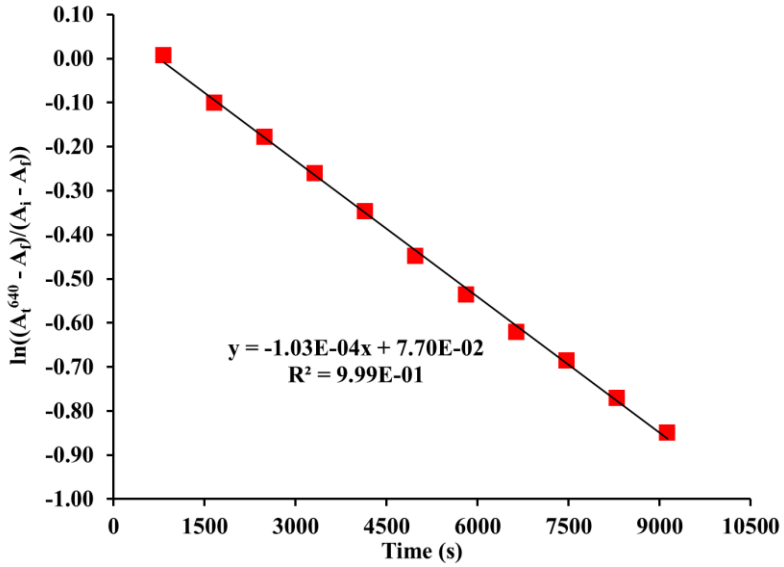

Figure 5.20. First order kinetics plot for the decay of **8** at 298 K. The observed rate constant, k_{obs}, was obtained from the slope.

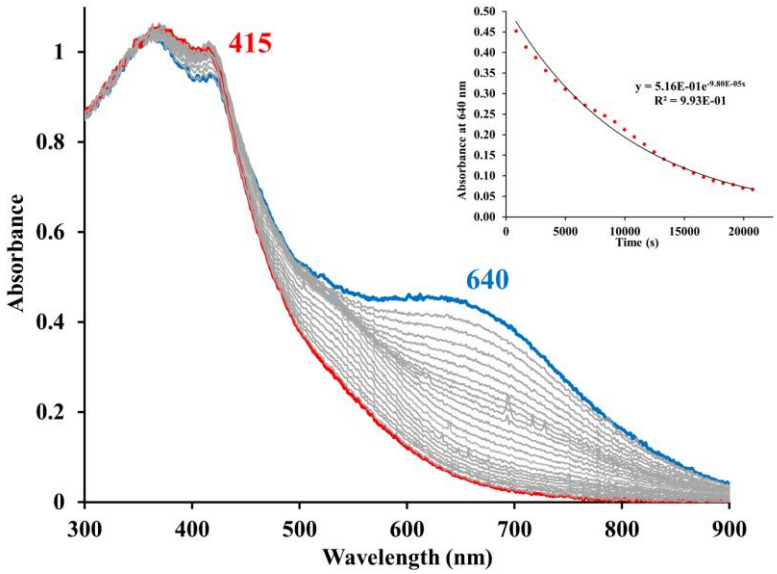

Figure 5.21. EAS spectrum monitoring the decay of [Mn^{III}($O^{Me2}N_4$(6-Me-DPEN))(OO^tBu)](BPh_4) (**8**) in DCM at 298 K over 5.76 hours, demonstrating its increased stability relative to the thiolate derivative [Mn^{III}($S^{Me2}N_4$(6-Me-DPEN))(OO^tBu)]$^+$ (**1**). Insert shows the exponential decay curve at 640 nm. Spectrum recorded in 13.8 minutes interval. [Mn^{II}(**7**)] = 1.0 mM.

5.3.8 *DFT Minimized Structure and TD-DFT Calculated Spectra*

In order to obtain insights into the relative stabilities of thiolate-ligated **1** versus alkoxide-ligated **8** (*vide supra*) DFT and time-dependent DFT (TD-DFT) calculations were performed using the experimentally obtained electronic absorption spectrum (Figure 5.9), vibrational spectrum (Figure 5.11), and crystal structure (Table 5.4, Figure 5.16) as calibration points. The optimized structure was calculated using the ORCA v.4.1.1 quantum chemistry package,[41] the B3LYP functional with a polarized triplezeta def2-TZVP basis set, a def2/J auxiliary basis set for coulombic density fitting,[41] and a resolution of identity (RI) chain-of-spheres (RIJCOSX) approximation.[43,44] The crystallographic coordinates and a high-spin state (S = 2 for Mn^{III}) were used as a starting point. Scalar relativistic effects were accounted for using the ZORA approximation and dispersion correction with DBJ. Metrical parameters associated with the DFT optimized structures are within ≤ 2.0% for **1** (Table 5.5) and ≤ 3.98% for **8** (Table 5.6) of the crystallographically determined parameters. Importantly, the DFT calculated structures display elongated Mn•••N^{Ar} bonds, well outside the sum of covalent radii, in agreement with the crystal structures. (Table 5.5 and 5.6)

Table 5.5. DFT calculated versus crystallographically measured bond distances for thiolate-ligated [Mn^{III}($S^{Me2}N_4$(6-Me-DPEN))(OO^tBu)](BPh_4) (**1**).

Bond	X-ray Bond Distance (Å)	Calculated Bond Distance (Å)	% Error
Mn-N(1)	2.015	2.041	1.29
Mn-N(2)	2.163	2.200	1.71
Mn-N(3)	2.353	2.346	0.30
Mn-N(4)	2.470	2.521	2.06
Mn-S(1)	2.241	2.252	0.49
Mn-O(1)	1.852	1.824	1.51
O(1)-O(2)	1.469	1.451	1.23
		Average error	1.23

Table 5.6. DFT calculated versus crystallographically measured bond distances for alkoxide-ligated $[Mn^{III}(O^{Me2}N_4(6\text{-Me-DPEN}))(OO^tBu)](BPh_4)$ (**8**).

Bond	X-ray Bond Distance (Å)	Calculated Bond Distance (Å)	% Error
Mn-N(1)	2.004	2.025	1.05
Mn-N(2)	2.161	2.247	3.98
Mn-N(3)	2.355	2.316	1.66
Mn-N(4)	2.431	2.362	2.84
Mn-O(1)	1.854	1.837	0.92
Mn-O(2)	1.856	1.836	1.08
O(2)-O(3)	1.473	1.454	1.29
		Average error	1.83

The time-dependent density function theory (TD-DFT) calculated electronic absorption spectrum of alkoxide-ligated **8** is in good agreement with the experimental spectrum. (Figure 5.22, right) The calculated vibrational spectrum of **8** (Figure 5.23) is also in good agreement with the experimentally obtained spectrum (Figure 5.11), and reveals, in addition to the $\upsilon_{O\text{-}O}$ stretch at 880 cm^{-1}, a Mn-peroxo stretch at $\upsilon_{Mn\text{-}O}$ = 686 cm^{-1}. The TD-DFT calculated electronic absorption spectrum of thiolate-ligated **1** is also in good agreement with the experimentally obtained spectrum (Figure 5.22, left). The low energy bands in the ~600 nm region of the spectra are shown to involve a peroxo π^*(O-O) → σ^*(Mn(d_{xy})-O, N) charge transfer transition with **8** (Figure 5.24), and a π^*(O-O) + S_π → σ^*(Mn(d_{xy})-S, N) charge transfer transition with **1** (Figure 5.25). The highest occupied molecular orbital (HOMO) of thiolate-ligated **1** possesses significant thiolate sulfur character, in contrast to the HOMO of alkoxide-ligated **8**, which possesses very little alkoxide character. As shown in Figure 5.26 (13), the predominant character of both of these HOMO orbitals is peroxo π^*(O-O) would weaken the peroxo O-O bond, and contrasts with the bonding interaction of alkoxide-ligated **8**. This provides insights as to why the peroxo O-O bond of **1** cleaves more readily than that of **8** (*vide infra*).

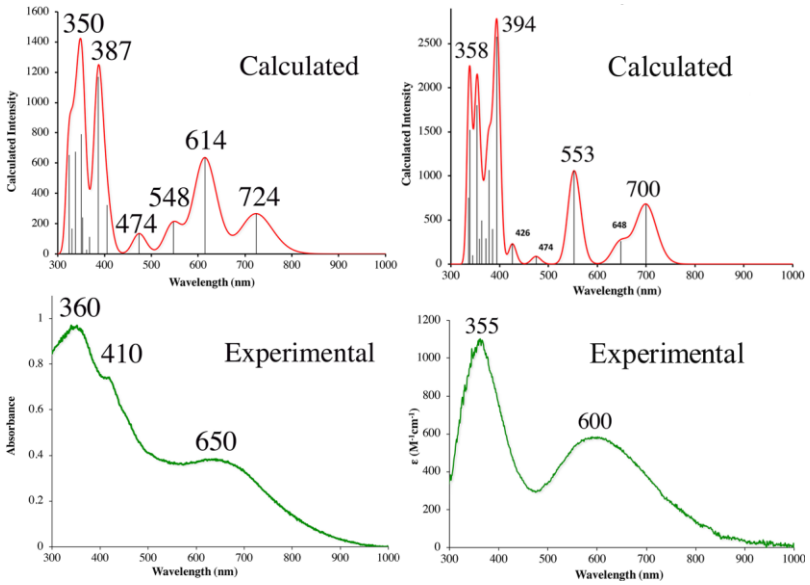

Figure 5.22. TD-DFT calculated (top) versus experimental (bottom) electronic absorption spectra of thiolate-ligated RS-Mn-OOR (**1**, left) and alkoxide ligated RO-Mn-OOR (**8**, right).

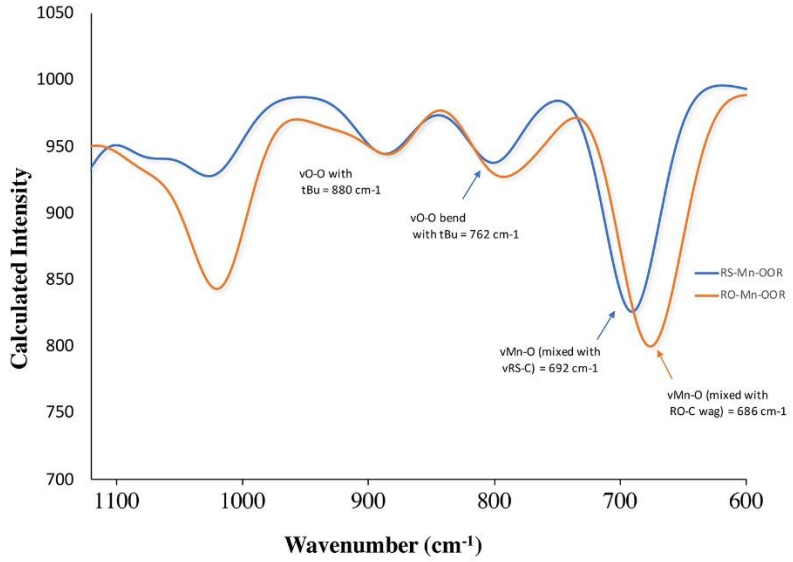

Figure 5.23. DFT calculated vibrational spectrum for alkoxide-ligated **8** (orange) versus thiolate-ligated **1** (blue).

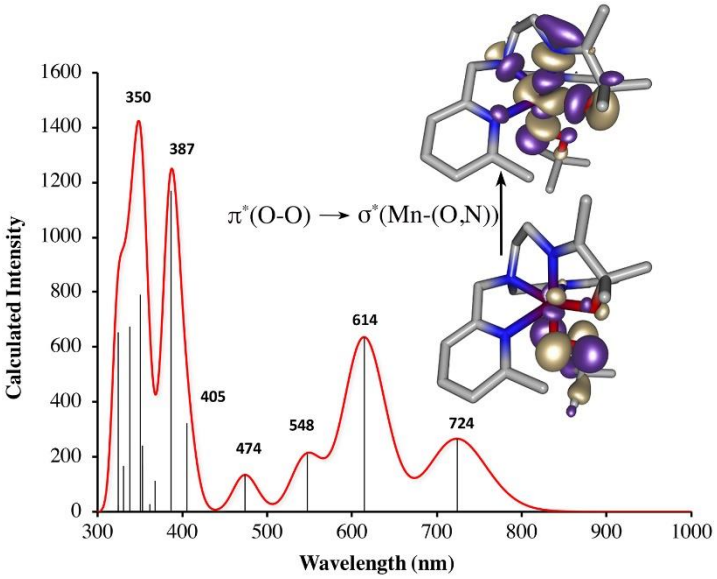

Figure 5.24. Time-dependent density functional theory (TD-DFT) calculated electronic absorption spectrum of alkoxide-ligated RO-Mn-OOR (**8**) including natural transition orbitals (NTO) describing the charge transfer (CT) transitions. Illustrated is the low energy peroxo π*(O-O) → σ*(Mn-L) transition and the associated donor and acceptor orbitals.

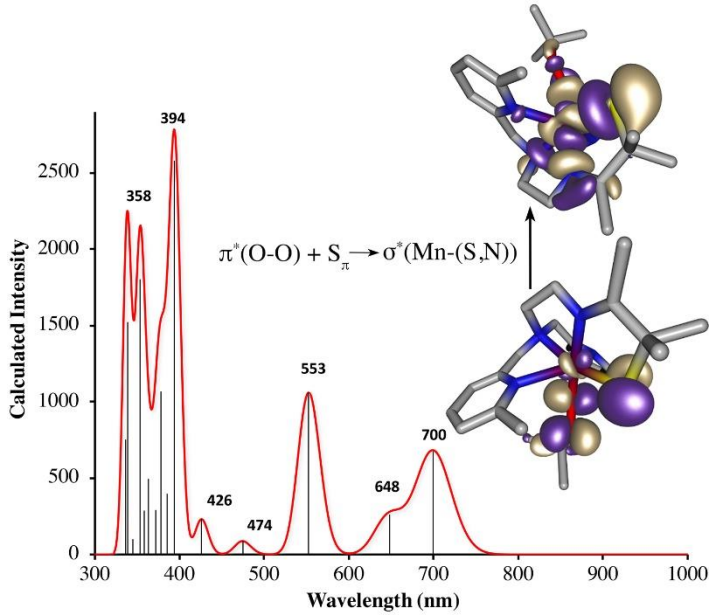

Figure 5.25. Time-dependent density functional theory (TD-DFT) calculated electronic absorption spectrum of thiolate-ligated RS-Mn-OOR (**1**) including natural transition orbitals (NTO) describing the charge transfer (CT) transitions. Illustrated is the low energy peroxo S_π + π*(O-O) → σ*(Mn-L) transition and the associated donor and acceptor orbitals.

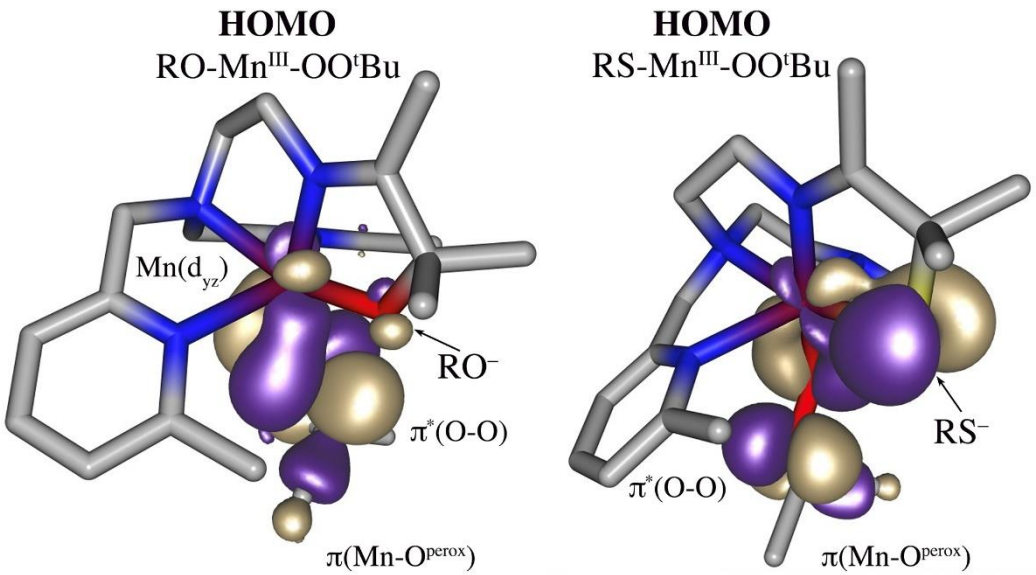

Figure 5.26. Electronic structure calculations show that the highest occupied orbital of **1** (right) contains significant thiolate sulfur character, in contrast to that of **8** (left), which has less alkoxide oxygen character.

The relative stability of alkoxide-ligated **8** versus thiolate-ligated **1** also correlates with metal ion Lewis acidity. This is in agreement with our previous studies where we showed that, albeit for peroxo-bridged dimers, the relative stability of Mn-peroxo intermediates ($t_{1/2}$(6-Me-pyridine) = 249 sec, $t_{1/2}$(quinoline) = 23 sec, and $t_{1/2}$(6-MeO-pyridine) = 11.5 sec) correlates with metal ion Lewis acidity.[33] In our previous study, the primary coordination sphere were identical. Only the ligand scaffold and substituents were varied. Peroxo stability was shown mainly to be dictated by the mean Mn•••N^{Ar} distance (2.56 Å (6-Me-pyridine), 2.5 Å (quinoline), and 2.413 Å (6-MeO-pyridine).[33] While preferrable, experimentally measured redox potentials were not used, since the limited stability of the peroxo complexes precluded their measurement.

In the current study, we varied the heteroatom in the primary coordination sphere (RO^- versus RS^-) while maintaining an identical ligand framework. As shown in Table 5.7, the calculated Mulliken charge, and thus metal ion Lewis acidity, is greater for alkoxide-ligated **8** (+0.451) relative to thiolate-ligated **1** (+0.306). This reflects the electron donating properties of

thiolates. That the alkoxide is less electron donating is reflected in the higher negative Mulliken charge of the alkoxide oxygen (-0.531) relative to the thiolate sulfur (-0.327).

Table 5.7. Comparison of DFT Calculated Mulliken Charges for Thiolate-ligated **1** versus Alkoxide-ligated **8**.

Atom	Alkoxide-ligated 8	Thiolate-ligated 1
Mn	+0.451	+0.306
$O^{Alkoxide}$	-0.531	N/A
$S^{Thiolate}$	N/A	-0.327
$O^{Peroxo, proximal}$	-0.396	-0.375
$O^{Peroxo, distal}$	-0.180	-0.166

5.4 Summary and Conclusions

The work herein shows that peroxo O-O bonds cleave more readily when there is a thiolate in the coordination sphere. One of few crystallographically characterized Mn-alkylperoxo compounds is reported. We show that the previously established correlations between structural and spectroscopic parameters is adhered to, even when an alkoxide is incorporated into the coordination sphere in place of a thiolate. Despite their structural and spectroscopic similarities, however, alkoxide-ligated RO-Mn^{III}-OO^{t}Bu, was shown to be an order of magnitude more stable than the corresponding thiolate-ligated RS-Mn^{III}-OO^{t}Bu derivative. Insight into the factors responsible were provided by DFT and TD-DFT calculations. The highest occupied molecular orbital (HOMO) of thiolate-ligated RS-Mn^{III}-OO^{t}Bu is shown to possess significant sulfur character and π-backdonation from the thiolate competes with π-backdonation from the peroxo π*(O-O). The latter helps to stabilize the peroxo O-O bond since it facilitates the removal of electron density from an antibonding orbital. In addition, DFT calculated Mulliken charges show that the Mn ion of alkoxide-ligated RO-Mn^{III}-OO^{t}Bu is more Lewis

acidic than that of thiolate-ligated RS-Mn^{III}-OO^{t}Bu. The significance of these results is that it helps to explain why the majority of Mn-enzymes incorporate O- and/or N-ligands as opposed to ^{cry}S-ligands. This is especially important for the photosynthetic oxygen evolving complex, which catalyzes O-O bond formation as opposed to cleavage. This work also provides experimental evidence to support the proposed role of cysteinates in promoting O-O bond cleavage in key metalloenzyme intermediates.

5.5 References

(1) Cotruvo, J. A.; Stubbe, J. An Active Dimanganese(III)-Tyrosyl Radical Cofactor in Escherichia Coli Class Ib Ribonucleotide Reductase. *Biochemistry* **2010**, *49*, 1297–1309.

(2) Jackson, T. A.; Karapetian, A.; Miller, A. F.; Brunold, T. C. Probing the Geometric and Electronic Structures of the Low-Temperature Azide Adduct and the Product-Inhibited Form of Oxidized Manganese Superoxide Dismutase. *Biochemistry* **2005**, *44*, 1504–1520.

(3) Skrzypczak-Jankun, E.; Bross, R. A.; Carroll, R. T.; Dunham, W. R.; Funk, J. O. Three-Dimensional Structure of a Purple Lipoxygenase. *J. Am. Chem. Soc.* **2001**, *123*, 10814–10820.

(4) Oliw, E. H.; Jernerén, F.; Hoffmann, I.; Sahlin, M.; Garscha, U. Manganese Lipoxygenase Oxidizes Bis-Allylic Hydroperoxides and Octadecenoic Acids by Different Mechanisms. *Biochim. Biophys. Acta - Mol. Cell Biol. Lipids 1811*, 138–147.

(5) Kovaleva, E. G.; Lipscomb, J. D. Crystal Structures of Fe2+ Dioxygenase Superoxo, Alkylperoxo, and Bound Product Intermediates. *Science (80-.).* **2007**, *316*, 453–457.

(6) Mbughuni, M. M.; Chakrabarti, M.; Hayden, J. A.; Meier, K. K.; Dalluge, J. J.; Hendrich, M. P.; Münck, E.; Lipscomb, J. D. Oxy Intermediates of Homoprotocatechuate 2,3-

Dioxygenase: Facile Electron Transfer between Substrates. *Biochemistry* **2011**, *50*, 10262–10274.

(7) Liu, W.; Groves, J. T. Manganese Catalyzed C-H Halogenation. *Acc. Chem. Res.* **2015**, *48*, 1727–1735.

(8) Shook, R. L.; Peterson, S. M.; Greaves, J.; Moore, C.; Rheingold, A. L.; Borovik, A. S. Catalytic Reduction of Dioxygen to Water with a Monomeric Manganese Complex at Room Temperature. *J. Am. Chem. Soc.* **2011**, *133*, 5810–5817.

(9) Goldsmith, C. R.; Cole, A. P.; Stack, T. D. P. C-H Activation by a Mononuclear Manganese(III) Hydroxide Complex: Synthesis and Characterization of a Manganese-Lipoxygenase Mimic? *J. Am. Chem. Soc.* **2005**, *127*, 9904–9912.

(10) Murphy, A.; Stack, T. D. P. Discovery and Optimization of Rapid Manganese Catalysts for the Epoxidation of Terminal Olefins. *J. Mol. Catal. A Chem.* **2006**, *251*, 78–88.

(11) Cox, N.; Pantazis, D. A.; Neese, F.; Lubitz, W. Biological Water Oxidation. *Acc. Chem. Res.* **2013**, *46*, 1588–1596.

(12) Paul, S.; Neese, F.; Pantazis, D. A. Structural Models of the Biological Oxygen-Evolving Complex: Achievements, Insights, and Challenges for Biomimicry. *Green Chem.* **2017**, *19*, 2309–2325.

(13) Suga, M.; Akita, F.; Hirata, K.; Ueno, G.; Murakami, H.; Nakajima, Y.; Shimizu, T.; Yamashita, K.; Yamamoto, M.; Ago, H.; Shen, J. R. Native Structure of Photosystem II at 1.95A° Resolution Viewed by Femtosecond X-Ray Pulses. *Nature* **2015**, *517*, 99–103.

(14) Gilbert, N. C.; Bartlett, S. G.; Waight, M. T.; Neau, D. B.; Boeglin, W. E.; Brash, A. R.; Newcomer, M. E. The Structure of Human 5-Lipoxygenase. *Science (80-.).* **2011**, *331*, 217–219.

(15) Sheng, Y.; Gralla, E. B.; Schumacher, M.; Cascio, D.; Cabelli, D. E.; Valentine, J. S. Six-Coordinate Manganese(3+) in Catalysis by Yeast Manganese Superoxide Dismutase. *Proc. Natl. Acad. Sci. U. S. A.* **2012**, *109*, 14314–14319.

(16) Wu, A. J.; Penner-Hahn, J. E.; Pecoraro, V. L. Structural, Spectroscopic, and Reactivity Models for the Manganese Catalases. *Chemical Reviews*. American Chemical Society February 2004, pp 903–938.

(17) Gunderson, W. A.; Zatsman, A. I.; Emerson, J. P.; Farquhar, E. R.; Que, L.; Lipscomb, J. D.; Hendrich, M. P. Electron Paramagnetic Resonance Detection of Intermediates in the Enzymatic Cycle of an Extradiol Dioxygenase. *J. Am. Chem. Soc.* **2008**, *130*, 14465–14467.

(18) Hamberg, M.; Chao, S.; Oliw, E. Manganese Lipoxygenase. *J. Biol. Chem.* **1998**, *273*, 13080–13088.

(19) Jackson, T. A.; Brunold, T. C. Combined Spectroscopic/Computational Studies on Fe-and Mn-Dependent Superoxide Dismutases: Insights into Second-Sphere Tuning of Active Site Properties. *Acc. Chem. Res.* **2004**, *37*, 461–470.

(20) Vance, C. K.; Miller, A. F. Novel Insights into the Basis for Escherichia Coli Superoxide Dismutase's Metal Ion Specificity from Mn-Substituted FeSOD and Its Very High Em. *Biochemistry* **2001**, *40*, 13079–13087.

(21) Sen, A.; Hongpaisan, J. Hippocampal Microvasculature Changes in Association with Oxidative Stress in Alzheimer's Disease. **2018**.

(22) De Leo, M. E.; Borrello, S.; Passantino, M.; Palazzotti, B.; Mordente, A.; Daniele, A.; Filippini, V.; Galeotti, T.; Masullo, C. *Oxidative Stress and Overexpression of Manganese Superoxide Dismutase in Patients with Alzheimer's Disease*; 1998.

(23) Ihara, Y.; Chuda, D.; Kuroda, S.; Hayabara, T. Hydroxyl Radical and Superoxide Dismutase in Blood of Patients with Parkinson's Disease: Relationship to Clinical Data. *J. Neurol. Sci.* **1999**, *170*, 90–95.

(24) Yano, J.; Yachandra, V. Mn4Ca Cluster in Photosynthesis: Where and How Water Is Oxidized to Dioxygen. *Chem. Rev.* **2014**, *114*, 4175–4205.

(25) Cox, N.; Retegan, M.; Neese, F.; Pantazis, D. A.; Boussac, A.; Lubitz, W. Electronic Structure of the Oxygen-Evolving Complex in Photosystem II Prior to O-O Bond Formation. *Science (80-.).* **2014**, *345*, 804–808.

(26) Umena, Y.; Kawakami, K.; Shen, J. R.; Kamiya, N. Crystal Structure of Oxygen-Evolving Photosystem II at a Resolution of 1.9Å. *Nature* **2011**, *473*, 55–60.

(27) Coggins, M. K.; Martin-Diaconescu, V.; Debeer, S.; Kovacs, J. A. Correlation between Structural, Spectroscopic, and Reactivity Properties within a Series of Structurally Analogous Metastable Manganese(III)-Alkylperoxo Complexes. *J. Am. Chem. Soc.* **2013**, *135*, 4260–4272.

(28) Geiger, R. A.; Wijeratne, G. B.; Day, V. W.; Jackson, T. A. Steric and Electronic Influences on the Structures of Peroxomanganese(III) Complexes Supported by Tetradentate Ligands. *Eur. J. Inorg. Chem.* **2012**, *2012*, 1598–1608.

(29) Geiger, R. A.; Chattopadhyay, S.; Day, V. W.; Jackson, T. A. A Series of Peroxomanganese(III) Complexes Supported by Tetradentate Aminopyridyl Ligands: Detailed Spectroscopic and Computational Studies. *J. Am. Chem. Soc.* **2010**, *132*, 2821–2831.

(30) Geiger, R. A.; Leto, D. F.; Chattopadhyay, S.; Dorlet, P.; Anxolabéhère-Mallart, E.; Jackson, T. A. Geometric and Electronic Structures of Peroxomanganese(III) Complexes

Supported by Pentadentate Amino-Pyridine and -Imidazole Ligands. *Inorg. Chem.* **2011**, *50*, 10190–10203.

(31) Coggins, M. K.; Kovacs, J. A. Structural and Spectroscopic Characterization of Metastable Thiolate-Ligated Manganese(III)-Alkylperoxo Species. *J. Am. Chem. Soc.* **2011**, *133*, 12470–12473.

(32) Coggins, M. K.; Sun, X.; Kwak, Y.; Solomon, E. I.; Rybak-Akimova, E.; Kovacs, J. A. Characterization of Metastable Intermediates Formed in the Reaction between a Mn(II) Complex and Dioxygen, Including a Crystallographic Structure of a Binuclear Mn(III)-Peroxo Species. *J. Am. Chem. Soc.* **2013**, *135*, 5631–5640.

(33) Poon, P. C. Y.; Dedushko, M. A.; Sun, X.; Yang, G.; Toledo, S.; Hayes, E. C.; Johansen, A.; Piquette, M. C.; Rees, J. A.; Stoll, S.; Rybak-Akimova, E.; Kovacs, J. A. How Metal Ion Lewis Acidity and Steric Properties Influence the Barrier to Dioxygen Binding, Peroxo O-O Bond Cleavage, and Reactivity. *J. Am. Chem. Soc.* **2019**, *141*, 15046–15057.

(34) Kovacs, J. A. Tuning the Relative Stability and Reactivity of Manganese Dioxygen and Peroxo Intermediates via Systematic Ligand Modification. *Acc. Chem. Res.* **2015**, *48*, 2744–2753.

(35) Borovik, A. S. Bioinspired Hydrogen Bond Motifs in Ligand Design: The Role of Noncovalent Interactions in Metal Ion Mediated Activation of Dioxygen. *Acc. Chem. Res.* **2005**, *38*, 54–61.

(36) Stone, K. L.; Borovik, A. S. Lessons from Nature: Unraveling Biological C–H Bond Activation. *Curr. Opin. Chem. Biol.* **2009**, *13*, 114–118.

(37) Shook, R. L.; Gunderson, W. A.; Greaves, J.; Ziller, J. W.; Hendrich, M. P.; Borovik, A. S. A Monomeric MnIII-Peroxo Complex Derived Directly from Dioxygen. *J. Am. Chem.*

Soc. **2008**, *130*, 8888–8889.

(38) Parham, J. D.; Wijeratne, G. B.; Rice, D. B.; Jackson, T. A. Spectroscopic and Structural Characterization of Mn(III)-Alkylperoxo Complexes Supported by Pentadentate Amide-Containing Ligands. *Inorg. Chem.* **2018**, *57*, 2489–2502.

(39) Coggins, M. K.; Toledo, S.; Shaffer, E.; Kaminsky, W.; Shearer, J.; Kovacs, J. A. Characterization and Dioxygen Reactivity of a New Series of Coordinatively Unsaturated Thiolate-Ligated Manganese(II) Complexes. *Inorg. Chem.* **2012**, *51*, 6633–6644.

(40) Coggins, M. K. Small Molecule Activation Studies Involving Thiolate-Ligated Manganese(II) Complexes and Biologically-Relevant Oxidants, Univeristy of Washington, Seattle, 2012.

(41) Neese, F. The ORCA Program System. *Wiley Interdiscip. Rev. Comput. Mol. Sci.* **2012**, *2*, 73–78.

(42) Grimme, S.; Ehrlich, S.; Goerigk, L. Effect of the Damping Function in Dispersion Corrected Density Functional Theory. *J. Comput. Chem.* **2011**, *32*, 1456–1465.

(43) Adamo, C.; Barone, V. Toward Reliable Density Functional Methods without Adjustable Parameters: The PBE0 Model. *J. Chem. Phys.* **1999**, *110*, 6158–6170.

(44) Neese, F.; Wennmohs, F.; Hansen, A. Efficient and Accurate Local Approximations to Coupled-Electron Pair Approaches: An Attempt to Revive the Pair Natural Orbital Method. *J. Chem. Phys.* **2009**, *130*, 114108–114018.

(45) Hirata, S.; Head-Gordon, M. *Time-Dependent Density Functional Theory within the Tamm-Dancoff Approximation*; 1999; Vol. 314.

(46) Neese, F.; Olbrich, G. Efficient Use of the Resolution of the Identity Approximation in Time-Dependent Density Functional Calculations with Hybrid Density Functionals.

Chem. Phys. Lett. **2002**, *362*, 170–178.

(47) Pettersen, E. F.; Goddard, T. D.; Huang, C. C.; Couch, G. S.; Greenblatt, D. M.; Meng, E. C.; Ferrin, T. E. UCSF Chimera - A Visualization System for Exploratory Research and Analysis. *J. Comput. Chem.* **2004**, *25*, 1605–1612.

(48) Bruker (2007) APEX2 (Version 2.1-4), SAINT (Version 7.34A), SADABS (Version 2007/4), BrukerAXS Inc, Madison, Wisconsin, USA.

(49) Sheldrick, G. M. SHELXT - Integrated Space-Group and Crystal-Structure Determination. *Acta Crystallogr. Sect. A Found. Crystallogr.* **2015**, *71*, 3–8.

(50) Altomare, A.; Cascarano, G.; Giacovazzo, C.; Guagliardi, A. *Completion and Refinement of Crystal Structures with SIR92*; 1993; Vol. 26.

(51) Altomare, A.; Burla, M. C.; Camalli, M.; Cascarano, G. L.; Giacovazzo, C.; Guagliardi, A.; Moliterni, A. G. G.; Polidori, G.; Spagna, R. SIR97: A New Tool for Crystal Structure Determination and Refinement. *J. Appl. Cryst* **1999**, *32*, 115–119.

(52) Sheldrick, G. M. SHELXL97, Program for the Refinement of Crystal Structures, University of Göttingen, Germany, 1997. University of G ttingen 2000.

(53) Mackay, S.; Edwards, C.; Henderson, A.; Gilmore, C.; Stewart, N.; Shankland, K.; Donald, A. MaXus: A Computer Program for the Solution and Refinement of Crystal Structures from Diffraction Data. University of Glasgow, Scotland 1997.

(54) Waasmaier, D.; Kirfel, A. New Analytical Scattering-factor Functions for Free Atoms and Ions. *Acta Crystallogr. Sect. A* **1995**, *51*, 416–431.

(55) Kennepohl, P.; Neese, F.; Schweltzer, D.; Jackson, H. L.; Kovacs, J. A.; Solomon, E. I. Spectroscopy of Non-Heme Iron Thiolate Complexes: Insight into the Electronic Structure of the Low-Spin Active Site of Nitrile Hydratase. *Inorg. Chem.* **2005**, *44*, 1826–1836.

(56) Kovacs, J. A.; Brines, L. M. Understanding How the Thiolate Sulfur Contributes to the Function of the Non-Heme Iron Enzyme Superoxide Reductase. *Acc. Chem. Res.* **2007**, *40*, 501–509.

(57) Kim, J.; Zang, Y.; Costas, M.; Harrison, R. G.; Wilkinson, E. C.; Que, L. A Nonheme Iron(II) Complex That Models the Redox Cycle of Lipoxygenase. *J. Biol. Inorg. Chem.* **2001**, *6*, 275–284.

(58) Kitajima, N.; Komatsiizaki, H.; Hikichi, S.; Osawa, M.; Moro-oka, Y. A Monomeric Side-On Peroxo Manganese(III) Complex: Mn(O2)(3, 5-IPr2pzH)(HB(3, 5-IPr2pz)3). *J. Am. Chem. Soc.* **1994**, *116*, 11596–11597.

(59) Singh, U. P.; Sharma, A. K.; Hikichi, S.; Komatsuzaki, H.; Moro-Oka B, Y.; Akita, M. Hydrogen Bonding Interaction between Imidazolyl N-H Group and Peroxide: Stabilization of Mn(III)-Peroxo Complex Tp IPr2 Mn(g 2-O 2)(Im Me H) (Im Me H = 2-Methylimidazole) Q. *Inorganica Chim. Acta* **2006**, *359*, 4407–4411.

(60) Badger, R. M. The Relation between the Internuclear Distances and Force Constants of Molecules and Its Application to Polyatomic Molecules. *J. Chem. Phys.* **1935**, *3*, 710–714.

(61) Green, M. T. Application of Badger's Rule to Heme and Non-Heme Iron-Oxygen Bonds: An Examination of Ferryl Protonation States. *J. Am. Chem. Soc.* **2006**, *128*, 1902–1906.

(62) Coggins, M. K.; Downing, A. N.; Kaminsky, W.; Kovacs, J. A. Comparison of Two Mn IV Mn IV -Bis-μ-Oxo Complexes {[Mn IV (N 4 (6-Me-DPEN))] 2 (μ-O) 2 } 2+ and {[Mn IV (N 4 (6-Me-DPPN))] 2 (μ-O) 2 } 2+. *Acta Crystallogr. Sect. E Crystallogr. Commun.* **2020**, *76*, 1042–1046.

(63) Shannon, R. D. Revised Effective Ionic Radii and Systematic Studies of Interatomie Distances in Halides and Chaleogenides. *Acta Crystallogr. Sect. A* **1976**, *32*, 751–767.

(64) Annaraj, J.; Cho, J.; Lee, Y.-M.; Kim, S. Y.; Latifi, R.; de Visser, S. P.; Nam, W. Structural Characterization and Remarkable Axial Ligand Effect on the Nucleophilic Reactivity of a Nonheme Manganese(III)-Peroxo Complex. *Angew. Chemie Int. Ed.* **2009**, *48*, 4150–4153.

(65) Vanatta, R. B.; Strouse, C. E.; Hanson, L. K.; Valentine, J. S. [Peroxotetraphenylporphinato] Manganese(III) and [Chlorotetraphenylporphinato] Manganese(II) Anions: Syntheses, Crystal Structures, and Electronic Structures. *J. Am. Chem. Soc.* **1987**, *109*, 1425–1434.